Vers des nouveaux systèmes pi-conjugués pour des applications photovoltaïques

Michèle Chevrier

Collège Doctoral du Languedoc-Roussillon

THÈSE

Pour obtenir le grade de

Docteur

Délivré conjointement par les **Universités de Montpellier et de Mons (Belgique)**

Préparée au sein de l'école doctorale Sciences Chimiques Balard (ED459)

Et de l'unité de recherche Institut Charles Gerhardt de Montpellier

Spécialité : **Ingénierie moléculaire**

Présentée par **Michèle CHEVRIER**

Towards new π-conjugated systems for photovoltaic applications

Soutenue le 15 septembre 2016 devant le jury composé de

Pr. Philippe DUBOIS, Université de Mons	Directeur de thèse
Pr. Ahmad MEHDI, Université de Montpellier	Directeur de thèse
Pr. Roberto LAZZARONI, Université de Mons	Co-directeur de thèse
Dr. Sébastien CLEMENT, Université de Montpellier	Co-encadrant de thèse
Pr. Mario LECLERC, Université de Laval (Québec)	Rapporteur
Dr. Philippe GROS, Université de Lorraine	Rapporteur
Dr. Johann BOUCLE, Université de Limoges	Examinateur
Dr. Bruno AMEDURI, Université de Montpellier	Examinateur

UMONS Université de Mons

UNIVERSITÉ DE MONTPELLIER

REMERCIEMENTS

Je voudrais commencer ces remerciements par le Professeur Philippe Dubois, le Professeur Ahmad Mehdi, le Professeur Roberto Lazzaroni et le Docteur Sébastien Clément, mes superviseurs durant cette thèse, pour l'opportunité qu'ils m'ont donnée de réaliser cette thèse en cotutelle entre les universités de Mons et Montpellier, et, la confiance qu'ils m'ont accordée tout au long de ces trois années. Merci pour votre encadrement, vos conseils et votre soutien pendant ces trois ans.

Je tiens à remercier tout particulièrement Sébastien, qui m'a encadré tous les jours pendant trois ans et sans qui je n'aurais pu arriver là aujourd'hui. Je ne saurais jamais le remercier pour tout ce qu'il a fait pour moi pendant ces trois années et qui je sais continuera encore à être là pour moi dans le futur.

Je voudrais ensuite remercier M. Mario Leclerc, Professeur à l'Université de Laval au Québec et M. Philippe Gros, Directeur de Recherche à l'Université de Lorraine, pour avoir accepté de juger mon travail.

Mes plus sincères remerciements vont également à Mr. Bruno Ameduri, Directeur de Recherche à l'Université de Montpellier et à Mr. Johann Bouclé, Maitre de Conférences à l'Université de Limoges pour avoir accepté d'examiner cette thèse.

Je tiens également à remercier toutes les personnes avec qui j'ai eu le plaisir de collaborer pendant ces trois années et elles sont nombreuses, tant cette thèse a été riche. Je commence tout d'abord par Mr. Sébastien Richeter, Maître de Conférences à l'Université de Montpellier, qui m'a aidé scientifiquement, notamment dans la chimie complexe des porphyrines, mais aussi humainement, pour tous les moments amicaux qu'on a passés ensemble. Un grand merci à Mr. Mathieu Surin, Chercheur FNRS, qui m'a formé à l'AFM et qui m'a permis d'obtenir nos célèbres « autoroutes de fibrilles ». Merci à Pascal Gerbaux et Julien de Winter d'avoir analysé mes polymères en spectrométrie de masse, même quand il n'y avait pas grand-chose à analyser ☺ Je tiens également à remercier Rachel C. Evans, Judith E. Houston pour toutes les analyses photophysiques réalisées durant cette thèse : les $q^{-\alpha}$ n'ont plus de secret pour moi…ou peut-être que si, en fait ☺ Je tiens également à exprimer toute ma gratitude à Mr. Wouter Maes, Professeur à l'Université de Hasselt (Belgique) et à Mr. Jurgen Kesters, son doctorant puis post-doctorant, pour l'étude des polymères en cellules à hétérojonction en volume. Un remerciement tout particulier à Jurgen qui m'a formé à la fabrication de cellules à hétérojonction durant un court séjour à Hasselt. Un grand merci à

Bernard Ratier qui m'a accueillie dans son laboratoire Optoplast et à nouveau, mille mercis à Johann Bouclé qui m'a encadré durant 3 mois au sein de ce laboratoire, qui a pris le temps de me former à la fabrication de cellules à colorant tout solide et, qui continue aujourd'hui de partager ses connaissances avec moi.

J'exprime toute ma sympathie à mes collègues du CMOS, d'IMNO, du SMPC et du CMN pour leur aide, leurs conseils et leur soutien. Je ne peux malheureusement pas tous les citer mais certains auront quand même droit à cette chance ☺ Je tiens à remercier tout particulièrement Danielle, Jeff, Chingone, Mathieu, Doudou, ma gitane et Coco ; la team 301 du SMPC : Noémie, Nicolas, Hamid, et Rital ; mais aussi Olivier, Antonya, Bertrand W., Alexandre, Rémi, Flopi, Mounch, Ben … Merci pour tous les moments qu'on a passé ensemble, qui ont été très importants durant ces trois ans de recherche intensive. Je finirai par remercier *the best scientific workshop association ever* : Ameni, Lucie, Sutima, Benjamin et Bertrand. On a passé des moments inoubliables durant mes séjours à Mons et on en passera encore beaucoup d'autres dans les années à venir.

Merci également à mes amis, qui sont toujours présents à mes côtés.

Je voudrais finir par les personnes les plus importantes dans ma vie, à savoir mes proches, pour leur soutien indéfectible depuis le début même si pour eux, tout ce qui va suivre dans ce manuscrit s'apparentera à du chinois : mes parents, Sarah, Nicolas, mes grands-parents, Luc, Stéphanie, Maxime et tous les autres à qui je pense mais qu'il serait trop long de citer. Enfin, je tiens à remercier tout particulièrement JB pour tout le soutien et l'amour que tu m'as apporté tous les jours pendant trois ans et à celui que m'apportera dans les années à venir.

Michèle

Ou Mimi, Mich, Mich-Mich, Blondie (selon les personnes ☺)

ABBREVIATIONS

1Zn	(5,10,15,20-tetrakis(phenyl)porphyrinato)zinc(II)
2Zn	(5,10,15,20-tetrakis(pentafluorophenyl)porphyrinato)zinc(II)
3HT	3-HexylThiophene
3HTBr	3-BromoHexylThiophene
ATR	**A**ttenuated **T**ransmission **R**eflectance
BHJ	**B**ulk-**H**etero**J**unction
Br^-	Bromide
C-AFM	**C**onductive **A**tomic **F**orce **M**icroscopy
CDCA	**C**heno**D**eoxy**C**olic **A**cid
DLS	**D**ynamic **L**ight **S**cattering
$CDCl_3$	Deuterated chloroform
$CHCl_3$	Chloroform
CPE	**C**onjugated **P**oly**E**lectrolyte
~~D~~	Dispersity index
D_h	Hydrodynamic diameter
DCM	**D**i**C**hloro**M**ethane
DS^-	**D**odecyl **S**ulfate
DSC	**D**ifferential **S**canning **C**alorimetry
DSSC	**D**ye-**S**ensitized **S**olar **C**ell
EQE	**E**xternal **Q**uantum **E**fficiency
ESI	**E**lectron **S**pray **I**onization
FF	**F**ill **F**actor
FTIR	**F**ourier **T**ransform **I**nfra**R**ed spectroscopy
FTO	**F**luorine doped **T**in **O**xide
HCl	Hydrochloride acid
HOMO	**H**ighest **O**ccupied **M**olecular **O**rbital
HRMS	**H**igh **R**esolution **M**ass **S**pectrometry
HTM	**H**ole **T**ransporter **M**aterial
ICT	**I**ntramolecular **C**harge **T**ransfer
IPCE	**I**ncident **P**hoton **C**onversion **E**fficiency
ITO	**I**ndium **T**in **O**xide
IR	**I**nfra**R**ed
J_{SC}	Short-circuit current densities
J-V	Current-voltage
KCTP	**K**umada **C**atalyst **T**ransfer **P**olycondensation

λ_{max}	Maximal wavelength
LUMO	Lowest Unoccupied Molecular Orbital
Maldi-ToF	Matrix-assisted laser desorption/ionisation time-of-flight
MeOD	Deuterated methanol
MeOH	Methanol
M_n	Number-averaged molecular weight
Ni(dppp)Cl_2	Dichloro[1,3-bis(diphenylphosphino)propane]nickel(II)
NIR	**N**ear-**I**nfra**R**ed
NMR	**N**uclear **M**agnetic **R**esonance
OPV	**O**rganic **P**hoto**V**oltaic
OS	**O**ctyl**S**ulfate
OVCD	**O**pen-**C**ircuit **V**oltage-**D**ecay
P3HT	**P**oly(**3**-**H**exyl**T**hiophene)
P3HTBr	**P**oly(**3**-(6'-**Br**omo**H**exyl)**T**hiophene
P3HT-*b*-CPE	**P**oly(**3**-**H**exyl**T**hiophene-2,5-diyl)-***b****lock***-**C**onjugated **P**oly**E**lectrolyte diblock copolymer
P3HT-*b*-P3HTBr	**P**oly(**3**-**H**exyl**T**hiophene-2,5-diyl)-***b****lock***-**P**oly[**3**-(6'-**Br**omo**H**exyl)**T**hiophene-2,5-diyl] diblock copolymer
P3HT-*r*-P3HTIm, PTIm	**P**oly(**3**-**H**exyl**T**hiophene-2,5-diyl)-***ran***-**P**oly[**3**-(6'-(1"-**Im**idazolyl)**H**exyl)**T**hiophene-2,5-diyl] random copolymer
PBDTTPD	Poly[[5-(2-ethylhexyl)-5,6-dihydro-4,6-dioxo-4*H*-thieno[3,4-c]pyrrole-1,3-diyl][4,8-bis[(2-ethylhexyl)oxy]benzo[1,2-b:4,5-b']dithiophene-2,6-diyl]]
$PC_{61}BM$	[6,6]-**P**henyl-**C_{61}**-**B**utyric acid **M**ethyl ester
$PC_{71}BM$	[6,6]-**P**henyl-**C_{71}**-**B**utyric acid **M**ethyl ester
PCE, η	**P**ower **C**onversion **E**fficiency
PCDTBT	Poly[N-9'-heptadecanyl-2,7-carbazole-alt-5,5-(4,7-di-2-thienyl-2',1',3'-benzothiadiazole]
PEDOT	**P**oly(3,4-**E**thylene**D**i**O**xy**T**hiophene)
PFOS	**P**er**F**luoro**O**ctyl**S**ulfonate
PS	**P**oly**S**tyrene
PSS	**P**oly(**S**tyrene**S**ulfonate)
RHC	**R**apid **H**eat–**C**ool
Ru	**Ru**thenium
SANS	**S**mall-**A**ngle **N**eutron **S**cattering
SEC	**S**ize **E**xclusion **C**hromatography
SEM	**S**canning **E**lectronic **M**icroscopy
Spiro-OMeTAD	2,2',7,7'-tetrakis(N,N-di-*p*-metoxyphenylamine)-9-9'-spirobifluorene

ss	Solid-state
T_c	**C**rystallization **T**emperature
T_g	**G**lass transition **T**emperature
T_m	**M**elting **T**emperature
TD-DFT	**T**ime-**D**ependent **D**ensity **F**unctional **T**heory
$TFSI^-$	Bis(trifluoromethane)sulfonimide
TGA	**T**hermo**G**ravimetric **A**nalysis
THF	**T**etra**H**ydro**F**uran
TIm	3-[6'-(1''-**Im**idazolyl)hexyl]**T**hiophene
TiO_2	Titanium dioxide
TLC	**T**hin **L**ayer **C**hromatography
TM-AFM	**T**apping-**M**ode **A**tomic **F**orce **M**icroscopy
UV-vis	**U**ltra**V**iolet-**vis**ible
V_{OC}	Open-circuit voltage
v/v	Volume/volume ratio
XRD	**X**-**R**ay **D**iffraction
wt/wt	Weight/weight ratio

TABLE OF CONTENTS

GENERAL INTRODUCTION

1. MOTIVATION

The growing energy needs and increasing environmental concerns during the last century have led to propose alternatives to the use of non-renewable and polluting fossil fuels. Due to the expansion of the world population, the explosion of economic development in emerging countries and the increasing use of technology, a rise of about 30 % in world energy demand is expected by 2040 (Figure 1).

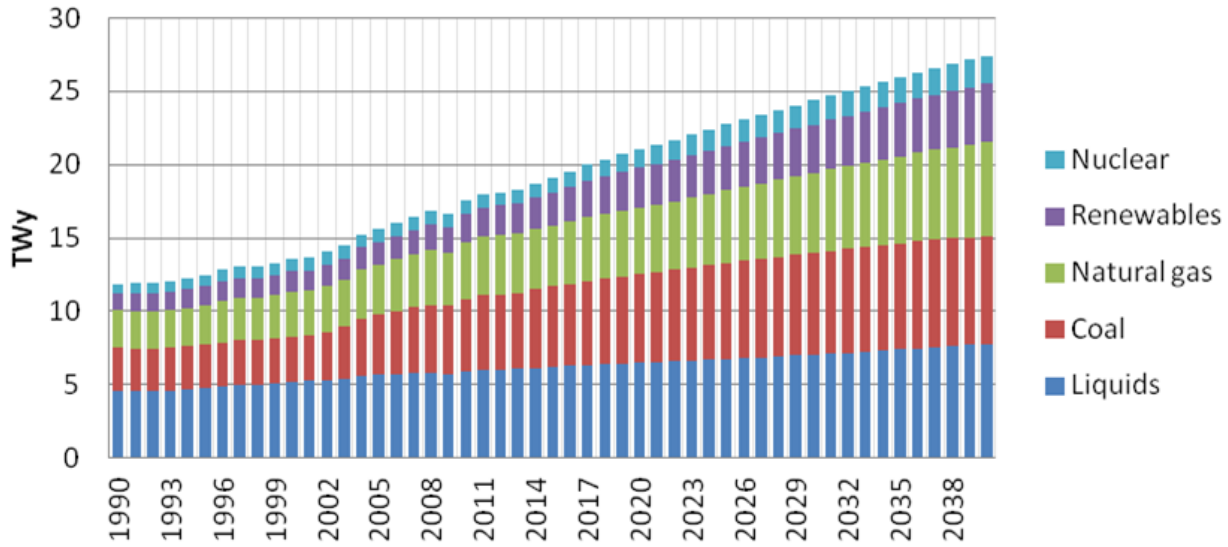

Figure 1 Energy Information Administration (EIA) projection of world energy growth in consumption by fuel type with historical data up to 2013.[1]

Currently, fossil fuels account for 86 % of the energy used by human activities but these resources are being depleted. Besides, carbon dioxide emissions are increasing as a result of fossil fuel combustion and our climate is changing rapidly (Figure 2).

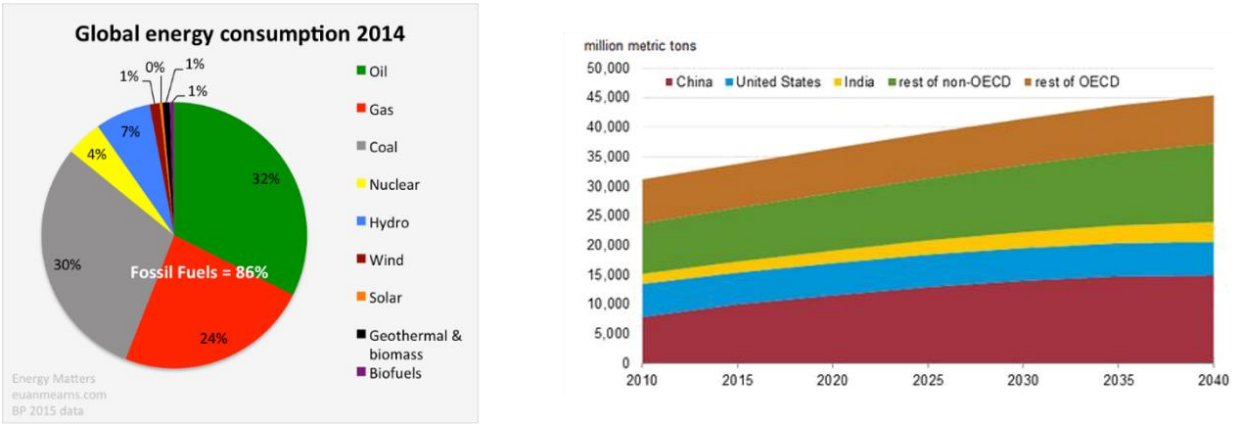

Figure 2 Energy share of global final energy consumption in 2014 (left) and global CO_2 emissions per region (right).[1]

Renewable energies such as wind, sun and water represent credible alternatives to fossil fuels and can provide energy to populations locally and cleanly. In 2009, a report has demonstrated that the global population could be independent from fossil fuels within 2030, if 30 % of renewable energy could be provided by the sun.[2] In 2015, Costa Rica has also proved that by using hydroelectricity and geothermy, it was possible to live for 75 days without burning fossil fuels.[3]

Among the energy sources, the solar one appears as the most promising renewable alternative. The sun creates its energy through a thermonuclear process that converts about 650 000 000 tons of hydrogen into helium every second, inducing heat and electromagnetic radiation. While the heat remains in the sun, maintaining the thermonuclear reaction, the electromagnetic radiation, including visible, infrared and ultraviolet lights, streams out into space in all directions. The amount of solar energy that hits the surface of the Earth in one hour is larger than the total amount of energy that the entire human population requires in one year (it corresponds to 174 PW/year *vs.* needs of 18 TW/year).

The French physicist Edmond Becquerel experimentally demonstrated the photovoltaic effect, *i.e.* the voltage generation in a material upon exposure to light, for the first time in 1839. 177 years later, photovoltaic technology has greatly progressed under the influence of aerospace industry. Now, wafer-based silicon modules with power conversion efficiencies (PCEs) up to 18 % are widely commercialized. The recent example of the *Solar Impulse* plane perfectly demonstrates the high importance that photovoltaic technology has acquired in our society (Figure 3). *Solar Impulse* carries more about 20 000 solar cells integrated to the wing sections to feed power to the electric motors and the surplus energy is stored in lithium batteries.[4] In 2015-2016, *Solar Impulse* is performing the first fossil-fuel-free round-the-world flight.

The solar-powered drone *Zephyr 7* from Airbus has also reached the record of the longest flight without refueling (14 days and 21 minutes) in 2010 (Figure 3). To accomplish this flight, Zephyr used the same technique as the *Solar Impulse* plane: the batteries were charged during the day thanks to sunlight and the accumulated energy is converted into electricity during the night. This method theoretically allows the drone flying indefinitely and thus, may replace the future satellites with a less expensive cost and a much higher flexibility of use.

Regarding photovoltaic technologies, 90 % of the device production is currently supplied by silicon-wafer based solar cells. Nevertheless, this technology has some drawbacks, in particular, the high purity of silicon required (99.9999 %), which results in high cost and energy payback times and its low efficiency under daylight.

Consequently, other low-cost photovoltaic technologies have been investigated based on, for example, the use of organic materials, less expensive and allowing lower fabrication cost.

Additionally to the π-conjugated small molecules or polymer–based organic solar cells, dye-sensitized, quantum dots and perovskite solar cells are also widely investigated, making them fast-advancing solar technologies with PCEs up to 11.9 %, 11.3 % and 22.1 %, respectively.[5]

Figure 3 Pictures of Solar Impulse 2 (left) and Zephyr 7 (right).[6]

In 2016, many records in PCEs for these alternative technologies have been reached. The highest PCE of 25.5 % was reported for perovskite-silicon tandem solar cells by the Hong Kong Polytechnic University. With this innovation, the cost of solar energy is estimated to be 0.35 $/W compared to 0.5 $/W for existing silicon-based solar cells available in the market.[7] A new record was also announced by Heliatek with a PCE of 13.2 % for an OPV multi-junction cell combining three different absorbers.[8] Those three materials are dedicated to efficiently convert green, red and near-infrared light between 450 and 950 nm into electricity. At the same time, First Solar reported its latest PCE record at 22.1 % for cadmium telluride (CdTe) thin-film solar cells. Even if this type of cells represents only 5 % of the worldwide solar power market today, CdTe photovoltaics combine cost effectiveness, reliability, high performance, and the modules are produced three times faster than the multi-crystalline silicon devices.[9]

These different examples show that photovoltaic energy remains one of the most burning issues of our time in view of providing clean and cheap energy to the growing worldwide population.

This co-supervised thesis, carried out between the universities of Montpellier (Institut Charles Gerhardt) and Mons (Laboratory for Polymer and Composites Materials and Laboratory for Chemistry of Novel Materials), falls into this context, aiming at developing new π-conjugated (macro)molecules for organic photovoltaics. These systems have been designed, synthesized, characterized and applied in two types of photovoltaic devices: bulk heterojunction (BHJ) polymer solar cells and dye-sensitized solar cells (DSSCs).

2. THESIS STRUCTURE

This manuscript will be divided into five chapters:

In the first chapter, the state-of-the-art of the research carried out for producing highly efficient bulk heterojunction polymer and dye-sensitized solar cells, including donor/acceptor materials, interfacial materials, photoanode, dye, electrolyte, counter electrode will be summarized.

In Chapter 2, porphyrin-based chromophores will be combined with poly(3-hexylthiophene) (**P3HT**), in order to increase its light-harvesting capability and thus, the power conversion efficiency. These chromophores are particularly interesting since they exhibit large absorption coefficients in the visible region and their reactive positions, *i.e.* four *meso* and eight β-pyrrolic positions, available for functionalization, allow fine tuning of their optical, physical, electrochemical and photovoltaic properties. Based on the results reported in the literature for ternary blends, side- and end-functionalization have been chosen, with the aim of maintaining the solubility and the morphological properties of **P3HT.**

In Chapter 3, polythiophene-based conjugated polyelectrolytes will be used as a cathodic interfacial layer to yield highly efficient BHJ solar cells. The influence of the topology (homopolymer *vs.* copolymer), the cationic side-groups and the anionic counterions will be studied in order to determine the relation between the chemical structure and the observed properties.

Chapter 4 will be devoted to the study of new materials for solid-state (ss)-DSSCs. On one hand, based on the advantages of vegetal dyes, chlorophyll *a* derivatives will be used as dye in ss-DSSCs. On the other hand, the commonly used hole transport material, **spiro-OMeTAD**, which displays some drawbacks, will be replaced by polythiophene derivatives.

Chapter 5 will summarize the characterization and analysis techniques used for our materials and by the fabrication process. The characterization of the organic solar cells based on our materials will be described. Finally, the work performed during this thesis will be concluded and future works will be outlined.

REFERENCES

[1] U.S. Energy Information Administration, *International Energy Outlook*, **2013**.

[2] The Swedish Government, *Government Bills*, **2009**.

[3] Justin Worland, *How Costa Rica went 75 days using only clean electricity*, **2015**. Retrieved May 19, 2016 from www.time.com

[4] La Souris Verte, *Solar Impulse*, **2015**. Retrieved April 27, 2016 from www.solarimpulse.com

[5] U.S. Department of Energy, *National Center for Photovoltaics*, **2016**. Retrieved April 27, 2016 from www.nrel.com

[6] Alain Dupiech, *Record-breaking first civil flight for the Airbus Zephyr*, **2014**. Retrieved April 27, 2016 from www.airbusdefenceandspace.com

[7] Energy Harvesting Journal, *Perovskite-silicon tandem solar cells with highest power conversion*, **2016**. Retrieved April 27, 2016 from www.energyharvestingjournal.com

[8] Heliatek, *Heliatek sets new Organic Photovoltaic world record efficiency of 13.2 %*, 2016. Retrieved April 27, 2016 from www.heliatek.com

[9] Eric Wesoff, *First Solar Hits Record 22.1% Conversion Efficiency for CdTe Solar Cell*, **2016**. Retrieved April 27, 2016 from www.greentechmedia.com

CHAPTER 1

PHOTOVOLTAICS: A GROWING TECHNOLOGY

1. GENERAL PRESENTATION

1.1. ENERGETIC CONTEXT

Faced with dwindling fossil resources, increase of the global population and environmental issues, renewable energies have been the subject of intense research since the last decades.

Among the renewable energies, the solar one, which accounts for only 1.3 % of the total electricity generated by renewable energy sources in 2013, is the only one able to provide enough energy per year to respond to the global demand, around 17 TW average per year (Figure 1.1).[1] Indeed, solar energy has unlimited potential and the amount of energy hitting the Earth's surface in one hour is roughly equal to the entire energy consumption of all human activity per year. Light energy is abundantly available and could be used to a far greater extent than today.[2]

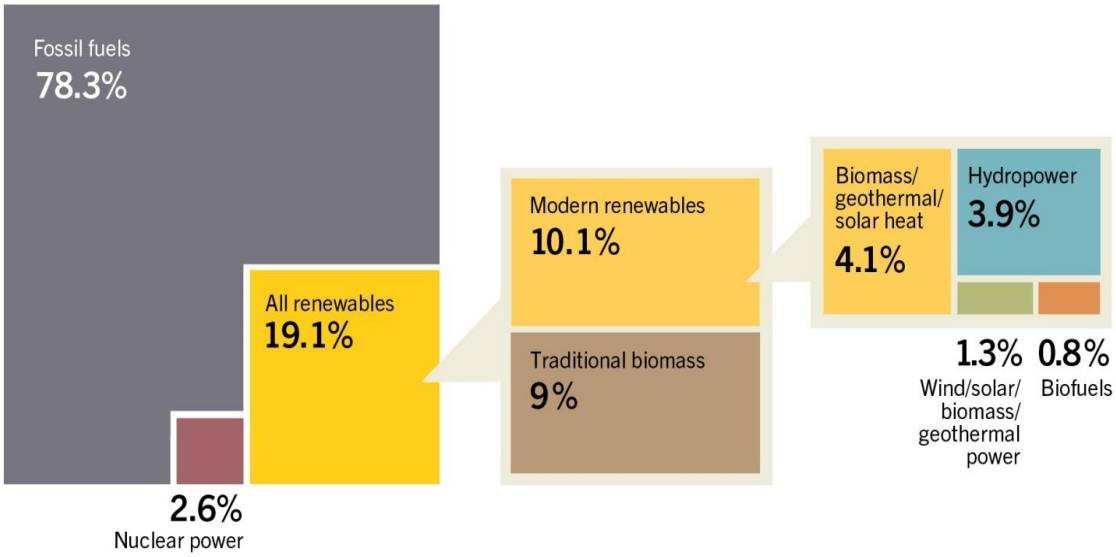

Figure 1.1 Renewable Energy Share of Global Final Energy Consumption in 2013.[1]

In this context, considerable interest has been paid to photovoltaic research, in particular, during the Aerospatiale conquest in the 1960's allowing to reach power conversion efficiencies (PCEs) around 18 % (monocrystalline: 24.5 %, polycristalline: 19 %) for silicon-based modules. However, even if the cost of silicon-based conventional solar cells becomes cheaper every year, *i.e.* 0.13 $/kW-hr compared to 250 $/W for the first device developed in 1954 by the Bell laboratories, it is still more expensive to produce electricity from the sun than from the fossil fuels (<0.10 $/kW-hr).[3] That is why important researches are currently under development to produce cheaper and highly efficient solar cells with new materials.[4] One of the most promising alternatives to silicon-based devices are actually the dye-sensitized (DS) solar cells and thin film-based organic photovoltaics (OPVs), also called bulk-heterojunction (BHJ) solar cells, that have reached PCEs up to 13 and 10.6 %, respectively, by using cheaper organic and polymer materials.[5]

In this dissertation, we will focus on the development of new materials for developing highly efficient BHJ and DS solar cells.

1.2. WORKING PRINCIPLE

The photovoltaic technology based on silicon was firstly developed for Aerospatiale applications, especially to ensure the operation of artificial satellites circling the Earth. This technology uses the properties of materials called semiconductors such as the silicon which is the most commonly used. A semiconductor is a material possessing electrical conducting properties between a conductor and an insulator (Figure 1.2). As an insulator, it presents a band gap between its valence and conduction bands. Some semiconductors display a gap sufficiently low to afford an electron transfer from the valence to the conduction band when the material is under illumination. Negative charges (*i.e.* electrons) and positive charges (*i.e.* holes) are thus simultaneously produced within the material, creating the so-called electron-hole pair (exciton). Upon an electric field, the charges of this electron-hole pair, called *p* (*i.e.* hole) and *n* (*i.e.* electron), are separated and collected by two distinct electrodes, giving a current. Such behaviour is the photovoltaic effect.

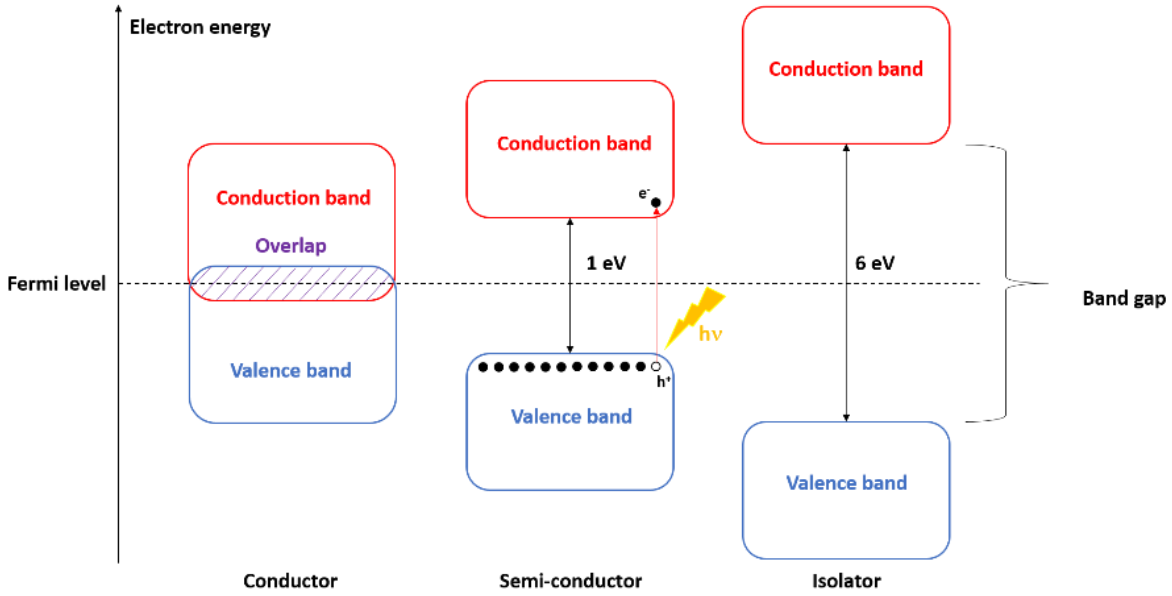

Figure 1.2 Schematic representations of a conductor, a semiconductor and an insulator.

In photovoltaic cells, in order to obtain this charge separation, the active layer is built upon two components: one containing an electron excess and the second which is electron deficient, so-called *n*- and *p*-doped, respectively. When these components are brought into contact, the electrons in excess in the *n*-type material diffuse in the *p*-type material, leading to a *p*-*n* junction. The component initially n-doped become positively charged, while it is the opposite for the *p*-doped component, thus, creating an electric field to counteract the diffusion of the charges (Figure 1.3).

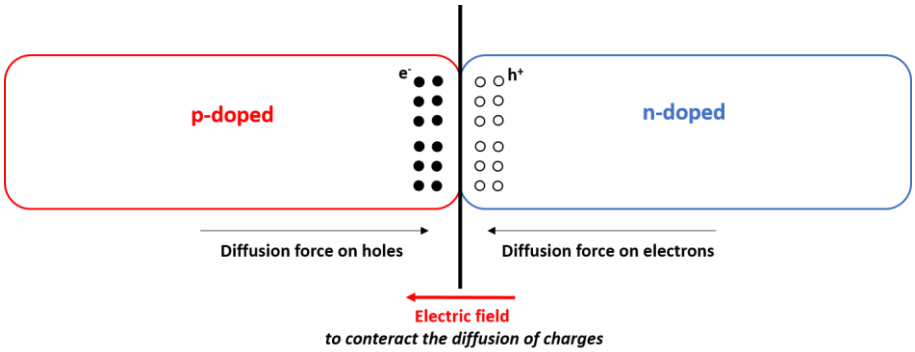

Figure 1.3 Schematic representation of a *p*-*n* junction.

Adding metallic contacts on the *n*- and *p*-doped zones induces the creation of a diode. Upon illumination, the photons having an energy equal or superior to the band gap collide with the electrons on the material, knocking them into a higher energy state, thus creating an electron-hole pair. When the junction is connected to an external circuit, the electron and hole are separated and their movement gives the electric current (Figure 1.4).

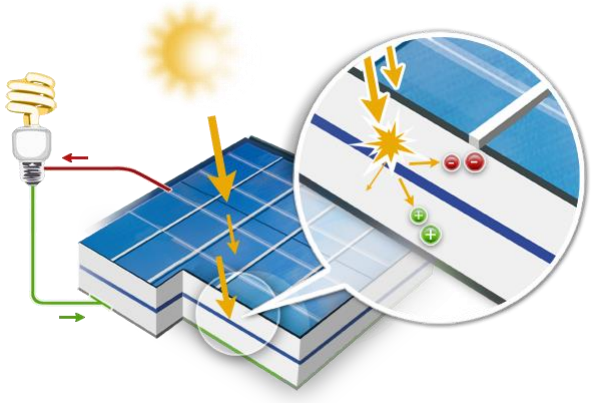

Figure 1.4 Schematic representation of the charge generation in photovoltaic devices based on *p*-*n* junction.[6]

1.3. KEY PARAMETERS OF SOLAR CELLS

The parameters used to describe the PCE of a solar cell are extracted from the J-V curves recorded under an AM 1.5G illumination by varying the potential between the electrodes (Figure 1.5). The incident power is a function of the solar spectrum and is generally given in terms of air-mass (AM) which is defined as follow:

$$AM = 1/\cos(\theta)$$

where θ is the angle of the sun, measured from the zenith (Figure 1.6). The air-mass indicates the amount of atmosphere that is passed by the light to reach the surface of the Earth. The standard AM 1.5G corresponds to an angle of 48.2° and a total power density of 100 mW.cm^{-2} (1 sun).[7]

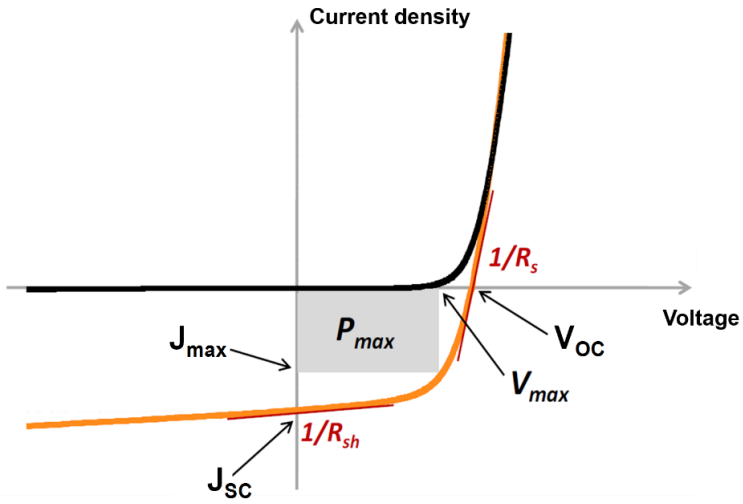

Figure 1.5 Current-Voltage curves in the dark (black line) and under illumination (orange line).

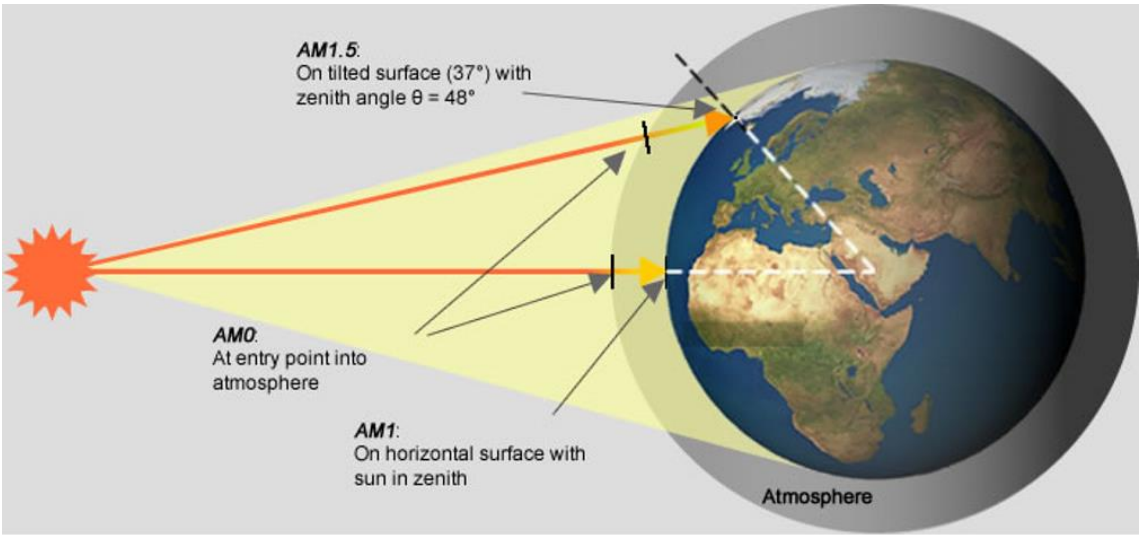

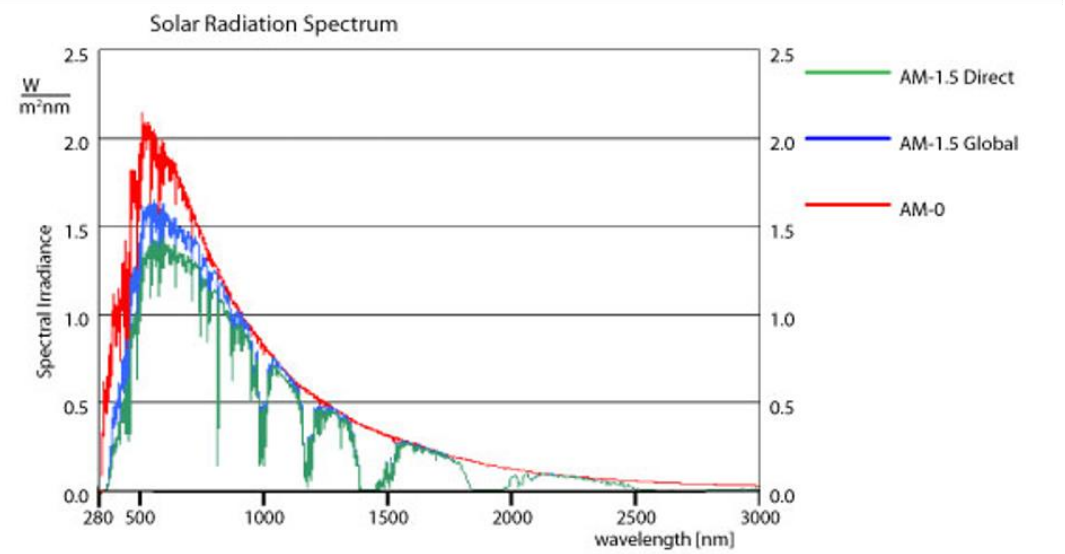

Figure 1.6 AM 1.5G solar spectrum.[7]

Five parameters can be then directly extracted from the J-V measurements:

- **The short circuit current density (J_{SC})**

The short circuit current density, noted J_{SC}, corresponds to the current density when no potential is applied between the electrodes of the device. This current is proportional to the light intensity, the surface of the device and the charge carrier mobility.

- **The open circuit voltage (V_{OC})**

The open circuit voltage, noted V_{OC}, corresponds to the potential measured under illumination between the electrodes when no current flows in the device. This potential is linked to the materials used in the active layer and also, to the recombination kinetics of charge carriers.

- **The maximum power**

The maximum power generated by the device (P_{max}) is the maximum power than can be delivered by the photovoltaic device and corresponds to the product of the potential V_{max} and current J_{max}. In the graph, P_{max} represents the surface of the rectangle defined by the origin and the P_{max} point (V_{max}; J_{max}).

- **The fill factor (FF)**

The fill factor, noted FF, is the ratio between the maximum power (P_{max}) and the cell power (P).

$$FF = \frac{Jmax \times Vmax}{Jsc \times Voc} = \frac{Pmax}{P}$$

More the fill factor increases, more the photovoltaic device has an ideal behavior. The deviation from the ideal behavior involves the contact resistance, the low mobility of the charge carriers or the leakage current in the device.

- **The power conversion efficiency (η)**

The power conversion efficiency, noted η or PCE, is defined as the ratio between the maximal power generated by the device (P) and the incident power due to the sunlight (P_{in}).

$$\eta = \frac{P}{Pin} = \frac{FF \times Voc \times Jsc}{Pin}$$

Another fundamental measurement of a solar cell is the “external quantum efficiency” (Figure 1.7), which is commonly called the **incident photon to current conversion efficiency** (IPCE). The IPCE value corresponds to the photocurrent density produced in the external circuit of the cell under monochromatic illumination divided by the photon flux that strikes the cell and is calculated following the equation:

$$IPCE(\lambda) = \frac{Jsc(\lambda)}{e\,\phi(\lambda)} = 1240 \times \frac{Jsc(\lambda)}{\lambda\, Pin(\lambda)}$$

where λ is the wavelength in nm, e is the elementary charge in coulomb, ϕ is the incident flux in $W.cm^{-2}$, J_{SC} the short circuit current density ($A.cm^{-2}$) and P_{in} the power of the incident light.

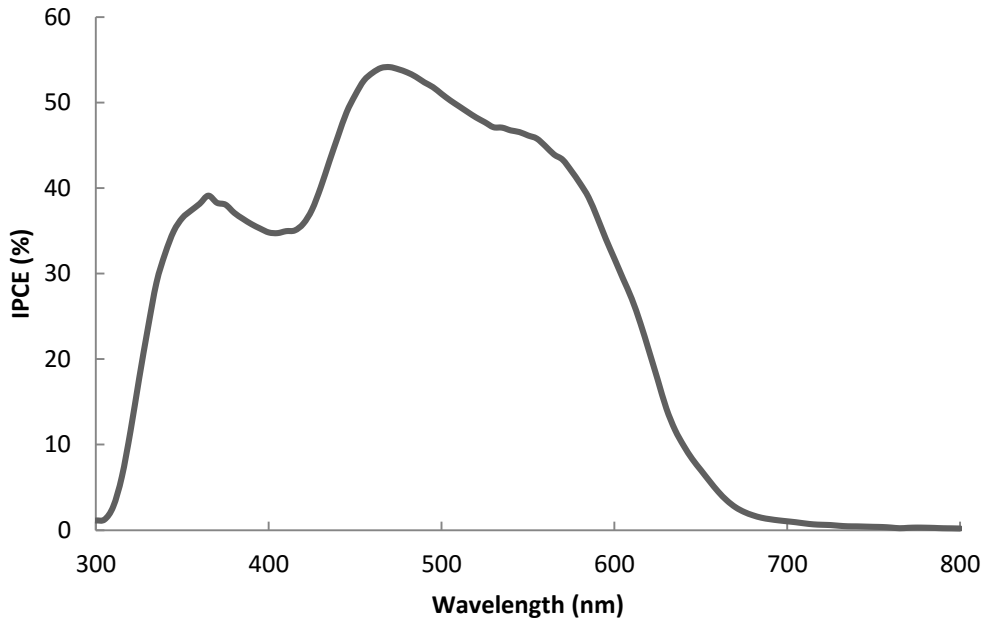

Figure 1.7 IPCE curve of a solid-state dye-sensitized solar cell based on **an indoline dye**.

1.4. TECHNOLOGY ADVANCES

Since 1993, M. A. Green *et al.* have updated the PCEs obtained for the different types of solar cells.[4b] As shown on Figure 1.8, multilayer-solar cells based on inorganic compounds (silicon, gallium, telium etc.) lead currently to the best PCEs.

Generally, three generations of solar cells can be listed depending on the photovoltaic technology used (Figure 1.9).

The first generation consists essentially in monocrystalline and amorphous silicon-based solar cells (c- and a-Si, respectively), leading to PCEs up to 20 % for the commercialized modules (Figure 1.9, a).[8] The manufacturing process of crystalline silicon requires high purity that induces expensive production cost. The a-Si-based solar cells are obtained from the melting of silicon crystals and use two times less energy than the fabrication of c-Si-based solar cells. The efficiency is lower but the production cost is more advantageous. Currently, 90 % of the photovoltaic devices used at the surface of the Earth are from the first generation. Nevertheless, their costly and energy-hungry manufacturing process, their high weight and their lack of flexibility still remain disadvantages. Furthermore, devices tend to heat up during their operation, thus reducing significantly their PCE.

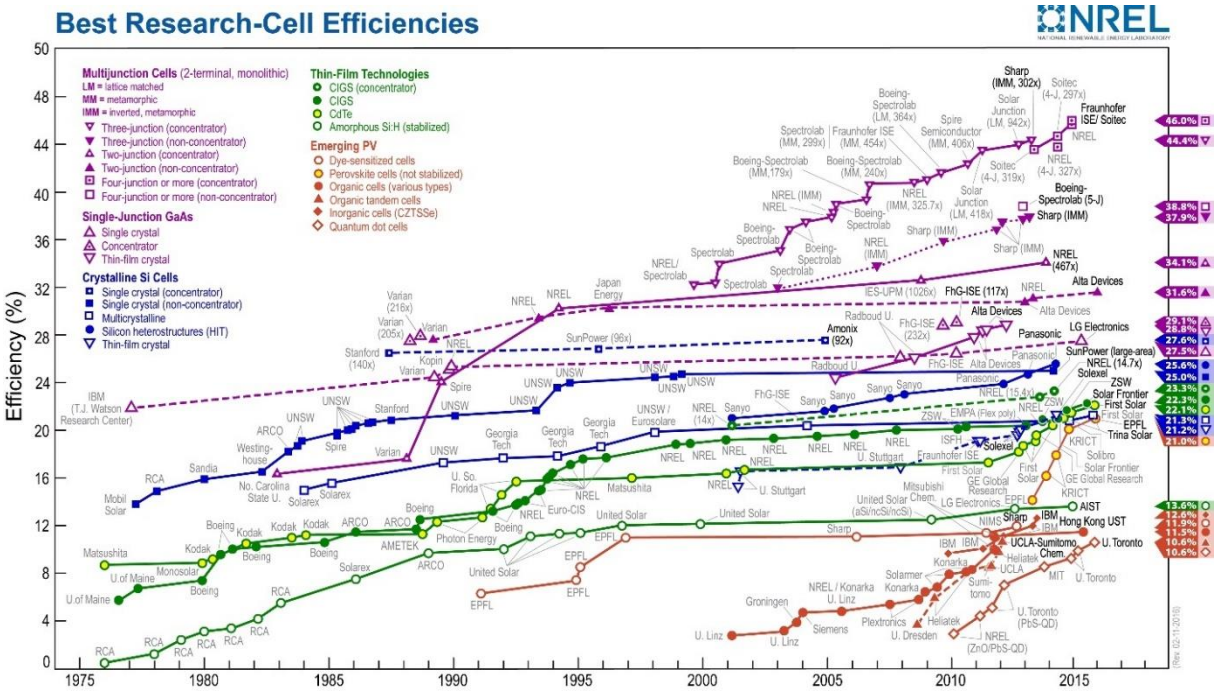

Figure 1.8 Best Research-cell PCEs updated by NREL.[4b]

The second generation of solar cells such as amorphous silicon, copper-indium-gallium-selenide (CIGS) and cadmium telluride (CdTe) is based on thin-film technologies (Figure 1.9, b).[8] As such, the thin thickness allows reducing the production cost to about \$1/W and reaching a wide range of applications with attractive appearances. The most established thin-film technology is amorphous silicon (a-Si)-based solar cells with PCEs between 5 and 9 % for commercialized modules. CIGS and CdTe exhibit higher PCEs (from 9 to 11 % for commercialized modules in thin-films) due to the use of a costly alloy with a high light-harvesting ability.

Finally, the third generation gathers several emerging technologies (Figure 1.9, c). Among various types of new developed concepts, three main examples are described below:[8]

- The **multijunction solar cells** are used for Aerospatiale applications since around 20 years and consist in different semiconductor layers, converting sunlight into electricity on the overall solar emission spectrum. PCEs up to 37 % have been reached in laboratories.[9] These cells are more performing, resulting in higher cost. However, the use of solar concentrators affords to considerably reduce the semiconductor surface and thus, the fabrication cost. This solar technology, still in development, allows reaching PCEs up to 46 % in laboratories.

- The **organic solar cells** or OPVs are constituted by small organic molecules or π-conjugated polymers, able to transport charge carriers in the device.[10] Because these materials are soluble in common solvents, they can be deposited onto the substrate using impression techniques which reduces considerably the costs. As depicted in the Figure 1.8, the first OPVs reaching significant PCEs were developed in the 2000's and since then, major

improvements advances have been reported. In particular, some record PCEs have even been reached for multilayered molecules and oligomers based-OPVs prepared by thermal evaporation (12 %, 1.1 cm², Heliatek GmbH, Dresde/Ulm, Germany)[11] or tandem cells based on π-conjugated polymers, processed from liquid solution (10.6 %, 0.1 cm²).[12] The solution process is particularly attractive regarding its easy manufacturing and its low cost. Besides, thanks to the low weight and the flexibility of the organic constituents, these cells can be used in mobile technologies. However, the low stability of the materials facing temperature variations and oxidative/reductive phenomena reduces considerably the solar cell lifetime. Thus, improvements are still required for this promising technology to meet potential commercialization in the next few years.

- The **dye-sensitized solar cells** (DSSCs), invented in 1991 by M. Grätzel, consist in an inorganic semiconductive oxide sensitized with a dye.[13] In these cells, the dye ensures, upon the absorption of photons, the generation of the electron-hole pair which is separated by injection of the electron into the conduction band of the semiconductor. The DSSCs are produced by a less energy-intensive manufacturing process than silicon-based solar cells, can be fabricated on flexible substrates, work under daylight and their performances are not affected by the temperature increase. The energy payback time for, *i.e* the time it takes to produce all the energy used in their life cycles, is much lower than conventional silicon-based solar cells (months *vs.* years, respectively). PCEs of 13 % and 10 % have been reached in laboratory and for modules, respectively.[14] Despite these good performances, their widespread commercialization remains limited due to several disadvantages: (i) the triiodide/iodide (I_3^-/I^-) system, widely used as liquid electrolyte, is corrosive and dissolves many of the commonly used sealants and metal interconnects in devices; (ii) the production cost has to be reduced, alternatives to expensive sensitizing dyes are especially needed.

- The **perovskite solar cells** (PSCs) include a perovskite-type compound, more generally a hybrid organic-inorganic lead or tin halide-based material, as the light-harvesting active layer. Perovskite materials are cheap to produce and simple to manufacture. PCEs of these devices have considerably increased from 3.9 % in 2009[15] to 22.1% in early 2016, NREL making it the fastest-growing solar technology to date. PSCs seemed to have great promise to achieving even higher PCEs and lower production costs. For these reasons, PSCs have become commercially attractive, with start-up companies already promising modules on the market by 2017. Nevertheless, the long-term stability of these cells remains unproven and their performances are moisture sensitive. Lead content is another drawback to the viability of these cells and could be problematic for their future commercialization.

- The **quantum dot solar cells** (QDs) are based on quantum dots as the light-absorbing photovoltaic material, to replace bulk material such as silicon, CIGS or CdTe. Quantum dots exhibit tunable band gaps across a wide range of energy levels by changing their size. Due to

their effective light-harvesting in the NIR region, QDs-based solar cells yielded PCEs up to 7.4%.[16]

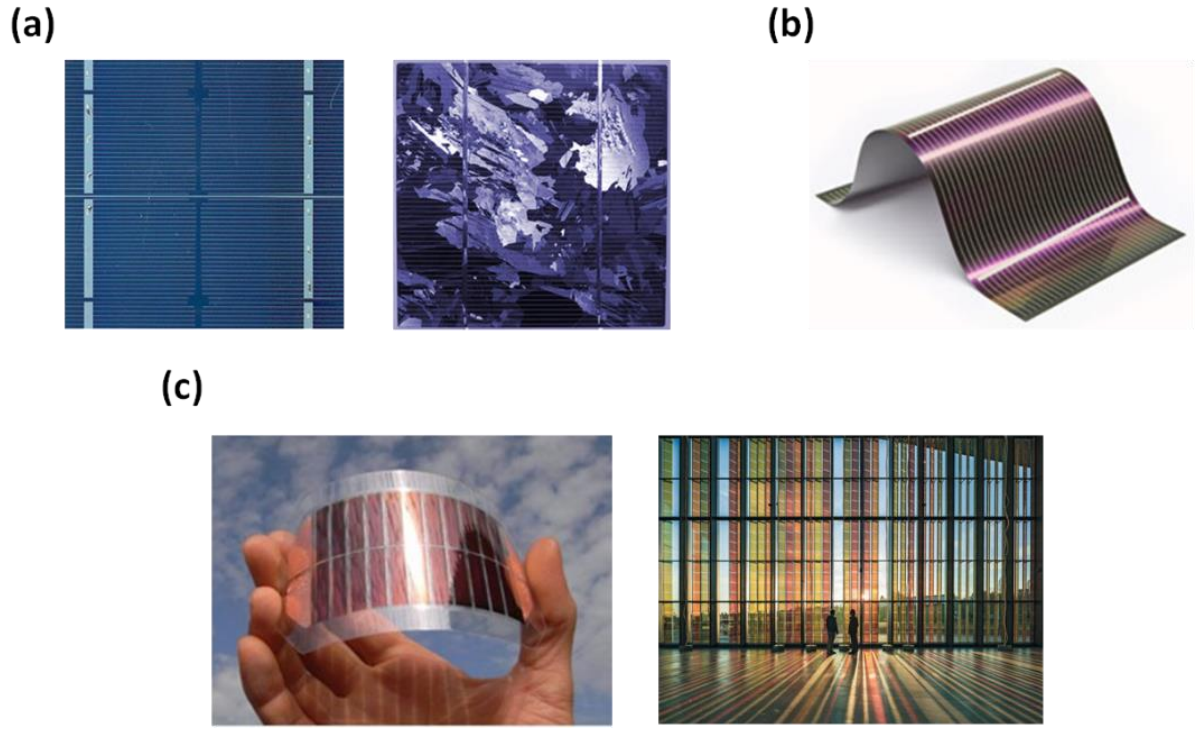

Figure 1.9 Pictures of first (a), second (b) and third (c) generations of solar cells (the right picture correspond to an organic solar cell and the left one is representative from the dye-sensitized solar cell).[17]

In the following sections, we will focus on BHJ and DS solar cells and describe more precisely their working principle, their composition as well as the recent advances.

2. BULK-HETEROJUNCTION SOLAR CELLS

2.1. HISTORY AND PRINCIPLES

The first organic solar cell was made in 1959 by Kallman and Pope from an anthracene active layer (Figure 1.10, a) leading to a photovoltage of 0.2 V with an extremely low power conversion efficiency.[18] Attempts to improve the efficiency of these devices based on a single organic material were unsuccessful, mainly due to the low dielectric constant of organic materials. Due to this low dielectric constant, the probability to form free charge carriers upon light absorption is very low. Instead, strongly bound excitons are formed in π-conjugated polymers, with a binding energy around 200 meV. As the excitons are strongly bound, the electric field applied in the photovoltaic device, arising from the work function difference between the electrodes, is too weak to dissociate them.

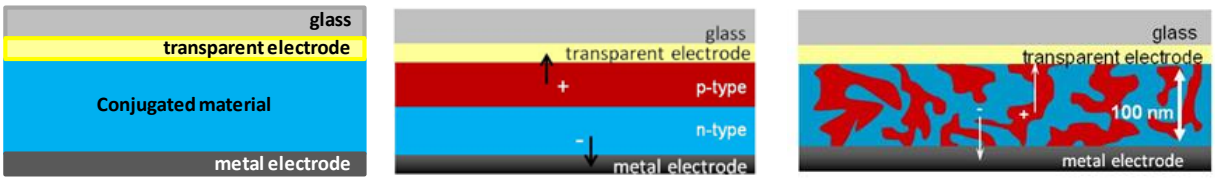

Figure 1.10 Schematic device structures of OPV cells: a) single layer, b) bilayer and c) bulk heterojunction (BHJ).

To overcome this limitation, the active layer was divided into two distinct material layers: the donor material (D), consisting generally in a π-conjugated polymer and the acceptor material (A), consisting generally in fullerene derivatives (Figure 1.10, b).[19] By carefully choosing these materials, the electron or hole transfer from the acceptor to the donor and from the donor to the acceptor, respectively, is thus energetically favored. The photovoltaic energy conversion in organic solar cells can be described in four steps (Figure 1.11):[10]

1) Light absorption: under illumination, an electron at the ground state is promoted to an excited state, thus creating an electron-hole pair. Right after its formation, the electron-hole pair relaxes into a bound state, called exciton. The excition binding energy prevents itself from separation in absence of energetically favorable conditions, such as the D/A interface and strong electric field within the layer. This exciton commonly sits on a single molecule and can either recombine or randomly diffuse to the nearly molecule, consisting in the following step, the exciton diffusion.

2) Exciton diffusion: the excitons in the organic layer can diffuse around via hopping among adjacent molecules, randomly regarding the directions. The presence of an electric field within the layer does not allow orienting their diffusion, as exciton can be considered as a neutral specie. The exciton diffusion length, *i.e.* the average distance of exciton diffusion before recombination process, is very short and is between 5 and 10 nm for most of the conjugated polymers. If an exciton can meet the D/A interface or if a strong electric field is applied within its diffusion length, it can be separated into two charge carriers: an electron and a hole.

3) Exciton dissociation: in a typical bilayer OPV cell (Figure 1.10, b), the electric field applied is not enough strong to allow separating the exciton. Therefore, the D/A interface is essential to dissociate the exciton. When an exciton formed in the donor material diffuses to the D/A interface, it can be separated through an electron transfer to the acceptor material. The opposite process is also true for the hole transport.

4) Charge transport and collection at the electrodes: since the electrons and holes are separated and free, they can be transported into the active layer, *i.e.* the electron in

the acceptor layer and the hole in the donor layer, and finally collected to the corresponding electrodes.

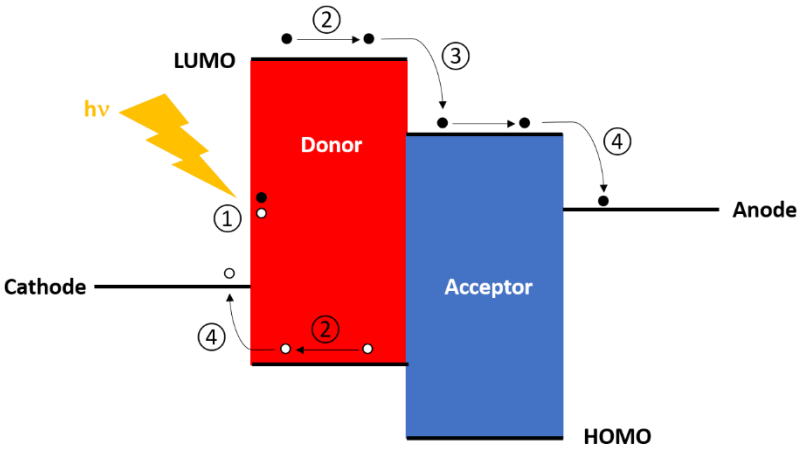

Figure 1.11 Schematic OPV device working principle from light absorption to charge collection.

In 1992, Saricifti *et al.* reported that an ultrafast electron transfer takes place from a π-conjugated polymer (polyphenylene vinylene or **PPV**) to fullerene (**C_{60}**), showing the great potential of these latter derivatives as acceptor materials.[20] Since the diffusion length of excitons is typically between 5 and 10 nm, only a low part of the active layer (around 100 nm) could contribute effectively to the photocurrent in bilayer OPV.

To overcome this limitation, Yu *et al.* suggested in 1995 to intimately mix donor and acceptor components in order to increase the interfacial area and thus, decrease the distance that excitons have to diffuse to reach the D/A interface.[21] This device structure is called bulk heterojunction (BHJ) and has been widely used and improved since its creation (Figure 1.10, c)[22]. In particular, it was demonstrated that the solvent used in the fabrication process has a significant effect on the morphology of the active layer and thus, on the photovoltaic performances of the devices. By optimizing the process conditions, an efficiency of 2.5 % was obtained and nowadays, PCEs up to 10 % have been obtained with BHJ solar cells based on π-conjugated polymers as donor and fullerene derivatives as acceptor.[23] However, these BHJ solar cells exhibit major drawbacks. Indeed, all created excitons are not dissociated because the length to rich the dissociation site is larger than the diffusion length and even after the dissociation, free charge carriers can recombine easily when they migrate to the collecting electrodes. Additionally, controlling the morphology of the active layer is difficult (domain sizes, crystallinity, etc.) and necessitates additional annealing steps, adequate solvents or additives.[23a]

2.2. CONSTITUENTS OF BHJ SOLAR CELLS

The structure of a typical BHJ solar cell is described in Figure 1.12.[23a] The active layer, *i.e.* an intimate blend between the donor and acceptor materials, is sandwiched between two electrodes, one transparent and one reflective, *i.e.* the anode and the cathode, respectively.

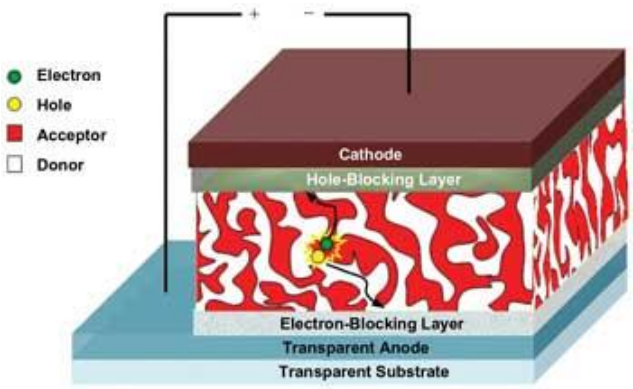

Figure 1.12 Schematic structure of a BHJ solar cell.

The glass substrate, *i.e.* the anode, is coated with indium tin oxide (**ITO**) and a poly(3,4-ethylenedioxythiophene): poly(styrenesulfonate) (**PEDOT**: **PSS**) layer is spin-coated on the top to reduce the **ITO** roughness (Figure 1.13). Then, the active layer, composed of the donor and acceptor materials is deposited followed by the thermal evaporation under vaccum of aluminum (cathode).

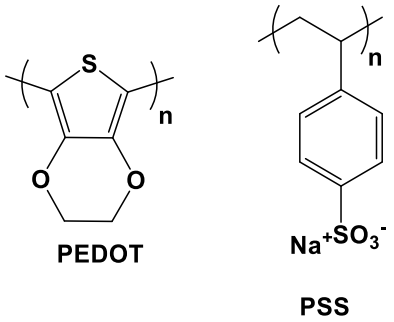

Figure 1.13 Structure of **PEDOT** and **PSS**.

The cathode can be further modified by depositing a thin layer of lithium fluoride (LiF) or ytterbium (Yb) between the metal electrode and the organic active layer. The use of these materials allows reducing the interface barrier height between the active layer and the metal electrode by changing the work function and the open circuit voltage.[24] In a similar manner, introducing a π-conjugated polyelectrolyte thin layer between the cathode and the active layer results in similar effects. This point will be discussed later in more details in this chapter.

The PCE of the solar cell depends on several parameters such as the nature of donor and acceptor materials, the morphology of the active layer and the introduction of interfacial layers. These points will be discussed in the following sections.

2.2.1. ACTIVE LAYER

2.2.1.A. DONOR MATERIALS

The development of new π-conjugated polymers is a major route to improve PCEs of BHJ solar cells (Figure 1.14).[25]

One of the first polymers used in this field was the poly(2-methoxy-5-(2'-ethylhexyloxy)-1,4-phenylenevinylene] (**MEH-PPV**, Figure 1.14) developed by Wudl *et al.*[26] Wudl invented also one of the most widely used acceptor material in OPVs : the phenyl-C_{61}-butyric acid methyl ester (**$PC_{61}BM$**).[27] Further optimizations in the fabrication process of these **MEH-PPV**:**$PC_{61}BM$** based solar cells allowed reaching PCE of 3 %.[28] Unfortunately, additional improvements of these cells were limited due to the low hole mobility of this polymer as well as its low light-harvesting. In order to replace it in BHJ solar cells, intense research activites were carried out on polythiophenes, in particular, on poly(3-hexylthiophene) (**P3HT**), which demonstrated better light-harvesting and high hole mobility and stability. By optimizing the solvents used for the fabrication process and thermal annealing, PCEs up to 5 % were obtained for **P3HT**:**$PC_{61}BM$** based solar cells.[29]

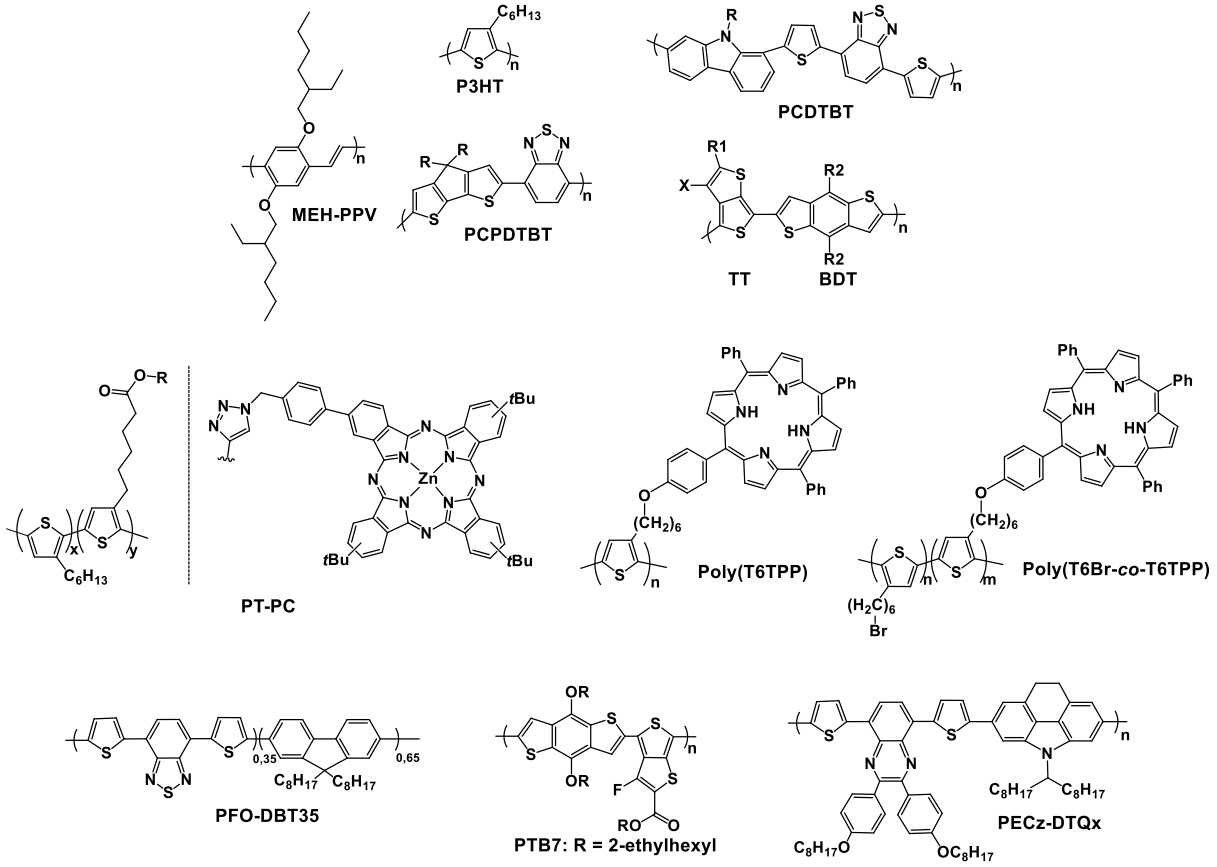

Figure 1.14 Examples of polymer donor materials used in BHJ solar cells.

Despite the developments of the **P3HT**:**PBCM** based BHJ solar cells, the performances still remain low compared to other technologies, especially due to the low absorption of the active layer in the infrared (IR) region. Indeed, the solar spectrum extends from the UV-visible to the IR regions: only 30 % of the incident solar light is represented in the UV-visible region while 50 % is in the IR. In order to overcome this limitation, low band gap π-conjugated polymers displaying a broaden absorption spectrum have been developed as donor materials.

The band gap is thus of a prior importance to improve the yield of OPVs by increasing the amount of photons absorbed by the photoactive layer. Nevertheless, such materials

need to be carefully designed. Even if the polymer displays a low band gap, the position of HOMO and LUMO orbitals must be carefully adjusted for efficient solar cells, in particular, regarding the open circuit voltage (V_{OC}), defined as follows: $V_{OC} = e^{-1} \times (|E_{HOMO}^{donneur}| - |E_{LUMO}^{accepteur}| - 0,3 \text{ eV})$, where e, E are the elementary charge and the energy value, respectively, and, 0.3 eV is the empiric value allowing to induce an efficient charge separation.[30]

As an example, poly[2,6-(4,4-bis-(2-ethylhexyl)-4H-cyclopenta[2,1-b ;3,4-b']dithiophene)-*alt*-4,7-(2,1,3-benzothiadiazole)] (**PCPDTBT**, Figure 1.14) having an absorption profile until 900 nm allows reaching PCE of 5.5 % when employed as donor material with alkanedithiol as additive.[31] In a similar way, Leclerc *et al.* reported the use of poly[N-9''-hepta-decanyl-2,7-carbazole-*alt*-5,5-(4',7'-di-2-thienyl-2',1',3'-benzothiazole)] (**PCDTBT**, Figure 1.14) as donor material allowing to reach PCE of about 6 %.[32] The low band gap polymers displaying the best performances, were described by Yu *et al.* and are built upon thieno[3,4,-b]-thiophene (**TT**) and benzodithiophene (**BDT**) moieties (Figure 1.14).[33] These polymers were the first to reach PCE up to 8 %. Following this strategy, PCEs up to 10 % have been obtained by using new π-conjugated low band gap polymers and by optimizing the fabrication process. One of the most popular approaches to decrease the band gap consists in alternating donor and acceptor units in the π-conjugated polymer backbone to stabilize the quinoid form of the polymer. The energy orbitals can be adjusted by changing the substituents of the monomer: adding some electrodonating groups (EDG) such as alkoxy groups tends to destabilize the LUMO orbital while adding some electrowithdrawing groups (EWG) such as nitro or cyano groups tends to stabilize the LUMO orbital. By associating different D and A units, HOMO and LUMO energy levels are decreased, thus inducing a low band gap polymer (Figure 1.15).

Another approach proposed to extend the light-harvesting of the donor material consists in adding a dye absorbing at higher wavelengths to the π-conjugated polymer. This dye can be added directly in the blend mixture as a third component[34] or integrated to the polymer backbone.[35] In the ternary blend, a perfect match between the energy levels of the three components is required to allow charge carriers separation at the interface D/A. In addition, the dye has to be miscible with donor and acceptor materials in order to well-control the morphology of the active layer, and thus, the charge transfer. Recent results have shown that adding a squaraine dye into a **P3HT**:**PBCM** blend leads to an enhancement of the PCE from 3.47 to 4.55 %.[36] Considering the dye integration into the polymer backbone, Torres *et al.* have introduced around 10 % of zinc phthalocyanine to the side chains of π-conjugated polymers based on **P3HT** and **MDMO-PPV**.[35a] More recently, Salatelli *et al.* have also described the synthesis of polythiophenes bearing porphyrins on their side-chains.[35d,35e] Although the absorption profiles of these polymers were expanded, PCEs were not improved due to a lack of solubility and the alteration of the polymer organization in the solid state. The phthalocyanines and porphyrins are indeed known as excellent chromophores exhibiting intense absorption in the infrared region. However, their tendency

to self-aggregate disturb the self-organization of the polymer, a crucial requirement for efficient hole mobility.

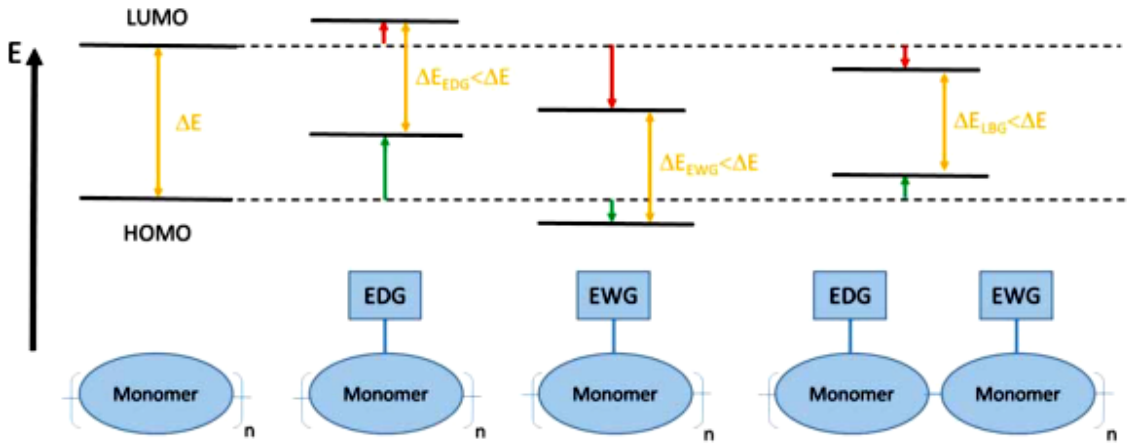

Figure 1.15 Effects on the energy levels of the introduction of EDG and EWG groups in the polymer structure.

Based on these latest strategies, we decided to incorporate porphyrins into the polymer backbone of the **P3HT**.[37] The synthetic method used for this functionalization as well as the physicochemical properties (thermal, morphological…) of the obtained **P3HT**-porphyrin will be described in Chapter 2.

2.2.1.B. ACCEPTOR MATERIALS

In the field of acceptor materials, organic molecules such as perylene diimide and fullerene derivatives, carbon nanotubes, inorganic semiconductors and π-conjugated polymers have been used in BHJ solar cells. Among these materials, fullerene derivatives play a dominant role due to their favorable LUMO energy, their excellent electron transport properties and their spherical shape allowing a three-dimensional charge transport.

Indeed, although the position of the HOMO and LUMO energy levels and their optical absorption spectrum are not ideal for most of the polymer donors, high PCEs have been reported for C_{60} and C_{70}. Fullerene requires also the use of organic solvents such as toluene, chlorobenzene or *o*-dichlorobenzene. For these reasons, a significant number of C_{60} and C_{70} derivatives have been synthesized to improve the processability, to tune the HOMO/LUMO levels in view of a better match with the polymer donor or to influence the morphology in the photoactive layer.

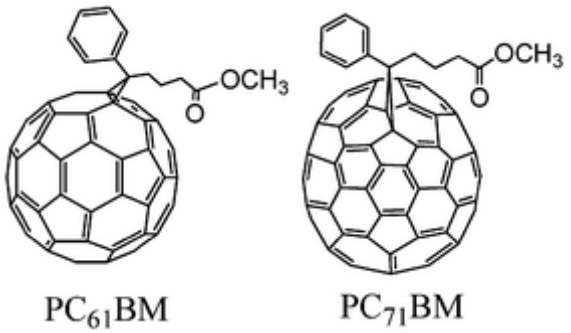

Figure 1.16 Chemical structures of fullerene derivatives widely used as acceptor materials.

More recently, polymer/polymer BHJ solar cells have attracted considerable attention.[38] Indeed, the tunable design of both donor and acceptor material chemical structure allows modulating optical, electronical and morphological properties of the blends. Since low band gap conjugated polymers exhibit intense absorption in the visible and near IR region, solar cells built upon these materials can harvest more sunlight and thus, lead to increased J_{SC}. The HOMO and LUMO energy levels can be also easily adjusted for both components, allowing a gain in V_{OC}. In addition, the formation of phase-separated interpenetrating domains offers continuous pathway for efficient charge transport. Finally, blends made from polymers only lead to superior thin-film properties, including flexibility, which is a real advantage for the large scale production via solution processing.

This explains why various polymer acceptors have been developed. Unfortunately, compared to the fullerene derivatives, they generally exhibited low electron mobility. Moreover, the D/A domains within the blends were found to be larger, resulting in lower charge transport efficiency. As a result, PCEs up to only 2 % polymer/polymer BHJ solar cells were reached until 2012. Significant improvements have been made very recently due to the development of low-band gap acceptor polymers with both high mobility and electron affinity, similar to fullerene derivatives (Figure 1.17).

Cyano-substituted phenylenevinylene polymers such as **MEH-CN-PPV** were first used as polymer acceptors leading to PCEs up to 2.0 %.[39] Then, fluorene and benzothiazole-based polymers were considered. In 2011, Ito *et al.* reported a PCE of 2 % for polymer/polymer BHJ solar cells based on **P3HT** and **PF12TBT** (Figure 1.17).[40] These polymers yielded to high V_{OC} (> 1 V) but J_{SC} and FF were very low due to their poor light absorption and mobility (10^{-5} $cm^2.V^{-1}.s^{-1}$).

Polymers based on tetraperylene (TP) dicarboxdiimides and naphtalene diimides (NDI) were developed exhibiting high mobility and absorption profile from the visible to the near-IR region. As an example, **P(TP)** afforded PCE of 4.4 % with isoindigo-based donor polymer with polystyrene side chains (Figure 1.17).[41] Considering NDI-based polymers, despite excellent mobility of 0.45-0.85 $cm^2.V^{-1}.s^{-1}$ in the FET configuration, **P(NDI2OD-T2)** firstly lead to PCE < 0.2 % when combined with **P3HT** because of the formation of large domains in the blends.[42] In 2012, the PCE was improved to 1.4 % thanks to the introduction of chloronaphtalene that suppressed the aggregation of **P(NDI2OD-T2)** polymers.[43] Very recently, **PNDIS-HD** and **P(NDI2OD-T2)** were combined with low band gap polymer donors to

enhance the light-harvesting of the active layer leading to considerable increase of PCE: 7.73 and 8.27 %, respectively.[44]

2.2.2. CONTROL OF THE PHOTOACTIVE LAYER MORPHOLOGY

As mentioned above, the control of the photoactive layer morphology is a crucial point in the solar cell fabrication. Indeed, simple spin-coating of the photoactive layer from a D/A blend solution usually results in an undesirable morphology, with problematic features as large phase separation, inhomogeneous internal phase composition and reduced ordering of polymer donor chains, which are well-known to induce poor performances. Therefore, controlling the morphology is a key requirement for highly efficient devices.

Optimization of the **P3HT:PBCM** blend morphology has been attempted using processing techniques, such as solvent engineering and solvent/thermal annealing but the domain size and the architecture of BHJ active layer are not well-controlled yet.[45] The morphology achieved by mixing **P3HT** and **PBCM** is generally thermodynamically unstable in time, leading to the deterioration of the device during fabrication and/or extended use. Specifically, macrophase separation of blend components can occur upon post-processing and extended device operation, resulting in significant changes compared to the as-deposited thin film morphology. Additional instability can also arise from the diffusion of **PBCM**. During device preparation and use, concentration gradients, depletion from active areas and sometimes, aggregation/crystallization of **PBCM** can occur, thus decreasing the interfacial area available for charge separation and impairing the device performance. Consequently, developing methods to precisely control the morphology at the nanoscale is a key-challenge towards efficient organic solar cells.

Recently, it was shown that modifying the molecular structure by adding various functionalities in end- or side-chains of **P3HT**-based polymers could improve the morphology of the **P3HT:PBCM** blend and thus, the device performance. Block copolymers have also emerged as promising candidates for OPVs applications due to their ability to form well-defined and controllable nanostructures by adjusting the polymer structure in bulk or thin films through microphase separation.[46] Thus, by judiciously choosing the block copolymer architecture, the degree of phase separation, ordering and the orientation of the crystalline domains in the blend films can be controlled thus facilitating the formation of morphology suitable for charge separation and transport. As such, many studies have explored block copolymers as the main component in the active layer for OPVs and as compatibilizer to improve the blend structure.[47]

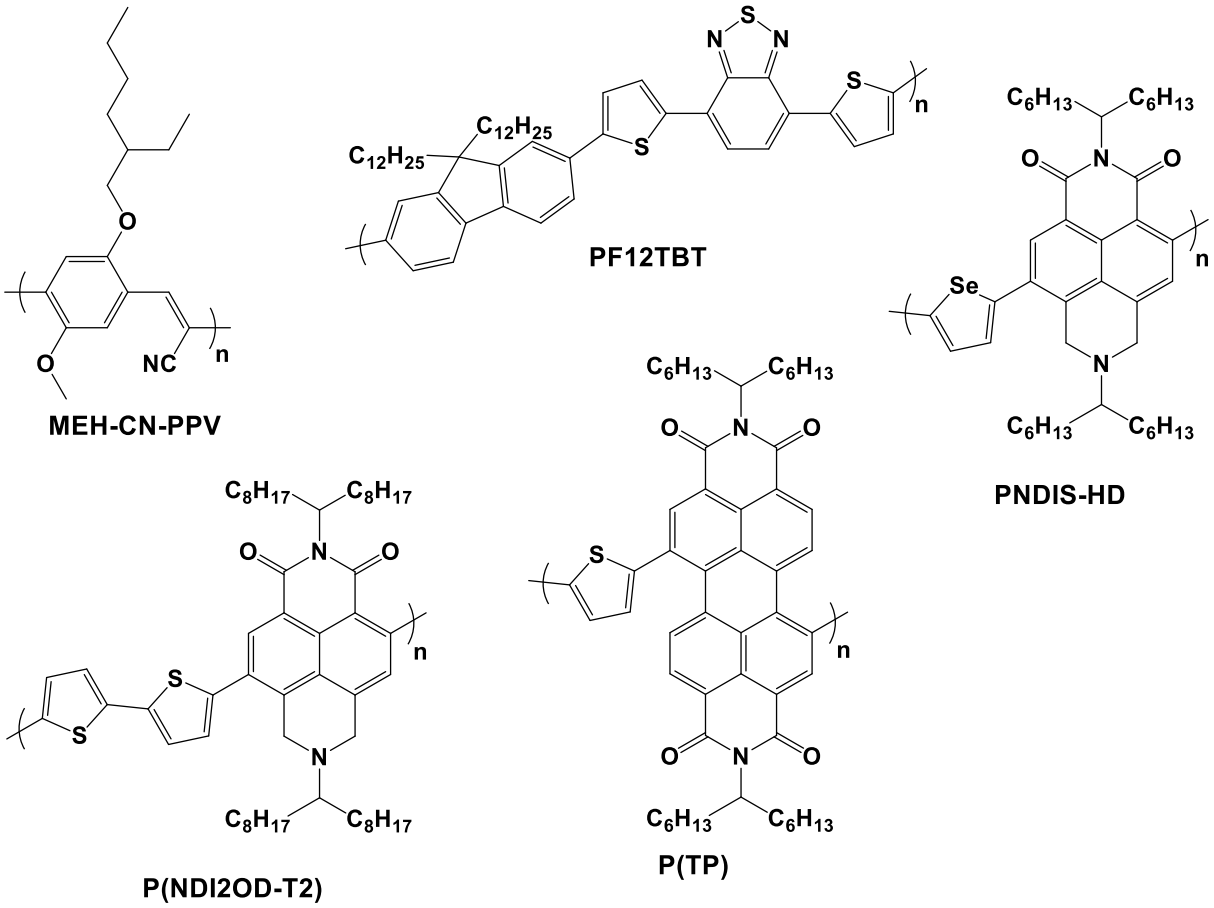

Figure 1.17 Examples of structures of π-conjugated polymers used as acceptor materials in BHJ solar cells.

2.2.3. INTERFACIAL LAYERS

In order to improve the performances of organic solar cells, interfacial layers were integrated in the device architecture.[48] They allow reducing the energy barrier between the active layer and the electrode and forming favored contacts with charge carriers. Some interfacial materials such as titanium oxide or cesium carbonate are also known to modify the working potential of the electrode and were involved in the fabrication of inverse solar cells. We will focus below exclusively on the modification of anode and cathode interfaces (Figure 1.12).

- *ANODE INTERFACIAL LAYER*

The anode of the BHJ solar cells are generally composed of transparent electrode based on ITO with a work function of 4.7 eV. A layer of **PEDOT**:**PSS** is spin-coated on this ITO surface to reduce its rugosity and form also an ohmic contact with the active layer, allowing an efficient collect of charges carriers. Nevertheless, the **PEDOT**:**PSS** layer can attack the ITO surface due to its acidic nature, and thus, reduce the solar cell lifetime.[49]

To overcome this limitation, some metal oxides have been used such as V_2O_5, MoO_3, WO_3 and NiO and have shown interesting results when used as anode interfacial layer. Shrotriya *et al.* have indeed reported that the use of V_2O_5 and MoO_3 as interfacial layer in

P3HT:**$PC_{61}BM$** based BHJ solar cells lead to J-V characteristics similar to those obtained with the **PEDOT**:**PSS** layer (Figure 1.18).[50] In a similar manner, a BHJ solar cell with an additional anode interfacial layer of NiO (between 5 and 10 nm of thickness) displayed PCE of 5.2 % with an excellent time stability.[51] The performances of these materials as anode interfacial layer were linked to the thickness of the oxide layer.

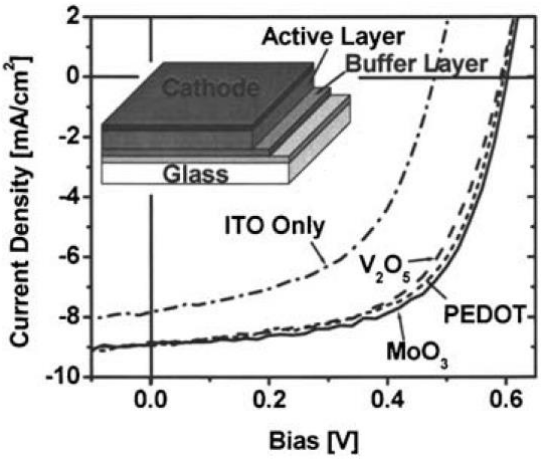

Figure 1.18 J-V characteristics of solar cells with different anode interfacial layers under illumination.[50]

Another developed strategy is the use of π-conjugated polyelectrolytes (**CPEs**) to replace the **PEDOT**:**PSS** layer. **CPEs** are polymers with extended π-conjugated backbone bearing pendant ionic side chains. Unlike the majority of π-conjugated polymers, **CPEs** are soluble in polar solvents and this orthogonal solubility with respect to organic materials used in the active layer of OPVs ensures sequential surface deposition without damaging the underlying films. These polymers have been widely studied as cathode interfacial layer (see below) but scarcely used as anode interfacial layer. This can be explained by the fact that these polymers usually lead to reduced working potential, which induces a more important gap for charge injection. Most of the anionic **CPEs** display a low conductivity but Heeger *et al.* has nevertheless described a low band gap **CPEK** that afforded PCE of 8.2 % when used as anode interfacial layer for solar cells based on D/A polymer **PTB7** (7.9 % for the reference).[52] Recently, this CPE was used in inverted-type perovskite solar cells afforded higher efficiencies than **PEDOT:PSS** (12.51 % *vs.* 10.77 %).[53] The device stability under ambient condition was also improved due to an excellent wetting of perovskite.

- *CATHODE INTERFACIAL LAYER*

In the case of the cathode interfacial layer, three approaches have been described in the literature.

The first one consists in using alkaline metals or analogue compounds such as Cs_2CO_3 or LiF. Brabec *et al.* have reported that a LiF-Al electrode could reach similar efficiencies than those obtained for Ca-Al electrodes in solar cells based on **MDMO-PPV**:**PBCM**.[54] However, the oxidation of alkaline metals could induce a fast degradation of the device.

The second one is based on metal oxides such as **TiO_2** and **ZnO** with working potential similar to the LUMO energy level of fullerenes. In contrast with alkaline metals, metal oxides have an excellent ohmic resistance to the oxygen and humidity. This approach is also advantageous in terms of process since **TiO_2** and **ZnO**, commonly prepared by sol-gel strategy can be deposited using spin-coating, ink-jet printing, etc. Furthermore, TiO_2 is working as an optical hole blocking layer, improving the absorption within the device. An increase of around 40 % in J_{SC} and EQE has been observed for **P3HT**:**PBCM**[55] system and 100 % in internal quantum efficiency (IQE) for **PCDTBT**:**PBCM**[55] system.

The third approach is based on the use of π–conjugated polymers, inspired by polymers used in PLEDs (Figure 1.19).[56] In 2009, Luo *et al.* have reported an increase in V_{OC} and PCE by using hydrosoluble polymers (*i.e.* **PFNBr-DBT15** and **PFPNBr**) as cathode interfacial layer in **PFO-DBT35**:**PBCM** based device (Figure 1.18).[57] Introducing **CPEs** leads to the formation of an interfacial dipole due to the strong interaction between the photoactive and interfacial layers, inducing a decrease in working potential. The energetic gap of the electron injection process is reduced, affording a J_{SC} increase. The other parameters (FF and V_{OC}) are also improved thanks to better charge collection, better charge carrier mobilities and reduced charge recombination.[58] Similar results were obtained for other polyfluorene (**PF**)-based CPEs in the following years. Nevertheless, the thickness of interfacial layers has to be very thin to overcome the shortcoming in most cathode mofication layers, i.e. having aliphatic or *p*-type backbones, of inefficient electron transport.[59] Besides, the PCE enhancement was found to be dependent on the polymer donor structure. Indeed, Bazan *et al.* have reported that the PCE of **P3HT**:**PBCM** and **MEH-PPV**:**PBCM** solar cells were not improved by introducing cathode interfacial layers based on cationic **PF** such as **PFN**, while excellent results have been obtained with other low bang gap polymers such as **PECz-DTQx** (6.07 *vs.* 3.99 % for the reference)[60] and **PTB7** (8.04 *vs.* 5.00 % for the reference).[61] In addition to the type of ionic terminal groups, the effect of the counterion must also be considered.[62] Bazan *et al.* have indeed reported that the modification of the counterion in donor-acceptor based CPE copolymer resulted in significant variations in the charge transport properties, ionisation potentiel and electron affinity.[62c] To avoid the counterion mobility, Duan *et al.* have proposed a **PF**-based **CPE** having zwitterionic (**PFNSO**) groups. PCE of 8.74 % was thus obtained for **PTB7**:**PBCM** device.[63] Surfactants as **CPEs** counterions were also proposed for hydrophobic photoactive layers such as **P3HT**:**PBCM** leading to a significant increase of PCE from 2.12 % to 4.01 %. The introduction of surfactants affords to well-control the self-assembling of the photoactive layer.[64a]

Polythiophene-derived polymers have also been developed for **CPEs** applications.[64] Maes *et al.* have notably described that PCEs could be influenced by the nature of the cationic side-chains group.[64b,c] Consequently, in devices based on **PCDTBT**:**PBCM**, lower PCEs have been obtained with ammonium-based polythiophene (**P3TMAHT**) than imidazolium-based one **P3MIHT** (Figure 1.19).

Modifying polymer topology has also emerged as an interesting strategy to improve the PCE of solar cells. Indeed, Scherf *et al.* have also designed polyfluorene-polythiophene

diblock **CPEs** (**PF2/6-*b*-P3TMAHT**, Figure 1.19), which exhibit improved PCE compared to homopolymer due to a better interfacial dipole formation.

Based on these results, polythiophene-based **CPEs** have been synthesized and introduced in OPVs as cathode interfacial layers.[65] In the present work, we have examined the influence of the cationic side-chains group, the counterion and the polymer topology on the PCEs in order to try to elucidate the structure-properties relationship.

As the work presented in this dissertation mainly deals with π-conjugated polymers based on **P3AT**, the next section will be focus on the synthesis and the properties of this widely used polymer in OPVs, before moving to the second main axis of this work, the dye-sensitized solar cells.

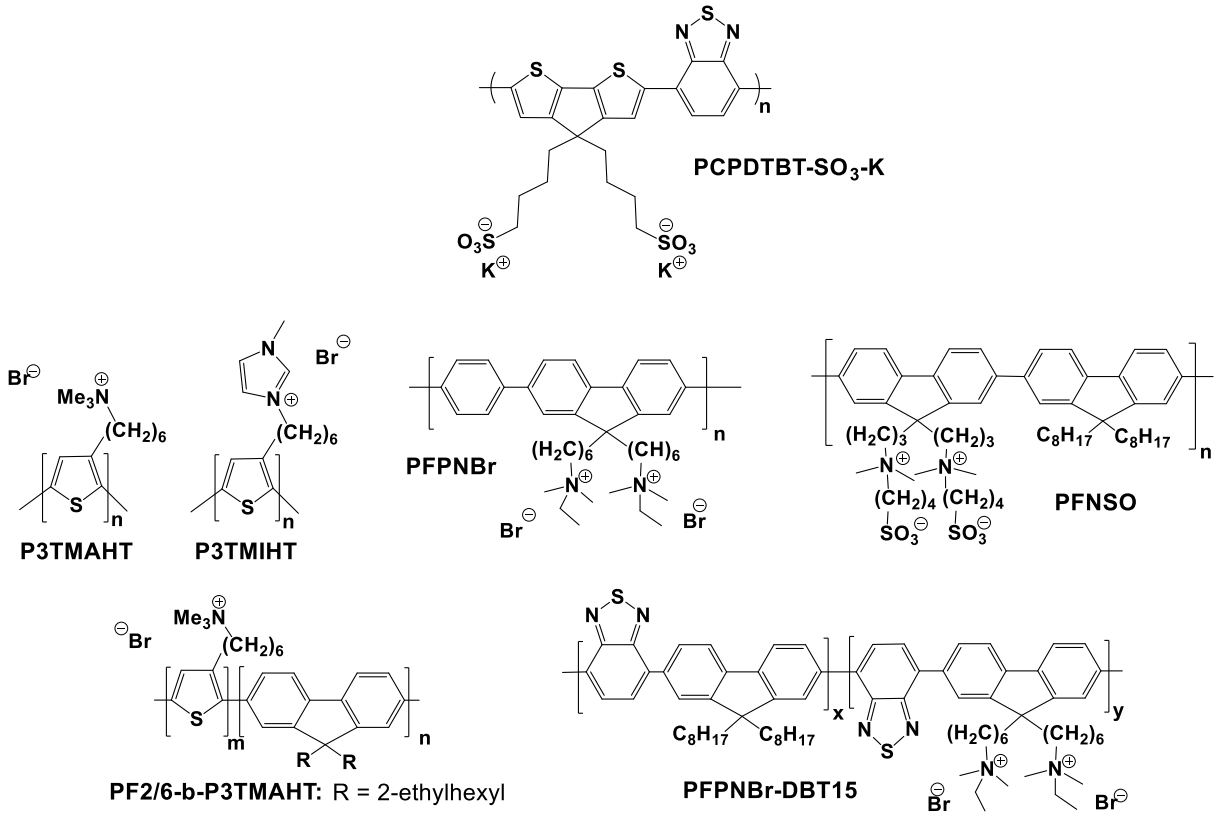

Figure 1.19 Chemical structures of some CPEs used as cathode interfacial layers in OPVs.

2.2.4. POLY(3-ALKYLTHIOPHENES)

2.2.4.A. GENERALITIES

The **P3AT** synthesis was inspired by the preparation of unsubstituted 2,5-polythiophenes (**PTs**). The first chemical syntheses of 2,5-coupled polythiophene were described independently by the groups of Yamamoto and the one of Lin and Dudek.[66] In their report, mono-Grignard of 2,5-dibromothiophene was polymerized through metal-catalyzed polycondensation (Scheme 1.1).

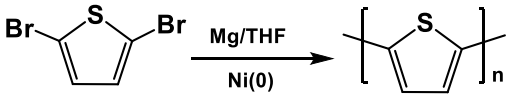

Scheme 1.1 Preparation of **PT**.

Since then, several synthetic methods were developed such as the metal-catalyzed polycondensation of 2,5-diiodothiophenes, the Wurtz coupling of 2,5-dilithiothiophene or the electrochemical polymerization.[67] However, these two latter polymerizations lead to a large number of 2,4 couplings and thus, decrease the conductivity of the obtained polymer. In general, **PTs** exhibit excellent thermal stability and conductivity, but they were found to be insoluble in various solvents due to the strong π-π interactions between the aromatic rings.

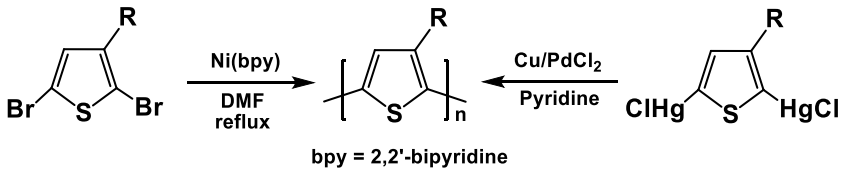

Scheme 1.2 Synthesis of **P3ATs** by dehalogenation and demercuration reactions.

As it was already known that the attachment of flexible side chains onto the backbone of insoluble polymers can dramatically improve their solubility, **P3ATs** became the subject of intense research. The first environmentally stable and soluble **P3ATs** were synthesized by Elsenbaumer *et al.* in 1986, using a metal-catalyzed coupling method similar to the one used to prepare 2,5-polythiophene.[68] Unfortunately, this metal-catalyzed polycondensation led to low molecular weight **P3ATs** (around 5 000 g.mol^{-1}, Đ around 2). In the same time, high molecular weight **P3ATs** (M_n = 30 000 - 300 000 g.mol^{-1}, Đ = 1.3-1.5) were prepared by oxidative polymerization using $FeCl_3$.[69] Other methods were also developed for synthesizing **P3ATs** such as the dehalogenation coupling reaction of 2,5-dibromo-3-alkylthiophene by nickel(0) or the demercuration reaction of 2,5-bis(chloromercurio)-3-alkylthiophene using copper and a catalytic amount of Pd(II) in pyridine (Scheme 1.2).[70] Although all these methods produce processible **P3ATs**, coupling of 3-alkylthiophenes occurs with no regiochemical control and produces structurally irregular polymers, called regioirregular poly(3-alkylthiophenes) (**irP3ATs**).

Indeed, due to the asymmetry of the 3-alkylthiophene, three relative orientations are possible when two 3-alkylthiophene rings are coupled between the 2- and 5-positions (Figure 1.20). The first orientation is 2,5' or head-to-tail (HT) coupling, the second is 2,2' or head-to-head (HH) coupling and the third is 5,5' or tail-to-tail (TT) coupling. The situation becomes more complicated with three thiophene rings. **irP3ATs** prepared by above-mentioned methods contain mixtures of these isomers, leading to 50-80 % HT couplings. The presence of the TT and in particular, the HH couplings causes a sterically twisted structure in the polymer backbone, giving rise to a loss of conjugation and thus, to a limited conductivity.[71] In addition to electronic properties, structural and optical properties of this polymer are also greatly affected.[29b,72] These considerations clearly indicate that synthetic polymerization methods which allow the formation of regioregular **P3ATs** with desired molecular weight and narrow dispersity are required to enhance the material self-assembly ability and therefore, its bulk properties. As indicated above, **P3ATs** could be synthesized by either chemical or electrochemical polymerizations. In this dissertation, we will focus on

chemical polymerizations since they offer a large scale synthesis, provide excellent yields and are used in this work.

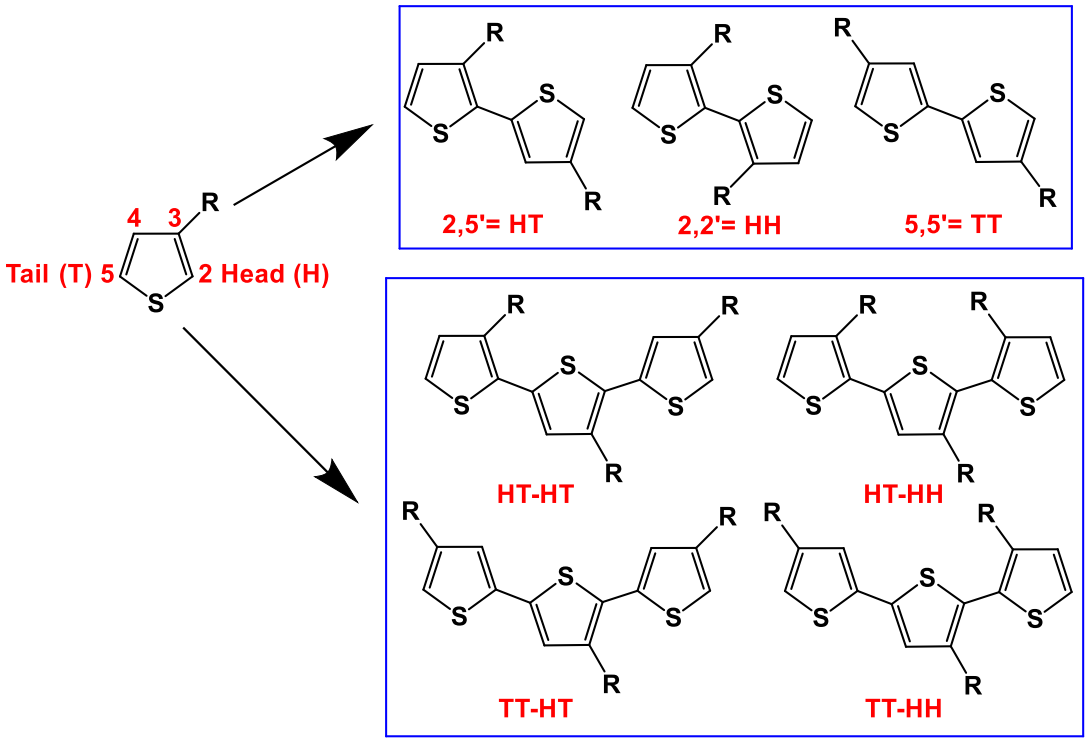

Figure 1.20 Possible regiochemical couplings of 3-alkylthiophenes.

2.2.4.B. SYNTHETIC METHODS OF REGIOREGULAR P3ATS

Nickel catalysts are probably the most common precatalysts used for Kumada and Negishi coupling reactions but palladium systems are also used for the synthesis of **rrP3AT**s as Stille, Suzuki or C-H arylation coupling methods.[73] As **P3AT** in this work was synthesized using Kumada coupling, the following part will be only focused on the nickel-catalyst cross-coupling reactions. The most commonly used methods for the synthesis of **rrP3ATs** are usually the three following ones: the McCullough, Rieke and Kumada Catalyst-Transfer Polycondensation (KCTP) methods.

Recently, Mori and coworkers developed a C-H coupling polymerization reaction based on the use of Knochel-Hauser base, *i.e.* TMPMgCl·LiCl, chloromagnesium 2,2,6,6-tetramethylpiperidide lithium chloride salt (Scheme 1.3). This method was found to be highly effective for the synthesis of oligothiophenes.[74] The treatment of 2-bromo-3-hexylthiophene with TMPMgCl·LiCl afforded the corresponding organometallic species, which were polymerized efficiently with dichloro[1,3-bis(diphenylphosphino)ethane]nickel (II) ($Ni(dppe)Cl_2$) or dichloro[1,3-bis(diphenylphosphino)propane]nickel (II) ($Ni(dppp)Cl_2$) as catalyst. **P3HTs** with high regioregularities (>97 %), molecular weight higher than 40 000 $g.mol^{-1}$ and relatively narrow dispersity (Đ ~ 1.3) were obtained.

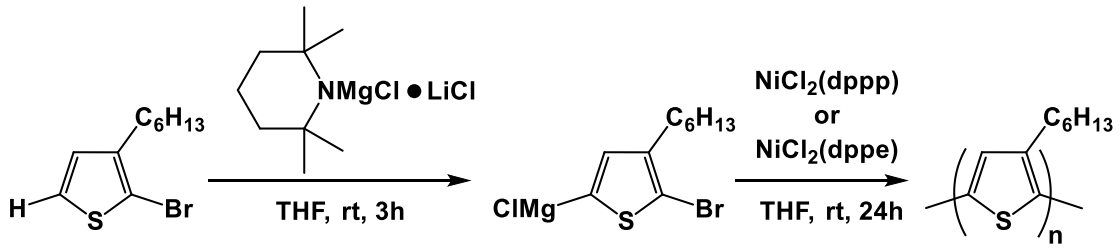

Scheme 1.3 C-H coupling polymerization applied to the generation of **rrP3HT**.

Details concerning each of these methods are shown and compared in the figure below (Figure 1.21).

The first synthesis of **rrP3ATs** was reported by McCullough *et al.* in 1992 and consists in a two-step process.[75] In the first step, 3-alkyl-2-bromo-5-bromomagnesiothiophene (**2**) is selectively prepared by treatment of 3-alkyl-2-bromothiophene (**1**) with lithium diisopropylamide (LDA) at -40°C, followed by the addition of $MgBr_2.Et_2O$ at -60°C. In a second step, an *in situ* polymerization of (**2**) by a Kumada cross-coupling reaction with dichloro[1,3-bis(diphenylphosphino)propane]nickel (II) ($Ni(dppp)Cl_2$) as catalyst is performed. By following this method, **rr-HT-P3AT** with regioregularity of 98-100 % and with isolated yields between 44 and 66 % were obtained. Molecular weights commonly obtained with McCullough method are typically 20 000-40 000 $g.mol^{-1}$ (Đ ~ 1.4).

Shortly after these first studies, an alternative method was described by Rieke *et al.*[76] The main innovation of this polymerization method lies in the use of highly reactive "Rieke zinc" (Zn*) for generating the asymmetric organometallic intermediate. Thus, zinc reacts with (**1**) and leads to the formation of two regioisomers: 3-alkyl-2-bromo-5-bromozinciothiophene (**2**) and 3-alkyl-5-bromo-2-bromozinciothiophene (**3**) in a 90:10 ratio. The control of the regioregularity in these polymerizations was explained by the steric hindrance of the molecule during the reductive elimination step of the catalytic cycle. Molecular weight commonly obtained with Rieke Method are typically 24 000-34 000 $g.mol^{-1}$ (Đ ~ 1.4). To avoid the use of the specially prepared zinc active metal (Zn*) in this reaction, Kim *et al.* replaced it by a commercially available and relatively cheap zinc powder.[77] By using zinc dust and 2-bromo-3-hexyl-5-iodothiophene whom C-I bond is more suitable to zinc insertion, polymerization of organozinc was easily achieved at room temperature. Regioregular **P3HT** with regioregularity up to 96 % and molecular weight of M_w = 28 000 $g.mol^{-1}$ (Đ = 1.98) were obtained. In later contributions, zinc dust was replaced by diisopropyl zinc,[78] readily and commercially available, or zincate thiophene monomer, prepared by treatment of 2-bromo-3-hexyl-5-iodothiophene with $t Bu_4ZnLi_2$.[79] Both methods afforded regioregular **P3HTs** with highly controlled molecular weights and low dispersity.

In 1999, another approach named Kumada Catalyst-Transfer Polycondensation (KCTP) was reported for the synthesis of **rrP3ATs**.[80] Compared to McCullough and Rieke methods, KCTP method does not require cryogenic temperatures or highly reactive metals ("Rieke zinc"). In this method, 3-alkyl-2,5-dibromothiophene (**1**) is treated with one equivalent of commercially available organomagnesium compounds leading to a mixture of 3-alkyl-2-bromo-5-bromomagnesiothiophene (**2**) and 3-alkyl-2-bromo-5-

bromomagnesiothiophene (**3**) in a 85:15 ratio. This ratio is independent of reaction time, temperature and used Grignard. As Rieke method, the choice of 3-alkyl-2-bromo-5-iodothiophene instead of 3-alkyl-2,5-dibromothiophene allows to obtain monomer (**2**) exclusively. This latter is polymerized *in situ* by a Kumada cross-coupling reaction with Ni(dppp)Cl_2 as a catalyst. In general, KCTP method leads to **rrP3ATs** with a very high regioregularity, above 99 % due to a combination of thermodynamic and kinetic effects. Molecular weight commonly obtained with KCTP method are typically between 20 000 and 35 000 g.mol^{-1} with low dispersities (Đ = 1.2-1.4).

More interesting, the KTCP method allows a better control of the polymer end-groups than the other methods. Yokozowa *et al.* described that the ratio between the monomer and the Grignard reagent is a critical factor to get narrow dispersity and homogenous H/Br end-groups.[80c] The nature and the speed of the quenching agent was also investigated: using methanol instead of HCl 5M can induce an increase in dispersity and a lack of the end-group control.[80d,81]

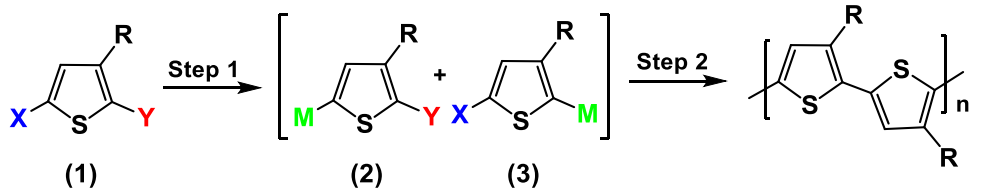

(1) (2) (3)

Method	X, Y	Step 1	M (ratio (2):(3))	Step 2	% of rr
McCullough	H, Br	1) LDA/THF, -40°C, 40 min 2) $MgBr_2.Et_2O(ZnCl_2)$, -60°C to -40°C, 40 min	MgBr (ZnCl) (98:2)	Ni(dppp)Cl_2, -5 to 25°C, 18 h	98-100
Rieke	Br, Br I, Br	Zn*/THF, -78°C to rt, 4 h	ZnBr (90:10) Zn (100:0)	Ni(dppp)Cl_2, 0°C to rt, 24 h	97-100
KCTP	Br, Br I, Br	R'MgX'/THF, rt or reflux, 1 h	MgX' (85:15) MgX' (100:0)	Ni(dppp)Cl_2, rt or reflux, few hours	>99
C-H coupling	H, Br	TMPMgCl.LiCl, rt, 30 min	MgCl.LiCl (99 :1)	$NiCl_2$(dppp) $NiCl_2$(dppe)	97 98

Figure 1.21 McCullough, Rieke, KCTP and C-H coupling methods for the synthesis of **rrP3ATs**.

Among the different methods, the KCTP is the most used for synthezing **P3HTs** with controlled molecular weights, low dispersity and controlled end-groups. The proposed mechanism for this polymerization reaction is described in Scheme 1.4. The first step consists in the reaction of 3-alkyl-2-bromo-5-bromomagnesiothiophene (**1**) with Ni(dppp)Cl_2 leading to the organometallic nickel complex (**2**). Complex (**2**) immediately undergoes a reductive elimination to obtain an associated pair, consisting of 2,2'-dibromo-3,3'-dialkyl-5,5'-bithiophene (**3**) (TT coupling) and Ni(0)(dppp) (**4**). This step is followed by an addition of dimer (**3**) on Ni(0) (**4**) leading to nickel complex (**5**). 3-Alkyl-2-bromo-5-bromomagnesiothiophene (**1**) reacts with (**5**) through a transmetallation reaction to form complex (**6**). Reductive elimination of complex (**6**) leads then to a new associated pair based

on terthiophene (**7**) and Ni(0) complex (**4**). The polymerization reaction continues to take place through successive insertions of monomer (**1**) following the catalytic cycle based on oxidative addition, transmetallation and reductive elimination. Ni(dppp) is systematically incorporated into the growing polymer chain. Thus, Ni(dppp)Cl_2 is not only a catalyst but also, a precursor of active species.

Based on this mechanism, it was thought that the KCTP method followed a step growth process. However, studies carried out by McCullough and Yokozawa showed that this polymerization followed a living chain-growth polymerization mechanism.[80d,82] The degree of polymerization of **rrP3ATs** was found to increase linearly with the monomer conversion and the molecular weight can be predicted by the molar ratio of the monomer to the nickel initator. Secondly, the addition of various Grignard reagents (R'MgX) at the end of the polymerization results in **rrP3ATs** with R' end-group. Moreover, sequential addition of monomer successfully led to chain extension of **rrP3ATs**. Thus, the KCTP method allows synthesizing **P3ATs** with narrow dispersity and defined molecular weight.

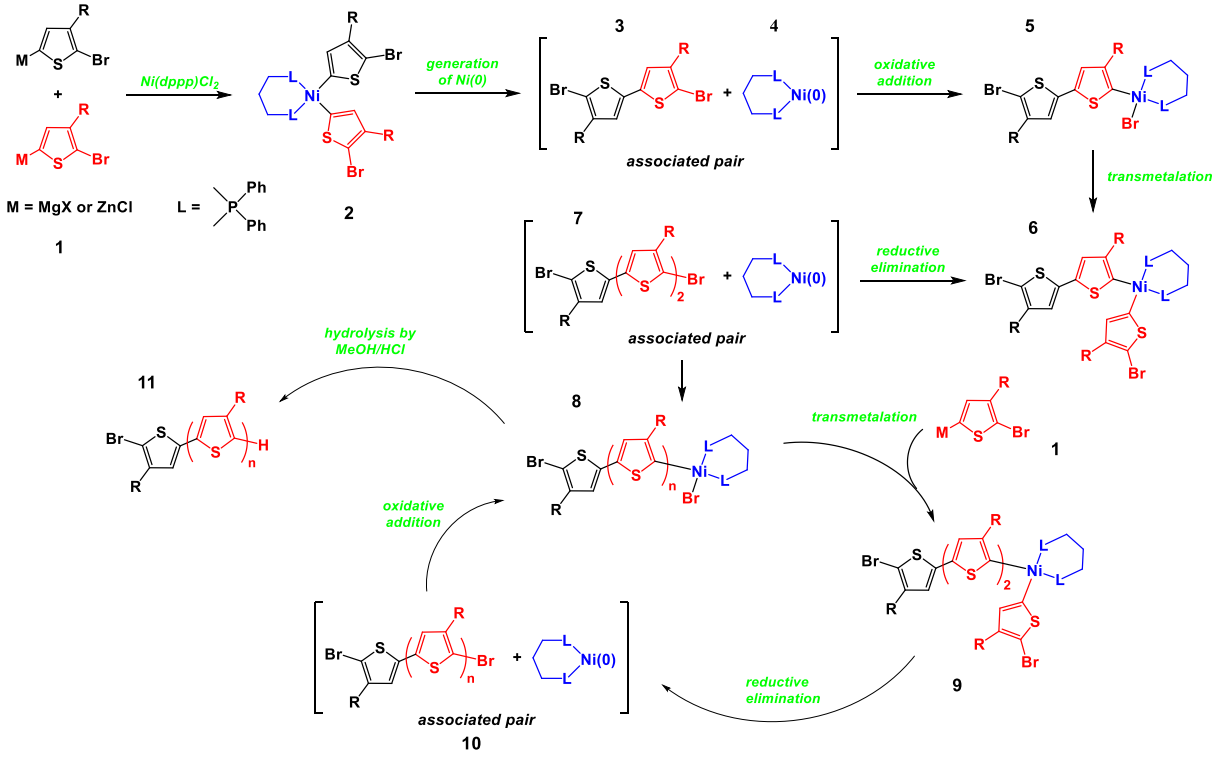

Scheme 1.4 Mechanism of the KCTP method proposed by McCullough and Yokozawa.[83]

Due to the living nature of KCTP polymerization, synthesis of block copolymers was achieved through the sequential addition of monomers. Nevertheless, after the report of Tchakov *et al.*, several methods were developed for having unidirectional growth.[84] Indeed, it was found that nickel catalyst walks along the polymerizing chain ans thus, inserts TT defect (Scheme 1.5). However, inclusion of TT defects leads to a reduced crystallinity and altered optical properties compared to the "defect-free" polymer.

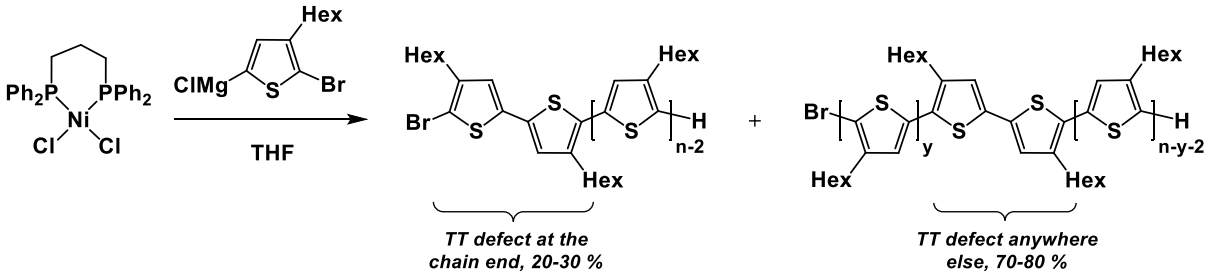

Scheme 1.5 Regioregular **P3HT** with one TT defect being distributed within the chain.

To overcome this limitation, which could be problematic for synthesizing well-defined block copolymers, synthetic methods for unidirectional polymer growth based on externally initiators (**ArNi(dppp)X** (**X** = **Cl**, **Br**)) were developed.

Kiriy *et al.* first described externally initiated **3HT** polymerization through the oxidative addition of **$Ni(PPh_3)_4$** with photocrosslinked poly(4-bromostyrene) films. [85] Unfortunately, such polymerization failed, probably because of the weak reactivity of the coordinatively saturated **$Ni(PPh_3)_4$** complex.

In this respect, Locklin *et al.* used **$Ni(COD)_2$** (COD = 1,5-cyclooctadiene) as the source of **Ni(0)**, and combined it with triphenylphosphine (**PPh_3**) to generate **Ni(0)** species for preparing surface grafted-conjugated polymers.[86] In that system, the weakly dissociating **COD** ligands are displaced by **PPh_3**, leading to the formation of a reactive intermediate species, **$Ni(COD)(PPh_3)_2$**. Unfortunately, **PPh_3** is an attendant ligand that offers poor results in KCTP in comparison to its bidentate **dppp** and **dppe** counterparts. The direct incorporation of **dppp** or **dppe** into KCTP initiators is not a trivial task, since **$Ni(dppp)_2$** and **$Ni(dppe)_2$** complexes are nearly inert toward oxidative addition.[87]

To overcome this problem, Luscombe[88] and Kiriy[89] independently developed ligand exchange reactions allowing the preparation of surface-bound initiators carrying state-of-the-art bidentate phosphine ligands. These initiators were prepared by reacting aryl halides with **$Ni(PPh_3)_4$**, followed by ligand exchange with **dppe** or **dppp**. Similar exchange processes have been also developed by the group of Locklin, where an immobilized arylhalide as initiator is immersed in a **$Ni(COD)_2$ / PPh_3** or **bpy** solution, followed by ligand exchange with **dppp**.[90]

In these initiators, the type of functional group present on the aryl halide plays nevertheless a crucial role in the polymerization. McNeil *et al.* reported that electron donating groups (OMe or NMe_2) lead to polymers with low dispersity whereas electron withdrawing groups (CF_3 or F) provided polymers with higher dispersity. The electronic properties of the ligand of the initiator were also found to influence the polymerization reaction.[91]

*2.2.4.c. **P3HTs***

Among the **P3ATs**, the regioregular poly(3-hexylthiophene)s (**rrP3HTs**) have attracted tremendous interest because of their high hole mobility and better self-organization properties, combined with a good solubility. The effects of alkyl side chain length on the electrical, optical and structural properties of **P3ATs** have extensively been investigated. It

was highlighted that the mobility of poly(3-butylthiophene) (**P3BT**) (1 x 10^{-2} $cm^2.V^{-1}.s^{-1}$) is higher than for **P3HT** (5 x 10^{-3} $cm^2.V^{-1}.s^{-1}$) and the mobility further decreased with poly(3-octylthiophene) (**P3OT**) (3 x 10^{-5} $cm^2.V^{-1}.s^{-1}$) and poly(3-dodecylthiophene) (**P3DDT**) (1 x 10^{-6} $cm^2.V^{-1}.s^{-1}$). These values can be explained by the π-stacking density: the shorter side-chain length results in a higher organized system in the charge transport region, leading to higher mobility.

P3HT has strong self-organization abilities: careful processing allowed self-assembly into densely packed elongated nanofibrils. Regioregular **HT-P3HT**s exhibits a supramolecular architecture consisting in a lamellar structure with two dimensional conjugated sheets formed by interchain stacking in contrast with **irP3HTs.**[92] Sirringhaus *et al.* suggested that **P3HT** adopts two different orientations (*i.e.* parallel and normal to the film), which depend on its regioregularity and processing conditions. Indeed, **P3HT** with high HT regioregularity (RR = 96 %) form lamellae with "edge on" arrangement while **P3HT** with low HT regioregularity (RR = 81 %) were found to adopt a "plane-on" or flat orientation (Figure 1.22). X-ray diffraction data of highly **rrP3HT** film exhibited three highly ordered (h00) scattering peaks that corresponded to the lamellar stacks in the out-of-plane direction (q_z) and a narrow single wide-angle reflection (010) peak was also observed, corresponding to the π–π stacking in the in-plane direction (qxy). On the X-ray diffraction spectrum, the peaks indicated a well-organized structure with edge-on geometry of the **rrP3HT** became weaker, as the RR decreased.

Like crystallinity, thermal properties of the **P3HT** are greatly impacted by the regioregularity. As the RR decreased, T_m and T_c decreased progressively until they disappeared. This strong decreasing trend in both T_m and T_c is concomitant with a remarkable decrease in the interchain interaction and the decreasing degree of crystallinity.

Electrical properties are also strongly correlated with the regioregularity. Due to their three dimensional self-assembled superstructure, **rrP3HT** exhibits efficient two-dimensional hole transport with high mobilities and current density. Jian *et al.* evaluated mobilities of charge carriers in films of **P3HTs** with different HT regioregularities of 97, 81, 70 and 54 %. The difference in regioregularity of **P3HT** resulted in a large mobility difference: from 0.4 to 0.01 $cm^2.V^{-1}.s^{-1}$ for 97 % **P3HT** and 54 % **P3HT**, respectively.

The regioregularity also plays an important role in the bandgap control. In UV-Vis absorption, **rrP3HT** showed a significant redshift of the maximum absorption (λ_{max}) with respect to **irP3HT**s. As an example, the λ_{max} in solution for **rrP3HT** with RR = 98 % and RR = 64 % were found to be 457 and 441 nm, respectively. This redshift indicates that the **rrP3HT** has a π-π* transition at lower energy and thus, a longer π-conjugation, attributed to the more planar conformation of the regioregular polymer chains. The difference in λ_{max} between regioregular and regioirregular PTs become more distinct in thin film. **rrP3HT** (RR = 98 %) shows a λ_{max} at 557 nm while **rrP3HT** (RR = 64 %) exhibits a λ_{max} at 496 nm. The vibronic peaks (A_{0-1} and A_{0-0}) were also significantly decreased as the RR decreased. As such, the corresponding optical bandgaps ($E_g$opt) of the **P3HTs** were increased gradually from 1.88 eV (RR = 98 %) to 1.94 eV (RR = 64 %).

Besides the HT regioregularity, **P3HT** molecular weight and dispersity are also important parameters to consider since they influence optical, electronic, electrochemical properties, and solid-state packing.[93]

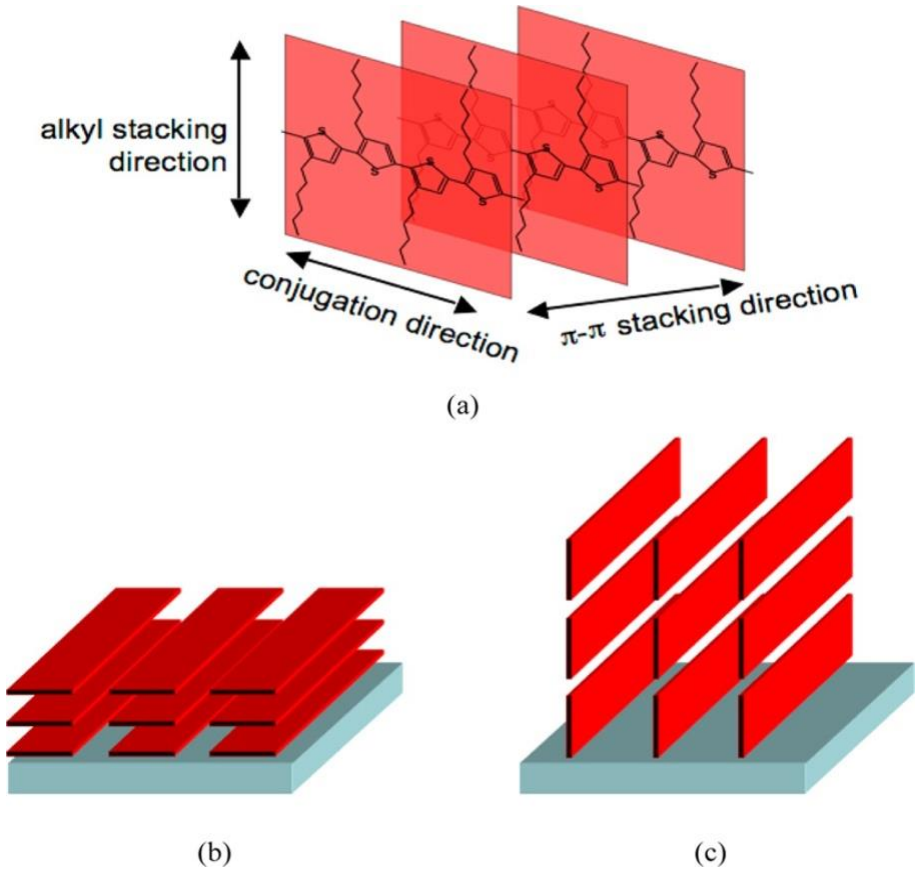

Figure 1.22 (a) Schematic structure showing the preferred arrangement of adjacent chains of regioregular **HT**-**P3HT**. (b) Plane-on orientation of **P3HT** with respect to an underlying surface. (c) Alternative edge-on arrangement.[94]

*2.2.4.D. FUNCTIONALIZATION OF **P3HT***

In view of enhancing and fully exploiting the properties of poly(3-hexylthiophenes), their facile chemical modification is required. In particular, the tailoring of **P3HT** properties has mainly focused on the modification of the hexyl side chains and the end-groups of **P3HT** to expand their structure-property relationships in view of improving their performance in photovoltaic devices.

END-GROUP FUNCTIONALIZATION

Three different approaches have been developed to alter end-group composition of **P3HT**: (a) *in situ* method mainly based on the introduction of Grignard reagents at the end of the polymerization, (b) *ex situ* method involving functional Ni-based initiators in combination with KCTP and (c) post-polymerization modification of end-functional **P3HT** relying on the conversion of aryl bromides or other groups to achieve the desired functionality.[81b,81c,95]

These end-functionalized **P3HT** could be used as a macroinitiator for preparing block copolymers.

The *in situ* method offers the advantage of modifying end-group(s) in a one pot procedure. This synthetic strategy is illustrated in Scheme 1.6 as well as a list of end-functional groups that can be easily introduced on **P3HT**. The first attempt toward *in situ* end-group functionalization was reported by Janssen *et al.* using McCullough method. In this strategy, the polymerization was quenched with 2-thienylmagnesium bromide or 5-methylsilyl-2-thienylmagnesium bromide, leading to a mixture of mono- and dicapped polymer chains.[96] Subsequently, McCullough and coworkers described a simple and versatile *in situ* method to achieve end-functionalization of **rrP3HT**. This strategy involves quenching of the KCTP polymerization with a wide range of Grignard reagents such as allyl, vinyl, aryl and alkyl. The degree of end-functionalization was found to be dependent on the nature of Grignard reagent. Indeed, when unsaturated group such as allyl, ethynyl or vinyl based-grignard reagent are used, only monofunctional polymers were obtained while other Grignard reagents result in dicapped polymer chains. It was suggested that such behavior originated from the formation of nickel-π complex with unsaturated group, which prevents further reaction with the aryl bromide end-group. Based on this statement, Pickel *et al.* showed that adding unsaturated additives such as 1-pentene and styrene immediately before the addition of the quenching Grignard reagent decreased significantly the amount of diccapped polymer chains.[97] In addition, Thelakkat and Lohwasser demonstrated that the nature of end-groups in KCTP polymerization could be perfectly controlled by controlling the consumption of the alkyl Grignard reagent necessary to the formation of the active monomer.[81] These findings facilitated the incorporation of reactive units such as –OH, -CHO, $-NH_2$ with the use of the adapted protecting groups but also, nitrogenous heterocyclic groups (pyridine, oxadiazole, triazole).

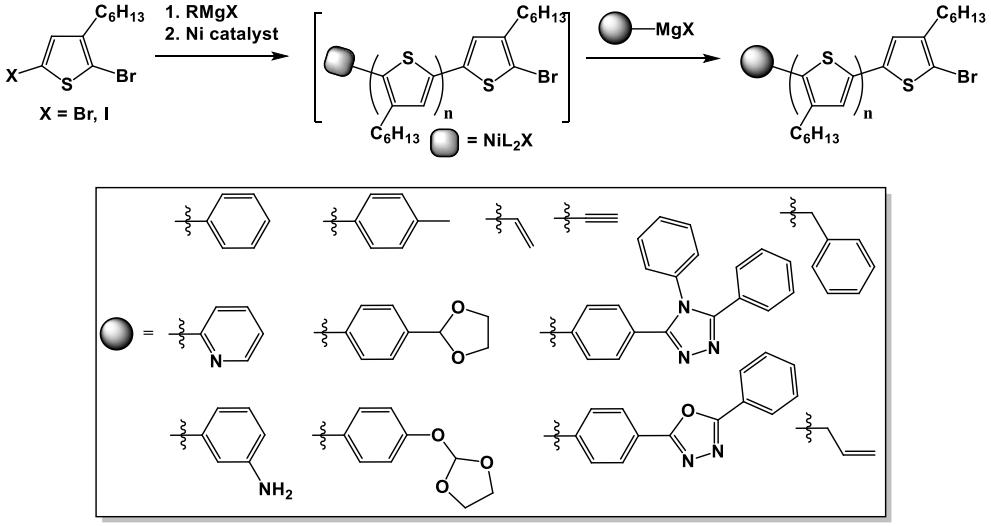

Scheme 1.6 Synthetic pathway to *in situ* end-group functionalization of **P3HT** and comprehensive list of **P3HT** end-functional groups incorporated by this method.

The *ex situ* method consists in the polymerization of 3-hexylthiophene based-monomers from Ni-initiators equipped with a functional group (Figure 2.6). As a matter of fact, a wide range of different nickel-initiators incorporating (protected) alcohol, ethynyl, carboxylic acid, amine, and phosphonate functional groups have been independently developed by the groups of Kiriy, Luscombe,[88,98] Bazan[99] and Koeckelberghs[96,100] (Scheme 1.7).

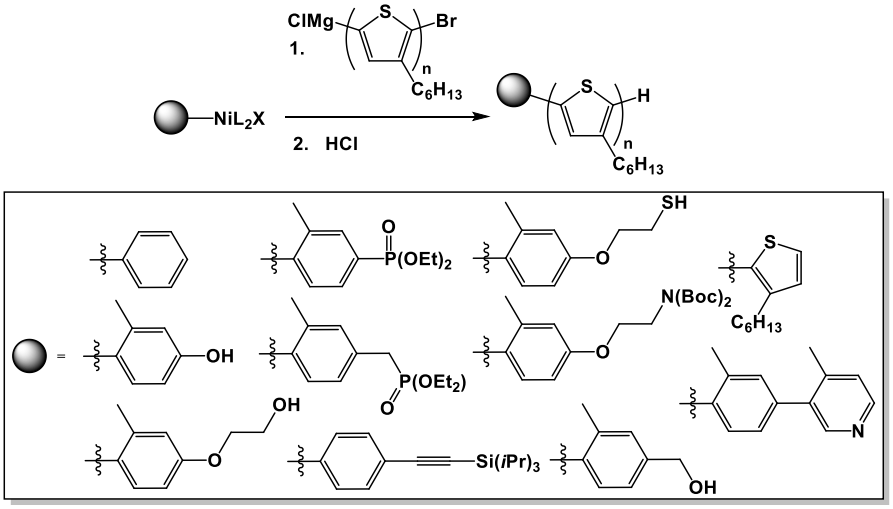

Scheme 1.7 Synthetic pathway to *ex situ* end-group functionalization of **P3HT** and comprehensive list of **P3HT** end-functional groups incorporated by this method.

The *ex situ* method opens the door to prepare hybrid materials with inorganic particles, in particular conjugated polymer brushes on inorganic surfaces via a "grafting from" approach.[81b,87,101] While this *ex situ* method for preparing end-functionalized **P3HT** seems straightforward in principle, its practical implementation starting from an aryl halide has proven to be very challenging. Indeed, the initiator must exhibit high purity and be quite stable otherwise polymer chain ends not functionalized by the desired group may be obtained. Furthermore, since a Grignard reagent is used, the choice of compatible derivatives is limited.

Compared to the previous methods, the post-polymerization modification strategy is compatible with a wide range of functional groups and allows functionalizing both chain-ends, either with the same or different groups (Scheme 1.8).
Regioregular **P3HT**s synthesized through the KCTP polymerization have fairly pure end-group composition with a proton at one end and a bromine at the other end (H/Br). McCullough and coworkers first demonstrated this strategy by selectively functionalizing one or two end-groups of **P3HT**. Thus, thienylzinc derivatives bearing protected amino and alcohol groups were selectively introduced at one end of the **P3HT** chain by a Negishi coupling reaction.[102] In contrast, by selectively preparing the H/H type **P3HT**, the same group converted these two end-groups to aldehyde, which were subsequently reduced into the corresponding hydroxymethyl groups.[103] Various functions were then introduced.[104]. Bromide end-groups were exploited for C-C cross-coupling reactions such as Stille and Suzuki-Miyaura[105] coupling reactions. Mono- and dicapped **P3HT** chains can also be selectively prepared by judiciously

choosing the reagent. Luscombe *et al.* have notably reported the synthesis of **P3HT** with thiol end-groups at one or both chain-ends using sulfur powder or triisopropylsilanethiol as the functionalization agent, respectively.[106] Although the post-polymerization strategy seems versatile, this method requires multi-step synthesis, tedious purification procedures and specific coupling reagents.

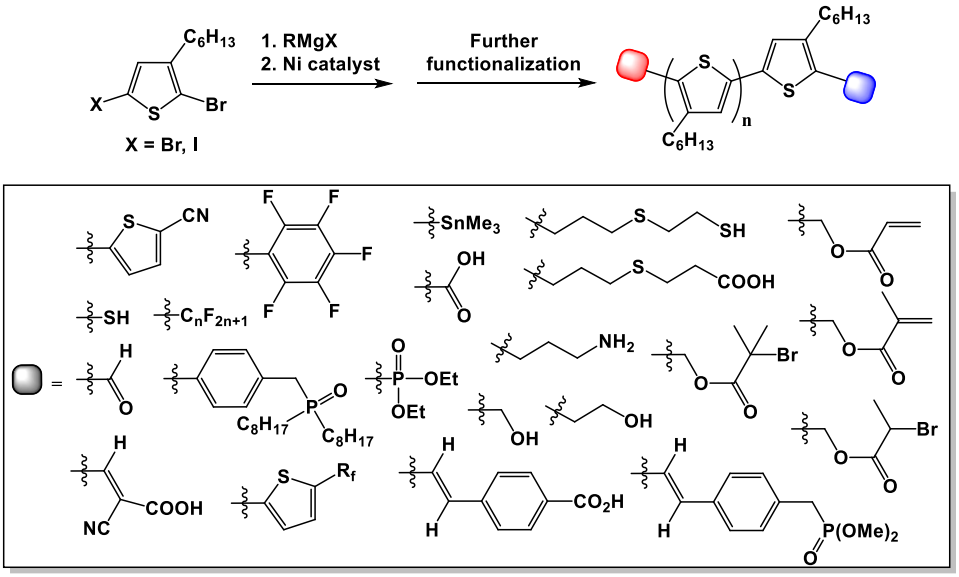

Scheme 1.8 Synthetic pathway to post-polymerization end-group functionalization of **P3HT** and comprehensive list of **P3HT** end-functional groups incorporated by this method.

SIDE-CHAIN FUNCTIONALIZATION

Studies involving side chain engineering are much less numerous whereas the nature of the side chain was found to be an important parameter for designing conjugated polymers.[107] Indeed, material synthesis, processing and device fabrication and thus, PCEs could be significantly improved by side chain engineering.[108] These effects of side chains can be due to size, density, topology (linear *vs.* branched), and in the case of multiple different side chains, composition and distribution (*e.g.* uniform, random, etc.). Regarding that, side-chain functionalized polythiophenes are particularly interesting since Kumada Catalyst-Transfer Polycondensation is available to prepare multiple polymer topologies (homopolymers, random/block copolymers) with a high degree of control over the final structure and molecular weight.

Two strategies were developed to end-functionalize side chains of **rrP3HTs**. The first one involves the polymerization of thiophene monomers with protective groups at the γ end of the side chains. These protective groups allow incorporating functional groups, which are sensitive to polymerization conditions. After polymerization, deprotected **rrP3HTs** can be functionalized with other functionalities such as 2,6-bis(hexylamino)pyrimidine groups to interact with a thymine-based fullerene via hydrogen bonding interactions and thus, stabilize the morphology of the active layer.

Another approach to functionalize the side chain of **rrP3HT**s consists in incorporating reactive groups at the γ end of the side chains that are stable towards polymerization

conditions. Among these reactive groups, bromine is the most used (Scheme 1.9). After optimizations, **rrP3HT**s with various groups such as carboxylic acid, amine, thiol[109], alkene,[110] imidazole, alkoxy,[111] fullerene[112] and azide[113] were developed starting from poly(3-(6'-bromohexyl)thiophene) precursors.

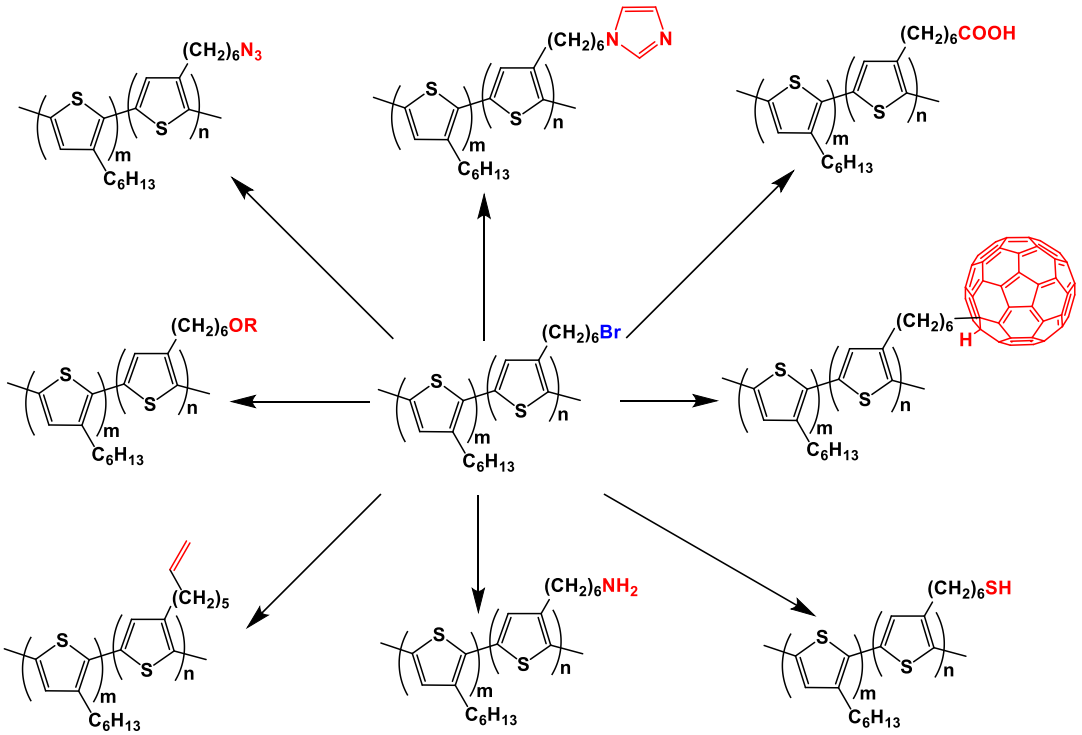

Scheme 1.9 γ end-functionalized side chain **rrP3HT** starting from poly(3-(6'-bromohexyl)thiophene).

After this brief overview of the synthesis and properties of **P3HT** derivatives, we will describe the working principle, the constituents and the advances for dye-sensitized solar cells.

3. DYE-SENSITIZED SOLAR CELLS

Dye-sensitized solar cells (DSSCs) can be viewed as an artificial photosynthesis because they mimic the nature. In natural photosynthesis, an electron release followed the sunlight absorption by the chlorophyll, a dye. Chlorophyll is then regenerated thanks to several chemical reactions.

The first work on DSSCs were first initiated in 1970 by H. Tributsh *et al.* who developed a device where a dye, *i.e.* the chlorophyll, was put in contact with a *n*-type semiconductor, *i.e.* zinc oxide. They demonstrated that it was possible to generate a charge carrier in the dye following the sunlight absorption and to transfer it to the semiconductor.[114] Then, M. Matsamura *et al.* showed that the electron injection from the dye to the semiconductor was only efficient if the dye is directly grafted onto the oxide.[115] However, the obtained currents still remained low (J_{SC} around 2.3 µA.cm^{-2}). Highly efficient DSSCs with PCE reaching 7.9 % were first reported in 1991 by O'Regan and Grätzel, emerging as an interesting alternative to inorganic solar cells.[13]

3.1. WORKING PRINCIPLE

A typical DSSC is constituted by a mesoporous film of a nanocrystalline semiconducting metal oxide, sensitized by a dye that is directly put in contact with a liquid electrolyte based on a redox couple (Figure 1.23). The whole is encapsulated between two electrodes of conductive glass to form a dye-sensitized solar cell, also called Grätzel cell. It can be noted that the semiconductor metal oxide generally consists in titanium oxide (TiO_2), which actually lead to the best PCEs for these cells.[4b] In this dissertation, we will focus only on TiO_2-based DSSCs (cf. Chapter 4).

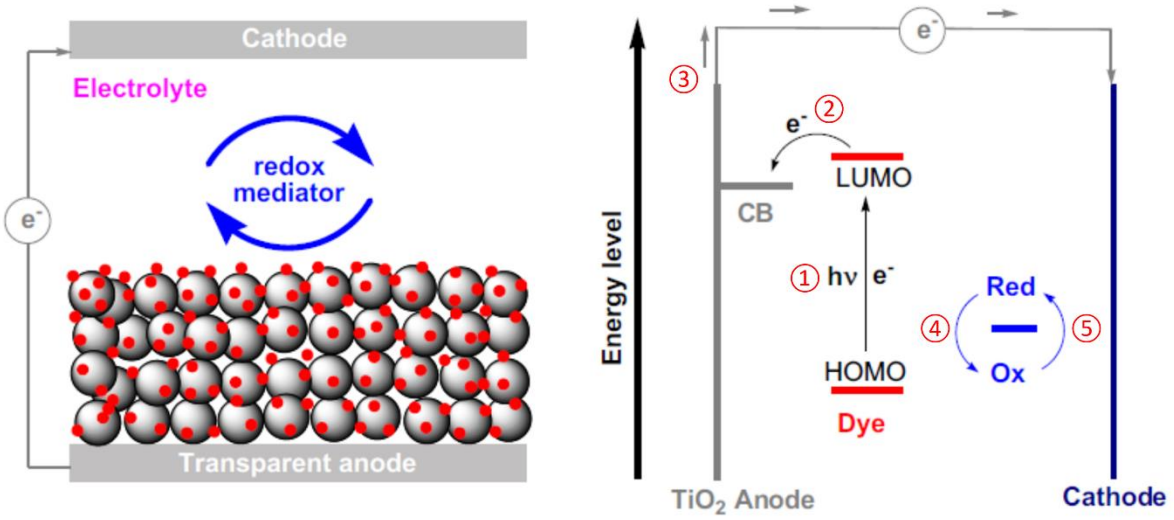

Figure 1.23 Schematic representation (left) and working principle (right) of a dye-sensitized solar cell.

After the absorption of a photon (**1**), dye molecules are promoted to an exited state ($S^0 \rightarrow S^*$), resulting in the electron transfer from the highest occupied molecular orbital (HOMO) to the lowest unoccupied molecular orbital (LUMO). This process is only possible if the incident photons have higher energy than HOMO-LUMO band gap. The dye can thus inject this electron upon oxidation in the conduction band of the metallic oxide on which it is grafted (**2**). After diffusion into the TiO_2 layer, the electron is collected by the external circuit via the transparent and conductive electrode: the photoanode (**3**). The electron transfer into the oxide is governed by diffusion and trapping/entrapping at the grain boundaries and defects. The oxidized dye, *i.e.* S^+, is then reduced by the redox couple in the electrolyte to refund its fundamental state, *i.e.* S^0 (**4**). The reduced form of the redox couple is regenerated at the counter-electrode that gives one electron from the external circuit (**5**). In summary, there is no consummation or formation of species under working, *i.e.* the electrons are the only one to move in the cell under illumination affording a photocurrent.

As for BHJ solar cells, we will show in the following section that the choice of the components is of crucial importance to ensure the effective operation of the device.

3.2. CHOICE OF COMPONENTS

3.2.1. THE PHOTOANODE

The photoanode consists on a conductive substrate on which is deposited the metal oxide layer.[14] Therefore, a large surface area is needed to ensure high dye loading and a fast charge transport rate is required to ensure high electron collection efficiency. In the case of inflexible DSSCs, the conductive substrate consists generally in glass having an additional layer of transparent conductive oxide (TCO), as indium tin oxide (ITO) or fluorine-doped tin oxide (FTO). This electrode must exhibit an adequate transparency for photovoltaic applications as well as a high electrical conductivity. The ITO substrate is known to be more conductive but the FTO substrate presents a better thermal stability, a key point regarding the fabrication process where thermal annealing until 500°C are necessary. Consequently, most of the DSSCs have a FTO substrate. In the case of flexible DSSCs, since fabrication process at low temperatures are required, polymer-ITO electrode such as polyethylene terephtalate-ITO (**PET-ITO**) or polyethylene naphtalate-ITO (**PEN-ITO**) are used.[14]

Then, a metal oxide layer is deposited on the substrate and can be distinguished in two parts:

- A dense metal oxide layer, which is deposited by spray pyrolysis, allowing to enhance the adhesion with the FTO layer and to avoide a direct contact between the electrolyte and the FTO layers. By introducing this layer, the short-circuits that could be generated at the interface are thus reduced.
- A mesoporous metal oxide layer, considered as the active one where the dye molecules are concentrated after the sensibilization. The porosity of this layer enables increasing the grafting surface and thus, the dye quantity and the sunlight absorption.

Metal oxides have to meet several requirements as a large band gap to avoid absorption in the visible region and a conduction band having an appropriate gap with the exited state of the dye to allow a fast electron injection without damaging the open circuit voltage (V_{OC}) value. The optimal gap is estimated to be around 100-150 mV. Other parameters like the charge mobility and lifetime into the metal oxide can also influence the choice of material. As indicated above, highest PCEs are still obtained with titanium oxide (TiO_2)[14b] but many other metal oxides have been tested such as ZnO,[116] SnO_2,[117] Nb_2O_5,[118] and Zn_2SnO_4..[119] (Table 1.1).

Metal oxide	PCE (%)	Dye	Electrolyte	P_{in} (mW.cm-2)	Surface (cm^2)
TiO_2[14b]	11.2	N719	I_3^-/I^-	100	0.158
ZnO[116]	7.5	N719	I_3^-/I^-	100	0.25
SnO_2[117]	4.4	N719	I_3^-/I^-	100	-
Nb_2O_5[118]	4.1	N3	I_3^-/I^-	100	0.25
Zn_2SnO_4[119]	3.8	N719	I_3^-/I^-	100	0.2

Table 1.1 Power conversion efficiencies as a function of the metal oxide used in DSSCs.

The most efficient DSSCs are currently composed of a nanoporous titanium oxide structure with nanoparticles around 20 nm. This porous structure exhibits a large surface area which allows grafting an important amount of dye molecules. Actually, many researches are underway to improve the performances of this mesoporous layer. For example, treating the TiO_2 mesoporous layer by titanium chloride ($TiCl_4$) before the sensitization leads to an enhancement of the photogenerated current. $TiCl_4$ treatment increased the surface roughness and necking of TiO_2 nanoparticles, which thus improved the dye adsorption.[120]
Recombinations are the main limitations of DSSCs. Electrons spend around 1 ms in TiO_2 layer which is a fairly time and can induce recombinations with dye and electrolyte.[14b] It was thus envisaged to replace the mesoporous structure by 1D structures (nanotubes, nanowires, etc.) to avoid the grain boundaries and defects that increase recombination probability. These 1D structures constitute a direct path for electron transfer compared to the mesoporous structure and have less boundaries grains, resulting in higher electron diffusion length than mesoporous ones.[121] By tuning the geometry, electron diffusion lengths up to 100 nm have been observed allowing to reduce the recombination. Despite these advantages, PCEs of 1D-based devices are still lower (5 and 7.6 % for nanowires and nanotubes, respectively).[121]
Other methods were also developed to obtain effective photoanodes such as the doping of the semiconducting metal oxide with ions or its decoration with noble metals.[122]

3.2.2. DYES

The dye, which can be considered as the heart of the DSSC should fulfill some essential characteristics:[14]

1) Its absorption spectrum should cover the whole visible region and even the part of the near-infrared (NIR), as 40 % of the solar light is emissive in this region.
2) It should have anchoring groups such as carboxylic group (-COOH), phosphoric acid (-H_2PO_3), sulfonic acid (-SO_3H), etc. to strongly bind the semiconductor surface. Carboxylic acids have different way to bind the surface but generally the dyes are coordinated to the metal oxide surface by ester covalent bonds also called unidentate or bidentate. This binding enables a strong anchoring of the dye as well as a good electronic communication between the two materials (Figure 1.24).
3) The excited state level of the dye should be higher in energy than the conduction band edge of the semiconductor to afford efficient charge transfer.
4) For the dye regeneration, the oxidized state level of the photosensitizer must be more positive than the redox potential of the electrolyte, to avoid the recombination between the oxidized dye and the oxide-injected electron.
5) Dye should have a molecular structure easily to modify to avoid unfavorable dye aggregation on the semiconductor surface. Some co-adsorbers can be used as additives to also prevent the dye aggregation. However, it can be noted that in some cases, dye aggregates (H- and J-type) improve the performances.[123]
6) The dye should be light, electrically and thermally resistant for at least 20 years.

Based on these requirements, many different sensitizers have been studied and significant progress in designing dyes for DSSC applications has been done. Dye can be classified into three dominant categories: (1) Ru-complexes, (2) organic dyes and (3) porphyrin dyes.

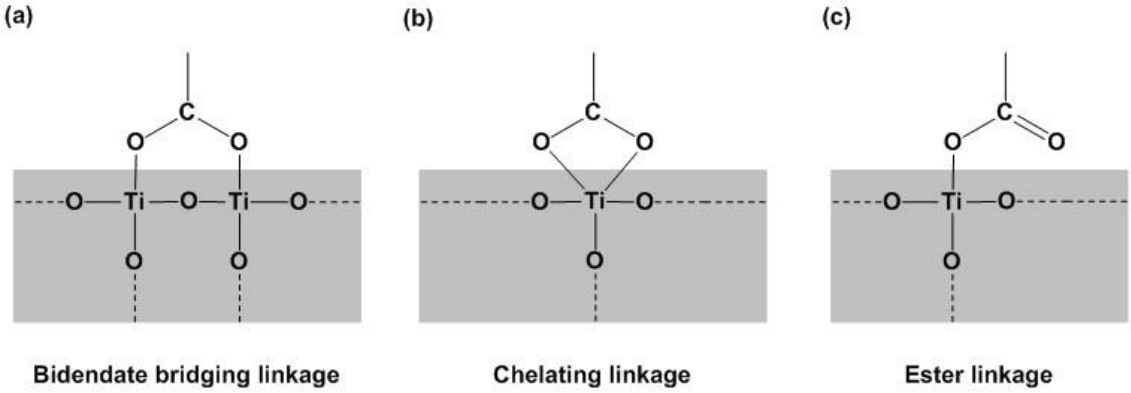

Figure 1.24 Binding modes of the COOH-group by the *p* orbital of oxygen to the 3d orbital of titanium on the TiO_2 surface: (a) bidendate bridging, (b) chelating and (c) ester linkages.

RU-COMPLEXES

Several types of ruthenium dyes have been developed for DSSCs since the original publication of O'Regan and Grätzel in 1991, where a trinuclear-Ru dye ($RuL_2((\mu\text{-}CN)Ru(CN)L_2')_2$, L = 2,2'-bipyridine-4,4'-dicarboxylic acid and L'= 2,2'-bipyridine) has been used. Up to date, the best photovoltaic performances have been reported for Ru(II)-polypyridyl complexes with carboxylated anchoring groups. These complexes display a broad absorption profile extending from the visible to near-infrared (NIR) regions with high molar extinction coefficients (ε), orbital energy levels matching with the conduction band of the metal oxide and the electrolyte thus inducing an IPCE over 80 % in the visible.[120] The most efficient Ru-polypyridyl dyes are **N3**,[124] **N719**[125] and **N749**[126] also called black dye (Figure 1.25). **N3** and **N749**-based DSSCs have similar V_{OC} (about 720 mV) and PCEs of 10 and 11.1 %, respectively. **N719**, which has almost the same structure as **N3** yielded to PCE of 11.2 %.

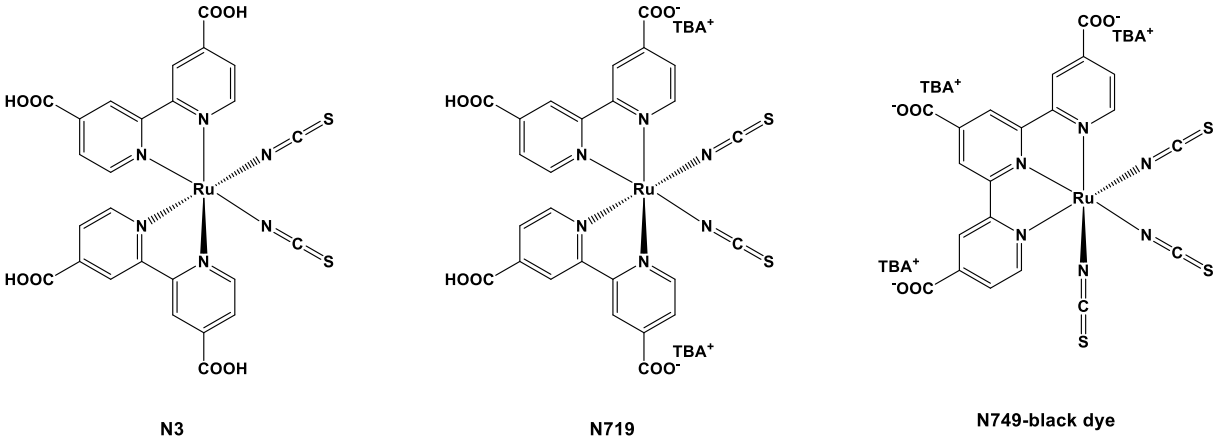

Figure 1.25 Structures of ruthenium complexes used in DSSCs with PCEs up to 10 %.

The main strategy to improve the photovoltaic performances of these dyes was to modulate the different peripheral ligands and anchoring groups (nature and number).[14] Hara *et al.* have notably investigated a series of Ru(II)-phenantroline complexes such as

$Ru(dcphn)_2(SCN)_2$ (dcphn = 4,7-dicarboxy-1,10-phenanthroline), for which the number and the position of carboxyl anchoring groups were different. These parameters were found to significantly affect the electronic coupling between the dye and the semiconducting metal oxide, a key requirement for efficient electron injection in the DSSC (Figure 1.26).[127]

Since 2003, novel amphiphilic ruthenium complexes were developed leading to PCEs up to 10.2 %.[128] The first one, **Z907** developed by Wang *et al.,* yielded to stable performances even after long-term thermal stress (around 1 000 hours): a PCE of 7.3 % and an IPCE over 80 % in the visible (Figure 1.26).[129] The hydrophobic alkyl chains attached to bypyridine ligand prevents the dye desorptionfrom the metal oxide surface by eliminating the presence of water at the interface between dye andsemiconductor .

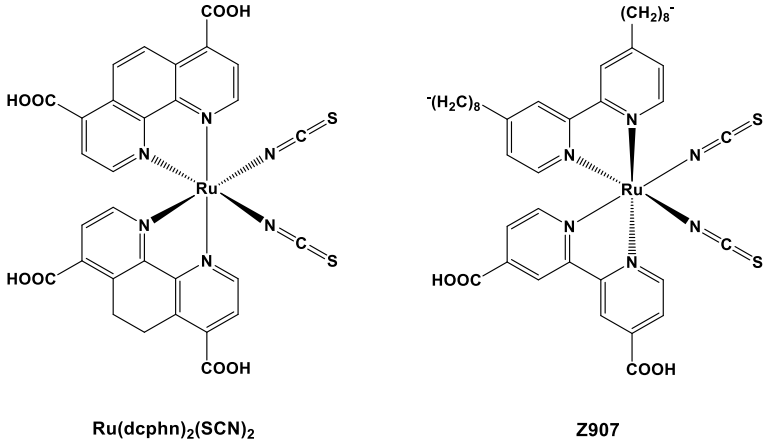

Figure 1.26 Structures of phenantroline- and amphiphilic ruthenium complexes used in DSSCs.

In 2008, Gao *et al.* developed new heteroleptic Ru-complexes, coded **C101** and **C102**, with thiophene and furane moieties attached to the bipyridine ligand (Figure 1.27).[130] These furane- and thiophene functionalized bipyridine ligands allowed increasing their ε and thus, their light-harvesting. For example, **C101** with a $\varepsilon_{407} = 1.75 \times 10^4\ M^{-1}.cm^{-1}$ yielded to a PCE of 11.3 %. Based on this finding, an analogue of **C101** was synthesized by Cao *et al.*, coded **C106**, where a sulfur atom was introduced between alkyl chain and thiophene ring (Figure 1.27).[131] The use of **C106** as dye in DSSC afforded PCE of 11.29 % ($\varepsilon_{550} = 1.87 \times 10^4\ M^{-1}.cm^{-1}$). Besides, by adding lithium salts to the electrolyte and optimizing the TiO_2 film, PCEs of **C106**-based devices were increased up to 11.9 %.[132]

In order to extend the π-conjugation length in these Ru-complexes, other heteroleptic dyes have been developed.[14] For example, **CYC-B11** ruthenium complex with an additional thiophene unit on bipyridine ligand, compared to **C106** dye leads to an enhanced PCE of 11.5 % (Figure 1.27).[133]

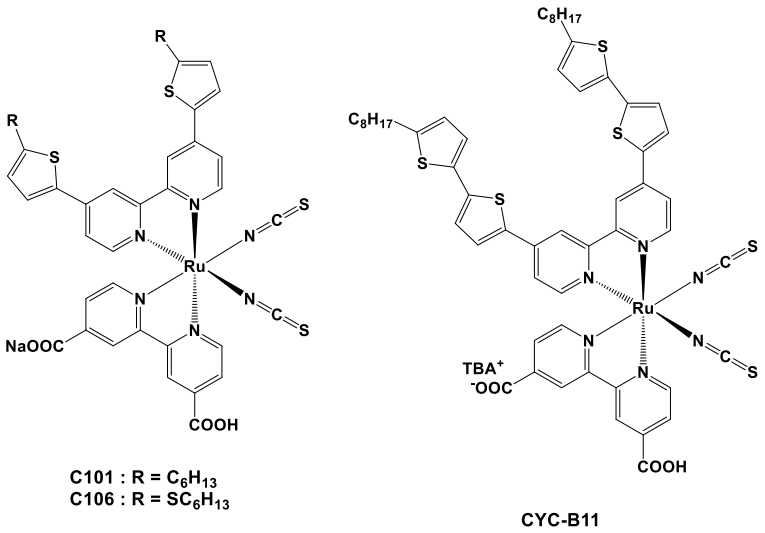

Figure 1.27 Structures of heteroleptic ruthenium complexes used in DSSCs.

In terms of chemical stability, the SCN^- donor ligands were found to be a drawback. In this respect, SCN-free Ru-complexes such as **YE05** have been designed leading to PCEs around 10 % (Figure 1.28).[14,134] Very recently, a near-infrared phosphine-coordinated Ru(II) sensitizer, coded **DX1**, achieved a DSSC with a J_{SC} of 26.8 $mA.cm^{-2}$, the highest value recorded for an organic photovoltaic. The tandem-type DSSC employing both **DX1** and **N719** sensitizers allowed reaching PCE > 12 % (Figure 1.28).[135]

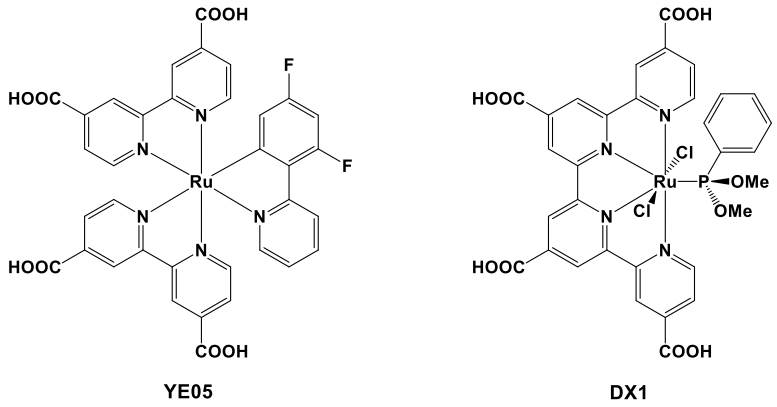

Figure 1.28 Structures of SCN-free and phosphine-coordinated ruthenium complexes used in DSSCs.

Despite their performances as dye in DSSCs, Ru-complexes present some disadvantages that need to be overcome: (i) their limited absorption in the NIR region; (ii) their rather low ε considering the thickness of TiO_2 layer; (iii) their rather poor thermal stability; (iv) their tedious and expensive multistep synthesis and purification and (v) their toxicity.

Alternative sensitizers based on platinum[136] and iridium[137] complexes have been developed but their performances in DSSCs were lower than Ru-complexes (around 3 % for Pt-complexes). Other inorganic compounds such as osmium-pyridine complexes, which have broader absorption profile, have also been investigated. However, osmium-based DSSCs suffer from very low PCE, mainly due to the slow electron transfer between the iodide electrolyte and the osmium dye cation. In addition, osmium derivatives are also considered as highly toxic.

As discussed above, ruthenium free hybrid-organic dyes have shown potential as efficient photosensitizers. Nevertheless, the search for alternative dyes is essential for the further large scale development of DSSCs.

ORGANIC DYES

In recent years, the development of DSSCs based on organic dye has been very rapid leading to PCEs close to that for polypyridyl ruthenium dyes.

Generally, an organic dye has a "Donor (D)-π conjugation bridge-acceptor (A)" structure (Figure 1.29).[138] Indeed, such organic dyes are usually based on electron-rich moities as donor parts (triarylamine, carbazole and indoline), π-conjugated groups as π-spacer parts (polyenes, thiophenes and benzothiazoles) and electronwithdrawing units as acceptor parts (cyanoacrylic acid, rhodamine and pyridine).[139] The π-conjugated expansion of the bridge can induce a shift of both HOMO and LUMO energy levels, resulting in tunable photophysical properties. Under illumination, the intramolecular charge transfer occurs from the donor to the acceptor moiety through the π-conjugated bridge, affording an efficient electron injection between the dye and the semiconductor. With the electron withdrawing/donating effects of acceptor/donor moieties, the absorption response of the visible light is red-shifted, which improves the light-harvesting and short-circuit photocurrent of solar cells.

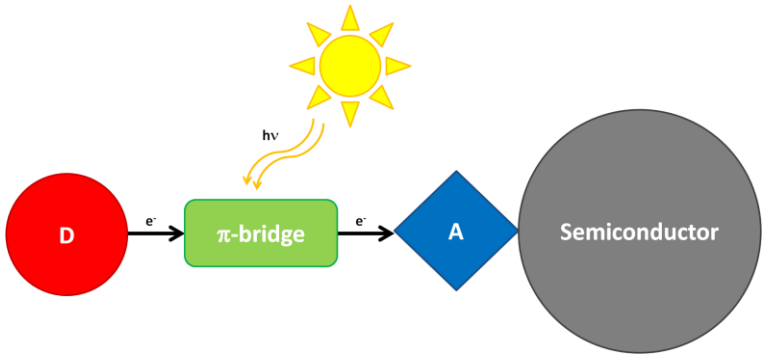

Figure 1.29 Schematic representation of a donor-π bridge-acceptor organic dye.

Significant progress in the use of organic dyes in DSSCs have been first made by Hara *et al.*, who have used oligoenes having dialkylaminophenyl groups as donor units and cyanoacrylic acid as acceptor units (**NKX-2569** and **NKX-2600**, Figure 1.30) Liquid DSSCs based on these dyes demonstrated PCEs up to 6.8 %.[140] During the last decades, oligoenes have been replaced by π-conjugated oligothiophenes in organic electronic materials because of their high polarizability and their tunable properties, *i.e.* optical and electrochemical ones.

The use of coumarins as donor groups and cyanoacrylic acids as acceptor groups, linked to oligothiophene afforded efficiencies up to 8.2 % (**NKX-2700**, Figure 1.30); a value comparable to Ru-dyes **N3**, **N749** and **N719**.[141] This value was nevertheless obtained by adding deoxycholic acid (**DCA**) to the dye solution during the impregnation. Co-adsorption of **DCA** significantly improved the PCE from 5.0 % to 8.2 % by dissociating the π-stacked aggregates. Despite the decrease of the dye coverage, the electron injection was further

enhanced and thus, the J_{SC} value (15.9 *vs.* 12.0 mA.cm^{-2}). Despite these optimizations, the V_{OC} of the coumarin dyes still remains lower than that of Ru dyes because of the recombination processes, which results from the strong π-π intermolecular interactions.

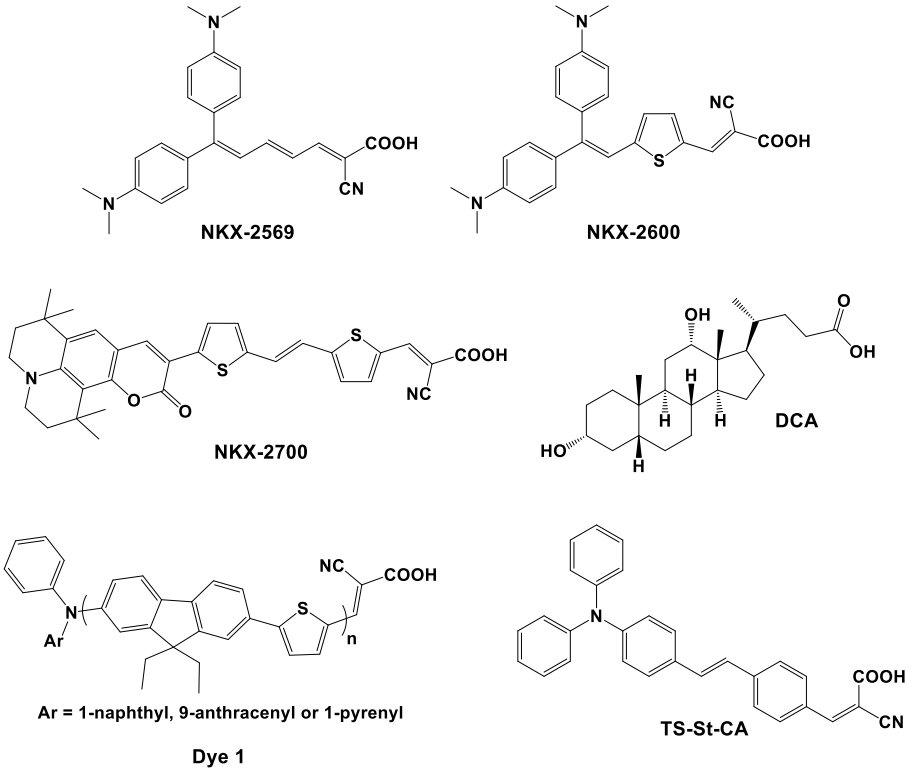

Figure 1.30 Structures of oligoenes, oligothiophene, thienylfluorene and triphenylamine organic dyes used in DSSCs.

In a similar way, fluorene units have also been used as π-conjugated bridge between diarylamine donor and cyanoacrylic acid acceptor (**Dye 1**, Figure 1.30).[142] By increasing the number of thienylfluorene units inside the structure, the PCEs significantly decreased from 5.2 (n = 1) to 3.8 % (n = 3). Indeed, although dye with longer bridges displayed higher ε, the charge separation was more efficient with the shortest oligomers due to the higher oxidation potential, more favourable for the reduction of the oxidized dye.

Triphenylamine-based dyes, with a rather simple structure, lead to excellent efficiencies in DSSCs. Even though their spectral response were in a narrow region between 400 and 500 nm, DSSCs based on dye **TA-St-CA** reached PCE of 9.1 % with a high short-circuit current of 18.1 mA.cm^{-2} (Figure 1.30).[143] Besides, when the phenylenvinylene moiety was replaced by thienylenevinylene or bithiophene groups, the J_{SC} decreased as well as the efficiencies, due to the higher rigidity of the molecular structure.[144] Furthermore, the influence of alkoxy groups was demonstrated with these dyes: their presence enabled to red-shift the absorption profile by 30 nm inducing better PCE.

Indoline-based dyes have been widely used in DSSCs thanks to their easy availability, their high ε and their promising photovoltaic performances (Figure 1.31). Horiuchi *et al*. first synthesized an indoline organic dye **D102** which was the precursor of a broader array of indoline sensitizers.[145] After structural optimizations, Uchida *et al.* obtained a PCE of 6.5 %

with the dye **D149.** This value was further increased to 8.0 % by adding chenodeoxycholic acid (**CDCA**) as coadsorbent, as discussed before.[146] After optimizing the TiO_2 films with an antireflection (ARF) layer, which enhanced the transmittance of the **FTO** substrate and prevented UV-light from passing through, efficiency was increased until 9 %.[147] Then, Ito *et al.* added a longer alkyl chain on the rhodanine unit to decrease aggregation phenomena (**D205**, Figure 1.31).[148] The V_{OC} was improved (710 mV *vs*. 644 mV for **D149**) and a PCE of 9.5 % was obtained, which is one of the best PCEs reported for indoline family.

This effect of alkyl chains was also described for quaterthiophene dyes (**MK-2** and **MK-5**, Figure 1.31) for which the PCE increased from 3.7 to 8.3 %.[149] This increase was due to the longer electron lifetime thanks to higher hydrophobicity that improved the packing of the dye onto the TiO_2 surface and avoided the contact of the electrolyte with the semiconductor.

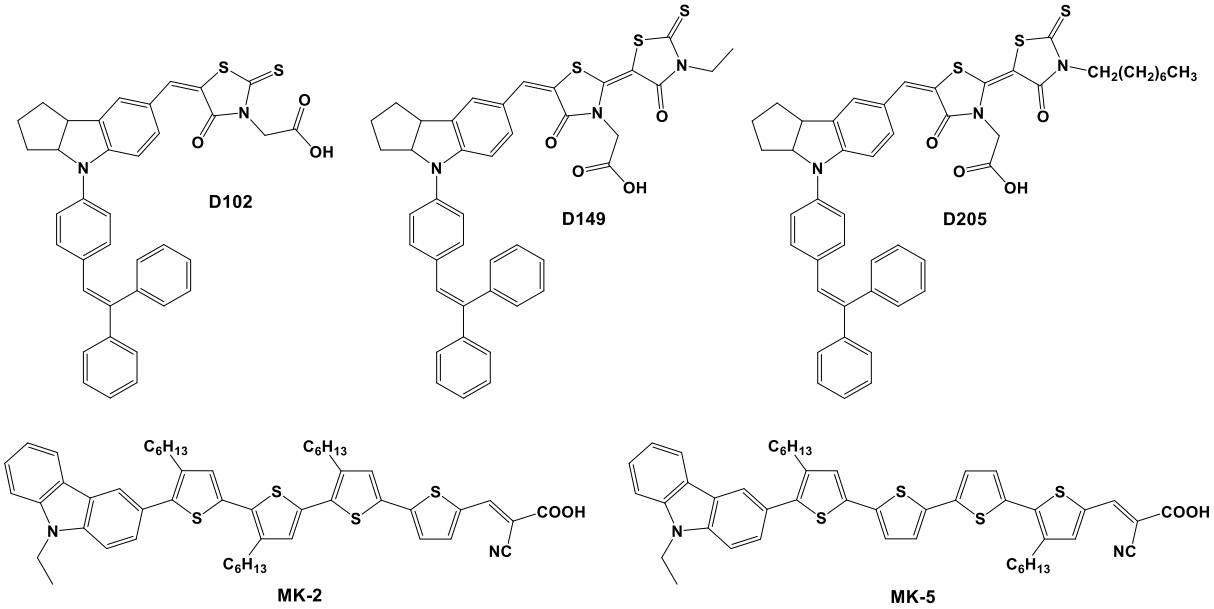

Figure 1.31 Indoline and quaterthiophene dyes used in DSSCs.

To date, the best PCEs of DSSCs reported using D-π-A type organic dyes are around 10 %. W. Zeng *et al.* have reported a push-pull dye **C219** with a binary π-conjugated spacer of ethylenedioxythiophene and dithienosilole. With this amphiphilic dye and a volatile electrolyte (1,3-dimethylimidazolium iodide/1-ethyl-3-methylimidazolium iodide/1-ethyl-3-methylimidazolium tetracyanoborate/I_2/tert-butylpyridine (tBP) /guanidinium thiocyanate), PCEs around 10 % were measured at the AM 1.5G conditions.[150] More importantly, a solvent-free ionic liquid solar cell incorporating this dye afforded a high PCE of 8.9 % under a low light intensity of 14.39 mW cm^{-2}, making it very promising for the practical indoor application of flexible DSSC. Comparable efficiencies were also obtained with dye **JF419**, structured around a 4*H*-cyclopenta[2,1-*b*:3,4-*b*']dithiophene bridge and a cyanoacrylic acid acceptor.[151] To add strong electronic push and favorable back-recombination features as already demonstrated by dyes **C218**[152] and **Y123**[153], a fluorene moiety was added into the donor part. DSSCs based on **JF419** allowed achieving PCEs up to 10.3 % under full sunlight

and 11.1 % at 50 % sunlight, in presence of a standard cobalt electrolyte ($[Co(bpy)_3](TFSI)_2$, $[Co(bpy)_3](TFSI)_3$, LiTFSI).[2733]

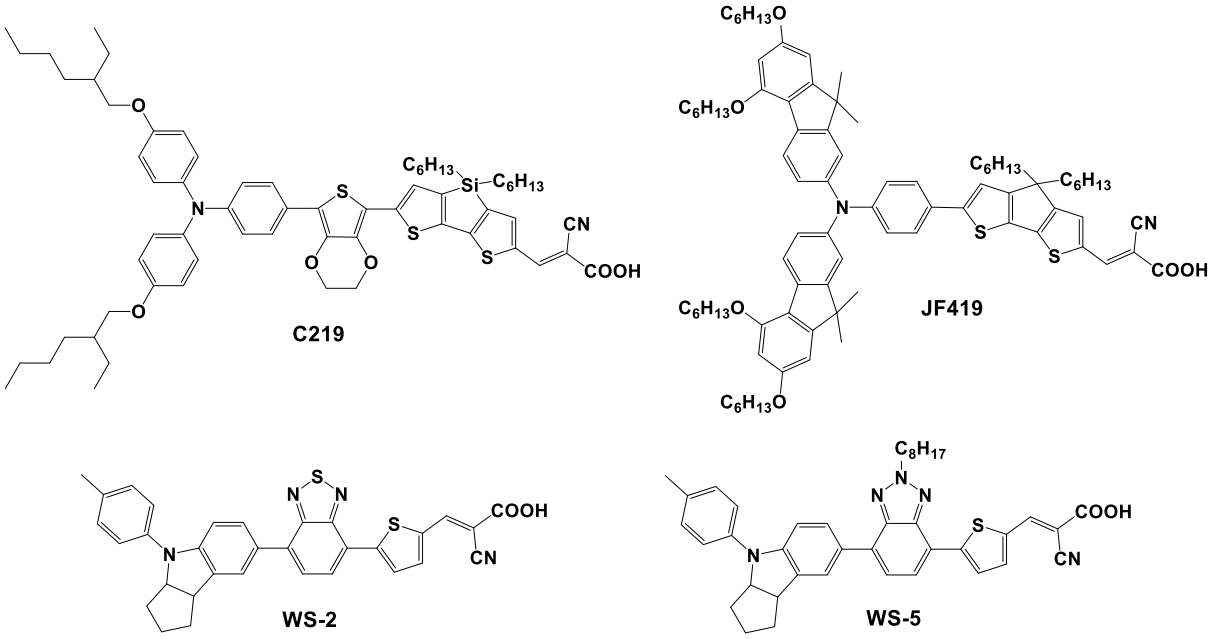

Figure 1.32 Organic dyes used in DSSCs.

Recently, another series of indoline-based dye, called **WS**, has also emerged and was found to be very popular. These dyes are based on a D-A-π-A "push-pull" structure which is considerably more stable than D-π-A structure and helps avoid one of the main problem of the indoline derivatives: their long-term desorption.[154] PCEs of 8.7 and 8 % were obtained for **WS-2** and **WS-5** dyes, respectively (Figure 1.32). Due to the additional alkyl chain, dye **WS-5** was found to be more stable, in particular towards possible water traces in the electrolyte. Decreased recombinations and thus, improved V_{OC} (780 *vs.* 615 mV for **WS-2**) were also obtained.

However, the relative narrow absorption, the adverse dye aggregation and instability represent major blocking points for further improvements in organic-based DSSCs.

PORPHYRIN DYES

Porphyrins as well as chlorins and bacterio(chlorin)s derivatives are well-known chromophores playing a key role in photosynthesis. The difference between these compounds depends on the reduction level of the macrocyclic tetrapyrrole (Figure 1.33).[155]

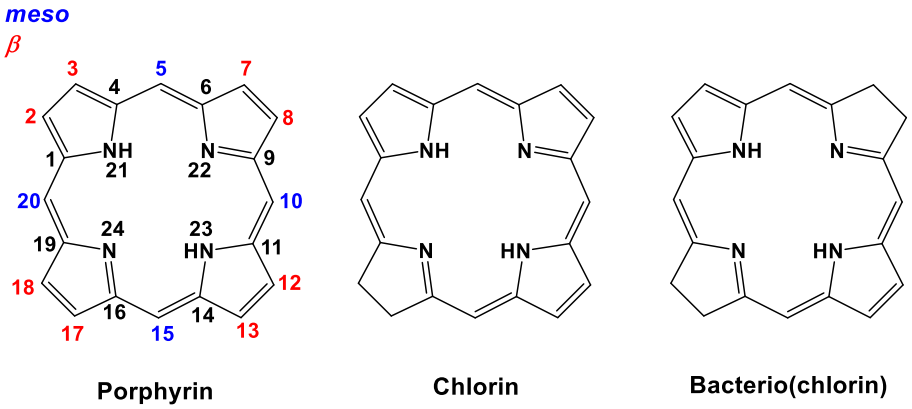

Figure 1.33 Basic structures of porphyrin, chlorin and bacterio(chlorin) compounds. The IUPAC numbering system of the carbon skeleton for porphyrin is also reported.

Porphyrins possess a rigid molecular structure and high ε (> 10^5 $M^{-1}.cm^{-1}$). Moreover, their optical, physical and electrochemical properties can be easily tuned by functionalization at the *meso* and β positions (Figure 1.33). As such, they represent promising candidates for solar energy conversion. During recent years, the efficiency of porphyrin sensitizers has increased exponentially in comparison with the stagnant performances of organic and ruthenium dyes.[156]

After the first experimental study carried out in 1993 on a copper chlorophyll derivative (PCE = 2.6 %),[157] β-linked zinc porphyrins have been developed reaching PCES up to 7.1 % (**GD2** in 2007) (Figure 1.34).[158] **GD2** incorporates a malonic acid as an anchoring group to enhance the electronic coupling of the dye with the semiconductor. This concept was further applied by Kim *et al.* who demonstrated that zinc porphyrin **tda-2b-bd-Zn** (Figure 1.34) with two π-conjugated acid linkers enhanced effectively the electron injection efficiency and retarded charge recombination, thus leading to a PCE of 7.5 %, a value comparable with that obtained for dye **N3** under the same conditions (PCE = 7.7 %).[159]

The concept for synthesizing *meso*-ethynyl linked porphyrins was first given by Therien *et al.*[160] Although the first *meso*-ethynyl substituted porphyrin-based solar cell gave an encouraging PCE of 3.5 %, no significant progress have been done until the strategy of Galoppini *et al.*[161] This porphyrin was built upon a phenylethynyl unit as π-conjugated bridge to control the distance between the dye and the metal oxide to retard charge recombination. Unfortunately, this approach failed due to serious dye aggregation. To overcome this problem, 3,5-di-*tert*-butylphenyl groups have been introduced on other *meso* phenyl groups allowing to reach PCEs up to 10.9 % for **YD2** (Figure 1.34), comparable to the best PCEs obtained with ruthenium complexes (**N719**, **N749** and **CYC-B11**).[162]

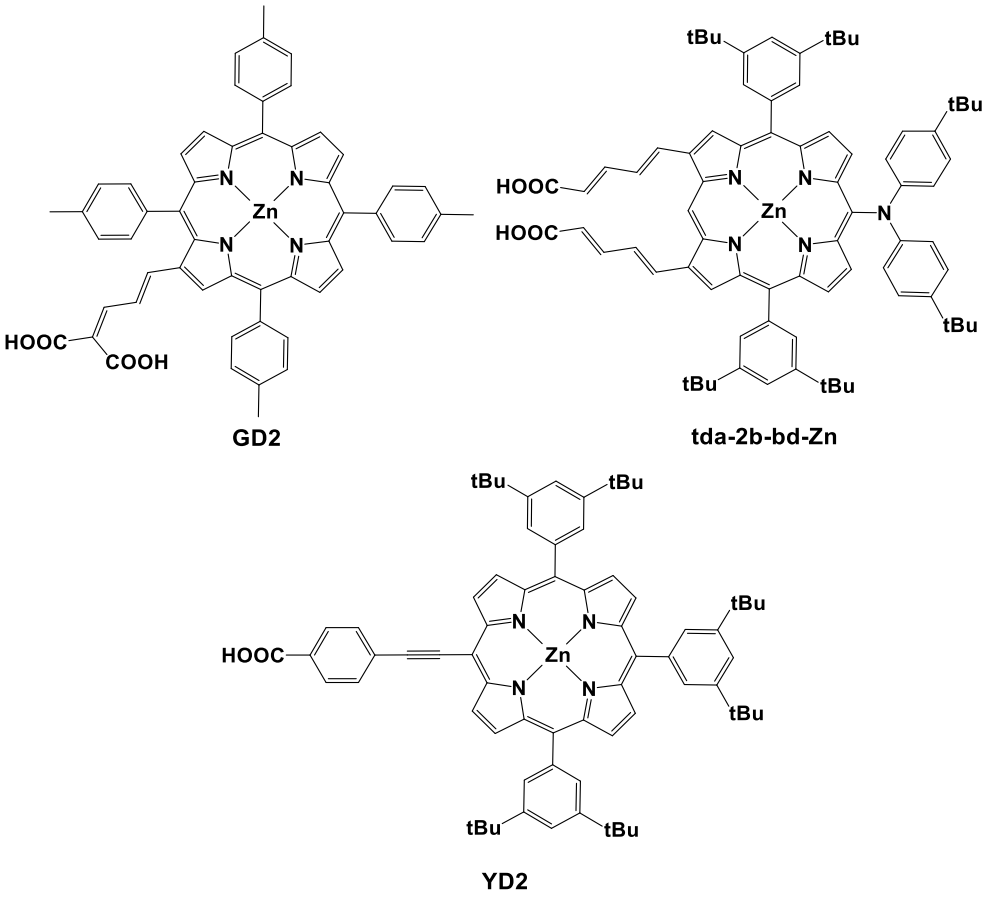

Figure 1.34 Porphyrin dyes used in DSSCs.

As mentioned above, the most viable way to enhance the performances is to extend the absorption profile of the dye. Generally, porphyrins show a Soret band at around 400 nm and Q bands between 500 and 650 nm. To extend their absorption to the NIR region, the band gap between the HOMO and LUMO orbitals has to decrease. To this aim, two strategies were involved: (i) the introduction of a highly π-conjugated chromophore coupled with the porphyrin macrocyle and (ii) the fusion/dimerision of porphyrins.

In this context, following the first strategy, various acene units have been coupled to porphyrin ring. Lin and Diau have indeed introduced acenes from benzene to pentacene through the ethynyl linkage.[156] The anthracene-functionnalized porphyrin **LAC-3** demonstrated the best performance (Figure 1.35). Based on the **YD2** structure, acenyl-ethynyl links have also been introduced affording efficiencies up to 6.8 % (**YD12**). Fluorene- and pyrene-functionnalized porphyrins (**LD22** and **LD4**) were also found to reach impressive PCEs of 8.1 and 10.1 %, respectively thanks to an enhanced light-harvesting with a IPCE spectrum covering the entire visible region (Figure 1.35).

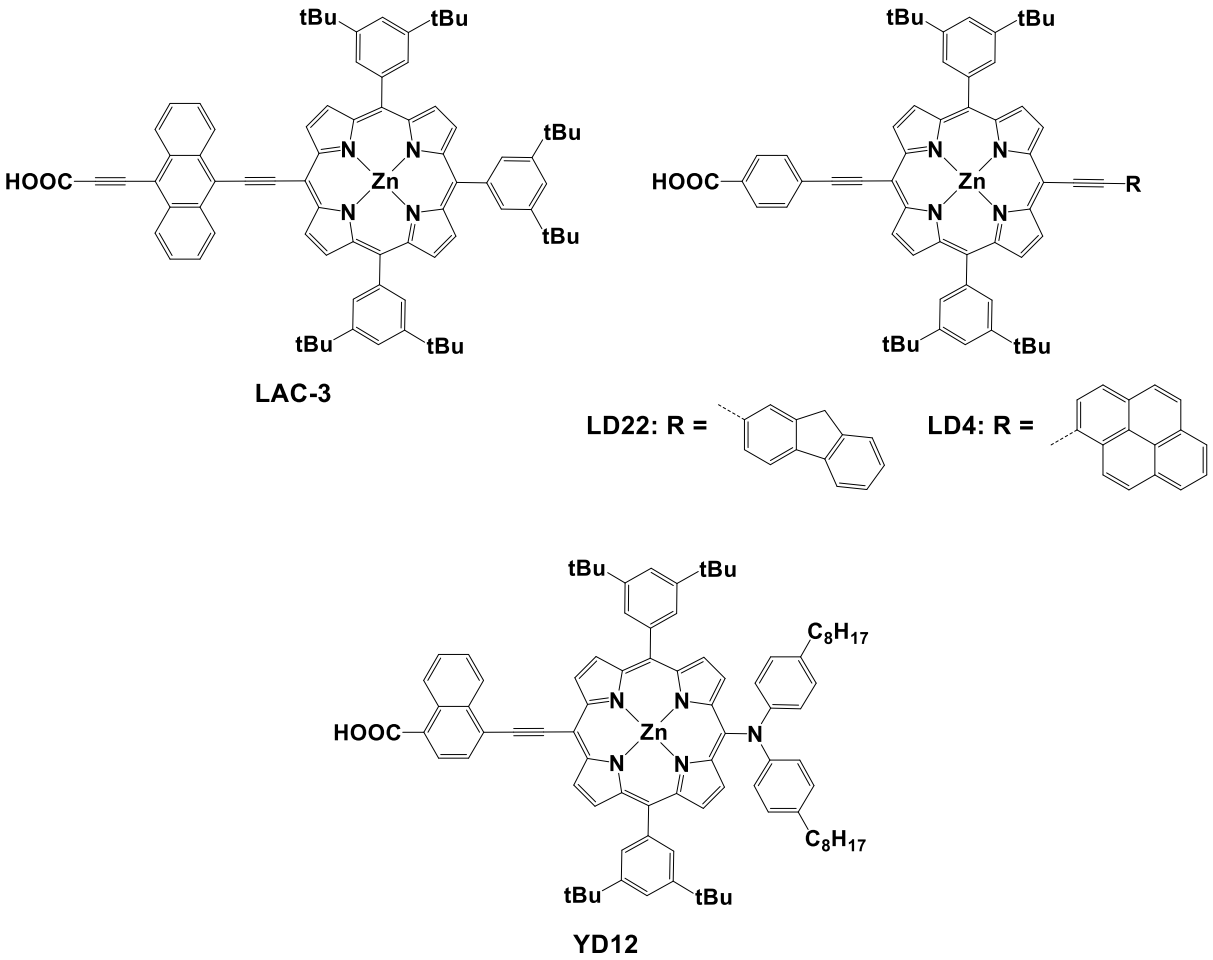

Figure 1.35 Porphyrin dyes used in DSSCs.

In the second strategy, chromophores have been fused with porphyrin macrocycles. The first example reported consisted in a naphthalene-based *meso*-β-edge fused zinc-porphyrin (**fused-Zn-1**) that leads to PCE of 4.1 % (Figure 1.36). Other examples concerned fused porphyrins with perylene, anthracene or porphyrin.[156] However, in all these cases, devices exhibited very low performances due to important dye aggregation and mismatched energy levels between the dye and the semiconductor, despite an absorption profile beyond 1 200 nm.[156]

Despite the great performances of porphyrins as dye in DSSCs, V_{OC} still remains lower than that of commonly used **N719** Ru-dye, due to lower electron lifetime and attachment of I_3^- ions of the electrolyte to the zinc metal center of the porphyrin, reducing the transfer to the semiconductor. To tackle this problem, long alkoxy chains have been introduced to protect the porphyrin from retarded charge recombination and decrease the dye aggregation for efficient electron injection. In a similar fashion, in 2011, the porphyrin dye **YD2-o-C8** co-sensitized with organic dye **Y123** and a cobalt-based electrolyte lead to a PCE of 12.3 % due to the complementary absorption of **Y123** in the green part of the electromagnetic spectrum (Figure 1.36).[163]

More recently, Mathew *et al.* reported the synthesis of a porphyrin dye with a donor–π-bridge–acceptor (**SM315**), which both maximize the compatibility with the

electrolyte and improve the light-harvesting. The DSSC reached a PCE of 13 % which is currently the record PCE for DSSCs (Figure 1.36).[5a]

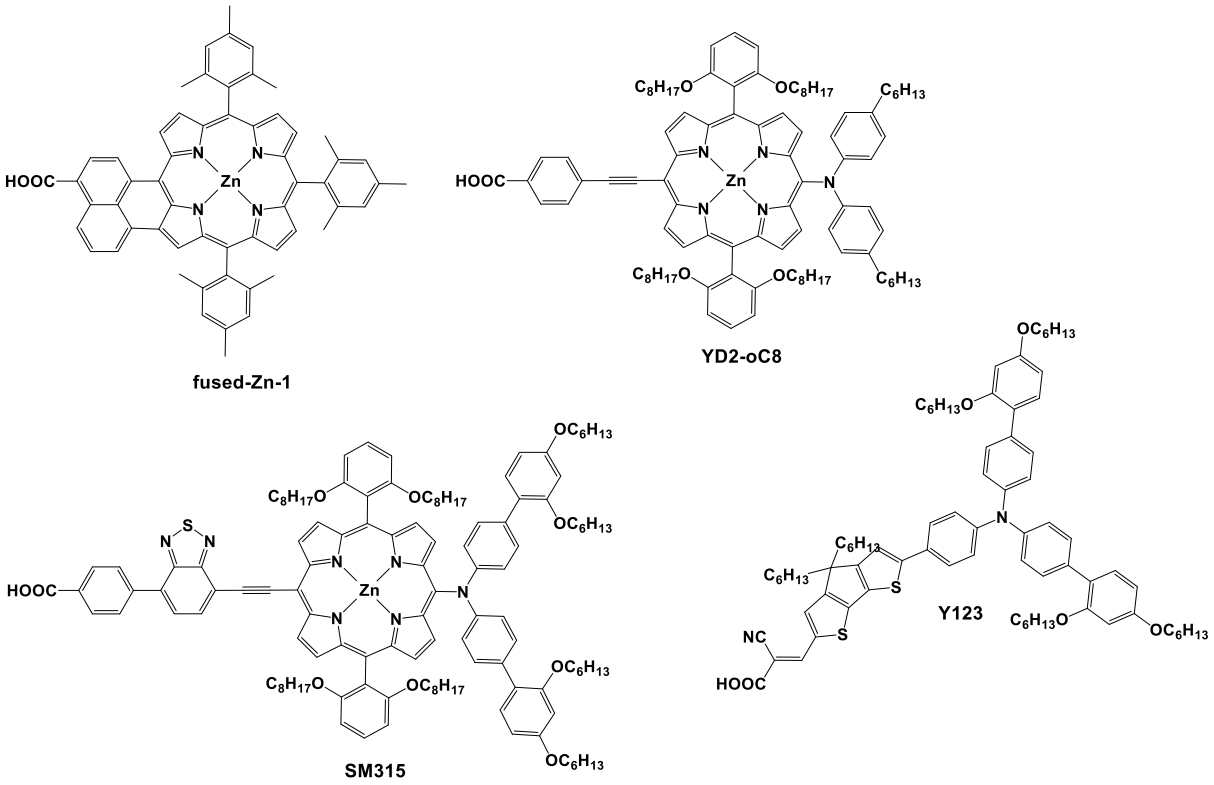

Figure 1.36 Porphyrin dyes used in DSSCs.

In contrast with organic dyes described above, natural pigments have emerged as a viable alternative due to their low cost, their easy attainability, the abundance of raw materials and their low environmental impact.[164] Various components of plants have been thus tested as suitable dyes for DSSCs. In particular, vegetable dyes such as the chlorophyll can be easily extracted from fruit, leaves, flowers and algae (Figure 1.37). In Chapter 4 of this dissertation, the use of dyes based on chlorophyll *a* in DSSCs will be described.

CHLOROPHYLLS

Chlorophyll is a green dye present in leaves and green plants which is responsible for the absorption of energy from light during the photosynthesis process.[165] Structurally, chlorophyll refers to a class of cyclic tetrapyrrole similarly to porphyrin as discussed above. Caventou and Pelletier identified chlorophyll as a chlorin ring having a magnesium ion at the center in 1817.[166] Unlike porphyrins, chlorophylls have a reduced pyrrole ring and a phytol group, a highly hydrophobic 20-carbon atom-based alcohol esterified to an acid side chain (Figure 1.33). (Bacterio)chlorophylls are similar to chlorophylls, except for the reduction of an additional pyrrole ring that induces a shift of their absorption maxima to the NIR region (1000 nm).

Since then, many chlorophyll structures have been identified. **Chl-a** ($C_{55}H_{72}O_5N_4Mg$, cyan), **Chl-b** ($C_{55}H_{70}O_6N_4Mg$, chartreuse) and **Chl-c** ($C_{35}H_{28}O_5N_4Mg$, blue-green) are known as the most common chlorophylls, especially **Chl-a** and **Chl-b** which are the most represented in

plants (Figure 1.38). Chemically, chlorophylls are instable in both acid and basic ambient and have a strong tendency to self-aggregate. Compared to porphyrins which require complicated and expensive synthesis, chlorophylls are cheap and environmentally friendly. Coloured and nontoxic chlorophylls are used as dyes in the cosmetic, textile, and food industries, as well as luminescent materials.[167]

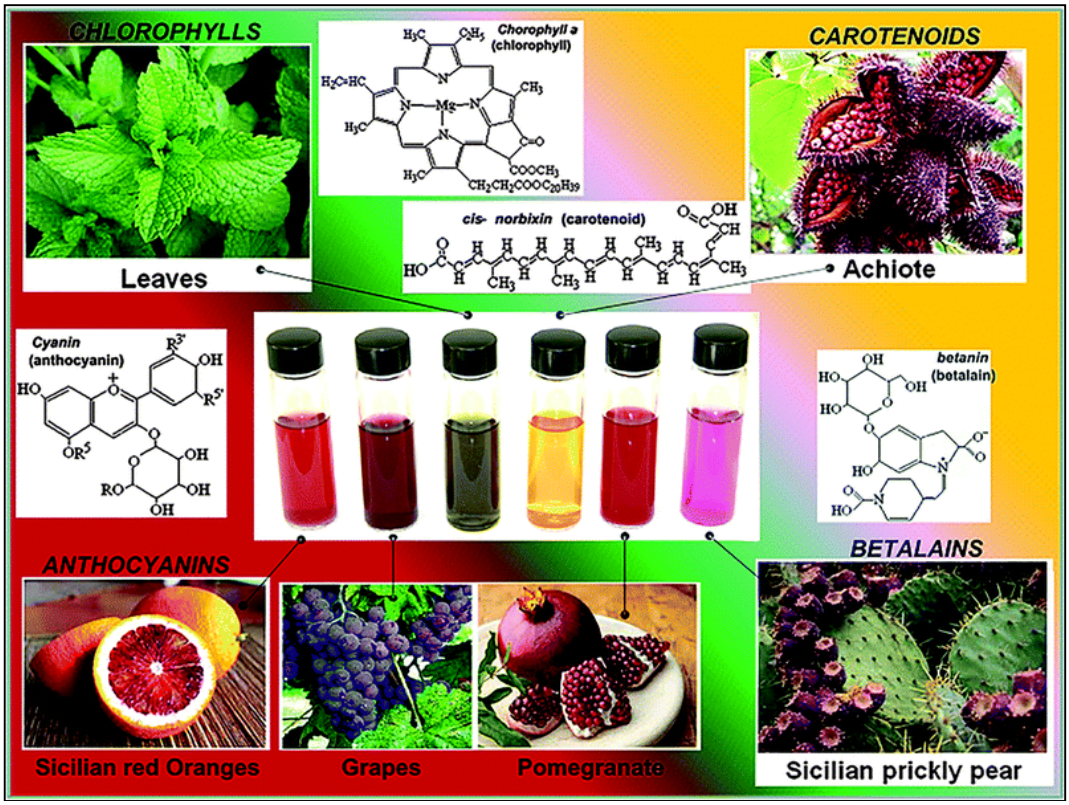

Figure 1.37 Dyes extracted from chlorophylls, anthocyanins, betalains and carotenoids exhibiting colors covering the entire visible part of the solar spectrum.[164]

Beyond their natural abundance, low toxicity and their capacity to absorb solar energy in different regions, the properties of chlorophylls can also be tuned by changing their chemical structure. For example, their excited state lifetimes are modulated by changing the inner metals (Zn, Mg, Ni, etc.). Consequently, it also allows adjusting the LUMO energy level of the sensitizers to match the energy level of the conduction band of the semiconductors. The absorption spectra of chlorophylls are composed of two main bands: (i) the Soret band located in the blue region (around 400 nm) and (ii) the Q bands in the red region (550-800 nm), consisting of Q_x and Q_y transitions, respectively. The positions and intensities of Q-bands can be adjusted by chemical modification of the macrocycle. Furthermore, chlorophylls display ε up to 10^5 M^{-1} cm^{-1}, which is among the highest observed for organic compounds. **Chl-a** and **Chl-b** have a highly stable polycyclic network of alternating single and double bonds (polyenes) conjugated structure which allows orbital delocalization, making chlorophylls ideal photosensitizers.

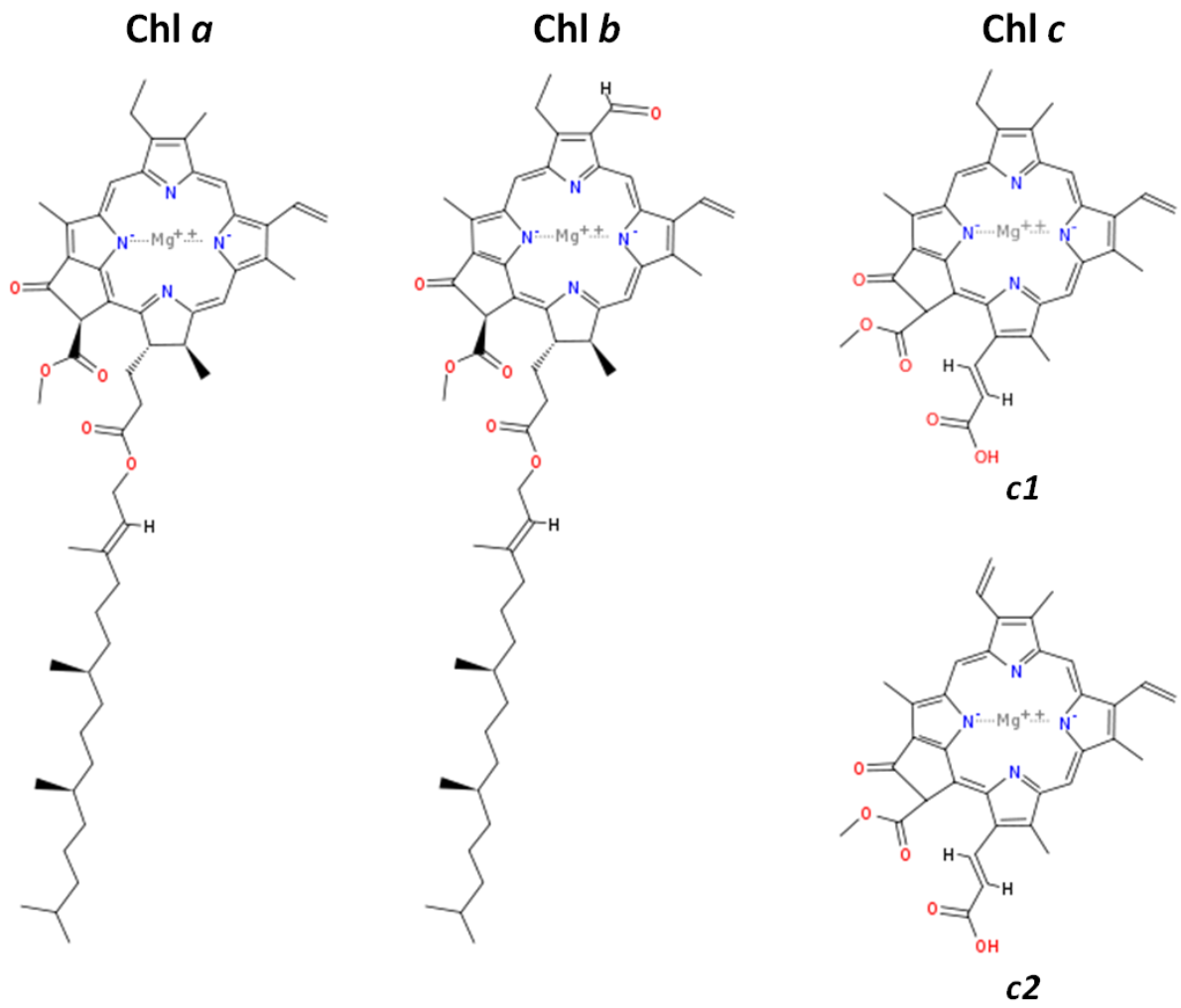

Figure 1.38 Structures of chlorophyll derivatives.

The first investigations on the TiO_2-sensitization using chlorophyll derivatives was carried out by Kamat and co-workers.[168] In 1993, Kay and Grätzel published an exhaustive study on TiO_2 electrodes sensitized with chlorophylls and related derivatives, achieving EQE up to 30 %.[157] These low EQE values were attributed to the chlorophylls structure, where the presence of alkyl groups rather than carboxyl or hydroxyl groups makes chlorophylls unable to efficiently bind the metal oxide surface.[169] Kay and Grätzel have also demonstrated that the **Chl-a** adsorption on TiO_2 is improved when the phytyl chain is replaced by a carboxylic one. The increase in performance with respect to other **Chl** and pheophorbide derivatives has been attributed to the suppression of the backward charge recombination between the TiO_2 and the electrolyte. In addition, long alkene chains were found to induce strong steric hindrances, thus preventing an orderly arrangement of the chlorophyll-dye molecules onto TiO_2 surface.[170] Because of these effects, it seems that only chlorophyll sensitizers bearing π-conjugated carboxylic groups could exhibit efficient electron injection into the TiO_2 electrode. In a similar way, Wang and Tamiaki have reported that the carboxyl group location on the chlorophyll affects their absorption profile and molecular orbitals. Based on these considerations, they investigated two **Chl-c** (c_1 and c_2) with their oxidized forms (c_1'

and c_2') and obtained PCEs of 3.4, 4.6, 2.5 and 2.6 %, respectively.[171] The higher PCEs obtained with **Chl-c_2** dye was attributed to several factors: (i) the π-extended conjugated system results in high electron densities, (ii) the favourable configurations of the peripheral vinyl carboxyl group with respect to other **Chl-c** and (iii) the absence of dye aggregation. All these results allowed determining a relationship between molecular structure, local electron density and photosensitizer properties of the different **Chl-c** types. Investigations based on the co-sensitization of **Chl** derivatives was also attempted with the aim of combining multiple dyes to mimic natural photosynthetic light-harvesting systems. Indeed, by following this approach, enhanced PCE (8.1 %) was achieved by co-sensitization of **Chl-a** and **Chl-c** derivatives due to enhanced light-harvesting and improved electron injection efficiency.[172]

As natural Chls can provide a sustainable solution to future solar energy conversion technologies, chlorophyll derivatives will be synthesized and used as dye for solid-state dye sensitized solar cells (ss-DSSCs) applications. Their synthesis and their introduction in devices will be discussed in Chapter 4.

3.2.3. ELECTROLYTE

As the dye, the electrolyte is a key-element of the solar cell. As already discussed, the electrolyte ensures the dye regeneration after the charge injection into the TiO_2 conduction band, and, modifying the redox couple affects directly the dye regeneration, the diffusion kinetics within the electrolyte, recombination phenomena and the charge transfer kinetics.[14,173]

Among DSSCs, liquid cells displayed the highest PCEs (after perovskite cells), thanks to a good infiltration of mesoporous layers. Porous layer can be thus reached about fifteen microns, inducing a high dye quantity. A liquid electrolyte should be chemically stable, slightly viscous to facilitate the charge transport and possess a high boiling temperature (over 80°C). The solvent has to be suitable for the redox couple and various additives but in the same time, not cause the dissolution of the adsorbed dye or even the electrode materials. Currently, the redox couple triodine/iodine (I_3^-/I^-) is the most widely used in liquid DSSCs. Its high efficiency is due to slow recombination kinetics between the electron and the I_3^- anion (around 10 ms).[14,173] This redox couple afford also fast dye regeneration (1 µs). Cell performances have been enhanced by adding additives in the liquid electrolyte like the 4-*tert*-butylpyridine (t-BP). t-BP allows, for example, increasing V_{OC} by reducing the charge recombination, induced by the incomplete coverage of the TiO_2 layer by the dye and by shifting the TiO_2 conduction band to higher energies. This additive can also form a protective layer on the TiO_2 surface, which limits the back electron transfers induced by a direct contact between the electrolyte and the semiconductor.

Despite the good performances obtained with I_3^-/I^- electrolyte, this later displays several disadvantages:[14,173]

- this system is highly corrosive and dissolves many of the commonly used sealants and metal interconnects;
- the dye regeneration by the couple results in a large loss (600 mV) in potential.

Indeed, since the V_{OC} is linked to the gap between the Fermi level of the oxide and the redox potential of the redox couple, the redox potential has to be close to the HOMO level of the dye which is not the case for Ru complexes-based DSSCs. Therefore, other alternatives such as Br^-/Br_3,[174] $SCN^-/(SCN)_2$, [175] Fc/Fc^+,[176] Cu/Cu^+[177] were also used to improve the V_{OC}. Recently, a DSSC using a cobalt(II/III) tris(bipyridyl)-based redox electrolyte lead to a PCE of 12.3 % with a V_{OC} of 935 mV.[163] This improvement was possible thank to a porphyrin-based dye bearing long alkoxy chains, which slows down recombination kinetics by reducing electrolyte-metal oxide contact. Although liquid DSSCs display PCEs over 11 %, using a liquid electrolyte is unavailable for industrial applications. The solvents used are volatile and leaks within the device are possible, especially for the I_3^-/I^- couple, very corrosive. Consequently, many quasi-solid and solid alternatives have been developed.

The quasi-solid electrolyte is generally constituted by an organic polymeric matrix incorporating a liquid electrolyte to form a stable gel network structure via physical/chemical interactions. Ionic liquids (*i.e* 1-propargyl-3-methylimidazolium iodide, bis(imidazolium) iodides and 1-ethyl-1-methylpyrrolidinium) and polymer gels (*i.e* poly(ethylene oxide), poly(vinylidinefluoride) and polyvinyl acetate) containing redox couples are commonly used as quasi-solid-state electrolytes to overcome the volatilization and leakage problems of liquid electrolytes.[173] To date, PCEs around 8-9 % have been reached using quasi-solid electrolyte.[178] However, because of their thermodynamic instability under high temperature, quasi-solid-state electrolytes still suffer from solvent leakage, and thus, also require careful sealing treatment when used in high temperature environments.[173] Consequently, solid-state electrolytes will be the major focus for DSSC electrolyte research and industrialization in the future.

The solid electrolytes consist in hole conducting materials (HTM), which can be distinguished in two types: inorganic and organic ones. The structure and the operation principle of the device are thus modified (Figure 1.39): the hole transfer occurs directly from the dye to the hole-transporting materials (HTM), *via* hopping between electronic states of the organic molecules to the metal counter electrode.[14,173]

Several inorganic *p*-type materials such as CuI, CuSCN and $CsSnI_3$ have been successfully used in ss-DSSCs.[14,173] Although CuI/CuSCN HTMs possess high mobility, PCEs remained low (≈3 %), due to its fast crytallisation which results in poor infiltration into photoanode.[179] By contrast, $CsSnI_3$ leads to PCEs up to 10.2 % due to its high hole mobility, low-cost and cheap processing.[180]

Compared to inorganic hole-transport materials, organic HTMs are attractive due to their abundant sources, low cost and easy preparation. Most of the organic HTMs, either polymers or molecules, are soluble in organic solvent thus allowing the use of simple methods (spin coating, electrochemical or photochemical polymerizations) to produce ss-DSSCs with good pore-filling TiO_2 mesoporous films.[14,173] Moreover, as the dyes, their

properties can be tailored by chemical modifications. Organic HTMs can be classified into two categories: molecular and polymeric HTMs.

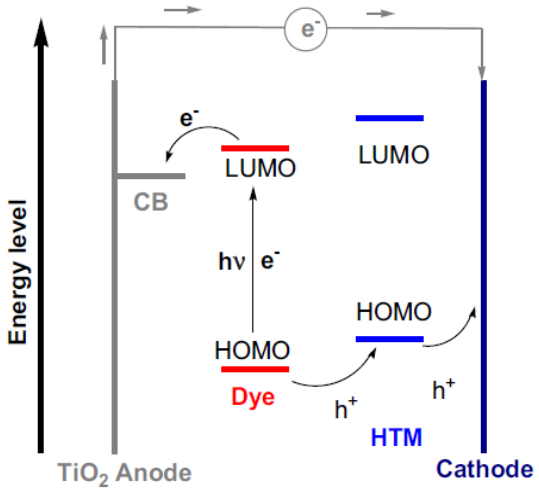

Figure 1.39 Operation principle of solid state DSSC device.

Among the organic HTMs, the 2,2',7,7'-tetrakis(*N*,*N*-di-*p*-methoxyphenylamine)-9,9'-spirobifluorene (**spiro-OMeTAD**) is the most commonly used in ss-DSSCs.[14,173] Grätzel *et al.* firstly used it in 1998 in **N719**-based ss-DSSC. Despite the doping with tris(4-bromophenyl)ammoniumyl hexachloroantimonate (**$N(PhBr)_3SbCl_6$**) and **LiTFSI**, PCE of only 0.74 % was obtained, due to the charge recombination at the TiO_2/**spiro-MeOTAD** interface. This PCE was then improved to 2.56 % in 2001 by Kruger *et al.*, who used **t-BP** and **LiTFSI** as additives. Since then, this HTM was widely used in combination with many organic dyes leading to the highest PCEs. Recently, **spiro-OMeTAD** was also used as HTM in combination with perovskite. The resulting solid-state solar cell allowed reaching a record PCE (≈ 20 %),[181] maybe opening the door to an important development axis in the future.

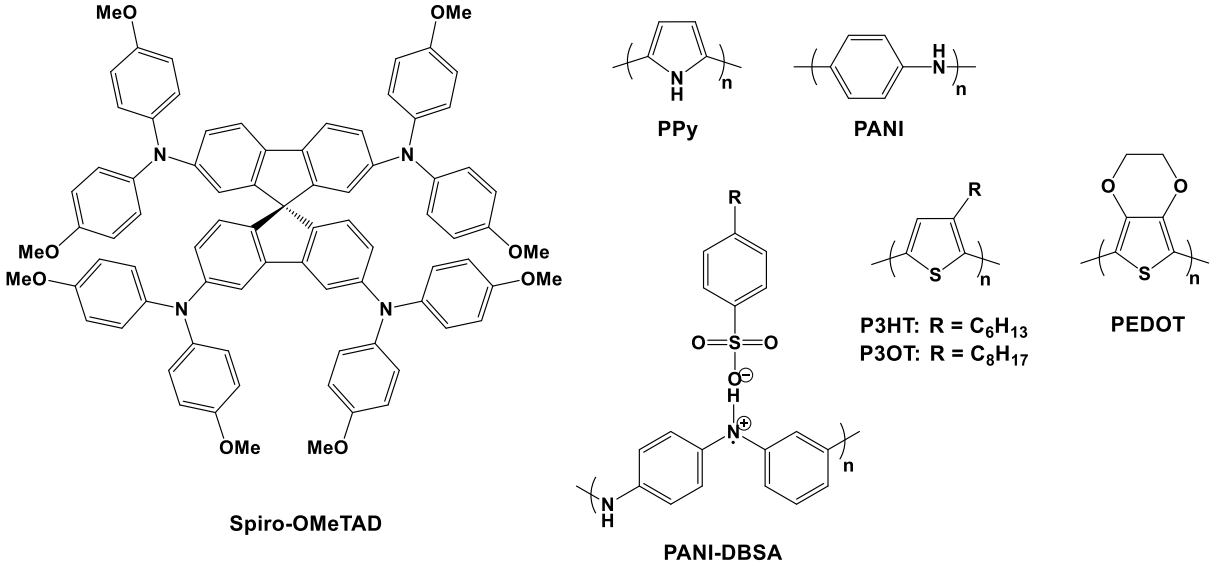

Figure 1.40 Structures of solid state hole transporter materials.

Although the use of **spiro-OMeTAD** as HTM in ss-DSSCs afforded PCEs up to 7.2 % through doping with **FK102** cobalt(III) complex and using an high absorbing D–π–A sensitizer (**Y123**),[182] it displays some drawbacks such as a low hole mobility of only 10^{-4} $cm^2/V^{-1}.s^{-1}$ and a relatively complex multistep synthesis.[183] For these reasons, due to their better electrical conductivity, organic conjugated polymers have also been the subject of great interest (Figure 1.40).

In 1997, Yanagida *et al.* first used polypyrrole (**PPy**) as organic HTM in ss-DSSCs.[184] **PPy** was deposited by *in situ* photoelectrochemical polymerization on **N3**-based TiO_2 surface, in order to improve the connectivity between both constituants. The ss-DSSC achieved a PCE of 0.1 % (P_{in} = 22 $mW{\cdot}cm^{-2}$) due to the poor light absorption of PPy. Polyaniline (**PANI**) was then used as HTM in ss-DSSCs.[14,173] The first devices showed very low PCEs up to 0.10 %. Nevertheless, PCE was further improved by using **LiI** and **t-BP** as additives and, acid-doped polyaniline (**PANI-DBSA**) (1.15 %).[185] The enhancement was attributed to the inhibition of charge recombination and a better wetting of TiO_2 film.

Poly(3-hexylthiophene) (**P3HT**) and derivatives were also studied as HTM in ss-DSSCs but relatively poor PCEs (η < 1%) were achieved due to the inefficient pore filling of polymers into mesoporous TiO_2 films which result in low charge separation and collection.[186] By optimizing several parameters such as TiO_2 film thickness, PCE of 1.3 % was obtained for **N719**-based ss-DSSC with **P3OT** as HTM.[187] These devices showed good stability after storage for three months under light and air. By adding lithium bis(trifluoromethanesulfonyl)imide (**LiTFSI**) and **t-BP** as additives, the **D102**-based ss-DSSC reached efficiency of 2.63 % with **P3HT** as HTM.[188] Further improvement in PCE (3.2 %) was achieved by infiltrating the **P3HT** into vertically aligned squraine-based TiO_2 nanotubes (**SQ-1**).[189] The exploration of perovskite as light absorbers provided also a new platform for research in HTMs. Recently, Giacomo *et al.* fabricated a perovskite-based solar cells with **P3HT** as HTM reaching a PCE of 9.3 %, which is the highest reported efficiency for **P3HT**-based solar cells.[190] Even the **P3HT**:**PBCM** blend widely used in BHJ solar cells was introduced in ss-DSSCs, PCE up to 4.11 % were obtained with the TiO_2/**N719**/**PBCM**/**P3HT**/**PEDOT**:**PSS**/carbon configuration.[191] It was demonstrated that **P3HT** heterojunctions could replace the electrolyte but also, the dye. These new iodide/triiodide-free conductors exhibit some advantages, such as simple device construction and low device cost.

Conjugated polymers used as HTMs generally absorb visible light which can compromise the light-harvesting efficiency of dye. In contrast, poly(3,4-ethylenedioxythiophene) (**PEDOT**) possesses high transparency in the visible region, high hole conductivity and remarkable stability at room temperature. Since its first used in 2004 by Yanagida *et al.* (PCE = 0.53 %), **PEDOT** achieved a conversion efficiency of 2.85 % by introducing some additives as **LiTFSI**. In 2010, Liu *et al.* assembled a **D149**-based ss-DSSC by *in situ* polymerization of 2,2'-bis(3,4-ethylenedioxythiophene) (**bis-EDOT**) in an electrolytic thin layer. The device reached a high PCE of 6.1 %.[14,173] Other π-type conjugated polymers, such as triarylamine-based polymers, polythiophene (**PT**), and poly[2-methoxy-5-(2-ethylhexyloxy)-1,4-phenylenevinylene] (**MEH-**

PPV) were also studied as organic HTMs in ss-DSSCs.[14,173] However, due to their limited pore infiltration, the PCEs of these HTM-based DSSCs does not often exceed 1 %.

In this context, conjugated polymers have been synthesized and used as solid-state hole conductors. In such materials, as well as for spiro-based small molecules, the carrier mobility, the recombination rate and the pore-filling are key factors for obtaining efficient ss-DSSCs and will be thus discussed in Chapter 4.

3.2.4. THE COUNTER ELECTRODE

The counter electrode has to regenerate the electrolyte.[14,192] To this aim, different counter electrodes have been developped and studied depending on the solar cell.

For liquid DSSCs, a **FTO** based conductive glass where platinum microcrystals are deposited, is generally used as counter electrode in DSSCs. Platinum is largely used because of its excellent chemical and thermal stabilities and its good conductivity. Platinium also exhibits a good electrocatalytic activity, which favors the reduction of the oxidized electrolyte. Generally, platinum can be in massive form, nanostructured, or nanocomposited. Jeong *et al.* have synthesized a "nanocups" platinium counter eletrode to increase the surface of the electrode.[193] The liquid DSSC based on this electrode displayed an increase of 24 % in PCE compared to the reference.[193]

Nevertheless, as platinium is an expensive material, alternatives counter electrodes based on carbon, less expensive and more stable, were developed. The first attempt to replace Pt in DSSCs has been carried out in 1996 by Kay *et al.* leading to a PCE of 6.7 %.[194] Since then, different carbon materials such as black carbon, mesoporous carbon, graphene, carbon nanotubes, etc. have been tested.

Conductive polymers have also been envisaged as an alternative to platinium. For example, a PCE of 5.08 % was reached using a **PEDOT** counter electrode.[195] Recently, **PPy** and **PANI** were also used leading to PCE around 6.6 %.[196]

In ss-DSSCs, gold and silver are both widely used as counter electrodes due to their good conductivity, their high work function and their chemical stability. They formed also an ohmic contact with **spiro-OMeTAD**, increased the quantity of adsorbed photons and strongly decreased the degradation of the organic layer with oxygen.

REFERENCES

[1] REN21, *Global Status Report*, **2015**. Retrieved July 3, 2016 from www.ren21.net/status-of-renewables/global-status-report/

[2] N. S. Lewis, G. Crabtree, « Basic Research Needs for Solar Energy Utilization », US Department of Energy, **2005**.

[3] (a) D. M. Cahpin, C. S. Fuller and G. L. Pearson, *J. Appl. Phys.* **1954**, *25*, 676; (b) "Annual Energy Outlook 2014", U.S. Energy Information Administration, **2014**.

[4] (a) M. A. Green, K. Emery, Y. Hishikawa, W. Warta and E. D. Dunlop, *Prog. Photovolt: Res. Appl.* **2012**, *20*, 606; (b) National Renewable Energy Laboratory, **2013.** Retrieved April 27, 2016 from www.nrel.gov

[5] (a) S. Mathew, A. Yella, P. Gao, R. Humphry-Baker, B. F. E. Curchod, N. Ashari-Astani, I. Tavernelli, U. Rothlisberger, M. K. Nazeeruddin and M. Grätzel, *Nature Chem.* **2014**, *6*, 242; (b) J. You, L. Dou, K. Yoshimura, T. Kato, K. Ohya, T. Moriarty, K. Emery, C.-C. Chen, J. Gao, G. Li and Y. Yang, *Nat. Commun.* **2013**, *4*, doi:10.1038/ncomms2411.

[6] Photovoltaique info, **2011**. Retrieved July 3, 2016 from http://www.photovoltaique.info

[7] C. A. Gueymard, D. Myers and K. Emery, *Solar Energy* **2002**, *73*, 443.

[8] EF4, *Cellules photovoltaiques*. Retrieved July 3, 2016 from http://www.ef4.be/fr/photovoltaique/aspects-techniques/cellules-photovoltaiques.html

[9] M. A. Green, K. Emery, Y. Hishikawa, W. Warta and E. D. Dunlop, *Prog. Photovolt. Res. Appl.* **2013**, *21*, 1.

[10] (a) C. Yi, X. Hu, X. Gong and A. El Zatahry, *Mater. Today* **2016**, *19*, 169; (b) R. Sondergaard, M. Hösel, D. Angmo, T.T. Larsen-Olsen and F.C. Krebs, *Mater. Today* **2012**, *15*, 36; (c) S.B. Darling and F. You, *RSC advances* **2013**, *3*, 17633.

[11] Matthew Peach, *Heliatek achieves 12 % organic solar cell efficiency*, **2013**. Retrieved July 3, 2016 from http://optics.org/news/4/1/36

[12] L. Dou, J. You, J. Yang, C.-C. Chen,Y. He, S. Murase, T. Moriarty, K. Emery, G. Li and Y. Yang, *Nature Photon*. **2012**, *6*, 180.

[13] B. O'Regan and M. Grätzel, *Nature* **1991**, *353*, 737.

[14] (a) A. Hagfeldt, G. Boschloo, L. Sun, L. Kloo and H. Pettersson, *Chem. Rev.* **2010**, *110*, 6595; (b) B. E. Hardin, H. J. Snaith and M. D. McGehee, *Nature Photon.* **2012**, *6*, 162.

[15] A. Kojima, K. Teshima, Y. Shirai and T. Miyasaka, *J. Am. Chem. Soc.* **2009**, *131*, 6050.

[16] A. H. Ip, S. M. Thon, S. Hoogland, O. Voznyy, D. Zhitomirsky, R. Debnath, L. Levina, L. R. Rollny, G. H. Carey, A. Fischer, K. W. Kemp, I. J. Kramer, Z. Ning, A. J. Labelle, K. W. Chou, A. Amassian and E. H. Sargent, *Nat. Nanotech*. **2012**, *7*, 577.

[17] (a) R. Guillo, *Les different types de cellules photovoltaiques*, Retrieved June 04, 2016 from http://www.ecosources.info; (b) B. Roux Dit Riche, *Disalor ambitionne d'imprimer des panneaux photovoltaiques organiques dès 2015*, **2012**, Retrieved June 04, 2016 from http://www.cleantechrepublic.com; (c) F. Giovanelli, *La carte de l'EPFL fait miroiter ses panneaux de verre colorés*, **2014**, Retrieved June 04, 2016 from https://www.fer-ge.ch.

[18] H. Kallman, M. Pope, *J. Chem. Phys.* **1959**, *30*, 585.

[19] W. Tang, *Appl. Phys. Lett.* **1986**, *48*, 183.

[20] N. S. Sariciftci, L. Smilowitz, A. J. Heeger and F. Wudl, *Science* **1992**, *258*, 1474.

[21] G. Yu, J. Gao, J. C. Hummelen, F. Wudl and A. J. Heeger, *Science* **1995**, *270*,1789.

[22] (a) L. Biam, E. Zhu, J. Tang, W. Tang and F. Zhang, *Prog. Polym. Sci* **2012,** *37,* 1292; (b) S. Sista, M.-H. Park, Z. Hong, Y. Wu, W. L. Kwan, G. Li and Y. Yang, *Adv. Mater.* **2010,** *22,* 3839; (c) G. Dennier, M. C. Scharber, C. J. Brabec, *Adv. Mater.* **2009,** *21,* 1323.

[23] (a) Z. He, B. Xiao, F. Liu, H. Wu, Y. Yang, S. Xiao, C. Wang, T. P. Russell and Y Cao, *Nat. Photonics* **2015,** *9,* 174; (b) Y. Liu, J. Zhao, Z. Li, C. Mu, W. Ma, H. Hu, K. Jiang, H. Lin, H. Ade

and He Yan, *Nat. Commun.* **2014,** *5,* 5293; (c) M. A. Green, K. Emery, Y. Hishikawa, W. Warta and E. D. Dunlop, *Prog. Photovolt. Res. Appl.* **2016,** *24,* 3.

[24] S. Günes, H. Neugebauer, N. S. Sarifitci, *Chem. Rev.* **2007**, *107*, 1324.

[25] Y. Li, *Acc. Chem. Res.* **2012**, *45*, 723.

[26] F. Wudl and G. Srdanov, US patent **1993**, *5*,189,136.

[27] J. C. Hummelen, B. W. Knight, F. LePeq and F. Wudl, *J. Org. Chem.* **1995**, *60*, 532.

[28] M. M. Wienk, J. M. Kroon, W. J. H. Verhees, J. Knol, J. C. Hummelen, P. A. van Hal and R. A. J. Janssen, *Angew. Chem. Int. Ed.* **2003**, *42*, 3371.

[29] (a) F. Laquai, D. Andrienko, R. Mauer and P. W. M. Blom, *Macro. Rapid. Com.* **2015**, *36,* 1001; (b) M. T. Dang, L. Hirsch and G. Wantz, *Adv. Mater.* **2011**, *23*, 3597.

[30] M. C. Scharber, D. Mühlbacher, M. Koppe, P. Denk, C. Waldauf, A. J. Heeger and C. J. Brabec, *Adv. Mater.* **2006**, *18*, 789.

[31] J. Peet, J. Y. Kim, N. E. Coates, W. L. Ma, D. Moses, A. J. Heeger and G. C. Bazan, *Nat. Mater.* **2007**, *6*, 497.

[32] S. H. Park, A. Roy, S. Beaupré, S. Cho, N. Coates, J. S. Moon, D. Moses, M. Leclerc, K. Lee and A. J. Heeger, *Nat. Photon.* **2009**, *3*, 297.

[33] Y. Liang, D. Feng, Y. Wu, S.-T. Tsai, G. Li, C. Ray and L. Yu, *J. Am. Chem. Soc.* **2009**, *131*, 56.

[34] (a) H. Xu, H. Ohkita, T. Hirata, H. Benten and S. Ito, *Polymer* **2014**, *55*, 2856; (b) B. Ananda Rao, M. Sasi Kumar, G. Sivakumar, S. P. Singh, K. Bhanuprakash, V. Jayathirtha Rao and G. D. Sharma, *ACS Sustainable Chem. Eng.* **2014**, *2*, 1743; (c) S. Honda, S. Yokoya, H. Ohkita, H. Benten and S. Ito, *J. Phys Chem C* **2011**, *115*, 11306.

[35] (a) B. J. Campo, J. Duchateau, C. R. Ganivet, B. Ballesteros, J. Gilot, M. M. Wienk, W. D. Oosterbaan, L. Lutsen, T. J. Cleij, G. de la Torre, R. A. J. Janssen, D. Vanderzande and T. Torres, *Dalton Trans.* **2011**, *40*, 3979; (b) E. M. J. Johansson, A. Yartsev, H. Rensmoand and V. J. Sundström, *J. Phys. Chem. C* **2009**, *113*, 3014; (c) S. Honda, T. Nogami, H. Ohkita, H. Benten and S. Ito, *ACS Appl. Mater. Interfaces* **2009**, *1*, 804; (d) L. Angiolini, V. Cocchi, M. Lanzi, E. Salatelli, D. Tonelli and Y. Vlamidis, *Mat. Chem. Phys.* **2014**, *146*, 464; (e) L. Angiolini, T. Benelli, V. Cocchi, M. Lanzi and E. Salatelli, *React. Funct. Polym.* **2013**, *73*, 1198; (f) E. Aguilar-Ortíz, G. Zaragoza-Galán, N. Solladié, R. Rein, M. Aguilar-Martínez, N. Macías-Ruvalcaba and E. Rivera, *Synth. Met.* **2012**, *162*, 1000.

[36] (a) G. Chen, H. Sasabe, X.-F. Wang, Z. Hong and J. Kido, *Synth. Met.* **2014**, *192*, 10; (b) G. Chen, H. Sasabe, T. Igarashi, Z. Hong and J. Kido, *J. Mater. Chem. A*, **2015**, *3*, 14517.

[37] (a) M. Chevrier, S. Richeter, O. Coulembier, M. Surin, A. Mehdi, R. Lazzaroni, R. C. Evans, P. Dubois and S. Clément, *Chem. Commun.* **2016**, *52*, 171 ; (b) M. Chevrier, J. Kesters, C. Blayo, S. Richeter, A. Van Der Lee, O. Coulembier, M. Surin, A. Mehdi, R. Lazzaroni, R. C. Evans, W. Maes, P. Dubois and S. Clément, *Macro. Chem. Phys*. **2016**, *217*, 445.

[38] (a) H. Benten, D. Mori, H. Ohkita and S. Ito, *J. Mater. Chem. A*, **2016**, *4*, 5340; (b) A. Fachetti, *Mater. Today*, **2013**, *16*, 123.

[39] T. W. Holcombe, C. H. Woo, D. F. J. Kavulak, B. C. Thompson and J. M. J. Fréchet, *J. Am. Chem. Soc.* **2009**, *131*, 14160.

[40] D. Mori, H. Benten, J. Hosaka, H. Ohkita, S. Ito and K. Miyake, *ACS Appl. Mater. Interfaces*, **2011**, *3*, 2924.

[41] Y. Zhou, T. Kurosawa, W. Ma, Y. Guo, L. Fang, K. Vandewal, Y. Diao, C. Wang, Q. Yan, J. Reinspach, J. Mei, A. L. Appleton, G. I. Koleilat, Y. Gao, S. C. B. Mannsfeld, A. Salleo, H. Ade, D. Zhao and Z. Bao, *Adv. Mater.* **2014**, *26*, 3767.

[42] H. Yan, B. A. Collins, E. Gann, C. Wang, H. Ade and C. R. McNeill, *ACS Nano*, **2012**, *6*, 677.

[43] M. Schubert, D. Dolfen, J. Frisch, S. Roland, R. Steyrleuthner, B. Stiller, Z. H. Chen, U. Scherf, N. Koch, A. Facchetti and D. Neher, *Adv. Energy Mater.* **2012**, *2*, 369.

[44] (a) Y. J. Hwang, B. A. E. Courtright, A.S. Ferreira, S.H. Tolbert and S. A. Jenekhe, *Adv. Mater.* **2015**, *27*, 4578; (b) L. Gao, Z.-G. Zhang, L. Xue, J. Min, J. Zhang, Z. Wei and Y. Li, *Adv. Mater.* **2016**, doi: 10.1002/adma.201504629.

[45] M. T. Dang, L. Hirsch, G. Wantz and J. D. Wuest, *Chem. Rev.* **2013**, *113*, 3734.

[46] (a) L. Dong and W. S. Li, *Nanoscale* **2011**, *3*, 3447; (b) A. Cuendias, R. C. Hiorns, E. Cloutet, L. Vignau and H. Cramail, *Polym. Int.* **2010**, *59*, 1452; (c) M. Sommer, S. Huettner and M. Thelakkat, *J. Mater. Chem.* **2010**, *20*, 10788; (d) S. B. Darling, *Energy Environ. Sci.* **2009**, *2*, 1266.

[47] M. Chevrier, R. Di Ciuccio, O. Coulembier, P. Dubois, S. Richeter, A. Mehdi and S. Clément, in *Novel Nanoscale Hybrids,* "Functionalization of P3HT-based hybrid materials for photovoltaic applications"*,* Wiley VCH (Eds. B. P. S. Chauhan)*, accepted*.

[48] H.-L. Yip and A. K.-Y Jen, *Energy Envir. Sci.* **2012**, 5, 5994.

[49] Y. H. Kim, S.-H. Lee, J. Noh and S.-H. Han, *Thin Solid Films* **2006**, *510*, 305.

[50] V. Shrotriya, G. Li, Y. Yao, C. Chu and Y. Yang, *Appl. Phys. Lett.* **2006**, *88*, 073508.

[51] M. D. Irwin, D. B. Buchholz, A. W. Hains, R. P. H. Chang and T. J. Marks, *Proc. Natl. Acad. Sci. U. S. A*. **2008**, *105*, 2783.

[52] H. Zhou, Y. Zhang, C.-K. Mai, S. D. Collins, T.-Q. Nguyen, G. C. Bazan and A. J. Heeger, *Adv. Mater.* **2014**, *26*, 780.

[53] N. Lu, K. Du, L. Lu and H. Q. Ye, *Nature Commun.* **2015**, *6*, 7648.

[54] C. J. Brabec, S. E. Shaheen, C. Winder, N. S. Sariciftci and P. Denk, *Appl. Phys. Lett.* **2002**, *80*, 1288.

[55] J. Y. Kim, S. H. Kim, H.-H. Lee, K. Lee, W. Ma, X. Gong and A. J. Heeger, *Adv. Mater.* **2006**, *18*, 572.

[56] (a) C. V. Hoven, A. Garcia, G. C. Bazan and T.-Q. Nguyen, *Adv. Mater.* **2008**, *20*, 3793; (b) F. Huang, H. B. Wu and Y. Cao, *Chem. Soc. Rev.* **2010**, *39*, 2500; (c) A. Duarte, K.-Y. Pu, B. Liu and G. C. Bazan, *Chem. Mater.* **2011**, *23*, 501.

[57] J. Luo, H. B. Wu, C. He, A. Y. Li, W. Yang and Y. Cao, *Appl. Phys. Lett.* **2009**, *95*, 043301.

[58] H. Choi, C-K. Mai, H-B. Kim, J. Jeong, S. Song, G. C. Bazan, J. Y. Kim and A. J. Heeger, *Nature Commun.* **2015**, *6*, 7648.

[59] (a) Z. A. Page, Y. Liu, V. V. Duzhko, T. P. Russel and T. Emrick, *Science*, **2014**, *346*, 441; (b) Y. Liu, Z. A. Page, T. P. Russell and T. Emrick, *Angew. Chem. Int. Ed.* **2015**, *54*, 11485.

[60] Z. C. He, C. Zhang, X. F. Xu, L. J. Zhang, L. Huang, J. W. Chen, H. B. Wu and Y. Cao, *Adv. Mater.* **2011**, *23*, 3086.

[61] Z. C. He, C. M. Zhong, X. Huang, W.-Y. Wong, H. B. Wu, L. W. Chen, S. J. Su and Y. Cao, *Adv. Mater.* **2011**, *23*, 4636.

[62] (a) A. Garcia, J. Z. Brzezinski and T.-Q. Nguyen, *J. Phys. Chem. C*, **2009**, *113*, 2950; (b) M. Kang, O. K. Nag, R. R. Nayak, S. Hwang, H. Suh and H. Y. Woo, *Macromolecules*, **2009**, *42*, 2708; (c) Z. B. Henson, Y. Zhang, T.-Q. Nguyen, J. H. Seo and G. C. Bazan, *J. Am. Chem. Soc.* **2013**, *135*, 4163; (d) D. Tordera, M. Kuik, Z. D. Rengert, E. Bandiello, H. J. Bolink, G. C. Bazan and T.-Q. Nguyen, *J. Am. Chem. Soc.* **2014**, *136*, 8500.

[63] C. H. Duan, K. Zhang, X. Guan, C. M. Zhong, H. Xie, F. Huang, J. W. Chen, J. B. Peng and Y. Cao, *Chem. Sci.* **2013**, *4*, 1298.

[64] (a) Y.-M. Chang, R. Zhu, E. Richard, C.-C. Chen, G. Li and Y. Yang, *Adv. Funct. Mater.* **2012**, *22*, 3284; (b) J. Kesters, T. Ghoos, H. Penxten, J. Drijkoningen T. Vangerven, D. M. Lyons, B. Verreet, T. Aernouts, L. Lutsen, D. Vanderzande, J. Manca and W. Maes, *Adv. Energy Mater.* **2013**, *3*, 1180; (c) J. Drijkoningena, J. Kesters, T. Vangervena, E. Bourgeois, L. Lutsen, D. Vanderzande, W. Maes, J. D'Haen and J. Manca, *Org. Elect.* **2014**, *15*, 1282; (d) J. H. Seo, A. Gutacker, Y. Sun, H. Wu, F. Huang, Y. Cao, U. Scherf, A. J. Heeger and G. C. Bazan, *J. Am. Chem. Soc.* **2011**, *133*, 8416.

[65] (a) A. Thomas, J. E. Houston, N. Van den Brande, J. De Winter, M. Chevrier, R. K. Heenan, A. E. Terry, S. Richeter, A. Mehdi, B. Van Mele, P. Dubois, R. Lazzaroni, P. Gerbaux, R. C. Evans and S. Clément, *Polym. Chem*. **2014**, *5*, 3352; (b) M. Chevrier, J. E. Houston, J. Kesters, N. Van den Brande, A. E. Terry, S. Richeter, A. Mehdi, O. Coulembier, P. Dubois, R. Lazzaroni, B. Van Mele, W. Maes, R. C. Evans and S. Clément, *J. Mater. Chem. A* **2015**, *3*, 23905; (c) J. Kesters, S. Govaerts, G. Pirotte, J. Drijkoningen, M. Chevrier, N. Van den Brande, X. Liu, M. Fahlman, B. Van Mele, L. Lutsen, D. Vanderzande, J. Manca, S. Clément, E. Von Hauff and W. Maes, *ACS Appl. Mater. Interfaces*, **2016**, *8*, 6309.

[66] (a) T. Yamamoto, K. Sanechika and A. Yamamoto, *J. Polym. Sci., Polym. Lett. Ed.* **1980**, *18*, 9; (b) J. W. P. Lin and L. P. Dudek, *J. Polym. Sci., Polym. Chem. Ed.* **1980**, *18*, 2869.

[67] (a) M. Kobayashi, J. Chen, T. C. Chung, F. Moraes, A. J. Heeger and F. Wudl, *Synth. Met.* **1984**, *9*, 77; (b) A. Berlin, G. A. Pagani and F. Sannicolo, *J. Chem. Soc., Chem. Commun.* **1986**, 1663; (c) K. Yoshino, S. Hayashi and R.-I. Sugimoto, *Jpn. J. Appl. Phys.* **1984**, *23*, L899.

[68] R. L. Elsenbaumer, K. Y. Jen and R. Oboodi, *Synth. Met.* **1986**, *15*, 169.

[69] M. Pomerantz, J. J. Tseng, H. Zhu, S. J. Sproull, J. R. Reynolds, R. Uitz, H. J. Arnott and M. I. Haider, *Synth. Met.* **1991**, *41*, 825.

[70] (a) T. Yamamoto, A. Morita, Y. Miyazaki, T. Maruyama, H. Wakayama, Z. H. Zhou, Y. Nakamura, T. Kanbara, S. Sasaki and K. Kubota, *Macromolecules* **1992**, *25*, 1214; (b) M. D. McClain, D. A. Whittington, D. J. Mitchell and M. D. Curtis, *J. Am. Chem. Soc.* **1995**, *117*, 3887.

[71] R. D. McCullough, S. Tristam-Nagle, S. P. Williams, R. D. Lowe and M. Jayaraman, *J. Am. Chem. Soc*. **1993**, *115*, 4910.

[72] P. Sista and C. K. Luscombe in *P3HT Revisited – From molecular scale to solar cells devices* (Eds: S. Ludwigs), **2014**, "*Progress in the synthesis of poly(3-hexylthiophene)"*, Springer-Verlag Berlin Heidelberg.

[73] A. Marrocchi, D. Lanari, A. Facchetti and L. Vaccaro, *Energy Environ. Sci.* **2012**, *5*, 8457.

[74] S. Tanaka, S. Tamba, D. Tanaka, A. Sugie and A. Mori, *J. Am. Chem. Soc.* **2011**, *133*, 16734.

[75] R. D. McCullough and R. D. Lowe, *J. Am. Chem. Soc., Chem. Commun.* **1992**, *70*.

[76] T.-A. Chen, X. Wu and R. D. Rieke, *J. Am. Chem. Soc.* **1995**, *117*, 233.

[77] S.-H. Kim and J.-G. Kim, *Bull. Korean Chem. Soc.* **2010**, *31*, 193.

[78] J.-G. Kim, S.-H. Kim and R. D. Rieke, *Macromol. Res.* **2011**, *19*, 749.

[79] E. Goto, S. Nakamura, S. Kawauchi, H. Mori, M. Ueda and T. Higashihara, *J. Polym. Sci., Polym. Chem.* **2014**, *52*, 2287.

[80] (a) R. S. Loewe, S. M. Khersonsky and R. D. McCullough, *Adv. Mater.* **1999**, *11*, 250; (b) A. Yokoyama, R. Miyakoshi and T. Yokozowa, *Macromolecules*, **2004**, *37*, 1169; (c) R. Miyakoshi, A. Yokoyama and T. Yokozowa, *J. Am. Chem. Soc.* **2005**, *127*, 17542; (d) R. Miyakoshi, A. Yokoyama and T. Yokozowa, *Macromol. Rapid. Comm.* **2004**, *25*, 1663.

[81] R. H. Lohwasser and M. Thelakkat, *Macromolecules*, **2011**, *44*, 3388.

[82] (a) A. Yokoyama and T. Yokozowa, *Macromolecules*, **2007**, *40*, 4093; (b) M. C. Iovu, E. E. Sheina, R. R. Gil and R. D. McCullough, *Macromolecules*, **2005**, *38*, 8649.

[83] (a) T. Yokozawa and Y. Ohta, *Chem. Commun.* **2013**, *49*, 8281; (b) Z. J. Bryan and A. J. McNeil, *Macromolecules* **2013**, *46*, 8395; (c) I. Osaka and R. D. McCullough in *Design and Synthesis of Conjugated Polymers* (Eds: M. Leclerc, J.-F. Morin), **2010**, "*Advanced Functional Regioregular Polythiophenes*", Wiley-VCH, Weinheim; (d) I. Osaka and R. D. McCullough, *Acc. Chem. Res.* **2008**, *41*, 1202.

[84] (a) R. Tkachov, V. Senkovskyy, H. Komber, J.-U. Sommer and A. Kiriy, *J. Am. Chem. Soc.* **2010**, *132*, 7803; (b) P. Kohn, S. Huettner, H. Komber, V. Senkovskyy, R. Tkachov, A. Kiriy, R. H. Friend, U. Steiner, W. T. S. Huck, J. U. Sommer and M. Sommer, *J. Am. Chem. Soc*. **2012**, *134*, 479.

[85] (a) N. Khanduyeva, V. Senkovsky, T. Beryokzkina, M. Horecha, M. Stamm, C. Uhrich, M. Riede, K. Leo and A. Kiriy, *J. Am. Chem. Soc.* **2009**, *131*, 153; (b) V. Senkovsky, N. Khanduyeva, H. Komber, U. Oertel, M. Stamm, D. Kuckling and A. Kiriy, *J. Am. Chem. Soc.* **2007**, *129*, 6626.

[86] N. Marshall, S. K. Sontag and J. Locklin, *Chem. Commun.* **2011**, *47*, 5681.

[87] E. Negishi, *Acc. Chem. Res.* **1982**, *15*, 340.

[88] H. A. Bronstein and C. K. Luscombe, *J. Am. Chem. Soc.* **2009**, *131*, 12894.

[89] (a) R. Tkachov, V. Senkovskyy, M. Horecha, U. Oertel, M. Stamm and A. Kiriy, *Chem. Commun.* **2010**, *46*, 1425; (b) V. Senkovskyy, R. Tkachov, T. Beryozkina, H. Komber, U. Oertel, M. Horecha, V. Bocharova, M. Stamm, S. A. Gevorgyan, F. C. Krebs and A. Kiriy, *J. Am. Chem. Soc.* **2009**, *131*, 16445.

[90] (a) S. K. Sontag, G. R. Sheppard, N. M. Usselman, N. Marshall and J. Locklin, *Langmuir* **2011**, *27*, 12033; (b) L. Yang, S. K. Sontag, T. W. LaJoie, W. Li, N. E. Huddleston, J. Locklin and W. You, *ACS Appl. Mater. Interfaces* **2012**, *4*, 5069.

[91] S. R. Lee, J. W. D. Bloom, S. E. Wheeler and A. J. McNeil, *Dalton Trans.* **2013**, *42*, 4218.

[92] (a) H. Sirringhaus, P. J. Brown, R. H. Friend, M. M. Nielsen, K. Bechgaard, B. M. W. Langeveld-Voss, A. J. H. Spiering, R. A. J. Janssen, E. W. Meijer, P. Herwig and D. M. de Leeuw, *Nature* **1999**, *401*, 685.

[93] (a) Z. Masri, A. Ruseckas, E. V. Emelianova, L. Wang, A. K. Bansal, A. Matheson, H. T. Lemke, M. M. Nielsen, H. Nguyen, O. Coulembier, P. Dubois, D. Beljonne and I. D. W. Samuel, *Adv. Mater.* **2013**, *3*, 1445; (b) F. Panzer, H. Bassler, R. Lohwasser, M. Thelakkat and A. Kohler, *J. Phys. Chem. Lett.* **2014**, *5*, 2742; (c) S. Himmelberger, K. Vandewal, Z. Fei, M. Heeney and A. Salleo, *Macromolecules* **2014**, *47*, 7151.

[94] A. Salleo, *Mater. Today* **2007**, *10*, 38.

[95] N. V. Handa, A. V. Serrano, M. J. Robb and C. J. Hawker, *J. Polym. Sci. Polym. Chem.* **2015**, *53*, 831.

[96] B. M. W. Langeveld-Voss, R. A. J. Janssen, R. A. J. Spiering, J. L. J. van Dongen, E. C. Vonk and H. A Claessens, *Chem. Commun.* **2000**, 81.

[97] W. M. Kochemba, S. M. Kilbey and D. L. Pickel, *J. Polym. Sci. Polym. Chem.* **2012**, *50*, 2762.

[98] N. Doubina, A. Ho, A. K. Y. Jen and C. K. Luscombe, *Macromolecules* **2009**, *42*, 7670.

[99] (a) S. L. Fronk, C.-K. Mai, Michael Ford, R. P. Noland and G. C. Bazan, *Macromolecules* **2015**, *48*, 6224; (b) P. A. Dalgarno, Traina, J. C. Penedo, G. C. Bazan and I. D. W. Samuel, *J. Am. Chem. Soc.* **2013**, *135*, 7187.

[100] (a) F. Monnaie, W. Brullot, T. Verbiest, J. De Winter, P. Gerbaux, A. Smeets and G. Koeckelberghs, *Macromolecules* **2013**, *46*, 8500; (b) A. Smeets, P. Willot, J. De Winter, P. Gerbaux, T. Verbiest and G. Koeckelberghs, *Macromolecules* **2011**, *44*, 6017.

[101] (a) V. Senkovsky, N. Khanduyeva, H. Komber, U. Oertel, M. Stamm, D. Kuckling and A. Kiriy, *J. Am. Chem. Soc.* **2007**, *129*, 6626; (b) F. Boon, D. Moerman, D. Laurencin, S. Richeter, Y. Guari, A. Mehdi, P. Dubois, Roberto Lazzaroni and S. Clément, *Langmuir* **2014**, *30*, 11340.

[102] J. Liu and R. D. McCullough, *Macromolecules* **2002**, *35*, 9882.

[103] (a) J. Liu, E. Sheina, T. Kowalewski and R. D. McCullough, *Angew. Chem. Int. Ed.* **2002**, *41*, 329; (b) J. Liu, R. S. Loewe and R. D. McCullough, *Macromolecules* **1999**, *32*, 5777.

[104] (a) R. A. Krüger, T. J. Gordon, T. Baumgartner and T. C. Sutherland, *ACS Appl. Mater. Interfaces* **2011**, *3*, 2031; (b) F. Boon, A. Thomas, G. Clavel, D. Moerman, J. De Winter, D. Laurencin, O. Coulembier, P. Dubois, P. Gerbaux, R. Lazzaroni, S. Richeter, A. Mehdi and S. Clément, *Synth. Met.* **2012**, *162*, 1615 ; (b) R. H. Lohwasser and M. Thelakkat, *Macromolecules* **2010**, *43*, 7611; (c) A. L. Briseno, T. W. Holcombe, A. I. Boukai, E. C. Garnett, S. W. Shelton, J. J. M. Fréchet and P. Yang, *Nano Lett.* **2010**, *10*, 334.

[105] (a) Z. Mao, K. Vakhshouri, C. Jaye, D. A. Fischer, R. Fernando, D. M. DeLongchamp, E. D. Gomez and G. Sauvé, *Macromolecules* **2013**, *46*, 103 ; (b) P. Giannopoulos, A. Nikolakopoulou, A. K. Andreopoulou, L. Sygellou, J. K. Kallitsisa and P. Lianos, *J. Mater. Chem. A* **2014**, *2*, 20748.

[106] K. Okamoto and C. K. Luscombe, *Chem. Commun.* **2014**, *50*, 5310.

[107] J. Mei and Z. Bao, *Chem. Mater.* **2014**, *26*, 604.

[108] (a) J. Lee, M. Kim, B. Kang, S. B. Jo, H. G. Kim, J. Shin and K. Cho, *Adv. Energy Mater.* **2014**, *4*, 1400087; (b) W.-H. Chang, J. Gao, L. Dou, C.-C. Chen, Y. Liu and Y. Yang, *Adv. Energy Mater.* **2014**, *4*, 1300864.

[109] (a) L. Zhai, R. L. Pilston, K. L. Zaiger, K. K. Stokes and R. D. McCullough, *Macromolecules* **2003**, *36*, 61.

[110] S. Miyanishi, K. Tajima and K. Hashimoto, *Macromolecules* **2009**, *42*, 1610.

[111] J. M. Lobez, T. L. Andrew, V. Bulovi and T. M. Swager, *ACS Nano* **2012**, *6*, 3044.

[112] M. Lanzi, E. Salatelli, T. Benelli, D. Caretti, L. Giorgini and F. Paolo Di-Nicola, *J. Appl. Polym. Sci.* **2015**, *132*, 42121.

[113] H. J. Kim, A.-R. Han, C.-H. Cho, H. Kang, H.-H. Cho, M. Y. Lee, J. M. J. Fréchet, J. H. Oh and B. J. Kim, *Chem. Mater.* **2012**, *24*, 215.

[114] H. Tributsch and M. Clavin, *Photochem. Photobiol* **1971**, *14*, 95.

[115] M. Matsumura, Y. Nomura and H. Tsubomura, *Bull. Chem. Soc. Jpn* **1977**, *50*, 2533.

[116] N. Memarian, I. Concina, A. Braga, S. M. Rozati, A. Vomiero and G. Sberveglieri, *Angew. Chem. Int. Ed.* **2011**, *50*, 12321.

[117] (a) Y. Fukai, Y. Kondo, S. Mori and E. Suzuki, *Electrochem Commun.* **2007**, *9*, 1439; (b) Z. Tebby, T. Uddin, Y. Nicolas, C. Olivier, T. Toupance, C. Labrugère and L. Hirsch, *ACS Appl. Mater. Interfaces* **2011**, *3*, 1485.

[118] J. Zhen Ou, R. A. Rani, M.-H. Ham, M. R. Field, Y. Zhang, H. Zheng, P. Reece, S. Zhuiykov, S. Sriram, M. Bhaskaran, R. B. Kaner and K. Kalantar-Zadeh, *ACS Nano.* **2012**, *6*, 4045.

[119] (a) T. W. Hamann, R. A. Jensen, A. B. F. Martinson, H. Van Ryswyk and Jo. T. Hupp, *Energy Environ. Sci.* **2008**, *1*, 66; (b) Q. Zhang, C. S. Dandeneau, X. Zhou, and G. Cao, *Adv. Mater.* **2009**, *21*, 4087.

[120] S. Ito, T. N. Murakami, P. Comte, P. Liska, C. Grätzel, M. K. Nazeeruddin and M. Grätzel, *Thin Solid Films* **2008**, *516*, 4613.

[121] P. Roy, D. Kim, K. Lee, E. Spiecker and P. Schmuki, *Nanoscale* **2010**, *2*, 45.

[122] M. Ye, X. Wen, M. Wang, J. Iocozzia, N. Zhang, C. Lin and Z. lin, *Mater. Today* **2015**, *18*, 155.

[123] J. R. Mann, M. K. Gannon, T. C. Fitzgibbons, M. R. Detty and D. F. Watson, *J. Phys. Chem. C* **2008**, *112*, 13057.

[124] M. K. Nazeeruddin, A. Kay, I. Rodicio, R. Humpry-Baker, E. Muller, P. Liska, N. Vlachopoulos and M. Grätzel, *J. Am. Chem. Soc.* **1993**, *115*, 6382.

[125] M. K. Nazeeruddin, S. M. Zakeeruddin, R. Humphry-Baker, M. Jirousek, P. Liska, N. Vlachopoulos, V. Shklover, C. H. Fischer and M. Grätzel, *Inorg. Chem.* **1999**, *38*, 6298.

[126] (a) M. K. Nazeeruddin, P. Péchy and M. Grätzel, *Chem. Commun.* **1997**, 1705; (b) M. K. Nazeeruddin, P. Pechy, P. Liska, T. Renouard, S. M. Zakeeruddin, R. Humphry-Baker, P. Comte, L. Cevey, E. Costa, V. Shklover, L. Spiccia, G. B. Deacon, C. A. Bignozzi and M. Grätzel, *J. Am. Chem. Soc.* **2001**, *123*, 1613; (c) M. Grätzel, *J. Photochem. Photobiol. A* **2004**, *164*, 3.

[127] K. Hara, H. Sugihara, Y. Tachibana, A. Islam, M. Yanagida, K. Sayama, H. Arakawa, G. Fujihashi, T. Horiguchi and T. Kinoshita, *Langmuir* **2001**, *17*, 5992.

[128] P. Wang, S. M. Zakeeruddin, J. E. Moser, K. Nazeeruddin, T. Sekiguchi and M. Grätzel, *Nat. Mater.* **2003**, *2*, 402.

[129] P. Wang, S. M. Zakeeruddin, R. Humphry-Baker, J. E. Moser and M. Grätzel, *Adv. Mater.* **2003**, *15*, 2101.

[130] F. Gao, Y. Wang, D. Shi, J. Zhang, M. Wang, X. Jing, R. Humphry-Baker, P. Wang, S. M. Zakeeruddin and M. Grätzel, *J. Am. Chem. Soc.* **2008**, *130*, 10720.

[131] Y. Cao, Y. Bai, Q. Yu, Y. Cheng, S. Liu, D. Shi, F. Gao and P. Wang, J. *Phys. Chem. C* **2009**, *113*, 6290.

[132] S. Bae, H. Kim, Y. Lee, X. Xu, J.-S. Park, Y. Zheng, J. Balakrishnan, T. Lei, H. R. Kim, Y. I. Song, Y.-J. Kim, K. S. Kim, B. Özyilmaz, J.-H. Ahn, B. H. Hong and S. Iijima, *Nat. Nanotechnol.* **2010**, *4*, 574.

[133] C. Y. Chen, M. K. Wang, J. Y. Li, N. Pootrakulchote, L. Alibabaei, C. H. Ngocle, J. D. Decoppet, J. H. Tsai, C. Grätzel, C. G. Wu, S. M. Zakeeruddin and M. Grätzel, *ACS Nano* **2009**, *3*, 3103.

[134] T. Bessho, E. Yoneda, J.-H. Yum, M. Guglielmi, I. Tavernelli, H. Imai, U. Rothlisberger, M. K. Nazeeruddin and M. Grätzel, *J. Chem.Soc.* **2009**, *131*, 5930.

[135] T. Kinoshita, J. T. Dy, S. Uchida, T. Kubo and H. Segawa, *Nat. Photonics* **2013**, *7*, 535.

[136] E. A. M. Geary, L. J. Yellowless, L. A. Jack, I. D. H. Oswald, S. Parson, N. Hirata, J. R. Durrant and N. Robertson, *Inorg. Chem.* **2005**, *44*, 242.

[137] E. Baranoff, J.-H. Yum, M. Grätzel and Md. K. Nazeeruddin, *J. Organomet. Chem.* **2009**, *694*, 2661.

[138] (a) C.-P. Lee, R. Y.-Y. Lin, L.-Y. Lin, C.-T. Li, T.-C. Chu, S.-S. Sun, J. T. Lin and K.-C. Ho, *RSC Adv.* **2015**, *5*, 23810; (b) A. Mishra, M. K. R Fischer and P. Bäuerle, *Angew. Chem. Int. Ed.* **2009**, *48*, 2474.

[139] S. Zhang, X. Yang, Y. Numata and L. Han, *Energy Environ. Sci.* **2013**, *6*, 1443.

[140] (a) K. Hara, M. Kurashige, S. Ito, A. Shinpo, S. Suga, K. Sayama and H. Arakawa, *Chem. Commun.* **2003**, 252; (b) K. Hara, T. Sato, R. Katoh, A. Furube, T. Yoshihara, M. Murai, M. Kurashige, S. Ito, A. Shinpo, S. Suga and H. Arakawa, *Adv. Funct. Mater.* **2005**, *15*, 246.

[141] Z.-S. Wang, Y. Cui, Y. Dan-oh, C. Kasada, A. Shinpo, and K. Hara, *J. Phys. Chem. C* **2007**, *111*, 7224.

[142] K. R. Justin Thomas, J. T. Lin, Y. C. Hsu and K. C. Ho, *Chem. Commun.* **2005**, 4098.

[143] S. Hwang, J. H. Lee, C. Park, H. Lee, C. Kim, C. Park, M.-H. Lee, W. Lee, J. Park, K. Kim, N.-G. Park and C. Kim, *Chem. Commun.* **2007**, 4887.

[144] (a) H. Choi, C. Baik, H. J. Kim, J.-J. Kim, K. Song, S. O. Kang and J. Ko, *Bull. Korean Chem. Soc.* **2007**, *28*, 1973; (b) Qin, S. Wenger, M. Xu, F. Gao, X. Jing, P. Wang, S. M. Zakeeruddin and M. Grätzel, *J. Am. Chem. Soc.* **2008**, *130*, 9202; (c) Xu, B. Peng, J. Chen, M. Liang and F. Cai, *J. Phys. Chem. C* **2008**, *112*, 874.

[145] T. Horiuchi, H. Miura and S. Uchida, *Chem. Commun.* **2003**, 3036.

[146] *T.* Horiuchi, H. Miura, K. Sumioka and S. Uchida, *J. Am. Chem. Soc.* **2004**, *126*, 12218.

[147] S. Ito, S. M. Zakeeruddin, R. Humphry-Baker, P. Liska, R. Charvet, P. Comte, M. K. Nazeeruddin, P. Péchy, M. Takata, H. Miura, S. Uchida and M. Grätzel, *Adv. Mater.* **2006**, *18*, 1202.

[148] S. Ito, H. Miura, S. Uchida, M. Takata, K. Sumioka, P. Liska, P. Comte, P. Pechy and M. Grätzel, *Chem. Commun.* **2008**, 5194.

[149] (a) N. Koumura, Z. S. Wang, S. Mori, M. Miyashita, E. Suzuki and K. Hara, *J. Am. Chem. Soc.* **2006**, *128*, 14256; (b) Z.-S. Wang, N. Koumura, Y. Cui, M. Takahashi, H. Sekiguchi, A. Mori, T. Kubo, A. Furube and K. Hara, *Chem. Mater.* **2008**, *20*, 3993.

[150] W. Zeng, Y. Cao, Y. Bai, Y. Wang, Y. Shi, M. Zhang, F. Wang, C. Pan and P. Wang, *Chem. Mater.* **2010**, *22*, 1915.

[151] A. Yella, R. Humphry-Baker, B. F. E. Curchod, N. A. Astani, J. Teuscher, L. E. Polander, S. Mathew, J.-E. Moser, I. Tavernelli, U. Rothlisberger, M. Grätzel, M. K. Nazeeruddin and J. Frey, *Chem. Mater.* **2013**, *25*, 2733.

[152] D. Zhou, Q. Yu, N. Cai, Y. Bai, Y. Wang and P. Wang, *Energy Environ. Sci.* **2011**, *4*, 2030.

[153] H. N. Tsao, C. Yi, T. Moehl, J.-H. Yum, S. M. Zakeeruddin, M. K. Nazeeruddin and M. Grätzel, *ChemSusChem* **2011**, *4*, 591.

[154] Y. Wu and W. Zhu, *Chem.Soc.Rev.* **2013**, *42*, 2039.

[155] X.-F. Wang and H. Tamiaki, *Energy Environ. Sci.* **2010**, *3*, 94.

[156] L.-L. Li and E. W.-G. Diau, *Chem. Soc. Rev.* **2013**, *42*, 291.

[157] A. Kay and M. Grätzel, *J. Phys. Chem.* **1993,** *97*, 6272.

[158] W. M. Campbell, K. W. Jolley, P. Wagner, K. Wagner, P. J. Walsh, K. C. Gordon, L. Schmidt-Mende, M. K. Nazeeruddin, Q. Wang, M. Grätzel and D. L. Officer, *J. Phys. Chem. C* **2007**, *111*, 11760.

[159] M. Ishida, S. W. Park, D. Hwang, Y. B. Koo, J. L. Sessler, D. Y. Kim and D. Kim, *J. Phys. Chem. C* **2011**, *115*, 19343.

[160] V. Lin, S. DiMagno and M. Therien, *Science*, **1994**, *264*, 1105.

[161] J. Rochford, D. Chu, A. Hagfelt and E. Galioppini, *J. Am. Chem. Soc.* **2007**, *129,* 4655.

[162] T. Bessho, S. M. Zakeeruddin, C.-Y. Yeh, E. Wei-Guang Diau and M. Grätzel, *Angew. Chem. Int. Ed.* **2010**, *49*, 6646.

[163] A. Yella, H.-W. Lee, H. N. Tsao, C. Yi, A. K. Chandiran, Md. K. Nazeeruddin, E. W.-G. Diau, C.-Y. Yeh, S. M. Zakeeruddin and M. Grätzel, *Science*, **2011**, *334*, 629.

[164] G. Calogero, A. Bartolotta, G. Di Marco, A. Di Carlo and F. Bonaccorso, *Chem. Soc. Rev.* **2015**, *44*, 3244.

[165] H. Scheer, *Chlorophylls and Bacteriochlorophylls: Biochemistry, Biophysics, Functions and Applications*, ed. B. Grimm, R. J. Porra, W. Rüdiger and H. Scheer, Springer, **2006**, *25*, ch. 1.

[166] M. Pelletier and J. B. Caventou, *Ann. Chim. Phys.* **1818**, *9*, 194.

[167] S. V. Eliseeva and J.-C G. Bünzli, *Chem. Soc. Rev.* **2010**, *39*, 189.

[168] P. V. Kamat, J.-P. Chauvet and R. W. Fessenden, *J. Phys. Chem.* **1986**, *90*, 1389.

[169] S. Hao, J. Wu, Y. Huang and J. Lin, *Sol. Energy* **2006**, *80*, 209.

[170] H. Chang, M.-J. Kao, T.-L. Chen, C.-H. Chen, K.-C. Cho and X.-R. Lai, *Int. J. Photoenergy* **2013**, 159502.

[171] X. F. Wang, C. H. Zhan, T. Maoka, Y. Wada and Y. Koyama, *Chem. Phys. Lett.* **2007**, *447*, 79.

[172] Y. Koyama, T. Miki, X. F. Wang and H. Nagae, *Int J Mol Sci.* **2009**, *10,* 4575.

[173] J. Wu, Z. Lan, J. Lin, M. Huang, Y. Huang, L. Fan and G. Luo, *Chem. Rev.* **2015**, *115*, 2136.

[174] Z.-S. Wang, K. Sayama and H. Sugihara, *J. Phys. Chem. B* **2005**, *109*, 22449.

[175] B. V Bergeron, A. Marton, G. Oskam and G. J. Meyer, *J. Phys. Chem. B* **2005**, *109*, 937.

[176] T. Daeneke, T. Kwon, A. Holmes, N. Duffy, U. Bach and L. Spiccia, *Nat. Chem.* **2011**, *3*, 211.

[177] Y. Bai, Q. Yu, N. Cai, Y. Wang, M. Zhang and P. Wang, *Chem. Commun.* **2011**, *47*, 4376.

[178] (a) M. B. Achari, *Phys. Chem. Chem. Phys.* **2013**, *15*, 17419; (b) X. Wang, *ACS Appl. Mater. Interfaces* **2012**, *5*, 444.

[179] G. Hodes and D. Cahen, *Acc. Chem. Res.* **2012**, *45*, 705.

[180] I. Chung, B. Lee, J. He, R. P. H. Chang and M. G. Kanatzidis, *Nature* **2012**, *485*, 486.

[181] W. S. Yang, J. H. Noh, N. J. Jeon, Y. C. Kim, S. Ryu, J. Seo and S. I. Seok, *Science* **2015**, *348*, 1234.

[182] J. Burschka, A. Dualeh, F. Kessler, E. Baranoff, N. Cevey, C. Yi, M. Nazeeruddin and M. Gratzel, *J. Am. Chem. Soc.* **2011**, *133*, 18042.

[183] I.-K. Ding, J. Melas-Kyriazi, N.-L. Cevey-Ha, K. G. Chittibabu, S. M. Zakeeruddi, M. Grätzel and M. D. McGehee, *Org. Electron.* **2010**, *11*, 1217.

[184] K. Murakoshi, R. Kogure, Y. Wada and S. Yanagida, *Chem. Lett.* **1997**, 471.

[185] S. Tan, J. Zhai, M. Wan, Q. Meng, Y. Li, L. Jiang and D. Zhu, *J. Phys. Chem. B* **2004**, *108*, 18693.

[186] (a) K. M. Coakley, Y. X. Liu, M. D. McGehee and K. L. Frindell, *Adv. Funct. Mater.* **2003**, *13*, 301; (b) K. M. Coakley and M. D. McGehee, *Appl. Phys. Lett.* **2003**, *83*, 3380.

[187] E. Lancelle-Beltran, P. Prene, C. Boscher, P. Belleville, P. Buvat and C. Sanchez, *Adv. Mater.* **2006**, *18*, 2579.

[188] R. Zhu, C. Y. Jiang, B. Liu and S. Ramakrishna, *Adv. Mater.* **2009**, *21*, 994.

[189] G. Mor, S. Kim, M. Paulose, O. Varghese, K. Shankar, J. Basham and C. Grimes, *Nano Lett.* **2009**, *9*, 4250.

[190] F. Giacomo, S. Razza, F. Matteocci, A. Epifanio, S. Licoccia, T. Brown and A. Carlo, *J. Power Sources* **2014**, *251*, 152.

[191] G. Yue, J. Wu, J. Lin, M. Huang, Y. Yao, L. Fan and Y. Xiao, *Front. Optoelectron. China* **2011**, *4*, 369.

[192] S. Thomas, T. G. Deepak, G. S. Anjusree, T. a. Arun, S. V. Nair, and A. S. Nair, *J. Mater. Chem. A* **2014**, *2*, 4474.

[193] H. Jeong, Y. Pak, Y. Hwang, H. Song, K. H. Lee, H. C. Ko and G. Y. Jung, *Small* **2012**, *8*, 3757.

[194] A. Kay and M. Grätzel, *Sol. Energy Mater. Sol. Cells* **1996**, *44*, 99.

[195] K. S. Lee, H. K. Lee, D. H. Wang, N.-G. Park, J. Y. Lee, O. O. Park and J. H. Park, *Chem. Commun.* **2010***, 46*, 4505.

[196] Q. Tang, H. Cai, S. Yuan and X. Wang, *J. Mater. Chem. A* **2013**, *1*, 317.

CHAPTER 2

EXPANDING THE LIGHT ABSORPTION OF P3HT DERIVATIVES BY FUNCTIONALIZATION WITH PORPHYRINS

EXPANDING THE LIGHT ABSORPTION OF P3HT DERIVATIVES BY FUNCTIONALIZATION WITH PORPHYRINS

INTRODUCTION

Polymer bulk-heterojunction (BHJ) solar cells have attracted considerable interest over the last decade due to their light weight, low-cost production and compatibility with flexible substrates.[1] Even though power conversion efficiencies (PCEs) have recently increased up to 10 % and their energy payback time is estimated to be 0.2-4 years,[2] further improvements are still required to extend their applicability compared to the traditional silicon-based solar cells.[3] As a result, tremendous efforts have been made to improve the PCEs of polymer solar cells and to reach potential commercialization of this technology.[4] BHJ polymer solar cells based on poly(3-hexylthiophene) (**P3HT**) as the electron donor material and [6,6]-phenyl-C_{61}-butyric acid methyl ester (**$PC_{61}BM$**) as the electron acceptor have been extensively studied, leading to PCEs of about 5 %.[5] The **P3HT**:**$PC_{61}BM$** blend system is well-understood and exhibits good processability.[6] The modest PCE of **P3HT**-based solar cells can be attributed to the weak absorption of **P3HT** in some parts of the visible and the near-infrared regions of the solar emission spectrum (Figure 2.1).[7]

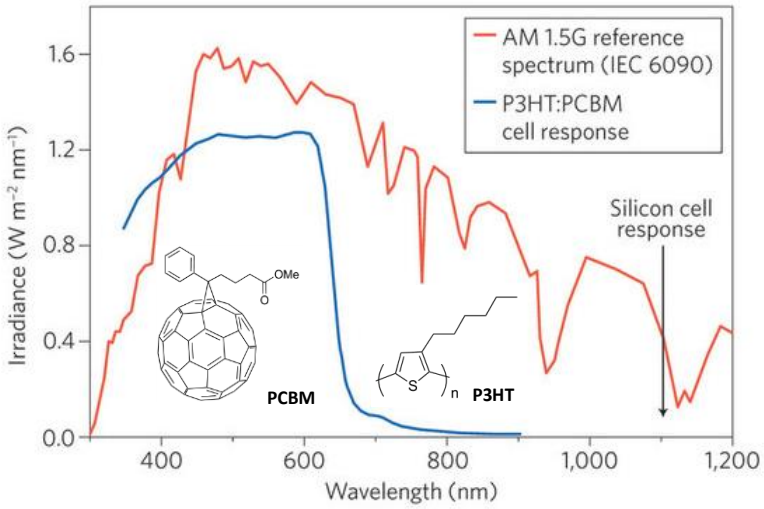

Figure 2.1 UV-visible absorption spectrum of **P3HT**:**PCBM** (blue) and solar emission spectrum AM 1.5G (red).

To overcome these absorption limitations, low bandgap (< 1.8 eV) polymer materials are required for a broader coverage of the solar spectrum. A popular and successful strategy to achieve this purpose consists in developing alternating donor-acceptor conjugated polymers. Indeed, due to intramolecular charge transfer (ICT) effects, their absorption profile is extended to higher wavelengths.[8] Nevertheless, this effect is also associated with a weakened absorption of the short-wavelength photons. Another strategy to expand the absorption spectrum of the active layer from the visible to the near-infrared (NIR) region consists in the tandem solar cell concept, where materials with different bandgaps and absorption can be combined. However, their multilayer architecture is a major drawback compared to the single junction BHJ solar cells

due to a more challenging fabrication process.[9] Another approach is based on the combination of a third component, a dye having a complementary absorption spectrum, to the polymer/fullerene blend.[10] As such, porphyrin chromophores have attracted increasing interest due to their unique optical absorption and photochemical stability, which can be tuned by modification of their molecular structure.[11] Porphyrins are also known to strongly interact with fullerenes, commonly used as acceptors in BHJ solar cells, with an interaction energy (ΔE_{int}) in the range of −16 to −18 kcal.mol^{-1}.[12] However, such ternary blends present several disadvantages. First, the energy offsets between the polymer, the dye and the fullerene have to match carefully in order to allow efficient charge separation. Besides, the miscibility of the three components is difficult to control, thus inducing inadequate nanoscale morphology and photoinduced charge transfer at the donor–acceptor interfaces. To overcome this problem, the dye can be directly incorporated into the polymer backbone.[13] As discussed in Chapter 1, Kumada Catalyst Transfer Polycondensation (KCTP) method allows easy side-chain and chain-end functionalization of **P3HT**.[14] In this context, the functionalization of **P3HT** end-groups and side-chains with porphyrins was envisaged to study its impact on the optical, thermal and morphological properties of the polymer as well as on its photovoltaic performances (Figure 2.2).

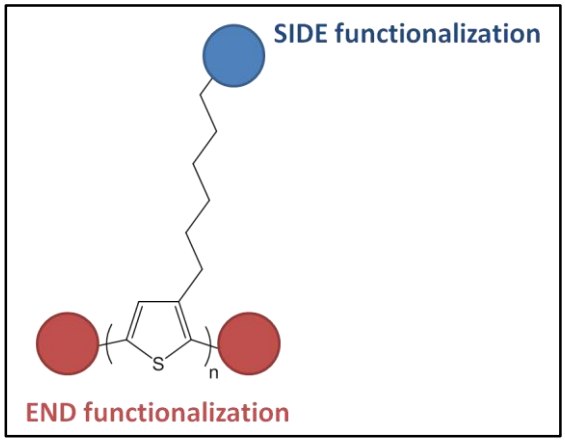

Figure 2.2 Schematic representation of the side-chain and end-group functionalization of **P3HT**.

Porphyrin-containing conjugated polymers have been widely studied for applications in polymer solar cells.[13,15] Torres and co-workers have reported for example, the “click” side-chain functionalization of a **P3HT**-based alkynyl-terminated copolymer with phthalocyanines, leading to broadened absorption window of the polymer material. Unfortunately, the moderate solubility of the resulting polymers induced poor nanoscale organization in the photoactive layer, thus resulting in low charge transport and PCE.[13a] Commonly, although porphyrin-containing conjugated polymers exhibit broadened absorption spectra, significant enhancement of the PCE has not been reached to date. Low short-circuit current densities (J_{SC}) and fill factors (FF) were obtained, which are mainly due to the non-optimal morphology of the active layer.[15c]

Indeed, porphyrins have a natural tendency to aggregate which can thus alter the morphology of thin polymer films, negatively impacting the transport of photogenerated charges and decreasing the PCE. Consequently, developing new porphyrin-containing conjugated polymers remains a major challenge.

In this chapter, two strategies will be developed for combining porphyrins with **P3HT**: both involving the functionalization of the polymer backbone (Figure 2.3).[16]

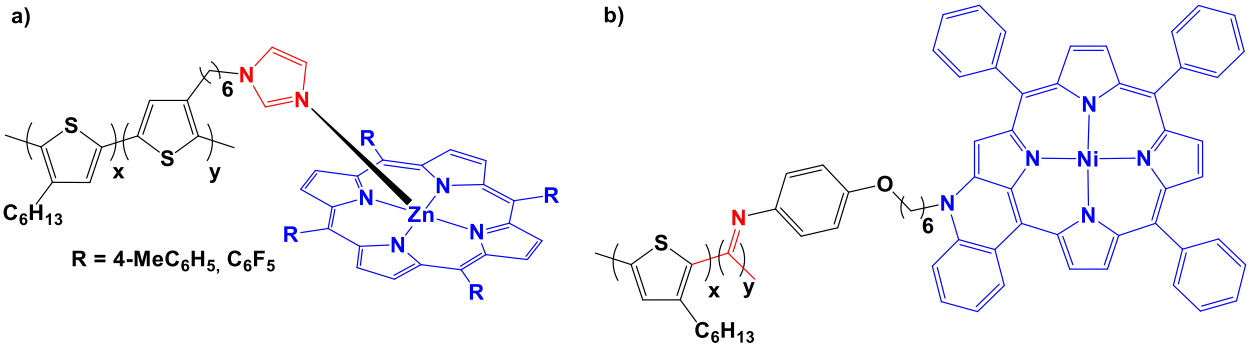

Figure 2.3 Structures of the porphyrin-polythiophene polymers studied in this chapter.

In the first strategy, two porphyrin-containing **P3HT**-type conjugated copolymers were synthesized using a supramolecular approach.[17] This supramolecular strategy is based on the coordination of the central zinc ions of metalloporphyrins to a polythiophene copolymer bearing imidazole ligand (Figure 2.3, a). This coordination strategy has been successfully used previously to prepare porphyrin–fullerene dyads with an ultrafast photoinduced electron transfer from the porphyrin to the fullerene. Since **P3HT** absorbs up to around 600 nm, porphyrins having an absorption profile in the near IR region (> 700 nm) should be chosen in view of expanding the light-absorption of the polymer. Nevertheless, to validate our approach, we decided to focus our attention on common porphyrins with absorption around 600 nm:

(i) the (5,10,15,20-tetrakis(phenyl)porphyrinato)zinc(II) (**1Zn**),

(ii) and the (5,10,15,20-tetrakis(pentafluorophenyl)porphyrinato)zinc(II) (**2Zn**). The choice of **2Zn** was motivated by the improved charge separation and relatively slower charge recombination observed in fluorinated zinc porphyrin–fullerene supramolecular dyads, which is expected to be beneficial for photovoltaic applications.[18,19]

To reach a compromise between the solubility of the material and enhanced absorption, the molar content of porphyrin units has been set to around 10 %.[13a,15a]

In the second approach, **P3HT** was end-functionalized with a controllable number of π-extended porphyrin units using chain-growth polymerization methods (Figure 2.3, b). Takashi *et al.* previously reported that aryl isocyanide bearing a porphyrin pendant group can be converted quantitatively into the corresponding poly(aryl isocyanide).[20] More recently, well-defined block copolymers containing **P3HT** and poly(isocyanide) blocks were synthesized in a one-pot

procedure.[21] Although the two block polymerizations are mechanistically distinct, the successive polymerization mediated by a common catalyst proceeded in a controlled manner and led to block copolymers with tunable molecular weights and compositions. Herein, by combining these strategies, the modification of the **P3HT** end-groups by π-extended porphyrins was pursued. To ensure good solubility of the final material, we have decided to limit the number of porphyrin units attached to the **P3HT** to around 3-4 molecules per **P3HT** chain.

In this chapter, we will describe the synthesis and the characterization of **P3HT**-porphyrin polymers prepared by side-chain and chain-end functionalization of **P3HT**. Their optical, thermal and morphological properties as well as their photovoltaic performance when used in the active layer in BHJ solar cells will be studied.

1. REGIOREGULAR POLYTHIOPHENE-PORPHYRIN SUPRAMOLECULAR COMPLEXES

Before coordinating zinc porphyrins **1Zn** and **2Zn** to the **P3HT** random copolymer bearing imidazole ligands (**P3HT-*r*-P3HTIm**), 3-[6′-(1″-imidazolyl)hexyl]thiophene-zinc porphyrin dyads **TIm-1Zn** and **TIm-2Zn** were synthesized as model compounds to gain information on the coordination mechanism (Scheme 2.1). As 3-[6′-(1″-imidazolyl)hexyl]thiophene (**TIm**) corresponds to the thiophene monomer unit bearing an imidazole ligand in the **P3HT** copolymer, this model study enabled us to determine more easily the complex stoichiometry and the binding constant of the polythiophene-porphyrin supramolecular complexes.

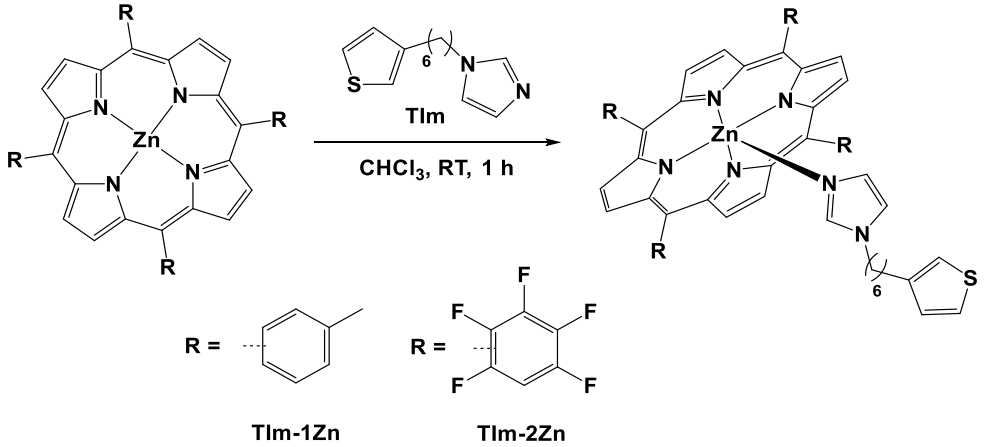

Scheme 2.1 Synthesis of model compounds: **TIm-1Zn** and **TIm-2Zn**.

1.1. SYNTHESIS OF ZINC PORPHYRINS

Porphyrins **1Zn** and **2Zn** were synthesized using Adler[22] and Lindsey[23] methods, respectively (Scheme 2.2). The reaction of *p*-tolualdehyde with pyrrole in propionic acid under reflux for 2 hours afforded the free-base **1** in 16 % yield after filtration and several washing steps with methanol (MeOH) (Scheme 2.2, a). The free-base **2** was obtained in a 54 % yield by

condensation of pyrrole with 2,3,4,5,6-pentafluorobenzaldehyde in presence of a catalytic amount of a Lewis acid ($BF_3.OEt_2$), followed by oxidation with 2,3-dichloro-5,6-dicyano-1,4-benzoquinone (DDQ) (Scheme 2.2, b).

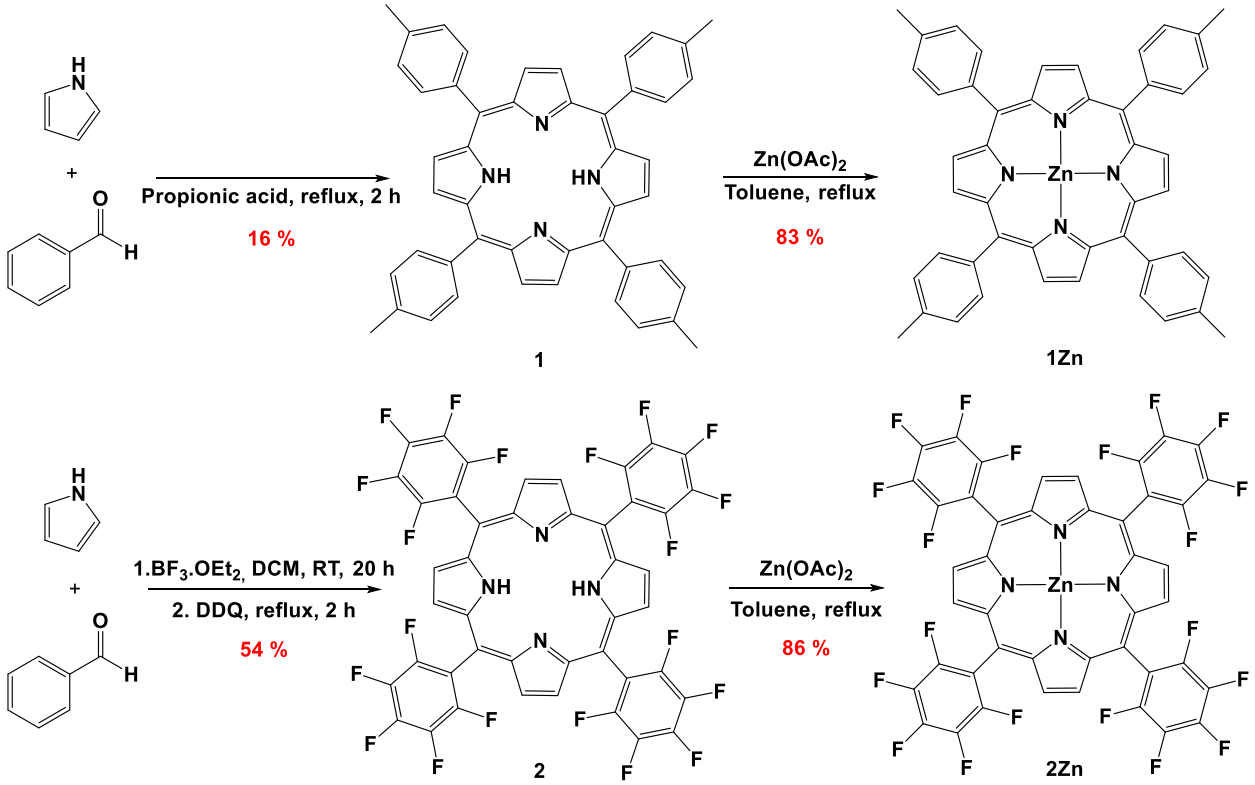

Scheme 2.2 Synthesis of free-base and the corresponding zinc porphyrins a) **1** and **1Zn** and b) **2 and 2Zn.**

The ^{1}H NMR spectra of the free-base porphyrins **1** and **2** exhibit a large signal at around -3 ppm and a singlet around 8-9 ppm, characteristic from the internal and pyrrolic protons, respectively.[24] Indeed, the π-delocalized electron system of the porphyrin macrocycle leads to a strong ring current in the molecules placed in the NMR external magnetic field. This ring current gives rise to a strong anisotropic shielding effect of the protons located in its action (Figure 2.4). Due to this anisotropic effect, the deshielded *meso* protons (protons on the bridging methine carbons) show low field shift, whereas the shielded protons on the inner nitrogen atoms resonate at very high field in the ^{1}H NMR spectrum.

The optical properties of the free-base porphyrins **1** and **2** were analyzed by UV-visible (UV-vis) spectroscopy, showing a strong band at around 420 nm, *i.e.* the Soret band, and four bands between 500 and 650 nm, *i.e.* the Q bands.[25] **1** and **2** were then metalated with zinc acetate ($Zn(OAc)_2$) in toluene under reflux, leading to **1Zn** and **2Zn** in 83 and 86 % yields, respectively (Scheme 2.2). The progress of the metalation reaction was monitored by ^{1}H NMR and UV-vis absorption spectroscopies. The broad singlet observed in the ^{1}H NMR spectrum around -3 ppm, characteristic of the inner NH protons, disappeared upon metalation. In

addition, due to the gain of symmetry, the UV-vis absorption spectrum of zinc porphyrins 1Zn and 2Zn showed a decreased number of Q bands going from 4 for free-base porphyrins to 2 for zinc-metalated porphyrins.

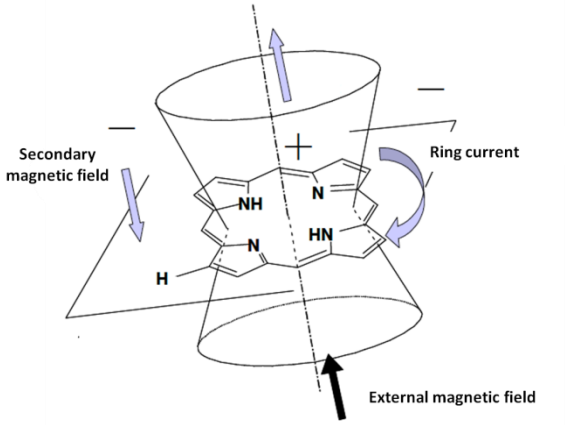

Figure 2.4 Anisotropic shielding effect of the porphyrin.

1.2. Synthesis of 3-[6′-(1″-imidazolyl)-hexyl]thiophene-Zinc Porphyrin Dyads

3-[6′-(1″-imidazolyl)hexyl]thiophene (**TIm**) was synthesized in a 87 % yield by reacting the imidazolide anion formed *in situ* with 3-(6′-bromohexyl)thiophene[26] in THF (Scheme 2.3).

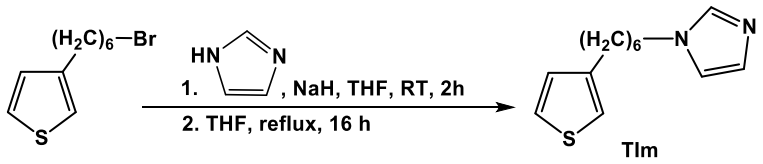

Scheme 2.3 Synthesis of 3-[6′-(1″-imidazolyl)hexyl]thiophene (**TIm**).

The success of this nucleophilic substitution reaction was attested by ^{1}H NMR spectroscopy. Indeed, the triplet at 3.45 ppm, characteristic of the CH_2Br group disappeared and three signals appeared in the aromatic region at 6.85, 6.97 and 7.35 ppm, corresponding to the imidazole ring. The formation was also supported by the presence of a peak at 235.1 Da ($[M+H]^+$) in the electron spray ionization (ESI) mass spectrum.

Then, one equivalent of zinc porphyrin (**1Zn** or **2Zn**) was added to a solution of **TIm** affording **TIm-1Zn** and **TIm-2Zn** dyads in quantitative yields (Scheme 2.1). The ^{1}H NMR spectra of the dyads **TIm-1Zn** and **TIm-2Zn** revealed a significant upfield shift (3–5 ppm) of the imidazole ligand protons owing to the influence of porphyrin ring current effects, consistent with the dyad formation.[27] Dyad formation was also confirmed by electron spray ionization (ESI) mass spectrometry, in which the *m/z* = 966 peak, corresponding to the sum of the molecular weights of **TIm** (*m/z* = 234) and **1Zn** (*m/z* = 732), was observed. A peak at *m/z* = 1270 was observed for **TIm**-**2Zn** (*m/z* = 1036 for **2Zn**). Besides, the mass spectra displayed no other adduct, confirming the 1:1 stoichiometry for these dyads.

Single crystals of the **TIm**-**1Zn** and **TIm**-**2Zn** dyads were grown from chloroform/*n*-hexane mixtures to gain insight into the packing and to learn more about the nature of the intermolecular interactions. As an example, the molecular structure of **TIm-1Zn** established by single crystal X-ray diffraction analyses is shown in Figure 2.5.

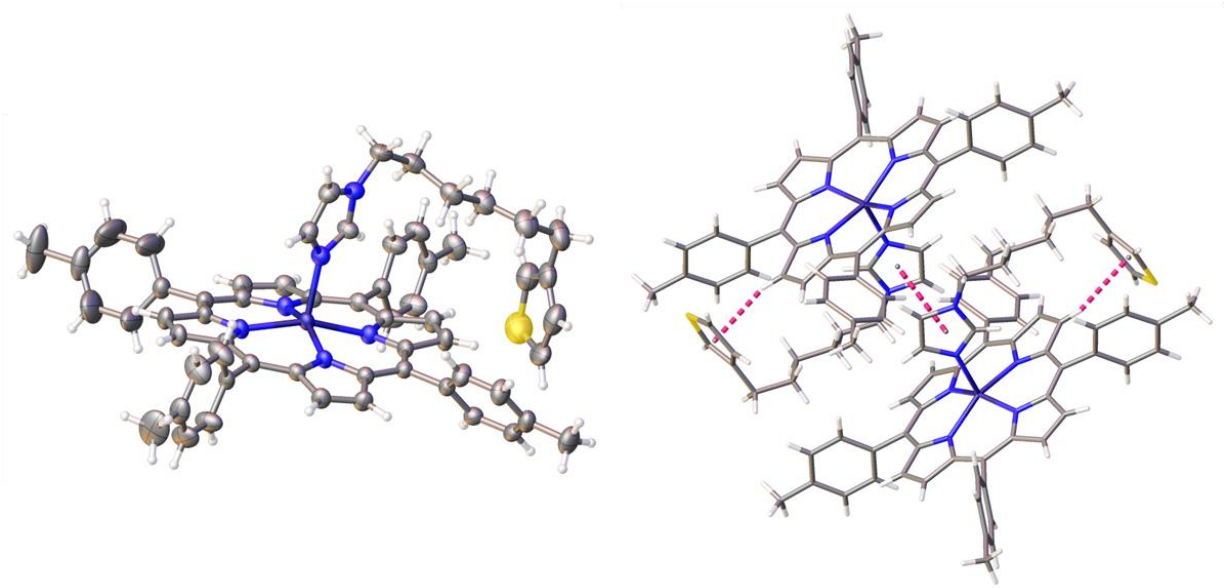

Figure 2.5 Single crystal structure of **TIm-1Zn** (left) and view of the intermolecular interactions present in **TIm-1Zn** (right).

The crystallographic data of **TIm-1Zn** support the formation of **TIm**:**1Zn** complex in a 1:1 ratio. In the crystal structure, the zinc atom is penta-coordinated, *i.e.*, with four pyrrolic nitrogen atoms and the nitrogen atom of the imidazole ring, thus inducing a square pyramid geometry. As a result, the zinc ion is located ≈ 0.4 Å above the plane defined by the four pyrrolic nitrogen atoms. The Zn–N distance is found to be 2.11; this value is slightly larger than in the pristine macrocycles (2.08 Å on average). This finding confirms that an interaction occurs between the imidazole ligand and the zinc metal center of the porphyrin. The same conclusions can be drawn for **TIm-2Zn**, for which a value of 2.09 Å was found for the Zn-N distance. As observed in the crystal structures of the two complexes, the alkyl chain of **TIm** is endocyclic with respect to the macrocycle, thus explaining why the protons of the imidazole ring are observed at very high field in the ^{1}H NMR spectra.

Finally, by investigating in more details the crystallographic data of **TIm-1Zn**, several intermolecular interactions were noticed. A C–H–π interaction between a pyrrolic C–H and the thiophene ring, with a distance between the hydrogen atom and the center of the thiophene ring of about 2.83 Å, was revealed. A π-π interaction between imidazole rings is also observed with a centroid–centroid distance of 3.77 Å. In the case of **TIm-2Zn**, a short centroid–centroid distance between thiophene and pentafluorophenyl rings (3.98 Å) was observed, indicating the

presence of thiophene-pentafluorophenyl interactions.[28] In contrast to **2Zn**, no short intermolecular contacts between zinc and fluorine atoms were detected, which may be related to the presence of solvent molecules ($CHCl_3$) in the **TIm-2Zn** dyad. However, the inclusion of these solvent molecules led to the formation of Cl…F halogen bonds, as indicated by of the fact that the distance between the halogen atoms is shorter than the sum of the van der Waals radii.

The interactions between **TIm** and zinc porphyrins **1Zn** and **2Zn** were then studied in solution in toluene using UV-vis absorption spectroscopy (Figure 2.6). This solvent was chosen because it does not solvate the zinc ion and does not interfere with the ability of the zinc ion to coordinate an additional molecular ligand.[29] The unbound zinc porphyrins exhibit a strong UV–vis absorption band at 419 nm and 424 nm for **1Zn** and **2Zn** respectively, corresponding to the Soret band, and two Q bands at 551 and 590 nm for **1Zn** and 546 and 580 nm for **2Zn**, respectively. Upon addition of **TIm** in a solution of **1Zn** or **2Zn**, the Soret and Q bands were redshifted and isobestic points were clearly observed, indicating the axial coordination of the zinc ion.[30] The UV-vis absorption spectra of **1Zn** after successive addition of **Tim** are shown as an example in Figure 2.6.

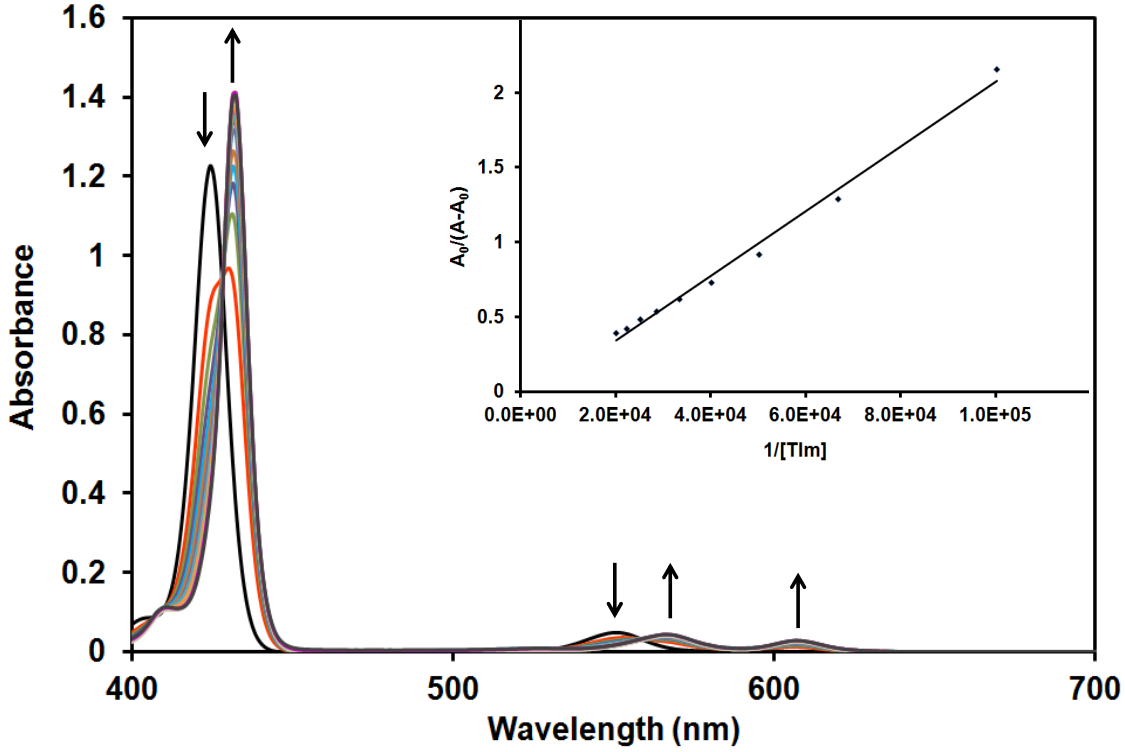

Figure 2.6 UV-vis absorption spectra of **1Zn** after successive addition of **TIm** and determination of the association constant for the complex **TIm-1Zn** using Benesi−Hildebrand plot (inset) in toluene.

Such spectral changes are in good agreement with the formation of a 1:1 complex.[25] By monitoring the decrease in the absorption of the unbound porphyrin and the increase in the

absorption of the bound porphyrin, the binding constant can be determined from UV-vis absorption titrations by constructing the Benesi–Hildebrand plots (Figure 2.6, inset)

$$\frac{1}{A_{c1}-A_0} = \frac{1}{A'-A_0} + \frac{1}{K(A'-A_0)C_{Imd}}$$

where A_{C1} is the absorbance of the complex after adding x equivalents of **TIm**, A' is the maximum absorbance of the complex and A_0 is the absorbance of the porphyrin before adding **TIm**.[31] Binding constants for dyad formation of 4 600 and 7 200 M^{-1} were found for **TIm**-**1Zn** and **TIm**-**2Zn**, respectively. These binding constants are in the same range as those reported in the literature for zinc porphyrin–imidazole complexes (around 10^3–10^4 M^{-1}). As expected, zinc porphyrin **2Zn** with electron-withdrawing fluorinated substituents binds the imidazole ligand more effectively than **1Zn**.[32]

1.3. Synthesis of Polythiophene-Porphyrin supramolecular copolymers

1.3.1. Synthesis of the **P3HT-*r*-P3HTIm** copolymer

Once the supramolecular approach was successfully proven for the model compounds, porphyrins **1Zn** and **2Zn** were coordinated to a polythiophene random copolymer bearing imidazole ligands in a proper molar ratio (*i.e.*, around 10 %) on the side chains. As discussed above, an appropriate content of porphyrins may lead to enhanced photocurrent generation by simultaneous photoexcitation of the porphyrins. Thus, a polythiophene copolymer containing 10 % of appended imidazole moieties was synthesized by a two-step procedure. In a first step, a regioregular head-to-tail bromide-bearing polythiophene random copolymer (**P3HT-*r*-P3HTBr**) was prepared via the Kumada Catalyst Transfer Polycondensation from a mixture of 2-bromo-3-hexyl-5-iodothiophene and 2,5-dibromo-3-(6'-bromohexyl)thiophene (Scheme 2.4,a).[33]

First, each thiophene monomer was transmetalated using isopropylmagnesium chloride (iPrMgCl) in THF at 0°C for around 30 minutes; the completion of the transmetalation was followed by Thin Layer Chromatography (TLC). Then, the polymerization was initiated by transferring the formed Grignard reagents onto a catalytic amount of Ni(dppp)Cl_2 in suspension in THF. The reaction mixture was stirred overnight at 4°C and then, quenched with 5M HCl aqueous solution, following the procedure described by Yokozawa and co-workers.[34] As discussed in Chapter 1, this quenching procedure allows preventing the polymer chains from undergoing dimerization in order to maintain the narrow dispersity while efficiently removing inorganic impurities from the product. After 30-minute stirring, the solution was poured into cold methanol and the precipitated polymer was collected by filtration. Low molecular weight fractions were removed by Soxhlet washing using appropriate solvents. SEC analysis of the **P3HT-*r*-P3HTBr** precursor displayed a number-averaged molecular weight (M_n) of 23 800 $g.mol^{-1}$ with a narrow dispersity (Đ = 1.17). The composition of the **P3HT-*r*-P3HTBr** copolymer was determined from its ^1H NMR spectrum by integrating the peaks observed at δ 0.92 (CH_3 groups in **3HT**) and 3.42 ppm (CH_2Br groups in **3HTBr**) (Figure 2.7, top). From the integration of

those two peaks, the molar ratio of the **3HT** and **3HTBr** segments was estimated to be 90:10 (feed ratio 88:12).[35]

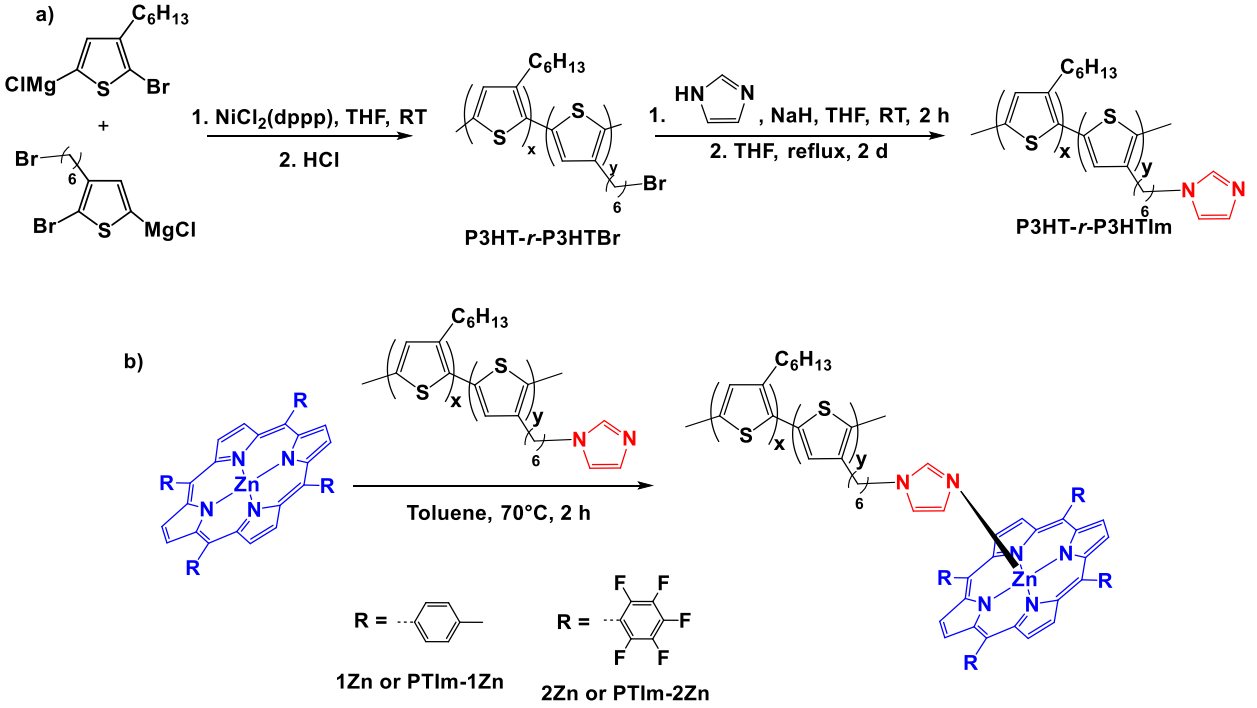

Scheme 2.4 Syntheses of a) random copolymer **P3HT-*r*-P3HTIm** and b) supramolecular polymers **PTIm-1Zn** and **PTIm-2Zn**.

In a second step, the bromine atom at the end of the alkyl side chain was converted into an imidazole moiety in THF by reaction of **P3HT-*r*-P3HTBr** with the imidazolide anion formed *in situ*, as carried out for the model compound. The conversion of the **P3HT-*r*-P3HTBr** copolymer into the corresponding **P3HT-*r*-P3HTIm** copolymer was followed using ^{1}H NMR spectroscopy. The disappearance of the signal at 3.42 ppm, characteristic from CH_2Br groups, and the appearance of additional signals at 6.82, 6.99, and 7.42 ppm, corresponding to the imidazole ring, were observed (Figure 2.7, bottom). Attempts of SEC analysis in various solvents such as THF, $CHCl_3$, chlorobenzene at room temperature and at 145 °C were unsuccessful for this polymer. As the NMR spectra were successfully recorded, it is suspected that there are adsorption effects between the sample and the SEC column due to the imidazole functionality. Analysis by MALDI-ToF mass spectrometry were also unsuccessful, due to the high molecular weight of **P3HT-*r*-P3HTIm**.

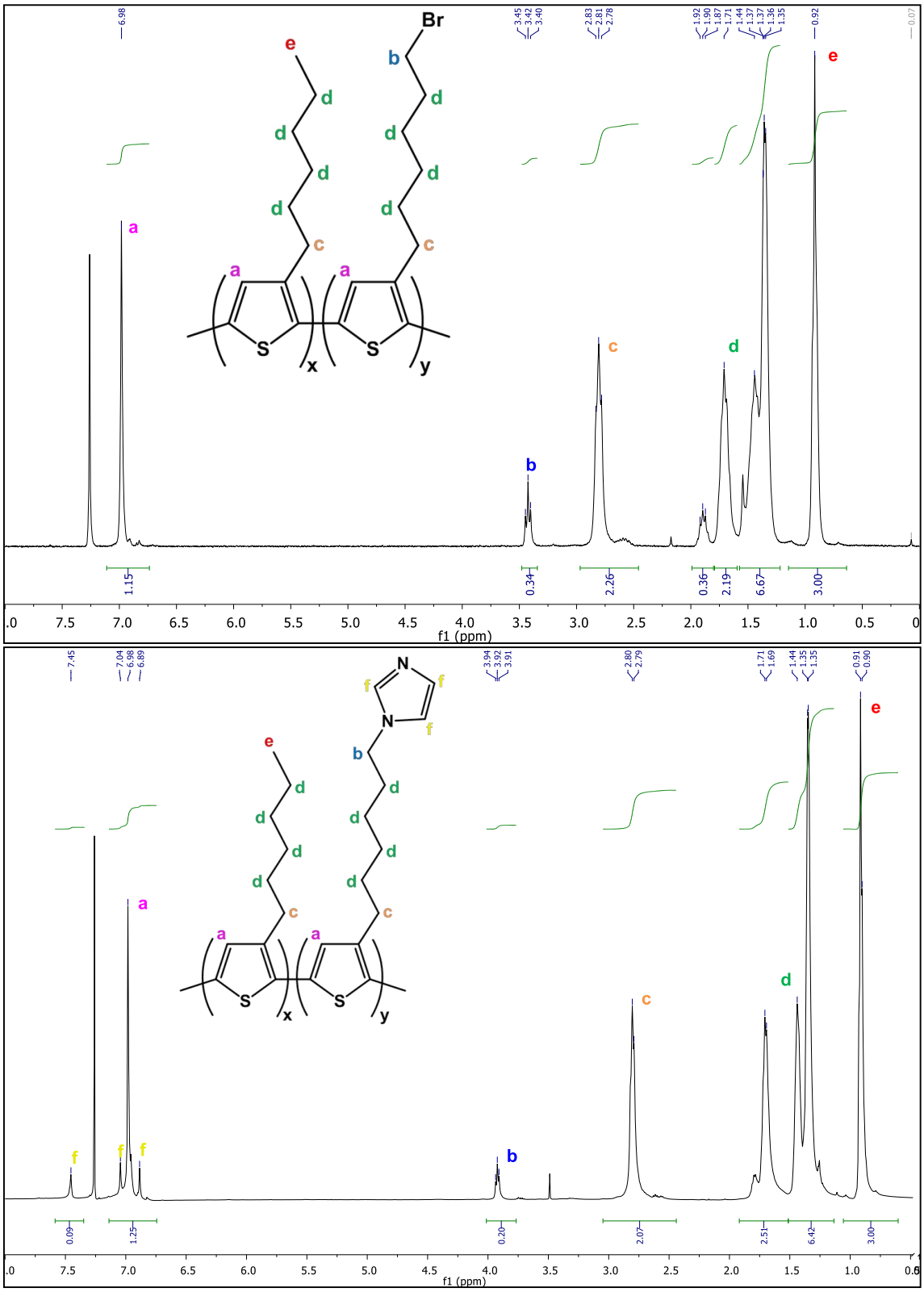

Figure 2.7 ^{1}H NMR spectra of **P3HT-*r*-P3HTBr** (top) and **P3HT-*r*-P3HTIm** (bottom) in $CDCl_3$.

1.3.2. COMPLEXATION BETWEEN ZINC PORPHYRINS AND **P3HT-*r*-P3HTIM**

With **P3HT-*r*-P3HTIm** in our hands and based on the results obtained with the model compounds, complexation of **1Zn** and **2Zn** was performed in a 1:1 ratio, calculated on the basis of the 3-[6'-(1"-imidazolyl)hexyl]thiophene monomer unit (Scheme 2.4, b). The corresponding **PTIm-1Zn** and **PTIm-2Zn** materials were obtained in quantitative yields. The efficiency of the complexation was monitored by ^{1}H NMR spectroscopy. In the ^{1}H NMR spectrum, the signal of the terminal methylene group connected to the imidazole ring in **P3HT-*r*-P3HTIm** was shifted upon complexation (Figure 2.8). As observed for model compounds **TIm-1Zn** and **TIm-2Zn**, the imidazole protons are shifted upfield due to the influence of porphyrin ring current effects. From the integration of the signals at ≈8.85 ppm, corresponding to the pyrrolic hydrogens of the porphyrin and at ≈ 0.90 ppm corresponding to the CH_3 groups of **3HT moiety**, the molar ratio copolymer: porphyrin was estimated to be ≈ 90:10. This result clearly indicates that all the imidazole groups in **P3HT-*r*-P3HTIm** have complexed the porphyrins **1Zn** and **2Zn**.

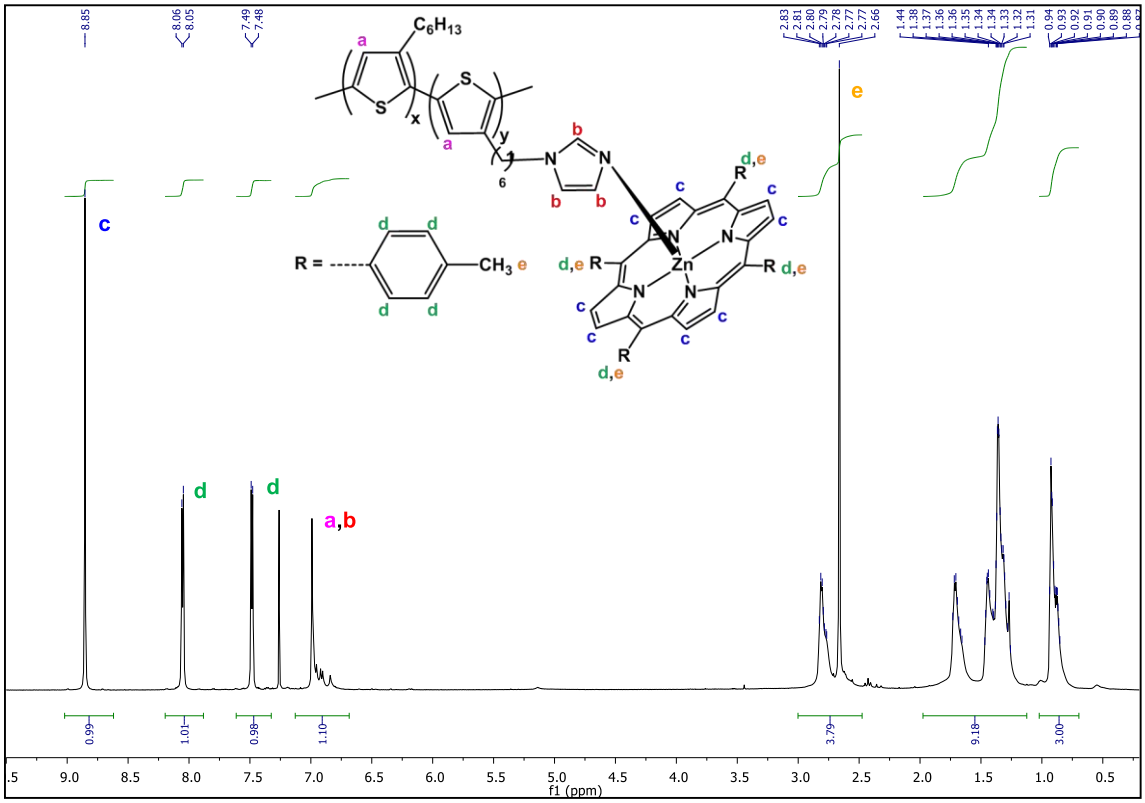

Figure 2.8 ^{1}H NMR spectrum of supramolecular polymer **PTIm-1Zn** in $CDCl_3$.

1.4. PROPERTIES OF THE SUPRAMOLECULAR COPOLYMERS

1.4.1. OPTICAL PROPERTIES

The complexation of **1Zn** and **2Zn** by random copolymer **P3HT-*r*-P3HTIm** was studied by UV–vis absorption spectroscopy in toluene. The UV-vis absorption spectra obtained of **1Zn** after successive addition of **P3HT-*r*-P3HTIm** are shown as examples in Figure 2.9. As observed for

model compounds **TIm-1Zn** and **TIm-2Zn**, a gradual redshift of the Q bands and the presence of isobestic points upon complexation were observed unambiguously indicating the formation of the supramolecular polymers **PTIm-1Zn** and **PTIm-2Zn**.[27a] With respect to pristine **P3HT,** supramolecular polymers **PTIm-1Zn** and **PTIm-2Zn** exhibit UV–vis absorption spectra extended into the 550 - 650 nm region, due to the Q band absorption of the porphyrins complexed to the side chains of the copolymers.

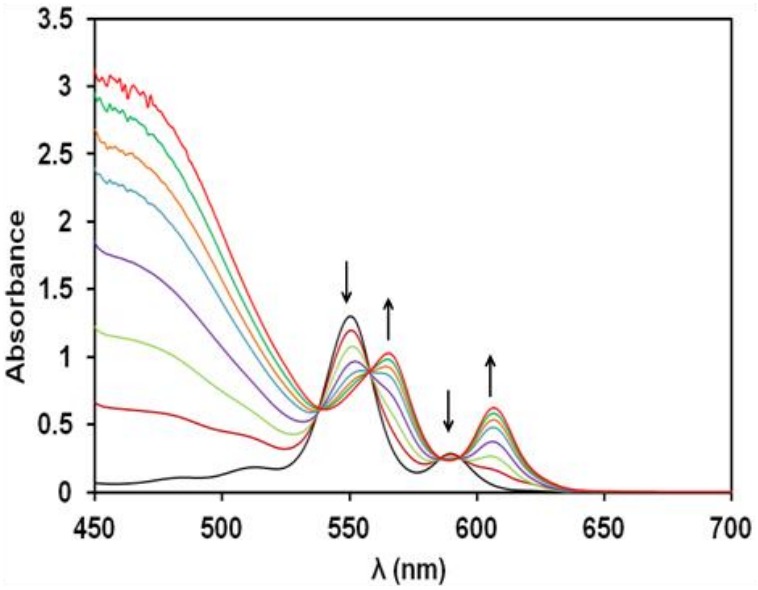

Figure 2.9 UV–vis absorption spectra of **1Zn** after successive addition of **P3HT-*r*-P3HTIm** in toluene.

To further investigate the optical properties of these complexes, photophysical studies were carried out in collaboration with Dr. Rachel C. Evans and Camille Blayo (PhD student) from Trinity College of Dublin (Ireland). The normalized UV–vis absorption and emission spectra of the individual components **2Zn** and **P3HT-*r*-P3HTIm** in dilute solution are shown in Figure 2.10 as examples. The absorption spectrum of **2Zn** is dominated by the intense Soret band at 420 nm with two weaker bands at 545 nm and 580 nm. Excitation into the Soret band resulted in a strong singlet emission band, exhibiting two well-resolved transitions at 587 nm and 642 nm. The absorption and emission spectra of **P3HT-*r*-P3HTIm** are typical of polythiophenes with maxima centered at 453 and 580 nm, respectively. The vibronic structure observed in the emission spectrum ($\Delta E \approx 0.13$ eV) is assigned to the vibronic progression of the C=C stretching mode.[36]

A significant spectral overlap, *i.e.* the grey filled area in the Figure 2.10, of the Q absorption bands of **2Zn** with the emission band of **P3HT-*r*-P3HTIm** is observed, suggesting that an energy transfer from polythiophene to porphyrin may occur in this system. Excitation at 420 nm will normally sensitize both **2Zn** and **P3HT-*r*-P3HTIm**. However, the huge oscillator strength of the Soret band for metalloporphyrins ($f \approx 1$) suggests that the porphyrin will be the primary

absorber at this wavelength for **PTIm-2Zn**.[37] In contrast, excitation at 450 nm enables selective excitation of **P3HT-*r*-P3HTIm**.

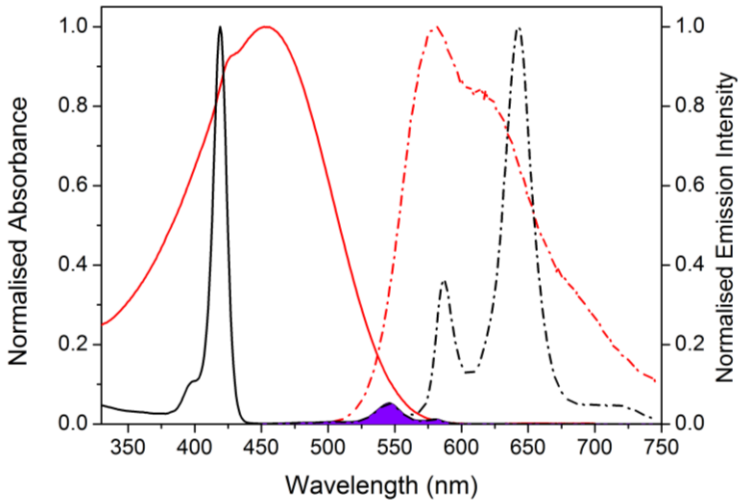

Figure 2.10 Normalized UV–vis absorption (solid lines) and emission (dashed lines) spectra of **2Zn** (black lines, C = 1.1 × 10^{-6} M in toluene) and **P3HT-*r*-P3HTIm** (red lines, C = 4.4 µg.mL^{-1} in chloroform) recorded upon excitation at 420 and 450 nm, respectively.

The photoluminescence emission and excitation spectra obtained for **PTIm-2Zn** as a function of concentration (from 0.08 to 1.36 × 10^{-6}M in toluene) are shown in Figure 2.11. Upon excitation at 420 nm, a broad emission band, with maxima at 585 and 645 nm, is observed, characteristic of the porphyrin emission. Besides, the emission profile is significantly broadened compared to the pure **2Zn**, indicating that **P3HT-*r*-P3HTIm** also provides a contribution. When the concentration is increased, strong quenching (99 %) of the fluorescence emission is observed due to the porphyrin aggregation, even at rather low concentrations in solution, which often leads to fluorescence quenching.[38] Excitation at 450 nm leads to a broad emission band with peak maxima at 582 and 657 nm. This emission profile is also reminiscent of the porphyrin, except for the lowest concentration, where the emission spectrum is very similar to that of the polymer. Since only **P3HT-*r*-P3HTIm** absorbs light at 450 nm, this observation suggests that energy transfer from **P3HT** to **2Zn** should occur at concentrations above 0.08 µM. As the concentration is increased from 0.08 to 0.12 µM, the intensity of the Q band at 582 nm initially increases, before subsequently decreasing with increasing sample concentration up to 1.36 µM. The energy transfer efficiency depends not only on the spectral overlap of the donor and acceptor moieties but also on their proximity.[39] The similarity of the photoluminescence spectrum to that of the parent **P3HT-*r*-P3HTIm** at the lowest concentration studied (Figure 2.11, b, solid black line) suggests that intramolecular energy transfer between the polymer and the porphyrin is absent. As the concentration is increased, the initial increase in the porphyrin emission (≈ 657 nm) intensity is thus attributed to enhanced intermolecular energy transfer due

to a decrease polythiophene-porphyrin distance, which effectively quenches the **P3HT** contribution. At higher concentrations, the fluorescence quenching becomes more important due to porphyrin aggregation. Further evidence for energy transfer can be obtained from the corresponding excitation spectrum (Figure 2.11, c). In dilute solution, the excitation spectrum measured at 650 nm is similar to the UV–vis absorption spectrum, clearly exhibiting the Soret and Q bands at 420 and 540 nm, respectively, along with a broader band contribution from **P3HT-*r*-P3HTIm**. However, as the concentration is increased to 1.36 μM, bleaching of the Soret band is accompanied by the emergence of two distinct peaks at 402 and 450 nm. The wavelength maximum and shape of the latter peak are characteristic of the polythiophene absorption band, suggesting that **P3HT** to **2Zn** energy transfer also occurs. The inversion of the Soret band and the emergence of new bands at higher energy in the excitation spectrum have previously been attributed to the formation of H- or J-type aggregates through π–π stacking interaction.[40] Since H-aggregates typically exhibit blue-shifted excitation bands and are typically non- or weakly fluorescent, **PTIm-2Zn** may form this class of aggregate. At higher concentrations, the Q band at 546 nm becomes more prominent in the excitation spectrum, supporting the observation that self-absorption also contributes to the decrease in the fluorescence intensity.

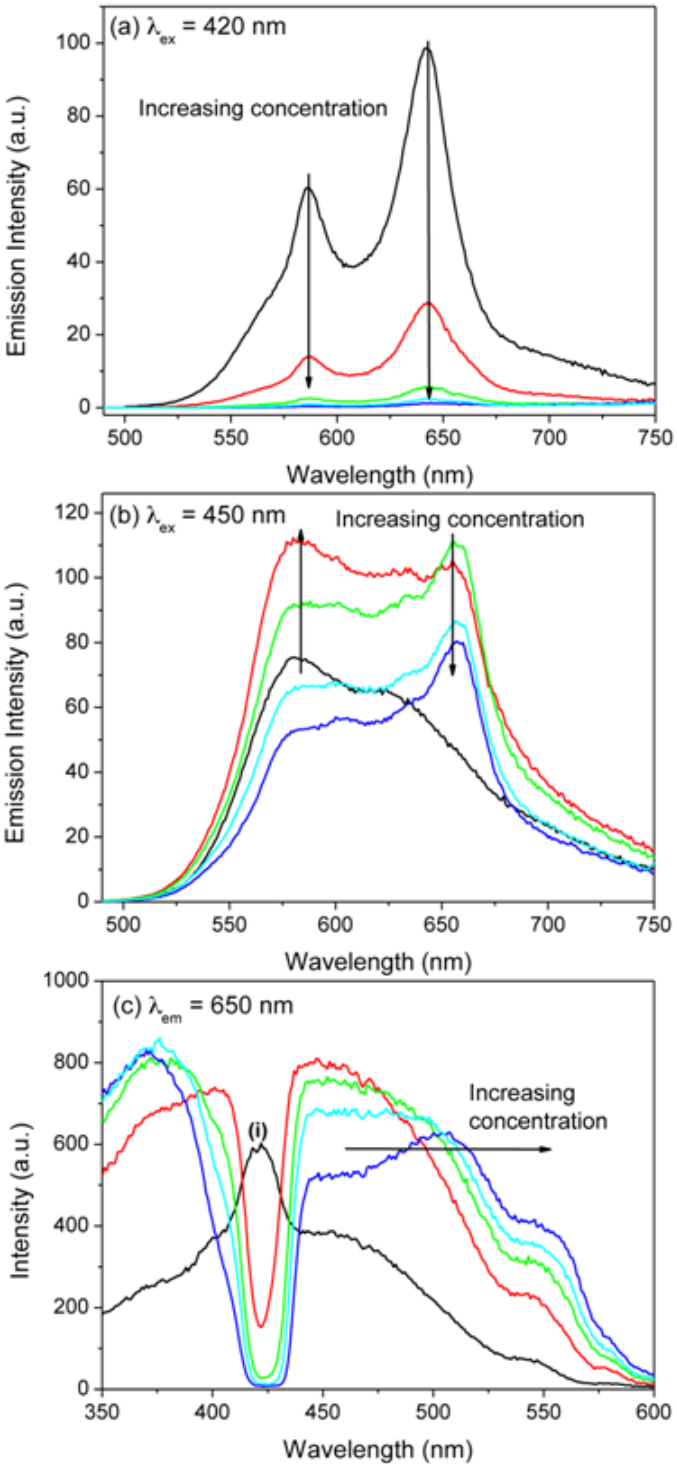

Figure 2.11 Concentration dependence of the steady-state photoluminescence properties of **PTIm-2Zn** in toluene (C = 0.08 μM (black), 0.12 μM (red), 0.49 μM (green), 0.87 μM (light blue), 1.36 μM (dark blue).

To investigate the self-assembly of the polymer chains in the solid-state, the UV–vis absorption spectra of **P3HT-*r*-P3HTIm**, **PTIm-1Zn**, and **PTIm-2Zn** in films were recorded (Figure 2.12). The solid-state spectrum of **P3HT-*r*-P3HTIm** exhibits a bathochromic shift of the absorption maximum attributed to the π–π* transition in the polymer main chain at 550 nm as well as a vibrational structure, which is quite similar to neat **P3HT**.[41] The presence of a shoulder at about 620 nm is assigned to the vibronic progression of the C=C stretching mode (ΔE ≈ 0.15 eV).[36] In the case of **PTIm-1Zn** and **PTIm-2Zn**, a strong contribution of the absorption of the porphyrins was observed at around 420 nm (Soret band) and between 550 and 650 nm (Q bands). Compared to **P3HT-*r*-P3HTIm**, the **P3HT** absorption in **PTIm-1Zn** and **PTIm-2Zn** dyads is blue-shifted (≈ 520 *vs.* 550 nm for **P3HT-*r*-P3HTIm**) indicating that the presence of porphyrins in the side chains disturbs the polymer organization and thus, decreases the effective conjugation length.

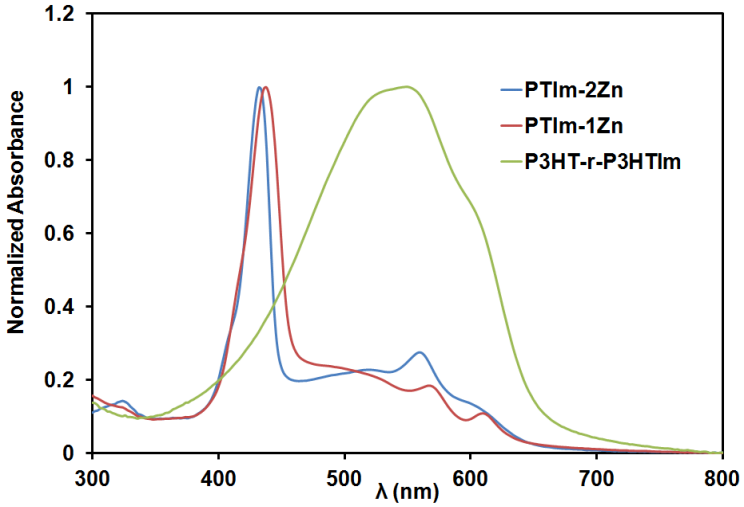

Figure 2.12 UV-vis absorption spectra of thin films of **P3HT-*r*-P3HTIm**, **PTIm-1Zn** and **PTIm-2Zn** drop-cast from solutions in toluene (C = 5 mg.mL^{-1}).

1.4.2. THERMAL PROPERTIES

The thermal properties of supramolecular copolymers **PTIm-1Zn** and **PTIm-2Zn** were examined by TGA and DSC measurements.

As indicated by the TGA curves, supramolecular copolymers **PTIm-1Zn** and **PTIm-2Zn** exhibit high thermal stability, with 5 % weight loss temperature (T_d) around 420 and 330 °C, respectively.

The DSC analyses showed different thermal behavior depending on the nature of the porphyrin complexed to **P3HT-*r*-P3HTIm** (Table 2.1). **PTIm-1Zn** exhibited indeed a clear first-order transition with a melting temperature (T_m) at 194 °C and crystallization temperature (T_c) at 140 °C, which are lower than the melting and crystallization temperatures of pristine **P3HT** (T_c = 200 °C and T_m = 210 °C).[42] In contrast, no melting and crystallization peaks were detected for

polymer **PTIm-2Zn**, suggesting that this polymer is amorphous. These results are consistent with the conclusion drawn from UV–vis absorption spectra described above (Figure 2.12).

Table 2.1 Melting and crystallization temperatures (T_m and T_c, respectively, in °C) of **P3HT** and supramolecular copolymers.

	P3HT	PTIm-1Zn	PTIm-2Zn
T_c	191	149	-
T_m	224	194	-

1.4.3. Morphological Properties

The microscopic morphology of **PTIm-1Zn** and **PTIm-2Zn** in thin films was analyzed by tapping-mode atomic force microscopy (TM-AFM). The samples were prepared by drop casting polymer solutions (around 0.1 mg.mL^{-1} in xylene) onto mica substrates, followed by solvent annealing. Xylene was used as solvent because in these film deposition conditions, neat **P3HT** is known to form fibrillar nanostructures,[43] as a result of the π-stacking of the polythiophene backbones and the lateral interdigitating of the alkyl groups.[44]

Thin films of **PTIm-1Zn** from xylene solutions showed fibrillar nanostructures having a width around 20 nm, in the range of what is observed for fibrils of neat **P3HT**, but with a shorter length and higher roughness (Figure 2.13, left). In contrast, thin films of **PTIm-2Zn** were relatively flat and exhibit no fibrillar morphology (Figure 2.13, right). These results are in agreement with the thermal characterization of the polymers, where crystallization was only observed for the copolymer **PTIm-1Zn**. The reduction or lack of crystalline order (*i.e.,* fibrillar morphology) in these polymers could be a drawback for their use as electron donor materials in BHJ organic solar cells, since the formation of ordered nanostructures is crucial for efficient hole transport.[45]

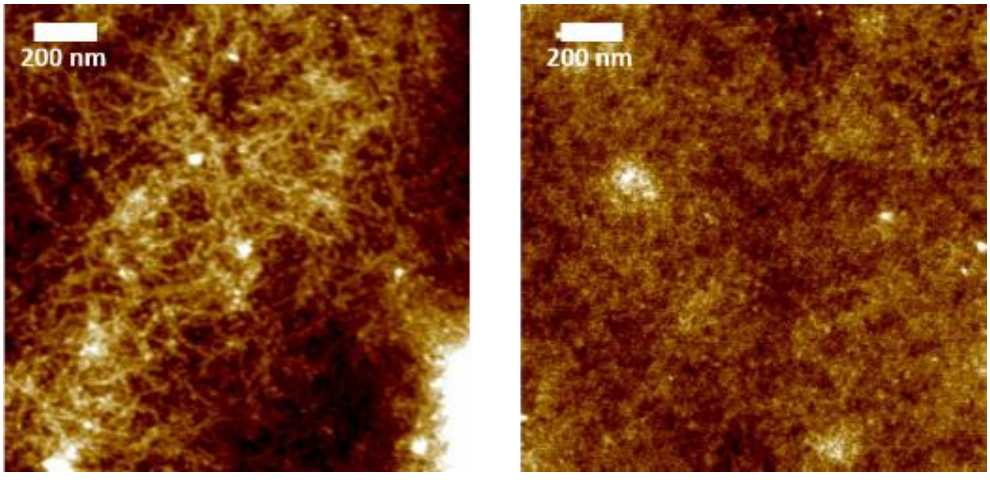

Figure 2.13 TM-AFM height images (2.0 x 2.0 μm²) of thin films of **PTIm-1Zn** (left) and **PTIm-2Zn** (right) drop-cast from xylene solutions (C ~ 0.2 mg.mL^{-1}).

1.4.4. PHOTOVOLTAIC PERFORMANCES

The above study of the supramolecular copolymers **PTIm-1Zn** and **PTIm-2Zn** showed that porphyrins tend to aggregate and thus, disturb the polymer organization, a key parameter for an efficient charge transfer in BHJ solar cells. Despite this finding, some preliminary photovoltaic studies were performed in collaboration with Pr. Wouter Maes and Dr. Jurgen Kesters from the University of Hasselt (Belgium).

BHJ polymer solar cells with a classical architecture (glass/ITO/**PEDOT**:**PSS**/active layer/Ca/Al) were fabricated. To have the best comparison possible with previous morphology results, the photoactive layers, consisting of one of the two supramolecular polymers blended with **$PC_{61}BM$** in a 1:0.8 (wt/wt) ratio, were spin-coated from xylene solutions. **$PC_{61}BM$** was preferred over other (methano)fullerenes (*e.g.* $PC_{71}BM$) for this initial screening because of its lower cost and similar efficiencies with **P3HT**-like donor materials.[46] As summarized in Table 2.2 and Figure 2.14, the resulting devices exhibit very low short-circuit current densities and fill factors in comparison with standard **P3HT**:**$PC_{61}BM$** cells.

Table 2.2 Photovoltaic performances of the polymer solar cells based on **PTIm-1Zn**:**$PC_{61}BM$** and **PTIm-2Zn**:**$PC_{61}BM$**.[a]

Donor material	V_{oc} (V)	J_{sc} (mA/cm²)	FF	Average PCE (%)[b]	Best PCE (%)
P3HT	0.56	6.49	0.66	2.41	2.57
PTIm-1Zn	0.79	0.60	0.29	0.14	0.15
PTIm-2Zn	0.84	0.75	0.29	0.23	0.24

[a] Device structure: glass/ITO/**PEDOT**:**PSS**/polymer:**$PC_{61}BM$**/Ca/Al. Active area: 3 mm². Spin-coated from a xylene solution with a (total) concentration of 36 mg mL^{-1}. [b] Average is calculated over at least 4 devices.

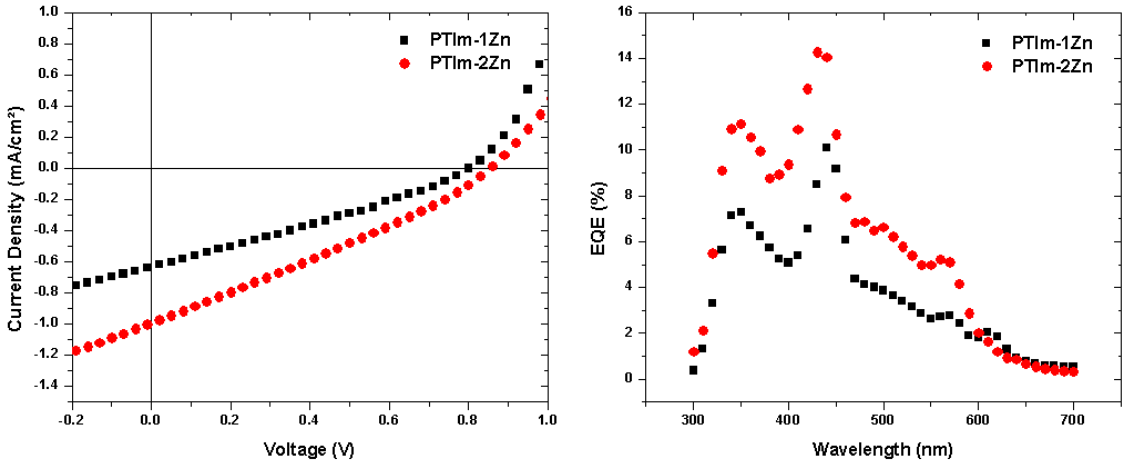

Figure 2.14 *J-V* curves (left) and IPCE (right) spectra for the best **PTIm-1Zn**:**$PC_{61}BM$** and **PTIm-2Zn**:**$PC_{61}BM$** solar cell devices processed from xylene.

To investigate whether the reduced performances were originating from limited absorption by the photoactive layer, incident-photon-to-current efficiency (IPCE) spectra were measured (Figure 2.14, right). As can be observed, the IPCE spectra from both **PTIm-1Zn** and **PTIm-2Zn** are similar to the UV–vis absorption spectra, with some **$PC_{61}BM$** contribution in the low-wavelength area. However, the absolute quantum efficiencies remain below 15 % over the entire absorption range. Consequently, the lower J_{SC} values might be related to the reduction or lack of crystalline order, as previously noticed from the UV-vis, DSC and AFM analyses. Further optimization of the processing conditions (solvent, annealing, additives, etc.) is mandatory to enhance the electron donor aggregation/crystallization and to optimize the photovoltaic performance.

2. END-FUNCTIONALIZATION OF **P3HT** WITH PORPHYRINS

After the side-chain functionalization of **P3HT** with porphyrins, which leads to very low PCEs, we decided to prepare end-functionalized **P3HT** with π-extended porphyrins.[16b] Since π-extended porphyrins exhibit an absorption profile in the NIR region, it allows extending the light harvesting. To this aim, a π-extended porphyrin has been designed in this section, following the work of Callot *et al.* (**CN-Spacer-NiTPP**, Scheme 2.5).[47] To facilitate the incorporation of this porphyrin at the extremity of the **P3HT** backbone, an alkyl spacer was introduced, functionalized with an isocyanide group. Such a group is indeed of crucial importance to modify **P3HT** using arylisocyanide polymerization, as already discussed in the introduction.

2.1. SYNTHESIS OF THE PORPHYRIN-END-FUNCTIONALIZED **P3HT**

The end-functionalization of **P3HT** using an π-extended porphyrin requires the prior synthesis of the different corresponding monomers: 2-bromo-3-hexyl-5-iodothiophene and the π-extended isocyanide porphyrin **CN-Spacer-NiTPP** (Scheme 2.5).

2.1.1. SYNTHESIS OF THE ISOCYANIDE PORPHYRIN MONOMER

The isocyanide-based porphyrin monomer **CN-Spacer-NiTPP** is synthesized from cyclic porphyrin **NH-NiTPP** and 1-(6-iodohexyloxy)-4'-nitrobenzene **NO_2-Spacer-NiTPP**. Since the isocyanide group is unstable under basic conditions, it cannot be envisaged to transform the nitro group into isocyanide before the N-alkylation step.

*2.1.1.1. SYNTHESIS OF THE CYCLIZED PORPHYRIN **NH-NiTPP***

The synthesis of the cyclized porphyrin **NH-NiTPP** was described by Callot, Ruppert *et al.* following a three-steps strategy starting from the 5,10,15,20-tetraphenylporphyrin (**TPP**) (Scheme 2.6).[47]

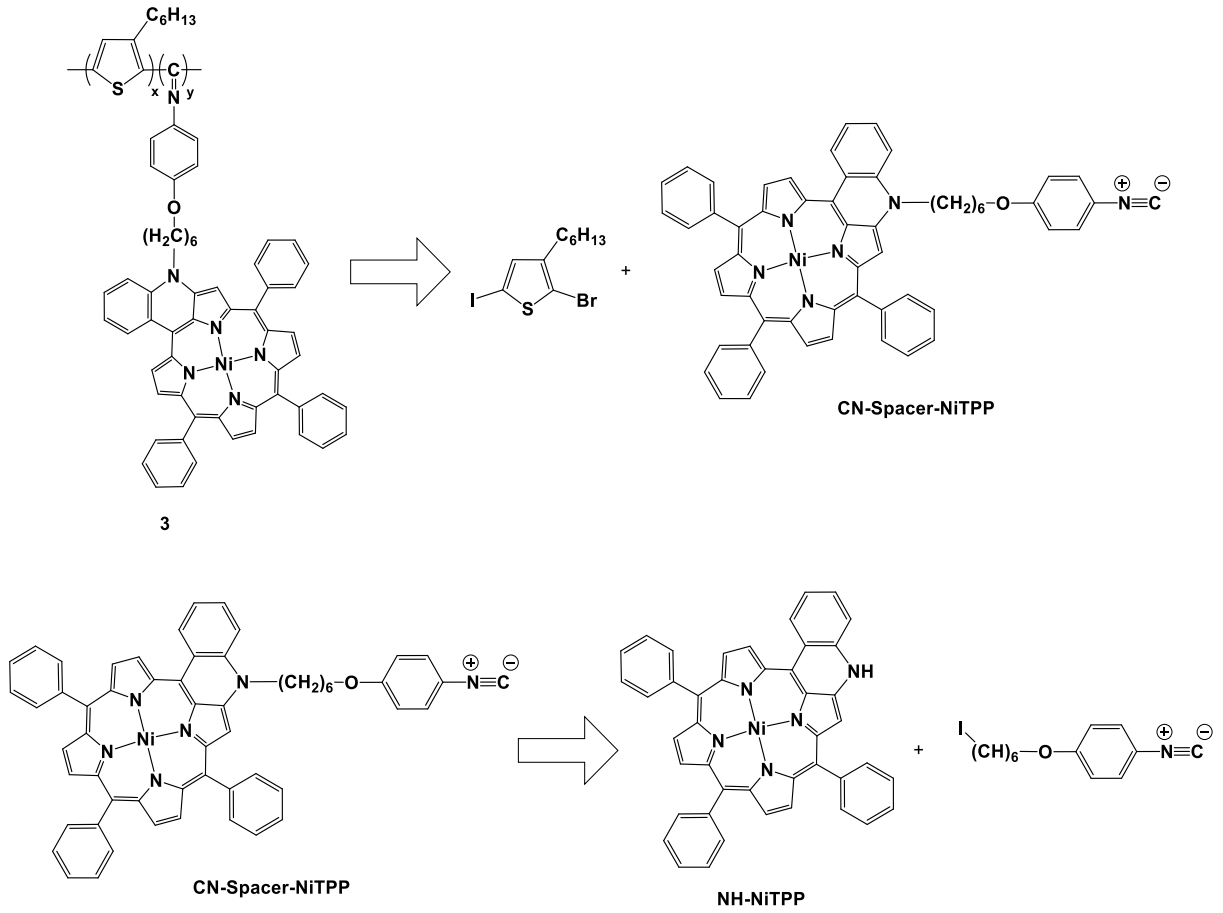

Scheme 2.5 Retrosynthesis of the porphyrin end-functionalized **P3HT**.

First, **TPP** was synthesized using the Adler condensation of pyrrole with benzaldehyde under reflux in propionic acid.[22] This porphyrin was obtained in a 16 % yield without further purification. The ^{1}H NMR spectrum of **TPP** in $CDCl_3$ displays a broad peak at -2.7 ppm, characteristic of the inner NH protons as well as a singlet at 8.87 ppm, characteristic of the pyrrolic protons. Then, the free-base porphyrin was nickel(II)-metalated through an exchange reaction with the nickel(II) acetylacetonate ($Ni(acac)_2$, $2H_2O$), leading to **NiTPP** with 95 % yield. The metalation was easily monitored using UV-vis absorption spectroscopy. The absorption profile of the nickel-metalated porphyrin exhibits only two Q bands instead of the four observed for the free-base analog, due the symmetry gain (D_{4h} instead of D_{2h}). A bathochromic shift of the first Q band, from 515 to 528 nm, also allows easily distinguishing the metalated and free-base compounds. The metalation of **TPP** was also confirmed by ^{1}H NMR spectroscopy since the signal corresponding to the inner NH protons of the free-base porphyrin around -2.7 ppm was no longer observable.

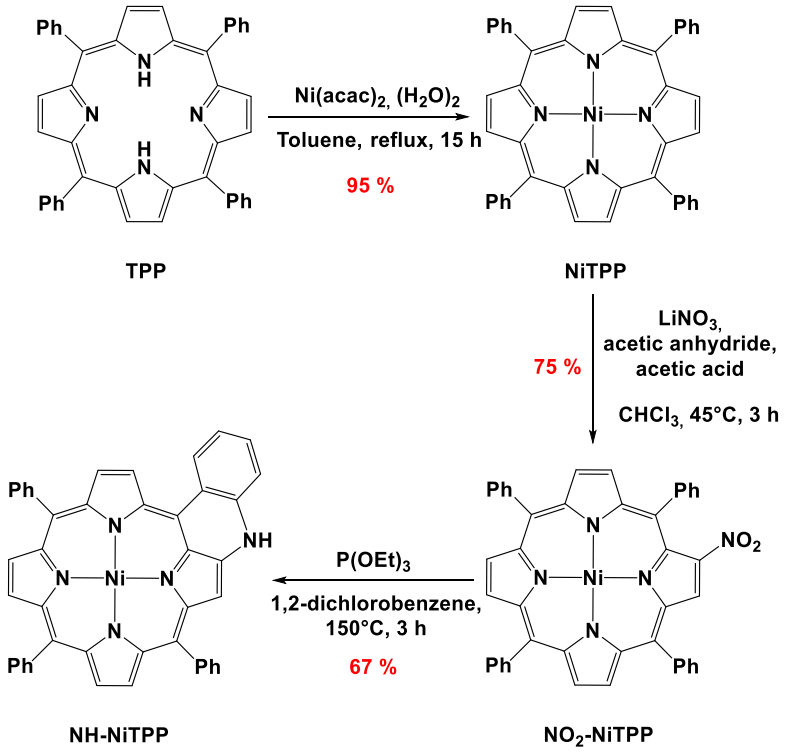

Scheme 2.6 Synthesis of the cyclized porphyrin **NH-NiTPP**.

In a second step, the introduction of a nitro group on a β-pyrrolic position of the porphyrin was carried out by using lithium nitrate ($LiNO_3$) in an acetic acid/acetic anhydride medium at 45°C in chloroform, affording the mono-nitro compound in 75 % yield. The ^1H NMR spectrum of the **NO_2-NiTPP** differs from that of the **NiTPP** by the presence of an upfield signal at 8.99 ppm, attributed to the β-pyrrolic proton in α-position to the nitro group. Compared to **NiTPP**, the nitration leads to a bathochromic shift of the first Q band from 528 to 540 nm and a hypsochromic shift of the second Q band from 616 to 584 nm in UV-visible absorption spectroscopy.

Finally, after 3 hours at 150°C in 1,2-dichlorobenzene with triethyl phosphite ($P(OEt)_3$), the cyclized porphyrin **NH-NiTPP** was isolated with a 67 % yield after purification by column chromatography on silica gel (Scheme 2.6). The cyclization is easily observed by the color change of the reaction mixture going from red/purple to green, which is the characteristic of cyclized porphyrins. The absorption profile of the cyclized porphyrin displays a new Q band at 628 nm due to the molecule dissymmetry. Bathochromic shifts of the other Q bands, from 540 to 554 nm and 584 to 598 nm, were also observed upon cyclization. In addition, a broad signal around 9.2 ppm appeared in the ^1H NMR spectrum of **NH-NiTPP**, corresponding to the amine proton of the cyclized porphyrin.

2.1.1.2. Synthesis of spacer 1-((6-bromohexyl)oxy)-4'-nitrobenzene

The 1-((6-bromohexyl)oxy)-4'-nitrobenzene spacer was prepared by extrapolation of the experimental process optimized in the laboratory for the synthesis of 1-((6-bromohexyl)oxy)-4'-methoxybenzene, which is a reagent in the synthesis of 2,5-dibromo-3-(6'-bromohexyl)thiophene (cf. Chapter 2, Part 1). The desired compound was obtained using a Williamson etherification between 4-nitrophenol and 1,6-dibromohexane with potassium carbonate (K_2CO_3) and 18-crown-6. After 72 hours under reflux in acetone, the spacer was obtained in a 95 % yield (Scheme 2.7).

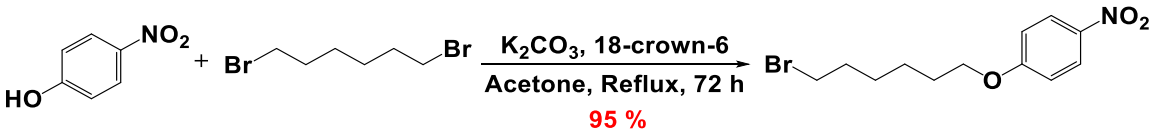

Scheme 2.7 Synthesis of the spacer 1-((6-bromohexyl)oxy)-4'-nitrobenzene.

The ^{1}H NMR spectrum of this spacer exhibits a triplet at 4.05 ppm due to the CH_2O group and two doublets at 6.93 and 8.19 ppm, corresponding to the aromatic protons of the benzene ring.

2.1.1.3. Synthesis of the isocyanide porphyrin

With the spacer in our hands, the cyclized porphyrin **NH-NiTPP** was then *N*-alkylated. This step was difficult to optimize. Indeed, when the reaction was monitored using Thin Layer Chromatography (TLC), several co-products were observed. Thanks to three purifications by column chromatography, the desired porphyrin was isolated in a 40 % yield.

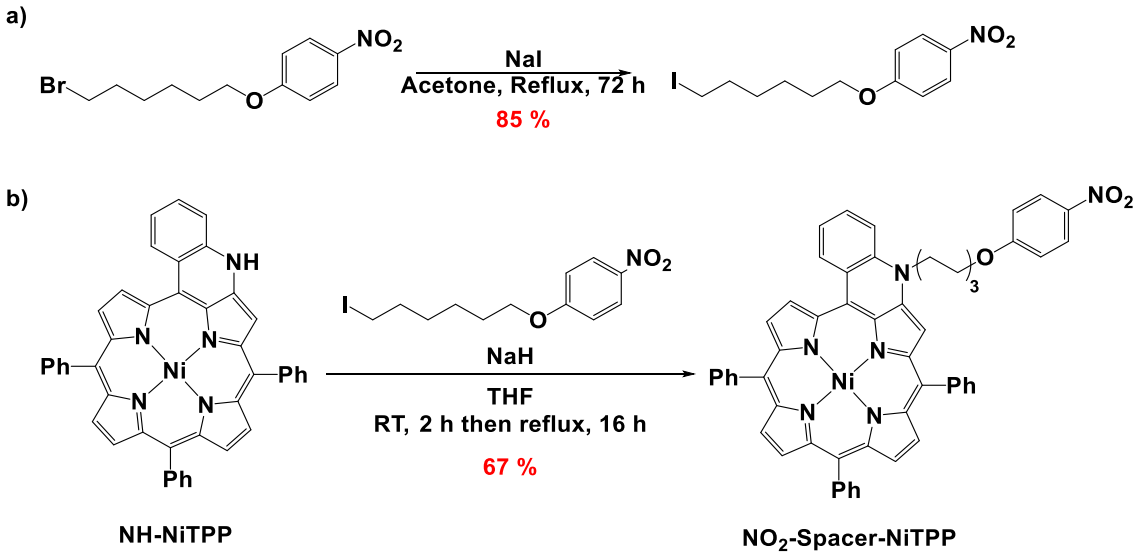

Scheme 2.8 Synthesis of the spacer 1-((6-iodohexyl)oxy)-4'-nitrobenzene (a) and the alkylated porphyrin **NO_2-Spacer-NiTPP.**

In order to improve the yield of the *N*-alkylation step, attempts with sodium iodide (NaI) were carried out to activating more accurately the brominated spacer, without satisfactory results. The yield of the reaction was enhanced up to 67 % by using the iodinated spacer (Scheme 2.8, b), which was obtained from the reaction of the brominated spacer with sodium iodide (Scheme 2.8, a).

In the ^{1}H NMR spectrum, the triplet characteristic of the CH_2Br group at 3.43 ppm was shifted to 3.21 ppm upon substitution with iodine. Regarding the ^{1}H NMR spectrum of the alkylated porphyrin **NO_2-Spacer-NiTPP**, the disappearance of the broad signal at 9.2 ppm, attributed to the amine group, was observed. Besides, signals due to the CH_2O et CH_2N groups of the spacer appeared between 4 and 5 ppm as well as two doublets at 6.8 and 8.1 ppm, corresponding to the aromatic protons of the benzene ring (Figure 2.15).

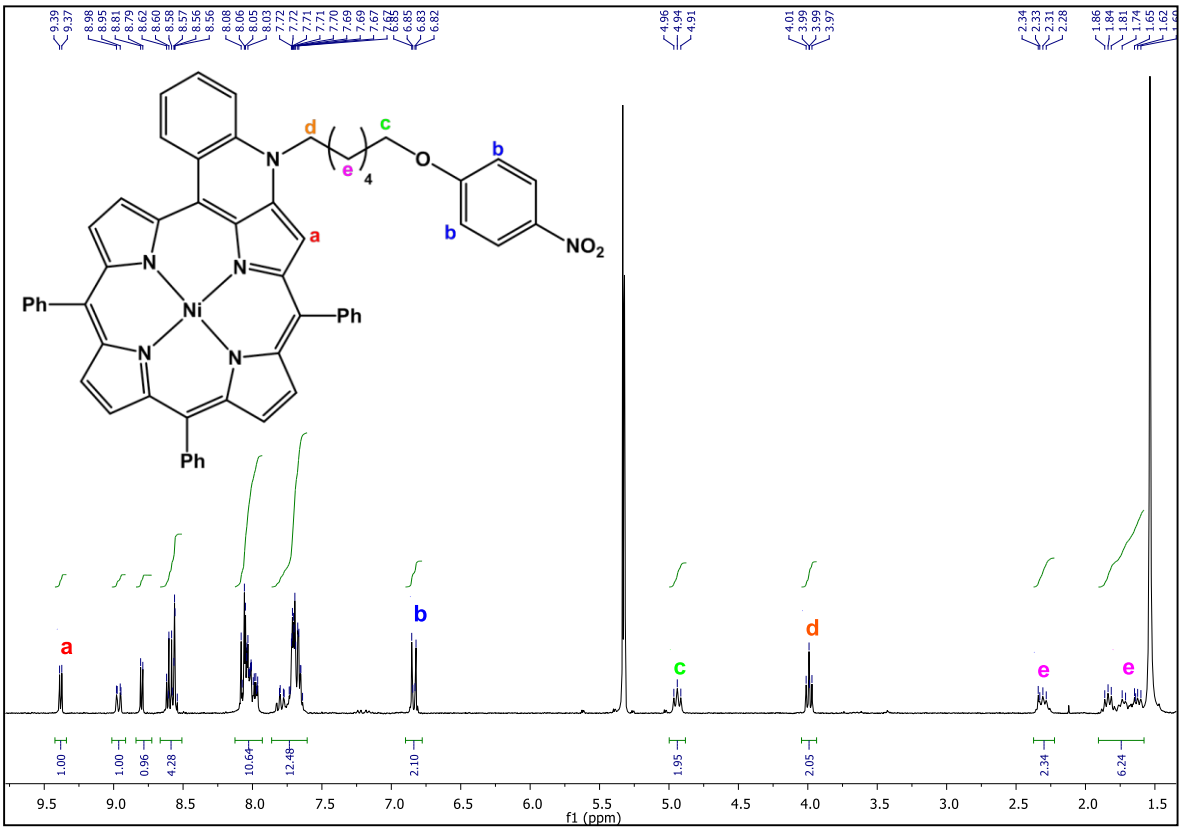

Figure 2.15 ^{1}H NMR spectrum of **NO_2-Spacer-NiTPP** in CD_2Cl_2.

Porphyrin **CN-Spacer-NiTPP** was then prepared in a three-step synthesis (Scheme 2.9). First, the reduction of the nitro compound followed by the formylation of the resulting amino compound were carried out without isolating the amino compound. The formation of the amino compound was performed by reducing **NO_2-Spacer-NiTPP** with sodium borohydride ($NaBH_4$) and palladium on carbon (Pd/C) in a dichloromethane/methanol mixture. Once the completion of the reduction was observed by TLC, the reaction mixture was filtered to eliminate the salts and

concentrated under reduced pressure. The crude product obtained was directly dissolved in toluene and formic acid was added. After 16 hours under reflux, the formylated compound **NHCO-Spacer-NiTPP** was obtained in 87 % yield after purification by column chromatography.

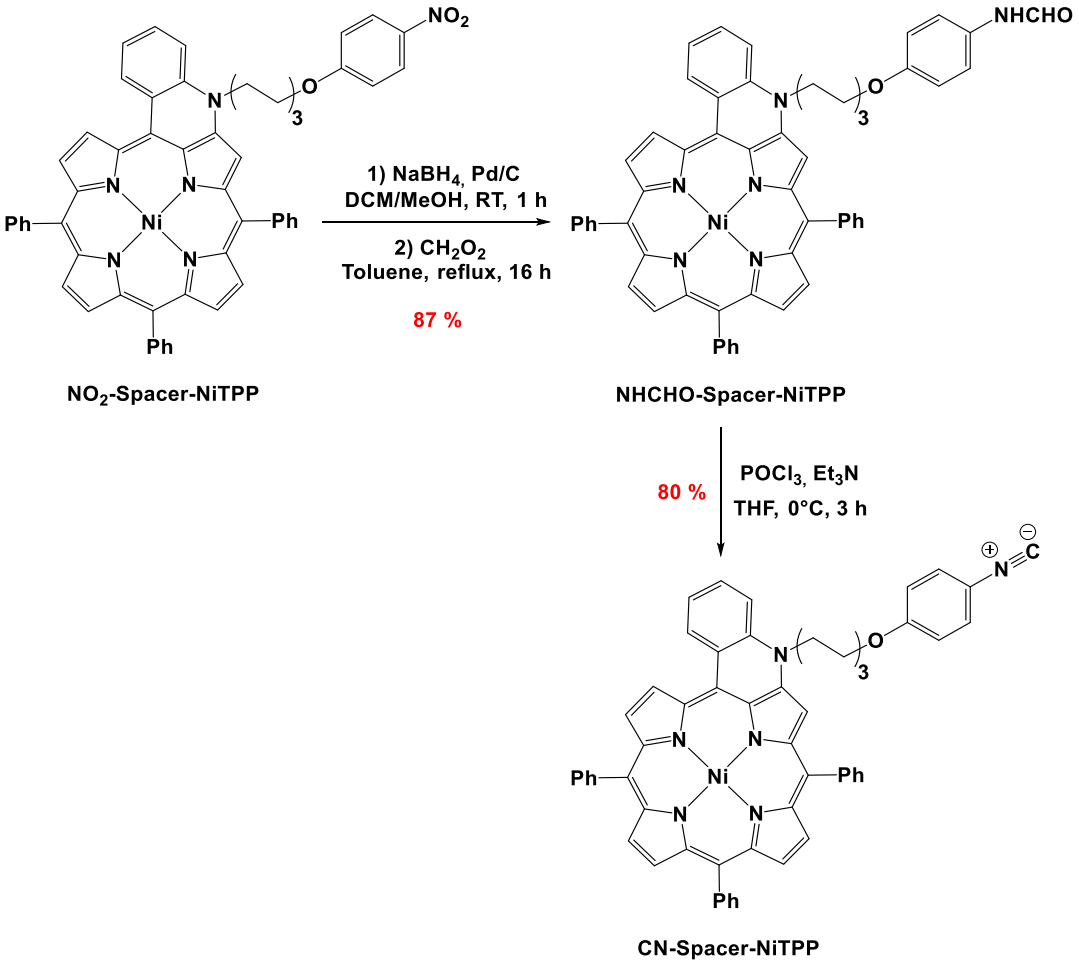

Scheme 2.9 Synthesis of the isocyanide porphyrin **CN-Spacer-NiTPP**.

Upon formylation, the doublets characteristic of the benzene ring were shifted from 8.96 to 8.91 ppm and 8.65 to 8.78 ppm, respectively. Nevertheless, the ^{1}H NMR spectrum was not easy to interpret. Indeed, the C-N bond between the carbonyl group and the nitrogen atom has significant double bond character thus inducing two possible conformations, *i.e. cis* and *trans*. Protons of the carbonyl group and the phenyl group located in α-position from the nitrogen atom were duplicated. As an example, proton of the carbonyl group displayed two doublets signals at δ 8.37 and 8.16 ppm, with the sum of both integration counting for one, and showed two different coupling constants of 11.5 and 1.8 Hz, respectively (Figure 2.16).

The structure of **NHCHO-Spacer-NiTPP** was also confirmed by IR spectroscopy and mass spectrometry, where a strong C=O band at 1655 cm^{-1} and a molecular ion peak at *m/z* = 903.3 were obtained, respectively.

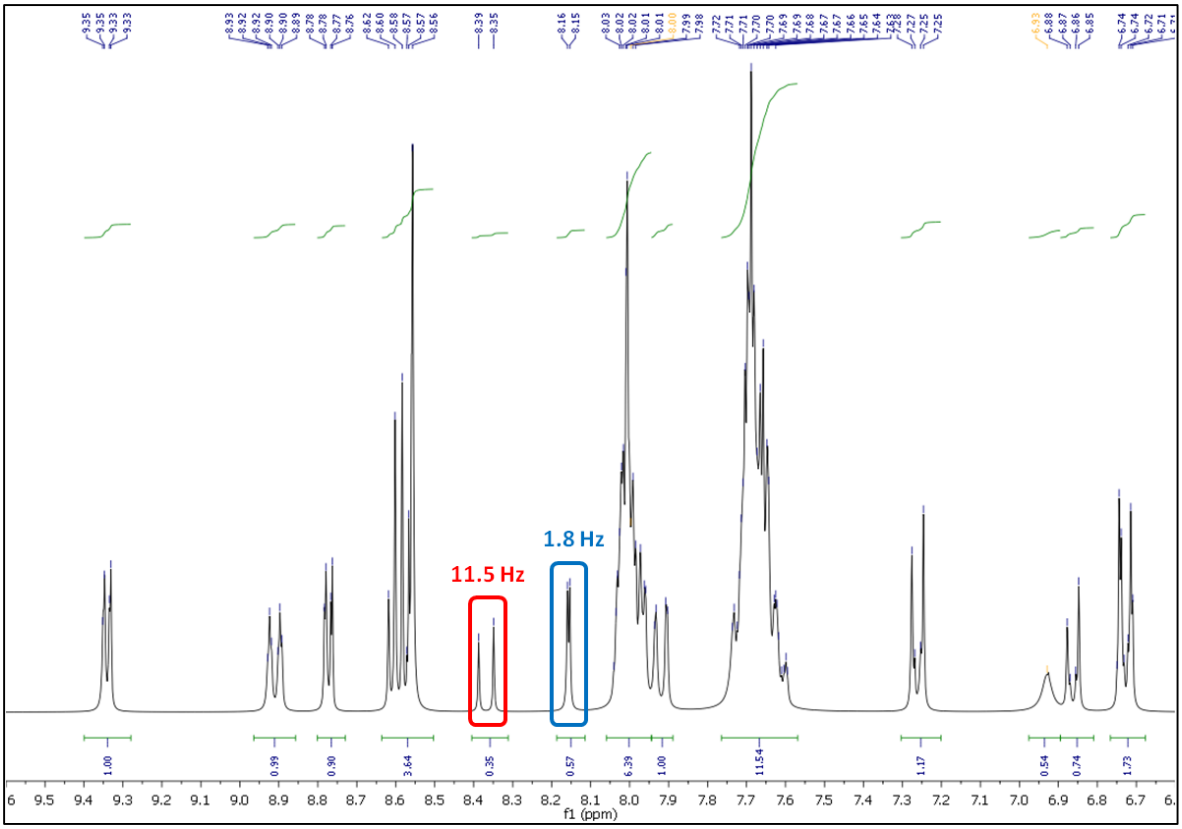

Figure 2.16 ^{1}H NMR spectrum of **NHCHO-Spacer-NiTPP** in CD_2Cl_2 between 6.6 and 9.8 ppm.

Finally, the dehydration of the formylated porphyrin **NHCHO-Spacer-NiTPP** by phosphoryl chloride/triethyl amine ($POCl_3$/Et_3N) in THF at 0°C afforded isocyanide porphyrin **CN-Spacer-NiTPP** in 80 % yield (Scheme 2.9). The formation of the isocyanide compound was easily observed by TLC; the porphyrin **NHCHO-Spacer-NiTPP** having a totally different polarity. The ^{1}H NMR spectrum was easier to interpret than the amide porphyrin (Figure 2.18). The formation of the isocyanide monomer was further proved by mass spectrometry where the molecular ion peak at *m/z* = 884.279 was found. The IR

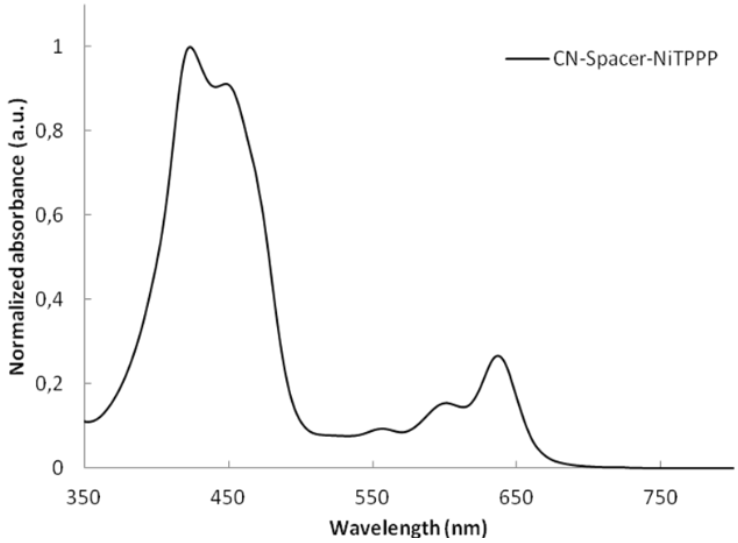

Figure 2.17 UV-visible absorption spectrum of **CN-Spacer-NiTPP** in CH_2Cl_2.

spectrum of **CN-Spacer-NiTPP** also revealed a band at 2 118 cm^{-1}, characteristic of the isocyanide vibration. The UV-visible absorption spectrum of the isocyanide-based porphyrin monomer exhibited a maximum absorption wavelength at 637 nm with a high extinction molar coefficient of around 13 000 $M^{-1}.cm^{-1}$ (Figure 2.17).

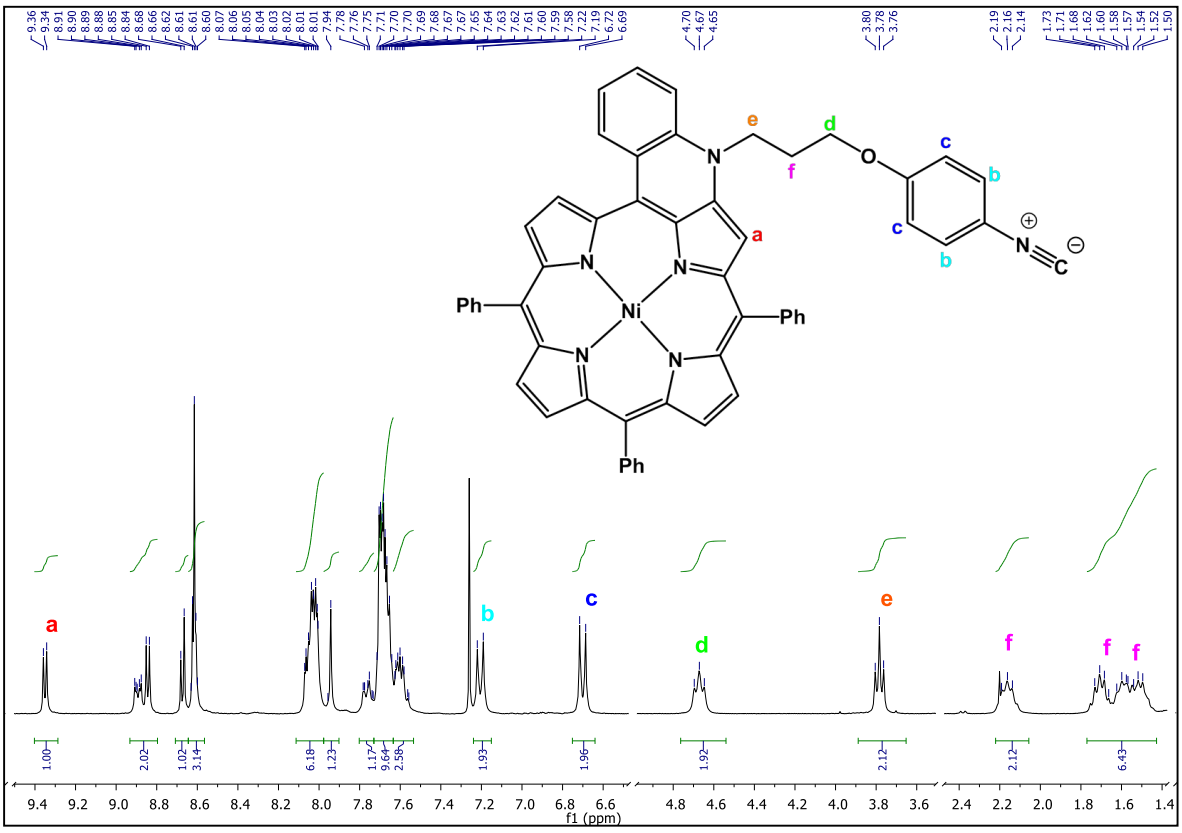

Figure 2.18 ^{1}H NMR spectrum of **CN-Spacer-NiTPP** in $CDCl_3$.

2.1.2. SYNTHESIS OF THE PORPHYRIN-END-FUNCTIONALIZED **P3HT**

With the isocyanide-based porphyrin monomer in our hands, the synthesis of end-functionalized **P3HT** was carried out. Using a standard Kumada Catalyst Transfer Polycondensation (KCTP) procedure, the 5-chloromagnesio-2-bromo-3-hexylthiophene Grignard reagent was polymerized using an appropriate amount of catalyst (dichloro[1,3-bis(diphenylphosphino)propane]nickel, Ni(dppp)Cl_2) in THF to afford the **P3HT** macroinitiator with a living nickel end-group (Ni(dppp)Br). An aliquot was removed from the reaction vessel and analyzed by Size Exclusion Chromatography (SEC) in order to determine the molecular weight of the **P3HT** macroinitiator. After three hours under stirring, a THF solution of **CN-Spacer-NiTPP** was added to the unquenched mixture. The reaction mixture, initially orange due to the color of **P3HT** in solution, became green and then brown upon addition of the isocyanide-based porphyrin. After the reaction mixture was stirred at room temperature for one more

hour, the polymerization reaction was quenched by adding 5M aqueous HCl and poured into an excess of methanol.[34a] The precipitate solids were then collected by filtration (Scheme 2.10).

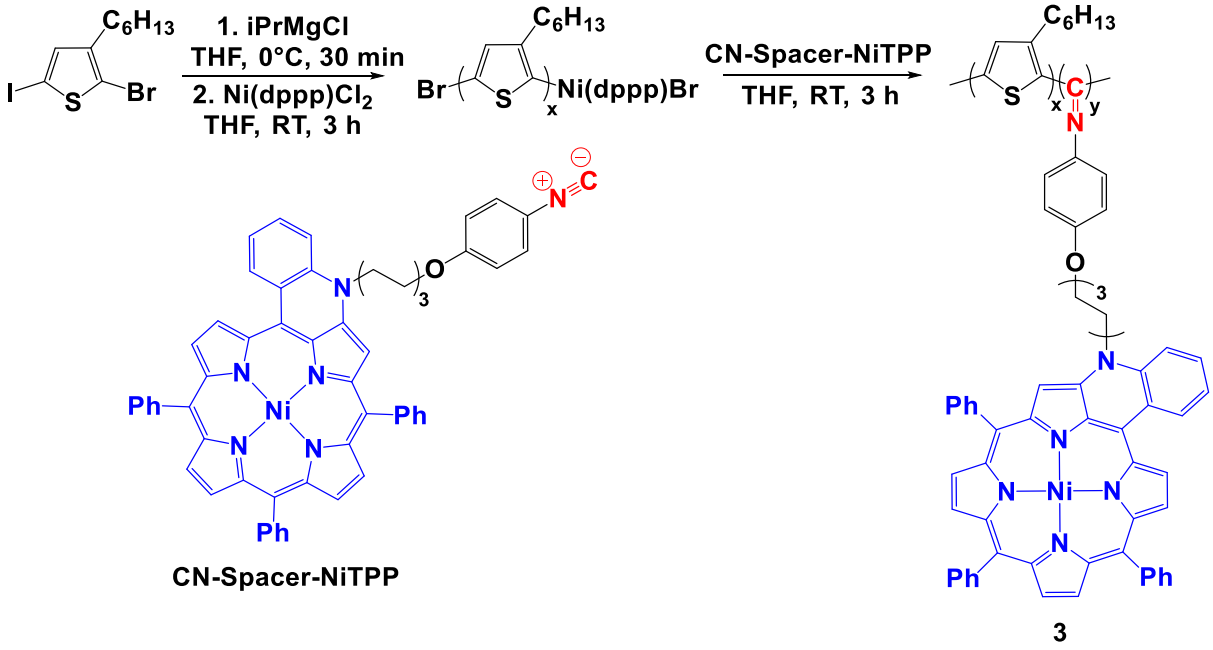

Scheme 2.10 Synthesis of end-functionalized **P3HT** via sequential monomer addition in a one pot procedure.

SEC analysis of the isolated material revealed a higher number-averaged molecular weight (M_n) compared to the **P3HT** macroinitator, indicating successful chain-growth polymerization. Both traces present monomodal peaks, showing that no chain termination or chain transfer took place during the polymerization (Figure 2.19).

Completion of the polymerization was also inferred from IR spectroscopy (Figure 2.20). FTIR spectrum of the obtained polymer **3** clearly revealed the presence of a band at 1 450 cm^{-1}, assigned to the symmetric C=C stretching of the thiophene ring. When compared with the FTIR spectrum of porphyrin isocyanide monomer **CN-Spacer-NiTPP**, the complete disappearance of characteristic isocyanide absorbance peak at 2 118 cm^{-1} indicated that the isocyanide-based porphyrin monomer was polymerized.

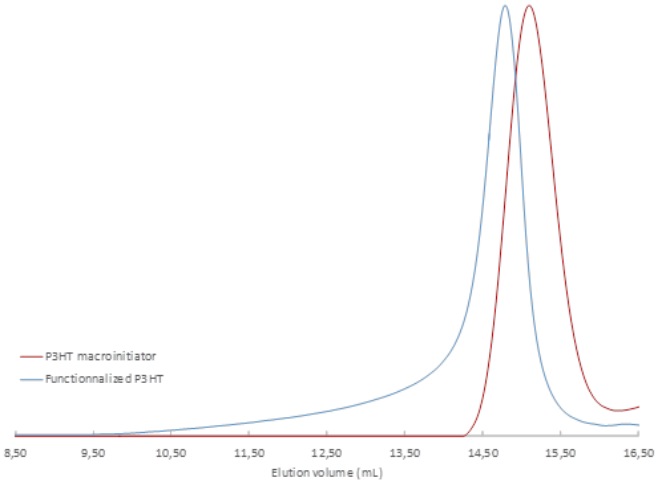

Figure 2.19 Representative SEC chromatograms of homopolymer **P3HT** (red line) and **P3HT** end-functionalized with π-extended porphyrin (**3b**, blue line).

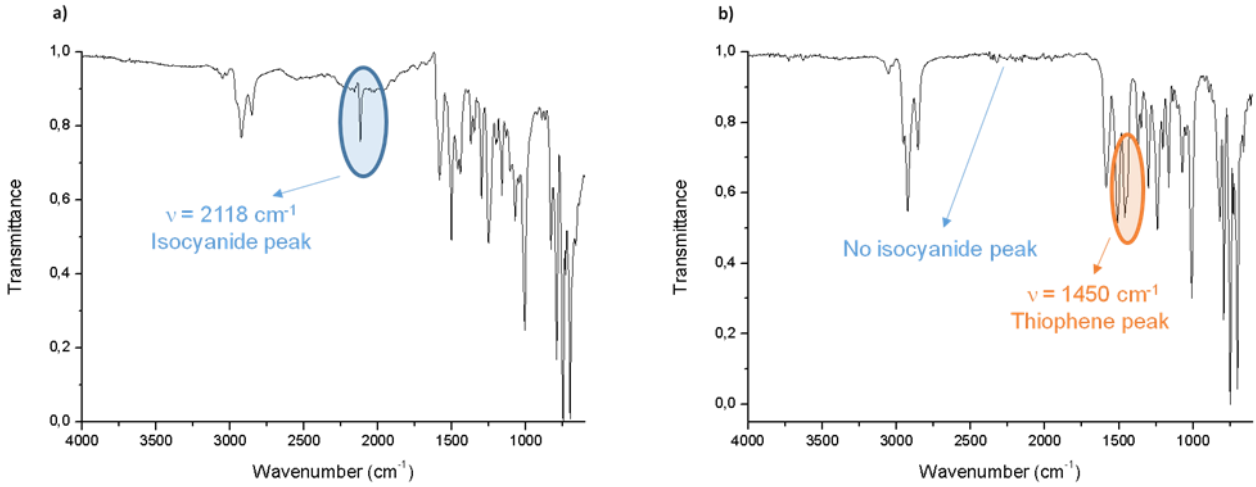

Figure 2.20 IR spectra of isocyanide porphyrin monomer **CN-Spacer-NiTPP** (a) and **P3HT** end-functionalized with π-extended porphyrins (**3**) (b) measured at room temperature by Attenuated Transmission Reflectance (ATR).

As summarized in Table 2.3, three **P3HTs** end-functionalized with π-extended porphyrins with different M_n and compositions were synthesized by varying the initial ratio of the aforementioned monomers and catalyst. All synthesized polymers were isolated in good yields (> 60 % over two steps) with narrow dispersity (< 1.4). Their compositions were determined from their ^{1}H NMR spectra (Figure 2.21) by integrating the signals observed at δ = 0.90 (terminal methyl group of the hexyl side chain of **P3HT**) and between δ = 7.30 and 9.00 ppm (β–pyrrolic and *meso* phenyl protons of the porphyrins). As desired, only a few porphyrin units (3-4) were incorporated as end-groups in the **P3HT** chains.

Table 2.3 Molecular weight and dispersity data for **P3HT** macroinitiators and the corresponding **P3HT** end-functionalized with π-extended porphyrin.

	P3HT		**3**		Yield (%)	Molar **3HT/1** ratio[c]
	M_n (kDa)[a,b]	M_w/M_n [a,b]	M_n (kDa)[b]	M_w/M_n [b]		
3a	8.0	1.28	12.2	1.39	70	90/10
3b	5.6	1.09	9.2	1.28	62	86/14
3c	1.7	1.24	5.0	1.18	60	68/32

[a] M_n and M_w/M_n of the **P3HT** moiety were determined by SEC analysis of aliquots removed from the reaction mixture before the addition of **CN-Spacer-NiTPP**. [b] M_n and M_w/M_n are reported as their polystyrene equivalents. [c] The molar ratio between 3-hexylthiophene (**3HT**) and **CN-Spacer-NiTPP** repeating units was determined by ^{1}H NMR spectroscopy in $CDCl_3$.

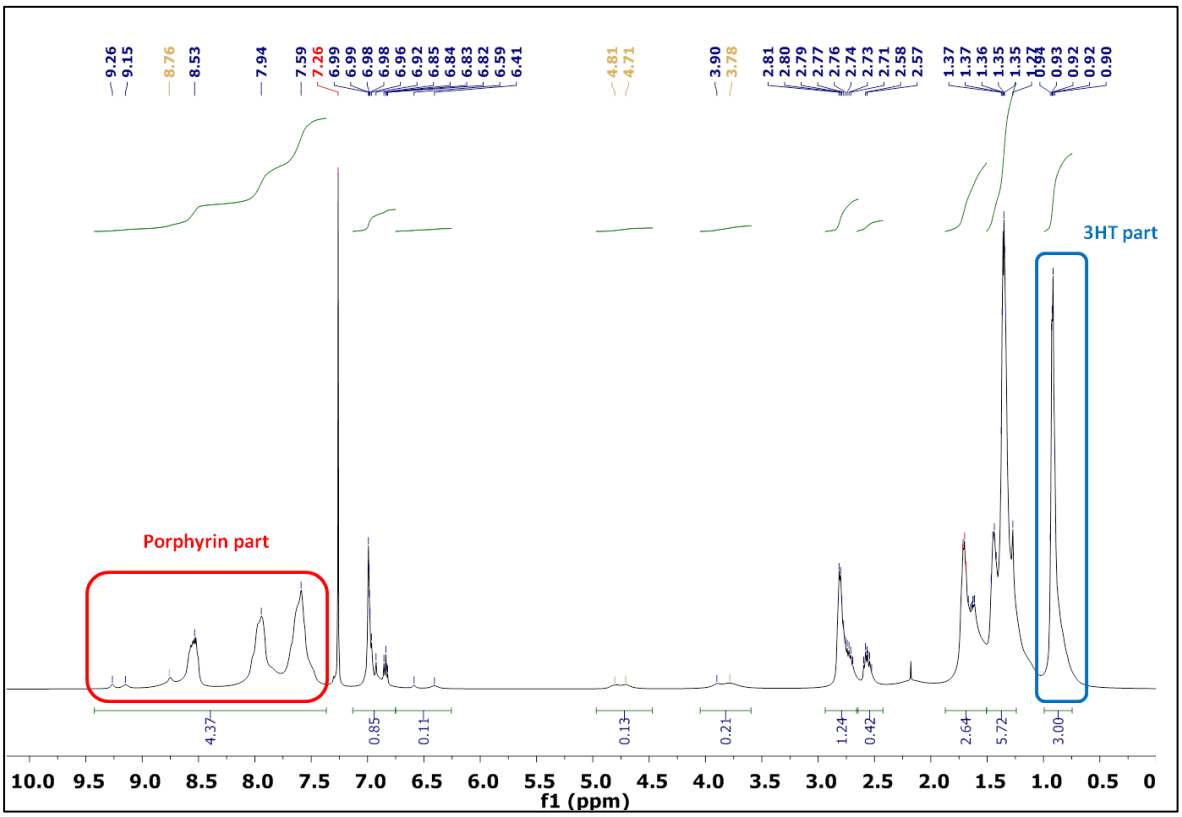

Figure 2.21 ^{1}H NMR spectrum of **3b** in $CDCl_3$.

2.2. PROPERTIES OF THE PORPHYRIN-END-FUNCTIONALIZED **P3HT**

2.2.1. OPTICAL PROPERTIES

The optical properties of polymers **3** were examined. As an example, the UV-visible absorption spectrum of polymer **3a** is shown in Figure 2.21. In chloroform solution, polymers **3** exhibit a similar absorption profile than the porphyrin isocyanide monomer **CN-Spacer-NiTPP** (Figure 2.22) with a strong absorption band between 420 and 450 nm and weaker absorption bands between 550 and 636 nm assigned to the Soret and Q bands of **CN-Spacer-NiTPP**, respectively. In addition, the absorption band appears broader in the 350-450 nm region due to the concomitant **P3HT** absorption.

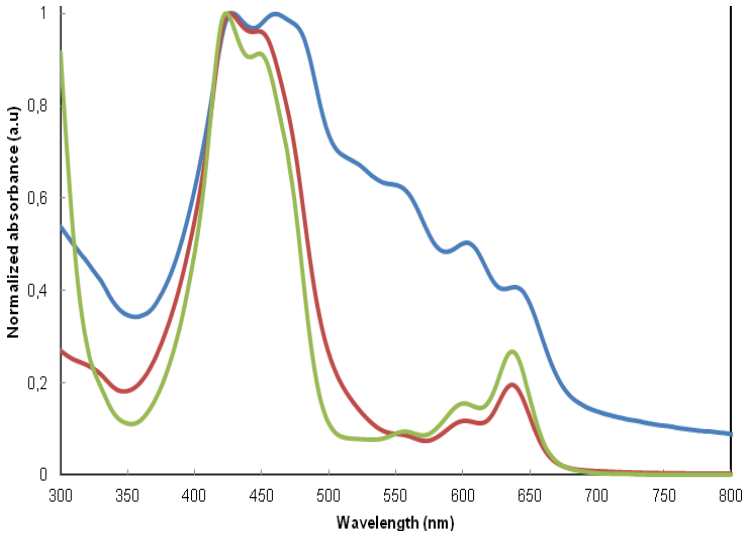

Figure 2.22 Normalized UV-visible absorption spectra of isocyanide-based porphyrin monomer **CN-Spacer-NiTPP** in chloroform (green curve), **3a** in chloroform (red curve) and **3a** in solid state (blue curve).

Usually, **P3HT** can be directed to self-assemble into crystalline nanowires by adding a nonsolvent to a polymer dissolved in a good solvent.[48] Thus, the optical properties of **3a** were studied in chloroform/methanol mixtures at different ratios. Polymer **3a** was initially dissolved in chloroform, a good solvent for both **P3HT** and porphyrin moieties. Aggregation was subsequently induced by adding methanol (MeOH) to the solution in increasing ratios. Upon MeOH addition, the color of the solution turned from green to brown, which seems to indicate self-assembly of the polymer chains (Figure 2.23). Moreover, further increasing of the MeOH content results in a gradual decrease in the absorbance at 426 and 447 nm and the growth of vibronic bands at 518, 556, 601 and 636 nm. An isobestic point was observed at 480 nm, indicating that two distinct species, *i.e.* isolated polymer chains and aggregates, contribute to the absorption profile in mixtures from 10/0 to 3/7 ($CHCl_3$/MeOH, v/v).[48] These results indicate that interchain π–π interactions are associated with the formation of semicrystalline aggregates.

To investigate the self-assembly of the polymer chains in the solid-state in more details, the UV-vis absorption spectra of polymer thin films were recorded and compared to **P3HT** and porphyrin **CN-Spacer-NiTPP** thin films (Figure 2.24). As observed in $CHCl_3$/MeOH (1:1), polymer **3a** thin films exhibit a vibronic structure with shoulder peaks at approximatively 520, 550 and 600 nm. These peaks correspond fairly well with those observed in pristine **P3HT** thin films, indicating that the bulky porphyrin end groups do not disrupt the packing of the **P3HT** chains.[49]

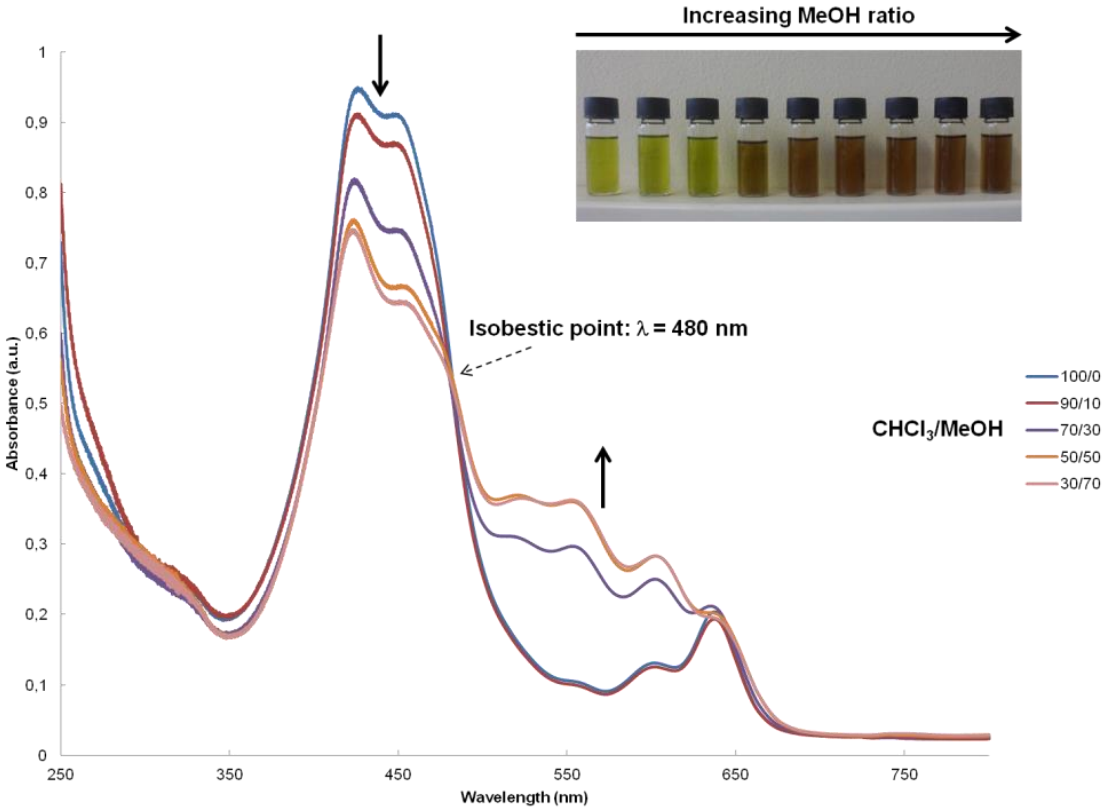

Figure 2.23 Photographs and UV-vis absorption spectra of **3a** in chloroform/methanol mixtures from 10/0 to 3/7 ($CHCl_3$/MeOH = v/v, C = 0.06 mg.mL^{-1}).

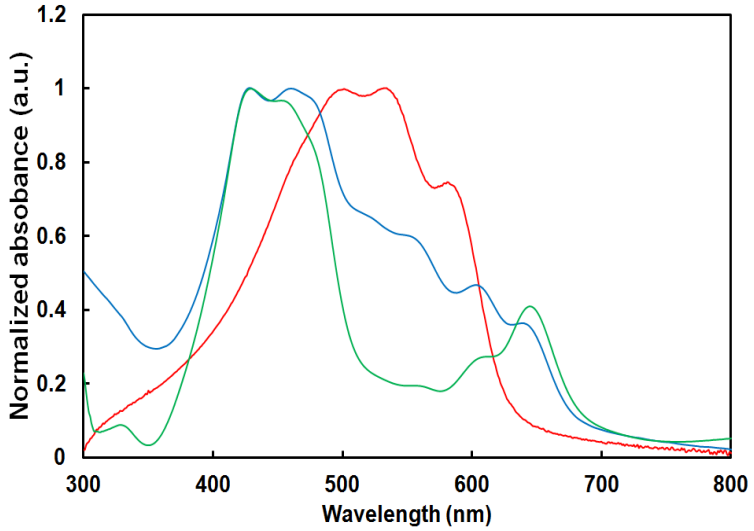

Figure 2.24 UV-visible absorption spectra of isocyanide-based porphyrin monomer **CN-Spacer-NiTPP** (green curve), **3a** (blue curve) and **P3HT** (red curve) in thin films.

The influence of the **3HT**:**CN-Spacer-NiTPP** molar ratio on the optical and self-assembly properties was then studied. The UV-vis absorption spectra of **3a** and **3b** in the solid state

exhibit the same profile but with a lower absorbance between 500 and 600 nm for **3b**, due to the lower polythiophene content (Figure 2.25). The absorption profile of **3c** appears to be almost identical to that of the porphyrin monomer **CN-Spacer-NiTPP** and exhibits no vibronic band between 500 and 600 nm. This indicates that introducing a larger number of porphyrin units prevents intermolecular interactions between polymer chains, leading to a reduction in overlap through π–π stacking and disturbed arrangement in the solid films.[15b] Thus, while the incorporation of π-extended porphyrin units into the **P3HT** chain-ends enables the absorption profile of the polymer material to be significantly extended, the porphyrin:**P3HT** ratio must be kept low enough to avoid the loss of the supramolecular organization of the **P3HT** segments in the solid state.

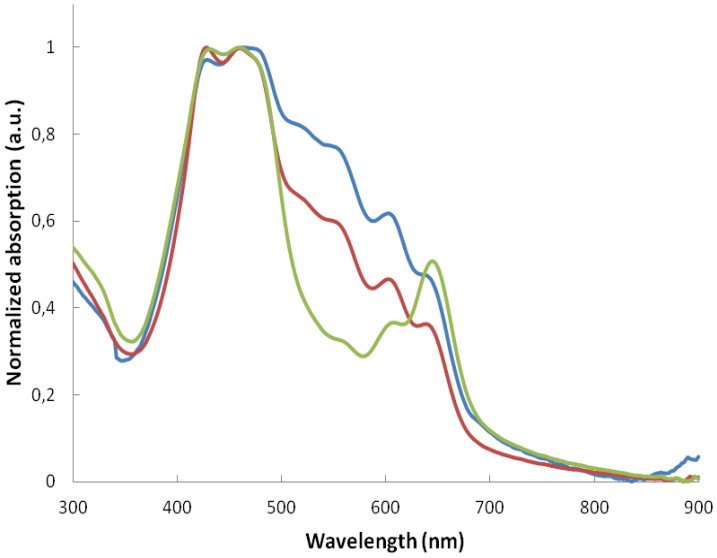

Figure 2.25 Solid-state UV-visible absorption spectra of **P3HT** end-functionalized with π-extended porphyrins at different molar ratios of the porphyrin block: **3a**, blue line; **3b**, red line; **3c**, green line.

2.2.2. THERMAL PROPERTIES

To investigate the effect of the porphyrin molar ratio on the thermal properties, thermogravimetric analysis (TGA) and differential scanning calorimetry (DSC) measurements were performed under an inert atmosphere at a heating rate of 10 °C.min^{-1}. Polymers **3a-c** display excellent thermal stability, with the first weight losses occurring upon heating only at temperatures exceeding 330 °C (Figure 2.26).

The DSC measurements show different thermal transitions depending on the porphyrin:**P3HT** molar ratio. The introduction of the porphyrin leads to a decrease in the melting and, to a lesser extent, crystallization temperatures in comparison with neat **P3HT** (Table 2.4).[42] Upon cooling/heating, a crystallization/melting temperature of 114°C and 181°C, respectively, were found for **3a** (compared to 191°C and 224°C for **P3HT**). The melting and crystallization temperatures of polymer **3b** are lower than for **3a**, whereas polymer **3c** appears to be fully amorphous. This evolution results from the increasing porphyrin molar ratio from **3a** to **3c**. These results are consistent with the observed changes in the UV-vis absorption spectra and confirm that the porphyrin:**P3HT** ratio needs to be carefully controlled in order to retain the semicrystalline nature of **P3HT**.

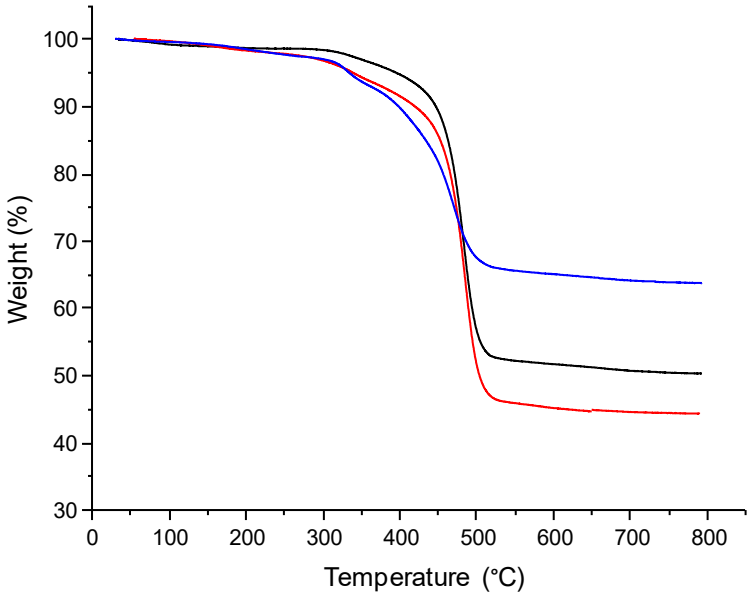

Figure 2.26 TGA thermograms of **P3HT**s end-functionalized with π-extended porphyrins at different molar ratios of the porphyrin block: **3a**, red line; **3b**, black line; **3c**, blue line.

Table 2.4 Melting and crystallization temperatures (in °C) of **P3HT**s end-functionalized with π-extended porphyrins depending on the molar ratio of porphyrin block.

	P3HT	**3a**	**3b**	**3c**
$\mathbf{T_c}$	191	181	156	-
$\mathbf{T_m}$	224	114	103	-

2.2.3. MORPHOLOGICAL PROPERTIES

To analyze the microscopic morphology of the polymers in the solid state, Atomic Force Microscopy (AFM) measurements were performed in Peak Force Tapping mode. The samples were prepared by drop casting polymer solutions (around 0.1 $mg.mL^{-1}$ in xylene) onto mica substrates, followed by solvent annealing. Polymer **3a** is the only sample with a well-defined nanostructured morphology. At a scale of 10 µm (Figure 2.27, a), a web of few hundred nm-wide tapes was observed. These tapes are composed of aligned fibrils, which can extend over a few micrometers in length (Figure 2.27, c and d) and which are characteristic of the assembly of highly regioregular **P3HT** chains.[43a,50]

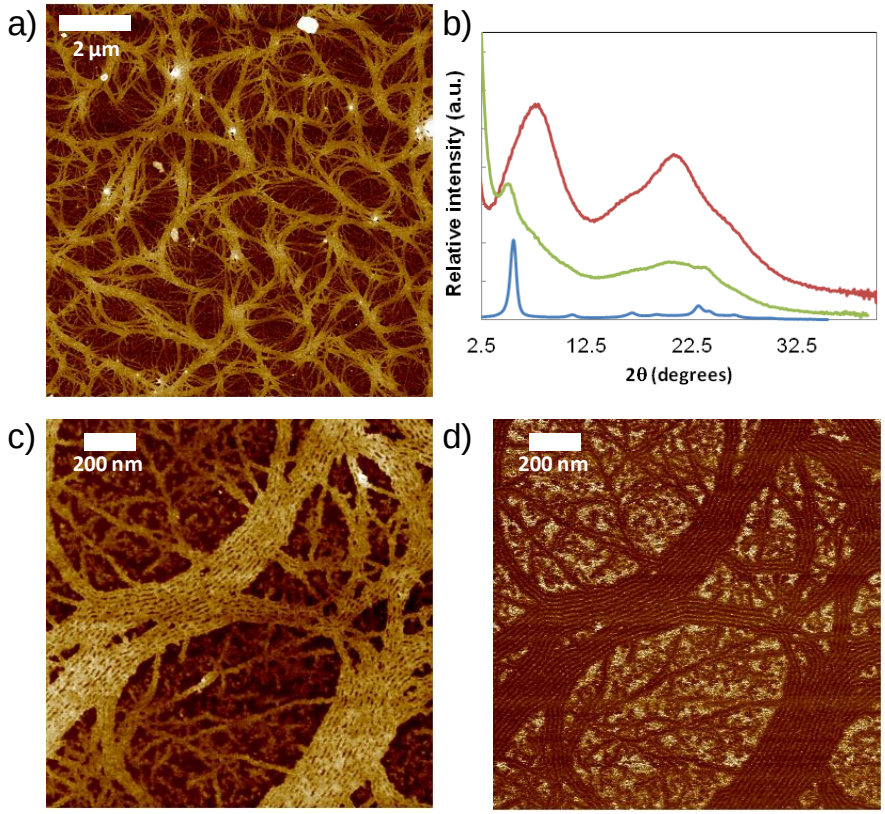

Figure 2.27 (a) 10 x 10 µm² Peak Force AFM height image of **3a** drop-cast from xylene onto a mica substrate; (b) X-ray diffraction pattern of isocyanide-based porphyrin monomer **CN-Spacer-NiTPP** (red), **P3HT** (blue) and **3a** (green); (c,d) 1.5 x 1.5 µm² Peak Force AFM height (c) and DMT modulus (d) images of **3a** showing the fibrillar morphology.

Powder X-ray diffraction (XRD) measurements were also performed on polymer **3a** and confirm the microstructure (Figure 2.27, b). The diffraction pattern exhibits reflections assigned to pristine **P3HT** and isocyanide-based porphyrin monomer **CN-Spacer-NiTPP**, indicating the retention of the crystalline structures inherent to both components. A peak at $2\theta \sim 5.0°$, typical of a lamellar structure is observed in the **P3HT** diffraction pattern ($2\theta \sim 5.5°$).[51] In addition, the broad reflection centered at $2\theta \sim 20.3°$ can be related to diffraction from the isocyanide-based porphyrin monomer **CN-Spacer-NiTPP** ($2\theta \sim 20.8°$), which corresponds to the π-π stacking distance (2.8 Å) between two porphyrin units. These similarities, in particular the position of the (100) lattice peak, indicate that the presence of the porphyrin moiety, if maintained in relatively low quantity, does not affect the **P3HT** crystalline structure.

In order to demonstrate the interest of this covalent strategy, the thin film morphology of a 90:10 molar blend of a **P3HT**, having a similar molecular weight to the end-functionalized one (M_n = 7.5 kDa, ~~Đ~~ = 1.19) and **CN-Spacer-NiTPP** was studied by AFM. No organization was

observed, indicating that blending the **P3HT** with porphyrin disturbs the well-defined structuration of the polymer. This finding was also supported by comparing the optical properties of the **P3HT**:**CN-Spacer-NiTPP** blend with polymer **3a**. Xylene solutions of **3a** and **P3HT**:**CN-Spacer-NiTPP** were prepared at the same concentration and deposited on a glass substrate by drop casting.

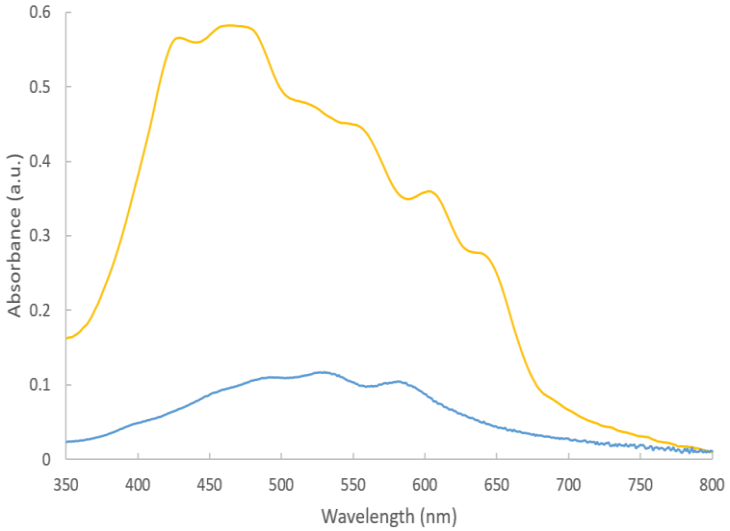

Figure 2.27 UV-visible absorption spectra of **3a** (yellow line), and **P3HT**:**CN-Spacer-NiTPP** blend mixture (blue line) in thin films.

While the end-functionalized **P3HT** displayed a broad, structured absorption profile, the **P3HT:CN-Spacer-NiTPP** blend has very low absorbance (Figure 2.28). In addition, no contribution of the porphyrin to the light absorption of the blend was observed since only absorption bands corresponding to **P3HT** can be distinguished. Regarding the optical and morphological properties, the interest of the end-functionalization strategy clearly appeared: compared to the blend mixture, this approach allowed extending the light harvesting of the **P3HT** whilst keeping its well-defined organization in the solid state.

2.2.4. PHOTOVOLTAIC PROPERTIES

Compared to the previous strategy, *i.e.* the supramolecular approach, the morphology of **P3HT** end-functionalized with π-extended porphyrin, especially **3a**, displayed well-defined fibrillar structure, a key parameter for an efficient charge transfer in BHJ solar cells. Based on this finding, preliminary photovoltaic studies were performed in collaboration with Pr. Wouter Maes and Dr. Jurgen Kesters (University of Hasselt, Belgium). BHJ polymer solar cells with a classical architecture (glass/ITO/**PEDOT**:**PSS**/active layer/Ca/Al) were fabricated. To have the best comparison possible with previous morphology results, the photoactive layer, consisting of polymer **3a** blended with **$PC_{61}BM$** in a 1:0.8 (wt/wt) ratio, was spin-coated from xylene solutions.

The values of open-circuit voltage (V_{OC}), short-circuit current density (J_{SC}), fill factor (FF) and power conversion efficiency (PCE) are summarized in Table 2.5. The device showed V_{OC} of 0.55 V, J_{SC} of 0.19 mA.cm^{-2} and FF of 28 %, resulting in an efficiency value of 0.04 %. Despite the interesting optical, thermal and morphological properties of the donor material, the PCE of these devices remains lower than for **P3HT**:**PC$_{61}$BM** cells. It can be noted that this result was obtained from only one series of three cells without reference with **P3HT**. Thus, the V_{OC} value of these non-optimized cells is quite similar to those previously obtained for the **P3HT** reference prepared for supramolecular polymers. The modest performance of polymer **3a** as donor material arises from the very low value of J_{SC}, maybe suggesting that charge transport in polymer **3a** is not efficient.

Table 2.5 Photovoltaic performances of the polymer solar cells based on **3a**:**PC$_{61}$BM**.[a]

Donor material	V_{oc} (V)	J_{sc} (mA/cm²)	FF	Average PCE (%)[b]	Best PCE (%)
P3HT[c]	0.56	6.49	66	2.41	2.57
3a	0.55	0.19	28	0.03	0.04

[a] Device structure: glass/ITO/**PEDOT**:**PSS**/polymer:**PC$_{61}$BM**/Ca/Al. Active area: 3 mm². Spin-coated at 1200 rpm from a xylene solution with a (total) concentration of 36 mg mL^{-1} followed by thermal annealing at 140°C for 5 minutes. [b] Average is calculated over 3 devices. [c] Parameters obtained for supramolecular attempts, as reference.

In order to better understand the aforementioned results, in particular, the low value of J_{SC}, conductive AFM (C-AFM) images were recorded on thin films of polymer **3a**. The polymer was deposited following the same conditions as before, *i.e.* drop casting on conventional glass substrates patterned with ITO electrodes from a xylene solution (0.1-0.2 mg.mL^{-1}). Before recording the C-AFM images, tapping mode AFM (TM-AFM) was used to determine if changing the substrate had an impact on the structuration of **3a**. No major difference was found with respect to the samples deposited on mica.

C-AFM is a powerful method to characterize conductive thin films. In conductive AFM, current images are acquired simultaneously with topographic images by measuring local currents in the contact mode when a bias voltage is applied between the sample and the AFM tip.[52] Thus, the current images show the local distribution of the current in the investigated layer, allowing determining the electrical properties of the conjugated polymers in thin films.

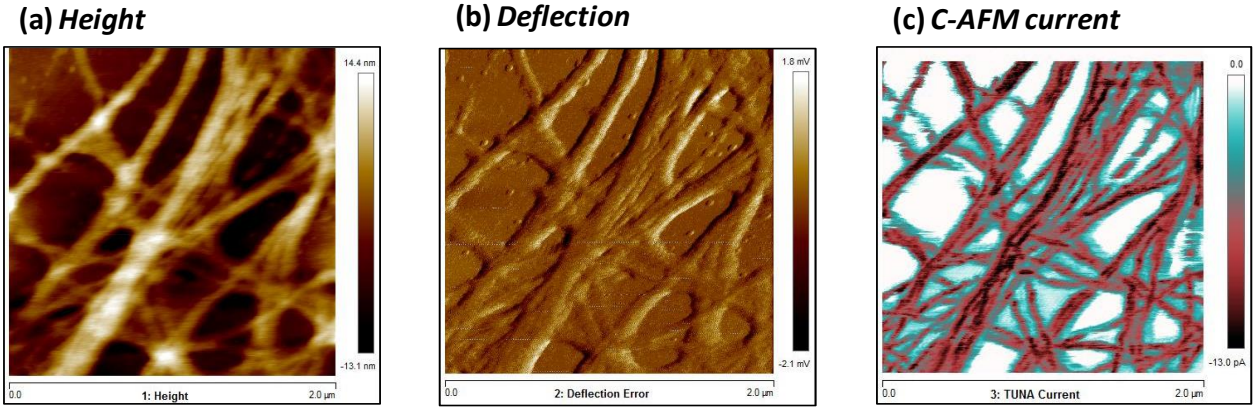

Figure 2.29 (a) 2 x 2 µm² AFM height images obtained in contact mode on a **3a** deposit. (b) Corresponding AFM deflection and (c) C-AFM current images obtained with a DC sample bias of -1 V. **3a** was drop-cast from xylene onto a ITO-patterned glass substrate, showing a fibrillar morphology.

The topography and deflection images (Figure 2.29, a and b) revealed that polymer **3a** displayed a web of fibrils, which can extend over a few micrometers in length, as previously observed on the mica substrate. On the current image (Figure 2.29, c), the glass substrate exhibits zero current, confirming that the current flow is coming from the charge transport within polymer **3a** indicating that the compound is conductive. Whatever the distance between the probe (anode) and the ITO electrode (cathode), a similar current density was measured, as already reported by D. Moerman *et al*.[52] Fibrils of **3a** are electrically interconnected and a current in the pico-ampere range is measured at negative DC sample bias. This is consistent with the fact that the high work function of $PtIr_5$ tip (≈ 5.2 eV) ensures injection of holes from the probe to the polymer when a negative DC sample bias is applied.[52]

These preliminary C-AFM images demonstrated that the end-functionalized **P3HT** is conductive along the fibrils. However, further information about the electronic properties and morphology of the polymer is required, especially when blended with the acceptor material **$PC_{61}BM$**. Indeed, a low value of FF was also noticed, explaining in part the low PCE obtained for the devices prepared from **3a**. Thus, performing TM-AFM and C-AFM on **3a**:**$PC_{61}BM$** blends would allow us to know whether polymer **3a** keeps its fibrillar morphology when combined with **$PC_{61}BM$** and to identify more precisely the domain structure, size and transport properties of the blends. Besides, local current-voltage (I-V) characteristics could be investigated with C-AFM to probe the transport properties within each domain in the blends.

In parallel, the processing parameters such as solvent, annealing temperature, use of additives, etc., could also be optimized in order to obtain an optimal microscopic blend morphology and thus, increased performances.

CONCLUSION

Two functionalization strategies, *i.e.* on the side- and end- groups respectively, were developed to incorporate porphyrins onto the **P3HT** backbone, in view of expanding its light absorption spectrum and thus, improving PCE of **P3HT**-based BHJ solar cells.

In the first approach, **P3HT** copolymers decorated with 10 % of fluorinated or nonfluorinated porphyrin sensitizers have been successfully prepared through the coordination of the central zinc ion of the porphyrin moieties with an imidazole-functionalized polythiophene copolymer. The relevance of this approach was demonstrated using a model compound, *i.e.* 3-(6'-imidazolhexyl)thiophene (**TIm**), which corresponds to the thiophene monomer units bearing an imidazole ligand in the **P3HT-*r*-P3HTIm** copolymer. By using a combination of ^{1}H NMR, UV-vis absorption spectroscopies, mass spectrometry and X-ray diffraction, the formation of a complex with a 1:1 stoechiometry was evidenced. Binding constants around 10^{3}-10^{4} M^{-1} were found by exploiting the optical data. These copolymers displayed excellent thermal stability as well as a significant contribution of both complexed moieties, *i.e.* polythiophene and porphyrin. However, a blue-shift of the **P3HT** absorption was observed upon complexation, which seems to indicate that porphyrins disturb the organization of the **P3HT** chains in the solid-state. This finding was confirmed by studying their morphological properties where a lack of crystallinity was demonstrated. This poor organization resulted in very low photovoltaic performances when combined with **PCBM** in the active layer of BHJ solar cells.

In the second approach, π-extended porphyrin chain ends were introduced into **P3HT** using a one-pot procedure based on the chain growth polymerization of **3HT** and a porphyrin-bearing arylisocyanide. First, the synthesis of a cyclic enamine nickel porphyrin bearing an arylisocyanide group was achieved. Then, **P3HTs** end-functionalized with this π-extended porphyrin having different composition and molecular weight have been prepared by tuning the molar ratio between **3HT** and porphyrin (between 10 and 30 %) and the amount of nickel catalyst. The optical, thermal and morphological properties of these polymers were studied. In contrast with the supramolecular strategy, this second approach was found not to disturb the well-known self-assembling properties of **P3HT**, a key requirement for efficient charge transport properties. By introducing these π-extended porphyrin chain ends, the absorption profile of the polymer was extended to higher wavelengths thanks to the combination of the absorption profiles of **P3HT** and porphyrin. Nevertheless, the molar ratio in porphyrin has to be judiciously adjusted. Indeed, by increasing the molar ratio until 30 %, the porphyrin end-functionalized polymer was found to be amorphous and no structured morphology was observed. The end-functionalized polymer with the best morphological properties, *i.e.* having a porphyrin molar ratio of 10 %, was introduced as donor in the active layer of BHJ solar cells with **$PC_{61}BM$** as acceptor material leading to very poor PCE (< 0.1 %). Many other studies are actually needed to determine if these low performances are intrinsically due to the nature of the donor material or

to the fabrication process, as only a serie of three cells has been tested. AFM analyses could be carried out on **3a**:**$PC_{61}BM$** mixtures to see if the morphology remains well-structured by adding the acceptor part. Others cells could be further processed by changing the deposition conditions to ensure the fibrillar structuration. If the future results are encouraging, other porphyrin derivatives with extended spectral features could be incorporated following this strategy.

EXPERIMENTAL PROCEDURE

1. MATERIALS AND INSTRUMENTATION

The details concerning the materials and instrumentation are described in Chapter 5.
The synthesis of 2,5-dibromo-3-(6'-bromohexyl)thiophene and the cyclized porphyrin **NH-NiTPP** were performed following reported procedures.[26a, 47]

2. SYNTHETIC PROCEDURES

2.1. REGIOREGULAR POLYTHIOPHENE-PORPHYRIN SUPRAMOLECULAR COMPLEXES

Synthesis of 3-[6'-(1"-imidazolyl)hexyl]thiophene (TIm). Dry THF (10 mL) was added to sodium hydride (60% in oil; 268 mg, 6.69 mmol). A solution of imidazole (414 mg, 6.08 mmol) in THF (10 mL) was added dropwise at 0 °C to this suspension. After stirring at room temperature for 2 hours, 3-(6'-bromohexyl)thiophene (1.00 g, 4.06 mmol) was added. The reaction mixture was then stirred for 16 h at reflux. After cooling to room temperature, the solvent was removed by evaporation. Water (50 mL) was added to the residue and the aqueous layer was extracted with dichloromethane (3×25 mL). The organic layer was then washed with water (25 mL) and a saturated solution of sodium chloride (25 mL), dried over $MgSO_4$, filtered off, and concentrated under vacuum. The residue was purified by column chromatography on silica gel eluting with dichloromethane - ethanol (95:5) to give the **TIm** as a colorless liquid (826 mg, 87 %). **^{1}H NMR (300 MHz, $CDCl_3$, δ):** 7.35 (m, 1H, ImH), 7.14 (m, 1H, ThH), 6.97 (s, 1H, ImH), 6.85 (s, 1H, ImH), 6.82 (s, 1H, ThH), 6.80 (s, 1H, ThH), 3.78 (t, $^3J_{H-H}$ = 7.1 Hz, 2H, NCH_2), 2.53 (t, $^3J_{H-H}$ = 7.3 Hz, 2H, $ThCH_2$), 1.53 (m, 4H, CH_2), 1.20 (m, 4H, CH_2) ppm. **^{13}C{^{1}H} NMR (75 MHz, $CDCl_3$, δ):** 143.1, 137.4, 129.6, 128.5, 125.5, 120.3, 119.1, 47.2, 31.3, 30.6, 30.5, 30.4, 28.9, 26.6, ppm. **MS (ESI):** *m/z* = 235.1 $[M+H]^+$.

Complexation procedure of the zinc porphyrins with TIm. To a solution of **TIm** (0.05 mmol) in chloroform (1 mL) was added a solution of zinc porphyrin **1Zn** or **2Zn** (0.05 mmol) in chloroform (4 mL). The reaction mixture was stirred at room temperature for 1 h and then, the solvent was removed by evaporation. The residue was recrystallized from a chloroform/*n*-hexane mixture affording the desired complexes **TIm**-**1Zn** and **TIm**-**2Zn** as purple crystals.

TIm-1Zn: Yield: 98 % (47 mg). **^{1}H NMR (300 MHz, $CDCl_3$, δ):** 8.85 (s, 8H, PyrH), 8.08 (d, $^3J_{H-H}$ = 6.0 Hz, 8H, ArH), 7.51 (d, $^3J_{H-H}$ = 6.0 Hz, 8H, ArH), 7.19 (m, 1H, ThH), 6.78 (m, 2H, ThH), 5.18 (m, 1H, ImH), 3.17 (m, 1H, ImH), 2.64 (m, 12H, CH_3), 2.42 (t, $^3J_{H-H}$ = 7.5 Hz, 2H, $ThCH_2$), 1.82 (m, 2H, NCH_2), 1.31 (m, 2H, CH_2), 0.87 (m, 4H, CH_2), 0.51 (m, 2H, CH_2) ppm. **MS (ESI):** *m/z* = 966.2 $[M+H]^+$. **UV–vis (toluene):** λ_{max} (ε) = 432 (538000), 566 (21500), 610 (13800) nm.

TIm-2Zn: Yield: 96 % (61 mg). **^{1}H NMR (300 MHz, $CDCl_3$, δ):** 8.90 (s, 8H, PyrH), 7.20 (m, 1H, ThH), 6.79 (m, 2H, ThH), 4.94 (m, 1H, ImH), 4.45 (m, 1H, ImH), 2.40 (m, 1H, ImH), 1.85 (m, $^3J_{H-H}$ = 7.5 Hz, 2H, $ThCH_2$), 1.26 (m, 2H, NCH_2), 0.81 (m, 2H, CH_2), 0.65 (m, 4H, CH_2), 0.28 (m, 2H, CH_2) ppm. **^{19}F NMR (282 MHz, $CDCl_3$, δ):** −136.2, −137.9, −152.7, −161.9, −162.7 ppm. **MS (MALDI-ToF):** *m/z* = 1270.2 $[M]^+$. **UV–vis (toluene):** λ_{max} (ε) = 423 (435000), 558 (22000), 593 (1500) nm.

Poly(3-hexylthiophene-2,5-diyl)-*ran*-Poly[3-(6'-bromohexyl)thiophene-2,5-diyl] random copolymer (P3HT-*r*-P3HTBr, 90:10). Two round-bottom flasks (100 mL) were dried by heating under reduced pressure and cooled to room temperature. 2-Bromo-3-hexyl-5-iodothiophene (0.68 g, 1.82 mmol) and 2,5-dibromo-3-(6'-bromohexyl)thiophene (0.10 g, 0.25 mmol) were dried by three successive azeotropic distillations with toluene and then, dried THF (10 mL) was added. One equivalent of *i*PrMgCl (2 M in THF) was added to those solutions via a syringe, and the mixtures were stirred at 0°C for 30 min (solutions A and B). Solutions A and B were brought together and then, added in one portion to the $Ni(dppp)Cl_2$ catalyst (8 mg) in THF (10 mL). The resulting solution was stirred overnight. The reaction was quenched quickly by pouring HCl aq. (5 M) into the solution and stirring for 0.5 h. Then, the mixture was precipitated in cold MeOH and filtered. The product was washed with MeOH and *n*-hexane to afford **P3HT-*r*-P3HTBr** (90:10) as a red solid. Yield: 82 % (0.99 g). **^{1}H NMR (600 MHz, $CDCl_3$, δ):** 6.98 (s, 2H, Th), 3.42 (t, 2H, CH_2Br, $^3J_{H-H}$ = 6.7 Hz), 2.80 (t, 4H, $ThCH_2$, $^3J_{H-H}$ = 7.9 Hz), 1.62 (m, 16H, CH_2), 0.90 (t, 3H, CH_3, $^3J_{H-H}$ = 6.8 Hz) ppm. **^{13}C{^{1}H} NMR (150 MHz, $CDCl_3$, δ):** 140.0, 139.8, 130.8, 130.7, 128.8, 34.0, 32.9, 31.8, 30.7, 30.5, 29.6, 29.4, 28.8, 28.1, 22.8, 14.3. **UV–vis (toluene):** λ_{max} = 458 nm; **SEC (THF, PS standards):** M_n = 23 800 g mol^{-1}, Đ = 1.17.

Poly(3-hexylthiophene-2,5-diyl)-*ran*-poly[3-(6'-(1"-imidazolyl)hexyl)thiophene-2,5-diyl] random copolymer (P3HT-*r*-P3HTIm, 90:10). THF (10 mL) was placed into a two-neck round-bottom flask (100 mL) containing sodium hydride (60 % in oil; 0.24 g, 6.10 mmol). Imidazole (0.35 g, 5.10 mmol) in THF (10 mL) was added dropwise to this suspension at 0 °C and then, the mixture was stirred for 2 h at room temperature. **P3HT-*r*-P3HTBr** (2.25 mmol) dissolved in THF (20 mL) was added to the previous solution and the mixture was refluxed for two days. After cooling to room temperature, the mixture was hydrolyzed. The organic layer was extracted with chloroform (100 mL), washed with water (3×100 mL), and then, dried over anhydrous $MgSO_4$. The solution was concentrated and the polymer was precipitated in cold MeOH. The polymer was isolated by filtration, washed with water and methanol. It was further purified with

refluxing methanol and pentane by using a Soxhlet apparatus and finally, dried under vacuum to afford **P3HT-*r*-P3HTIm** (90:10). Yield: 76 %. **^{1}H NMR (300 MHz, $CDCl_3$, δ):** 7.42 (s, 1H, Im), 7.02 (s, 1H, Th), 6.99 (s, 1H, Im), 6.82 (s, 1H, Im), 3.86 (m, 2H, CH_2-N), 2.83 (m, 2H, CH_2-Th), 1.41 (m, 8H, CH_2), 0.95 (m, 3H, CH_3) ppm. **^{13}C{^{1}H} NMR (75 MHz, $CDCl_3$, δ):** 140.1, 137.2, 133.9, 130.7, 129.6, 128.8, 118.9, 47.2, 31.9, 30.7, 29.6, 29.4, 26.6, 22.8, 14.3 ppm. **UV–vis (toluene):** λ_{max} = 458 nm.

Complexation procedure of the zinc Porphyrins with the P3HT-*r*-P3HTIm random copolymer. To a solution of zinc porphyrin **1Zn** or **2Zn** (0.5 mmol) in toluene was added **P3HT-*r*-P3HTIm** (0.4 mmol, calculated from the imidazole part). The reaction mixture was then stirred at 70 °C for 1 h. The complexation was followed by UV–vis absorption spectroscopy. A second portion of **P3HT-*r*-P3HTIm** (0.1 mmol, calculated from the imidazole part) was added to complete the complexation. The mixture was stirred for an additional hour at 70 °C and then, the solvent was removed by evaporation. The residue was redissolved in a minimum amount of chloroform and poured into *n*-pentane. The solid was filtered off, washed with *n*-heptane and dried under vacuum to afford a black solid.

PTIm-1Zn: Yield: 92 %. **^{1}H NMR (600 MHz, $CDCl_3$, δ):** 8.85 (s, PyrH), 8.05 (d, $^3J_{H\text{-}H}$ = 7.4 Hz, ArH), 7.48 (d, $^3J_{H\text{-}H}$ = 7.4 Hz, ArH), 6.99-6.84 (br., ThH and ImH), 5.14 (br., CH_2), 2.81 (br., CH_2), 2.66 (s, CH_3), 1.71 (br., CH_2), 1.44-1.37-1.26 (br., CH_2), 0.92 (br., CH_3) ppm. **^{13}C{^{1}H} NMR (150 MHz, $CDCl_3$, δ):** 150.2, 140.8, 140.1, 136.8, 134.6, 133.9, 131.6, 130.7, 128.8, 127.2, 120.6, 31.9, 30.7, 29.6, 29.4, 22.8, 21.6, 14.3 ppm. **UV–vis (toluene):** λ_{max} = 436, 500, 566, 610 nm.

PTIm-2Zn: Yield: 95 %. **^{1}H NMR (600 MHz, $CDCl_3$, δ):** 8.76 (s, PyrH), 6.84 (br., ThH and ImH), 4.93 (m, 2H, ImH), 2.73 (br., $ThCH_2$), 1.63 (br., CH_2), 1.44-1.37-1.26 (br., CH_2), 0.92 (br., CH_3) ppm. **^{13}C{^{1}H} NMR (150 MHz, $CDCl_3$, δ):** 150.2, 140.1, 136.8, 134.1, 131.7, 130.7, 128.8, 31.9, 30.7, 29.6, 29.4, 22.8, 14.3 ppm. **^{19}F NMR (282 MHz, $CDCl_3$, δ):** -136.3, -138.0, -152.8, -162.0, -162.8 ppm. **UV–vis (toluene):** λ_{max} = 438, 516, 566 nm.

2.2. END-FUNCTIONALIZATION OF THE **P3HT** USING PORPHYRIN

1-((6-iodohexyl)oxy)-4'-nitrobenzene. 1,6-diiodohexane (27.9 g, 82.5 mmol), 4-nitrophenol (2.30 g, 16.5 mmol), potassium carbonate (4.6 g, 33 mmol) and 18-crown-6 (0.44 g, 1.65 mmol) were dissolved in acetone (100 mL). The reaction mixture was stirred under reflux for 2 days. After cooling, the resulting solution was concentrated by evaporation and water (450 mL) was added. The aqueous layer was extracted with CH_2Cl_2 (3x100 mL). The combined extracts were washed with a solution of hydrochloric acid 1M (40 mL) and several times with water until pH=7. The organic layer was dried over $MgSO_4$, filtered, evaporated under reduced pressure and purified by column chromatography on silica gel eluting with a gradient of pentane – dichloromethane (100:0 to 50:50) to give the *title compound* as a colorless solid (5.5 g, 95 %). **^{1}H**

NMR (300 MHz, $CDCl_3$, δ): 8.20 (d, 2H, $^3J_{H-H}$ = 9.2 Hz, NO_2-ArH), 6.94 (d, 2H, $^3J_{H-H}$ = 9.2 Hz, O-ArH), 4.05 (t, 2H, $^3J_{H-H}$ = 6.4 Hz, OCH_2), 3.21 (t, 2H, $^3J_{H-H}$ = 6.9 Hz, ICH_2), 1.99 – 1.70 (m, 4H, CH_2), 1.64 – 1.39 (m, 4H, CH_2) ppm. **$^{13}C\{^1H\}$ NMR (75 MHz, $CDCl_3$, δ):** 164.2 (NO_2-C_q), 141.5 (O-C_q), 126.0 (CH), 114.5 (CH), 68.7 (OCH_2), 33.4 (CH_2), 30.2 (CH_2), 28.9 (CH_2), 25.0 (CH_2), 7.0 (ICH_2) ppm. **HRMS (ESI)**: *m/z* = $[M+H]^+$ Calcd for $C_{12}H_{17}INO_3$: 350.0253. Found: 350.0247.

NO_2-Spacer-NiTPP. A solution of **NH-NiTPP** (100 mg, 0.146 mmol) and sodium hydride 60 % (30 mg, 0.73 mmol) in THF (10 mL) was stirred for 15 minutes at room temperature under argon. 1-(6-iodohexyl)-4'-nitrobenzene (56 mg, 0.16 mmol) was then added to the resulting solution and the mixture was stirred under reflux overnight. The *N*-alkylation was followed by TLC. When finished, the solvent was evaporated under reduced pressure and the residue was diluted with dichloromethane. The organic layer was washed several times with water to pH=7, dried over $MgSO_4$, filtered, evaporated and purified by column chromatography on silica gel eluting with cyclohexane – ethyl acetate (90:10) to give the *title compound* as a purple solid (75 mg, 57 %). **^1H NMR (300 MHz, CD_2Cl_2, δ):** 9.38 (d, 1H, $^3J_{H-H}$ = 4.8 Hz, pyrrole), 8.96 (dd, 1H, $^3J_{H-H}$ = 8.1 and 1.6 Hz, ArH), 8.80 (d, 1H, $^3J_{H-H}$ = 4.7 Hz, pyrrole), 8.65-8.49 (m, 4H, pyrrole and ArH-NO_2), 8.13-7.93 (m, 10H, pyrrole and ArH), 7.86-7.59 (m, 11H, ArH), 6.94 (d, 2H, $^3J_{H-H}$ = 9.3 Hz, Ar-OCH_2), 4.94 (t, 2H, $^3J_{H-H}$ = 7.5 Hz, OCH_2), 3.99 (t, 2H, $^3J_{H-H}$ = 6.8 Hz, NCH_2), 2.31 (m, 2H, CH_2), 1.91-1.58 (m, 6H, CH_2) ppm. **$^{13}C\{^1H\}$ NMR (75 MHz, CD_2Cl_2, δ):** 164.7 (C_q-NO_2), 143.9 (C_q), 143.8 (C_q), 142.6 (C_q), 141.8 (C_q), 141.4 (C_q), 140.5 (C_q), 138.6 (C_q), 137.5 (C_q), 136.1 (C_q), 135.9 (CH), 134.3 (C_q), 134.3 (CH), 134.1 (CH), 134.0 (CH), 133.7 (C_q), 133.1 (CH), 132.7 (CH), 132.6 (CH), 132.4 (CH), 130.7 (CH), 130.7 (CH), 128.3 (C_q), 128.0 (CH), 128.0 (CH), 127.5 (CH), 127.5 (CH), 126.3 (CH), 122.6 (CH), 121.3 (CH), 116.0 (C_q), 114.9 (CH), 113.9 (CH), 113.3 (CH), 69.3 (OCH_2), 49.2 (NCH_2), 29.4 (CH_2), 27.7 (CH_2), 27.5 (CH_2), 26.5 (CH_2) ppm. **HRMS (ESI)** : *m/z* = $[M+H]^+$ Calcd for $C_{56}H_{43}N_6NiO_3$: 905.2750. Found: 905.2751. **UV-vis ($CHCl_3$):** λ (ε $M^{-1}.cm^{-1}$) = 423 (74 000), 448 (65 500), 556 (6 300), 602 (10 400), 636 (18 200) nm.

NHCO-Spacer-NiTPP. To a degassed solution of **5** (66 mg, 0.073 mmol) in CH_2Cl_2 (66 mL) and methanol (7.3 mL) was added 10 % Pd/C (3 mg, 0.03 mmol) and then, sodium borohydride (66 mg, 1.7 mmol). The mixture was stirred for 1 h at room temperature under argon. The reaction was followed by TLC. When finished, the solvent was evaporated under reduced pressure and the residue was diluted with dichloromethane. The organic layer was filtered to eliminate salts and evaporated. To a degassed solution of the residue in toluene (5 mL) was added formic acid (5 mL). The mixture was stirred under reflux overnight. The reaction was followed by TLC. When finished, the solvent was evaporated under reduced pressure and the residue was diluted with dichloromethane. The organic layer was washed with aqueous saturated $NaHCO_3$ and water to pH=7, dried over $MgSO_4$, filtered, evaporated and purified by column chromatography on silica gel eluting with dichloromethane to give the *title compound* as a purple solid (56 mg, 87 % in 2

steps). **^{1}H NMR (300 MHz, CD_2Cl_2, δ):** 9.34 (dd, 1H, $^3J_{H-H}$ = 4.8 Hz and 1.2 Hz, pyrrole), 8.91 (dd, 1H, $^3J_{H-H}$ = 8.0 and 1.7 Hz, ArH), 8.78 (dd, 1H, $^3J_{H-H}$ = 4.8 Hz and 1.3 Hz, pyrrole), 8.64-8.54 (m, 4H, pyrrole), 8.37 (d, 0.3H, $^3J_{H-H}$ = 11.5 Hz, amide), 8.16 (d, 0.7H, $^3J_{H-H}$ = 1.8 Hz, amide), 8.08-7.92 (m, 7H, ArH), 7.92 (dd, 1H, $^3J_{H-H}$ = 8.6 Hz and 1.3 Hz, ArH), 7.74-7.61 (m, 11H, ArH), 7.26 (d, 1.3 H, $^3J_{H-H}$ = 9 Hz, NHCHO-ArH), 6.93 (broad s, 1H, NH), 6.97 (d, 0.7 H, $^3J_{H-H}$ = 8.9 Hz, NHCHO-ArH), 6.73 (d, 2H, $^3J_{H-H}$ = 9 Hz, ArH-O), 4.75 (t, 2H, $^3J_{H-H}$ = 7.7 Hz, OCH_2), 3.83 (t, 2H, $^3J_{H-H}$ = 6.3 Hz, NCH_2), 2.20 (m, 2H, CH_2), 1.90-1.56 (m, 6H, CH_2) ppm. **^{13}C{^{1}H} NMR (150 MHz, CD_2Cl_2, δ):** 162.8 (NHCHO), 159.0 (C_q), 145.1 (C_q), 143.9 (C_q), 143.8 (C_q), 143.4 (C_q), 142.6 (C_q), 141.8 (C_q), 141.4 (C_q), 141.4 (C_q), 140.5 (C_q), 138.7 (C_q), 138.5 (C_q), 136.0 (C_q), 135.8 (CH), 134.3 (CH), 134.1 (CH), 134.0 (CH), 133.0 (CH), 132.8 (CH), 132.6 (CH), 132.4 (CH), 130.7 (CH), 130.6 (CH), 128.3 (CH), 128.1 (CH), 128.0 (CH), 127.9 (CH), 127.5 (CH), 127.5 (CH), 122.5 (CH), 122.0 (CH), 121.9 (CH), 121.2 (C_q), 116.0 (C_q), 115.8 (CH), 115.2 (C_q), 115.1 (CH), 113.8 (CH), 109.7 (C_q), 98.5 (CH), 68.5 (OCH_2), 49.2 (NCH_2), 29.7 (CH_2), 27.7 (CH_2), 27.5 (CH_2), 26.5 (CH_2) ppm. **HRMS (ESI)**: *m/z* = $[M+H]^+$ Calcd for $C_{57}H_{45}N_6O_2Ni$: 903.2957. Found: 903.2959. **IR ATR:** 3150 (NH), 1690 (C=O) cm^{-1}. **UV-vis ($CHCl_3$):** λ (ε, $M^{-1}.cm^{-1}$) = 427 (78 000), 448 (74 000), 558 (8 000), 602 (12 000), 638 (20 000) nm.

Synthesis of CN-Spacer-NiTPP. NHCO-Spacer-NiTPP (50 mg, 0.055 mmol) was dissolved in THF (5 mL) and cooled to 0°C. Triethylamine (39 µL, 0.28 mmol) and $POCl_3$ (6 µL, 0.06 mmol) were added by micro-syringe to the mixture and stirring was continued at 0°C for 3 hours. A saturated sodium carbonate solution (5 mL) wad added at room temperature and the resulting solution was stirred for 1 hour. Then, the aqueous layer was extracted with dichloromethane. The organic layer was washed several times with water and brine to pH=7, dried over $MgSO_4$, filtered, evaporated and purified by column chromatography on alumina gel eluting with cyclohexane – dichloromethane (50:50) to give the *title compound* as a purple solid (40 mg, 80 %). **^{1}H NMR (300 MHz, $CDCl_3$, δ):** 9.35 (d, 1H, $^3J_{H-H}$ =4.8 Hz, pyrrole), 8.92 (d, 1H, $^3J_{H-H}$ =7.6 Hz, ArH), 8.81 (d, 1H, $^3J_{H-H}$ = 4.8 Hz, pyrrole), 8.61 (d, 1H, $^3J_{H-H}$ = 5.1 Hz, pyrrole), 8.55 (s, 2H, pyrrole), 8.07-7.90 (m, 7H, ArH/pyrrole), 7.82-7.57 (m, 13H, ArH), 7.21 (d, 2H, J=8.9 Hz, O-ArH), 6.76 (d, 2H, $^3J_{H-H}$ = 8.9 Hz, CN-ArH), 4.67 (t, 2H, $^3J_{H-H}$ = 7.5 Hz), 3.78 (t, 2H, $^3J_{H-H}$ = 6.2 Hz), 2.12 (m, 2H, CH_2), 1.73-1.54 (m, 6H, CH_2) ppm. **^{13}C{^{1}H} NMR (75 MHz, $CDCl_3$, δ):** 159.3 (C_q), 144.6 (C_q), 143.4 (C_q), 143.3 (C_q), 143.0 (C_q), 142.2 (C_q), 141.5 (C_q), 141.1 (C_q), 141.0 (C_q), 140.2 (C_q), 138.3 (C_q), 138.1 (C_q), 135.5 (CH), 135.4 (C_q), 133.8 (CH), 133.7 (CH), 133.5 (CH), 132.8 (CH), 132.4 (CH), 132.2 (CH), 130.5 (CH), 130.4 (CH), 129.7 (C_q), 127.8 (CH), 127.7 (CH), 127.6 (CH), 127.6 (CH), 127.5 (CH), 127.3 (CH), 127.1 (CH), 127.0 (CH), 122.0 (CH), 120.9 (C_q), 120.8 (C_q), 115.7 (C_q), 115.0 (CH), 114.6 (C_q), 113.0 (CH), 109.2 (C_q), 98.0 (CH), 68.1 (OCH_2), 48.4 (NCH_2), 29.0 (CH_2), 27.2 (CH_2), 27.1 (CH_2), 26.0 (CH_2) ppm. **HRMS (ESI)** : *m/z* = $[M+H]^+$ Calcd for $C_{57}H_{43}N_6NiO$: 885.2841. Found: 885.2852. **IR ATR:** 2118 cm^{-1} ($\nu_{N\equiv C}$). **UV-vis ($CHCl_3$):** λ (ε $M^{-1}.cm^{-1}$) = 423 (48 000), 448 (44 000), 557 (4 300), 601 (7 300), 637 (13 000) nm.

EXPANDING THE LIGHT ABSORPTION OF P3HT DERIVATIVES BY FUNCTIONALIZATION WITH PORPHYRINS

General procedure for the synthesis of P3HT end-functionalized with π-extended porphyrins (3). To a dried round-bottomed flask containing 2-bromo-3-hexyl-5-iodothiophene (X mmol), previously dried by three successive azeotropic distillations with toluene, was added dry THF (C = 0.2 M). *i*PrMgCl.LiCl (1.3 M in THF, X mmol) was then added via a syringe and the mixture was stirred at 0°C for 30 minutes. To a second dried round-bottomed flask containing the Ni(dppp)Cl_2 catalyst ((166X+885Y)/M_n) in THF (C = 0.01 M), was added the first solution of 2-bromo-5-chloromagnesio-3-hexylthiophene. The resulting orange mixture was stirred at room temperature under nitrogen and the polymerization was monitored by GPC. After stirring the reaction mixture for 3 hours, the isocyanide porphyrin **CN-Spacer-NiTPP** (Y mmol) was added in one portion and the resulting green solution was stirred overnight. By pouring aq. HCl (5 M) quickly, the polymerization was quenched and then, the mixture was poured into cold MeOH causing a dark precipitate. The solids were filtered off, washed with methanol and dried under vacuum to afford a black solid.

3a: 70 %. **Ratio (3HT:Porphyrin):** 90:10. **^{1}H NMR (600 MHz, $CDCl_3$, δ):** 8.52 (br.), 7.92 (br.), 7.56 (br.), 7.00 (s), 2.89 (br.), 1.74 (br.), 1.46-1.29 (br.), 0.94 (br.) ppm. **^{13}C{^{1}H} NMR (150 MHz, $CDCl_3$, δ):** 140.03, 133.83, 130.62, 128.74, 127.54, 126.99, 31.82, 30.64, 29.83, 29.78, 29.60, 29.38, 22.78, 14.24 ppm. **SEC (THF, PS standards):** M_n = 12 200 g.mol^{-1}, Đ = 1.39. **UV-vis ($CHCl_3$):** λ = 426, 451, 555, 600, 636 nm.
3b: 62 %. **Ratio (3HT:Porphyrin):** 86:14. **^{1}H NMR (600 MHz, $CDCl_3$, δ):** 8.52 (br.), 7.94 (br.), 7.58 (br.), 6.99 (s), 4.80 (br.), 3.89 (br.), 2.81 (br.), 2.56 (br.), 1.72 (br.), 1.44-1.27 (br.), 0.92 (br.) ppm. **^{13}C{^{1}H} NMR (150 MHz, $CDCl_3$, δ):** 143.6, 141.2, 140.2, 140.1, 138.4, 135.7, 134.0, 133.9, 133.7, 132.4, 130.7, 130.4, 128.98, 127.8, 127.6, 127.1, 121.9, 120.8, 115.7, 114.7, 113.1, 109.1, 98.0, 33.9, 31.9, 30.7, 29.9, 29.7, 29.4, 27.1, 22.8, 14.2 ppm. **GPC (THF, PS standards):** M_n = 9 200 g.mol^{-1}, Đ = 1.28. **UV-vis ($CHCl_3$):** λ = 426, 451, 555, 600, 636 nm.
3c: 60 %. **Ratio (3HT:Porphyrin):** 68:32. **^{1}H NMR (600 MHz, $CDCl_3$, δ):** 8.47 (br.), 7.85 (br.), 7.47 (br.), 6.99 (br.), 6.80 (br.), 2.83 (br.), 2.61 (br.), 1.61 (br.), 1.35-1.29 (br.), 0.93 (br.) ppm. **^{13}C{^{1}H} NMR (151 MHz, $CDCl_3$, δ):** 143.4, 142.2, 141.2, 140.3, 138.3, 133.8, 133.5, 132.2, 130.3, 128.4, 127.5, 126.9, 125.7, 125.3, 124.7, 121.7, 120.7, 118.2, 115.7, 109.1, 97.8, 68.4, 48.8, 31.9, 31.8, 30.7, 29.9, 29.8, 29.6, 29.4, 29.0, 26.8, 22.7, 14.2 ppm. **GPC (THF, PS standards):** M_n = 5 000 g.mol^{-1}, Đ = 1.18. **UV-vis ($CHCl_3$):** λ = 426, 451, 555, 600, 636 nm.

REFERENCES

[1] (a) S. Savagatrup, A. D. Printz, T. F. O'Connor, A. V. Zaretski, D. Rodriquez, E. J. Sawyer, K. M. Rajan, R. I. Acosta, S. E. Root and D. J. Lipomi, *Energy Environ. Sci.* **2015**, *8*, 55; (b) I. Burgués-Ceballos, M. Stella, P. Lacharmoisea and E. Martínez-Ferrero, *J. Mater. Chem. A* **2014**, *2*, 17711;

(c) G. Li, R. Zhu and Y. Yang, *Nature Photon.* **2012**, *6*, 153; (d) P.-L. T. Boudreault, A. Najari and M. Leclerc, *Chem. Mater.* **2011**, *23*, 456.

[2] (a) M. A. Green, K. Emery, Y. Hishikawa, W. Warta and E. D. Dunlop, *Prog. Photovolt: Res. Appl.* **2014**, *22*, 1; (b) S. Lizin, S. Van Passel, E. De Schepper, W. Maes, L. Lutsen, J. Manca and D. Vanderzande, *Energy Environ. Sci.* **2013**, *6*, 3136; (c) F. C. Krebs, N. Espinosa, M. Hösel, R. R. Sondergaard and M. Jorgensen, *Adv. Mater.* **2014**, *26*, 29.

[3] W. Ma, C. Yang, X. Gong, K. Lee and A. J. Heeger, *Adv. Funct. Mater.* **2005**, *15*, 1617.

[4] (a) R. Po, A. Bernardi, A. Calabrese, C. Carbonera, G. Corso and A. Pellegrino, *Energy Environ. Sci.* **2014**, *7*, 925; (b) A. Rivaton, A. Tournebize, J. Gaume, P.-O. Bussière, J.-L. Gardette and S. Therias, *Polym. Int.* **2014**, *63*, 1335; (c) K. Vandewal, S. Himmelberger and A. Salleo, *Macromolecules,* **2013**, *46*, 6379.

[5] (a) D. Chi, S. Qu, Z. Wang and J. Wang, *J. Mater. Chem. C* **2014**, *2*, 4383; (b) A. Marrocchi, D. Lanari,A. Facchetti and L. Vaccaro, *Energy Environ. Sci.* **2012**, *5*, 8457; (c) M. T. Dang, L. Hirsch and G. Wantz, *Adv. Mater.* **2011**, *23*, 3597.

[6] S. H. Park, A. Roy, S. Beaupré, S. Cho, N. Coates, J. S. Moon, D. Moses, M. Leclerc, K. Lee and A. J. Heeger, *Nat. Photonics* **2009**, *3*, 297.

[7] C. J. Brabec, S. Gowrisanker, J. J. M. Halls,D. Laird, S. Jia and S. P. Williams, *Adv. Mater.* **2010**, *22*, 3839.

[8] (a) E. Zhou, K. Hashimoto and K. Tajima, *Polymer* **2013**, *54*, 6501; (b) H. Zhou, L. Yang and W. You, *Macromolecules* **2012**, *45*, 607; c) Y. Li, *Acc. Chem. Res.* **2012**, *45*, 723.

[9] (a) J. You, L. Dou, K. Yoshimura, T. Kato, K. Ohya, T. Moriarty, K. Emery, C. C. Chen, J. Gao, G. Li and Y. Yang, *Nat. Commun.* **2013**, *4*, 1446; (b) S. Sista, Z. Hong, L.-M. Chen and Y. Yang, *Energy Environ. Sci.* **2011**, *4*, 1606.

[10] (a) M. G. Murali, A. D. Rao,S. Yadava and P. C. Ramamurthy, *Polym. Chem.* **2015**, *6*, 962; (b) H. Xu, H. Ohkita, T. Hirata, H. Benten and S. Ito, *Polymer* **2014**, *55*, 2856; (c) B. Ananda Rao, M. Sasi Kumar, G. Sivakumar, S. P. Singh, K. Bhanuprakash, V. Jayathirtha Rao and G. D. Sharma, *ACS Sustainable Chem. Eng.* **2014**, *2*, 1743; (d) S. Honda, S. Yokoya, H. Okhita, H. Benten and S. Ito, *J. Phys. Chem. C* **2011**, *115*, 11306.

[11] (a) T. Higashino and H. Imahori, *Dalton Trans.* **2015**, *44*, 448; (b) M. Urbani, M. Grätzel, M. K. Nazeeruddin and T. Torres, *Chem. Rev.* **2014**, *114*, 12330; (c) L.-L. Li and E. W.-G. Diau, *Chem. Soc. Rev.* **2013**, *42*, 291; (d) J. Kesters, P. Verstappen, M. Kelchtermans, L. Lutsen,D. Vanderzande and W. Maes, *Adv. Energy Mater.* **2015**, *5*, 1500218; (e) H. Qin, L. Li, F. Guo, S. Su, S. Peng, Y. Cao and X. Peng, *Energy Environ. Sci.* **2014**, *7*, 1397; (f) L. Li, Y. Huang, J. Peng, Y. Cao and X. Peng, *J. Mater. Chem. A* **2013**, *1*, 2144; (g) Y. Huang, L. Li, X. Peng, J. Peng and Y. Cao, *J. Mater. Chem.* **2012**, *22*, 21841.

[12] T. Hasobe, P. V. Kamat,M. A. Absalom, Y. Kashiwagi, J. Sly, M. J. Crossley, K. Hosomizu, H. Imahori and S. Fukuzumi, *J. Phys. Chem. B* **2004**, *108*, 12865; b) Y.-B. Wang and Z. Lin, *J. Am. Chem. Soc.* **2003**, *125*,6072; c) F. Diederich and M. Gömez-Löpez, *Chem. Soc. Rev.* **1999**, *28*, 263.

[13] (a) B. J. Campo, J. Duchateau, C. R. Ganivet, B. Ballesteros, J. Gilot, M. M. Wienk, W. D. Oosterbaan, L. Lutsen, T. J. Cleij, G. de la Torre, R. A. J. Janssen, D. Vanderzande and T. Torres, *Dalton Trans.* **2011**, *40*, 3979; (b) Y.-H. Chao, J.-F. Jheng, J.-S. Wu, K.-Y. Wu, H.-H. Peng, M.-C. Tsai, C. Li Wang, Y.-N. Hsiao, C.-L. Wang, C.-Y. Lin and C.-S. Hsu, *Adv. Mater.* **2014**, *26*, 5205; (c) L. Angiolini, V. Cocchi, M. Lanzi, E. Salatelli, D. Tonelli and Y. Vlamidis, *Mat. Chem. Phys.* **2014**, *146*,464; (d) L. Angiolini, T. Benelli,V. Cocchi, M. Lanzi and E. Salatelli, *React. Funct. Polym.* **2013**, *73*, 1198; (e) E. Aguilar-Ortíz, G. Zaragoza-Galán, N. Solladié, R. Rein, M. Aguilar-Martínez, N. Macías-Ruvalcaba and E. Rivera, *Synth. Met.* **2012**,*162*, 1000.

[14] M. Chevrier, R. Di Ciuccio, O. Coulembier, P. Dubois, S. Richeter, A. Mehdi, S. Clément, "Functionalization of P3HT-based hybrid materials for photovoltaic applications" in *Novel Nanoscale Hybrids*, Wiley, VCH (Eds. B. P. S. Chauhan), *accepted*.

[15] (a) R. E. Andernach, Stephan Rossbauer, R. S. Ashraf, H. Faber, T. D. Anthopoulos, I. McCulloch, M. Heeney and H. A. Bronstein, *Chem. Phys. Chem.* **2015**, *16*, 1223; (b) L. Wang, S. Shi, D. Ma, S. Chen, C. Gao, M. Wang, K. Shi, Y. Li, X. Li and H. Wang, *Macromolecules*, **2015**, *48*, 287; (c) P. Jiang, S. Shi, S. Chen, X. Wang, H. Wang, Y. Li, X. Li, *J. Polym. Sci., Part A: Polym. Chem.* **2013**, *51*, 2243; (d) Y.-C. Wu, Y.-H. Chao, C.-L. Wang, C.-T. Wu, C.-S. Hsu, Y.-L. Zeng and C.-Y. Lin, *J. Polym. Sci., Part A: Polym. Chem.* **2012**, *50*, 5032; (e) S. Lamare, S. M. Aly, D. Fortin and P. D. Harvey, *Chem. Commun.* **2011**, *47*, 10942; (f) W. Zhou, P. Shen, B. Zhao, P. Jiang, L. Deng and S. Tan, *J. Polym. Sci., Part A: Polym. Chem.* **2011**, *49*, 2685.

[16] (a) M. Chevrier, J. Kesters, C. Blayo, S. Richeter, A. Van Der Lee, O. Coulembier, M. Surin, A. Mehdi, R. Lazzaroni, R. C. Evans, W. Maes, P. Dubois and S. Clément, *Macromol. Chem. Phys.* **2016**, *217*, 445 ; (b) M. Chevrier, S. Richeter, O. Coulembier, M. Surin, A. Mehdi, R. Lazzaroni, R. C. Evans, P. Dubois and S. Clément, *Chem. Comm.* **2016**, *52*, 171.

[17] (a) D. M. Guldi, C. Luo, M. Prato, A. Troisi, F. Zerbetto, M. Scheloske, E. Dietel, W. Bauer and A. Hirsch, *J. Am. Chem. Soc.* **2001**, *123*, 9166; (b) H. Imahori and Y. Sakata, *Adv. Mater.* **1997**, *9*, 537.

[18] S. K. Das, B. Song, A. Mahler, V. N. Nesterov, A. K. Wilson, O. Ito and F. D'Souza, *J. Phys. Chem. C* **2014**, *118,* 3994.

[19] (a) F. Meyer, *Prog. Polym. Sci.* **2015**, *47,* 70; (b) P. Verstappen, J. Kesters, W. Vanormelingen, G. H. L. Heintges, J. Drijkoningen, T. Vangerven, L. Marin, S. Koudjina, B. Champagne, J. Manca, L. Lutsen, D. Vanderzande and W. Maes, *J. Mater. Chem. A* **2015**, *3,* 2960; (c) R. S. Bhatta and M. Tsige, *ACS Appl. Mater. Interfaces* **2014**, *6,* 15889; (d) X. He, S. Mukherjee, S. Watkins, M. Chen, T. Qin, L. Thomsen, H. Ade and C. R. McNeill, J. *Phys. Chem. C* **2014**, *118,* 9918; (e) M. Zhang, X. Guo, S. Zhang and J. Hou, *Adv. Mater.* **2014**, *26,* 1118; (f) S. Albrecht, S. Janietz, W. Schindler, J.

Frisch, J. Kurpiers, J. Kniepert, S. Inal, P. Pingel, K. Fostiropoulos, N. Koch and D. Neher, *J. Am. Chem. Soc.* **2012**, *134,* 14932.

[20] F. Takei, K. Onitsuka, N. Kobayashi and S. Takahashi, *Chem. Lett.* **2000**, 914.

[21] (a) M. Su, S.-Y. Shi, Q. Wang, N. Liu, J. Yin, C. Liu, Y. Ding and Z.-Q. Wu, *Polym. Chem*. **2015**, *6*, 6519; (b) R. J. Ono, A. D. Tood, Z. Hu, D. A. Vanden Bout and C. W. Bielawski, *Macromol. Rapid. Commun.* **2013**, *35*, 204; (c) Z.-Q. Wu, J. D. Radcliffe, R. J. Ono, Z. Chen, Z. Li and C. W. Bielawski, *Polym. Chem.* **2012**, *3*, 874; (d) N. Liu, C.-G. Qi, Y. Wang, D.-F. Liu, J. Yin, Y.-Y. Zhu and Z.-Q. Wu, *Macromolecules*, **2013**, *46*, 7753.

[22] A. D. Adler, F. R. Longo, J. D. Finarelli, J. Goldmacher, J. Assour and L. Korsakoff, *J. Org. Chem.* **1967**, *32*, 476.

[23] J. S. Lindsey, I. C. Schreiman, H. C. Hsu, P. C. Kearney and A. M. Marguerettaz, *J. Org. Chem*. **1987**, 52, 827.

[24] J. M. Craig, K. Kadish, K. M. Smith and R. Guilard, *The Porphyrin Handbook Vol. 5*, *Academic Press: New York*, **2000**.

[25] H. B. F. Dixon, A. Cornish-Bowden, C. Liebecq, K. L. Loening, G. P. Moss, J. Reedijk, S. F. Velick, P. Venetianer and J. F. G. Vliegenthart, *Pure Appl. Chem.* **1987**, 59, 779.

[26] (a) P. Bäuerle, F. Würthner and S. Heid, *Angew. Chem. Int. Ed.,* **1990**, *29*, 419; (b) S. Clément, A. Tizit, S. Desbief, A. Mehdi, J. De Winter, P. Gerbaux, R. Lazzaroni and B. Boury, *J. Mater. Chem.* **2011**, *21*, 2733.

[27] (a) F. D'Souza and O. Ito, *Chem. Commun.* **2009**, 4913; (b) F. D'Souza, G. R. Deviprasad, M. E. Zandler, V. T. Hoang, A. Klykov, M. Van Stipdonk, A. Perera, M. E. El-Khouly, M. Fujitsuka and O. Ito, *J. Phys. Chem. A* **2002**, *106*, 3243.

[28] (a) S. Clément, F. Meyer, J. De Winter, O. Coulembier, C. M. L. Vande Velde, M. Zeller, S. Sergeiev, J.-Y. Balandier, R. Lazzaroni, Y. Geerts and P. Dubois, *J. Org. Chem.* **2010**, *75,* 1561; (b) S. Clément, O. Coulembier, P. Dubois, Y. Geerts, R. Lazzaroni, F. Meyer and C. Van de Velde, *Acta Crystallogr., Sect. E: Struct. Rep. Online* **2010**, E66, o896.

[29] S. V. Zaitseva, S. A. Zdanovich, A. S. Semeikin and O. I. Koifman, *Russ. J. Gen. Chem.* **2008**, *78*, 493.

[30] (a) C. B. KC, K. Ohkubo, P. A. Karr, S. Fukuzumi and F. D'Souza, *Chem. Commun*. **2013**, *49*, 7614; (b) F. D'Souza, A. N. Amin, M. E. El-Khouly, N. K. Subbaiyan, M. E. Zandler and S. Fukuzumi, *J. Am. Chem. Soc*. **2012**, *134*, 654.

[31] H. A. Benesi and J. H. Hildebrand, *J. Am. Chem. Soc.* **1949**, *71*, 2703.

[32] K. Yoosaf, J. Iehl, I. Nierengarten, M. Hmadeh, A.-M. Albrecht-Gary, J.-F. Nierengarten and N. Armaroli, *Chem. Eur. J.* **2014**, *20*, 223.

[33] (a) E. F. Palermo and A. J. McNeil, *Macromolecules,* **2012**, *45*, 5948; (b) F. Ouhib, A. Khoukh, J.-B. Ledeuil, H. Martinez, J. Desbrières and C. Dagron-Lartigau, *Macromolecules,* **2008**, *41*, 9736.

[34] (a) R. Miyakoshi, A. Yokozawa and T. Yokozawa, *J. Am. Chem. Soc.* **2005**, *127*, 17542; (b) R. Miyakoshi, A. Yokozawa and T. Yokozawa, *Macromol. Rapid Commun.* **2004**, *25*, 1663.

[35] A. Thomas, J. E. Houston, N. Van den Brande, J. De Winter, M. Chevrier, R. K. Heenan, A. E. Terry, S. Richeter, A. Mehdi, B. Van Mele, P. Dubois, R. Lazzaroni, P. Gerbaux, R. C. Evans and S. Clément, *Polym. Chem.* **2014**, *5*, 3352.

[36] M. Sundberg, O. Inganäs, S. Stafström, G. Gustafsson and B. Sjögren, *Solid State Commun.* **1989**, *71*, 435.

[37] X. Liu, E. K. L. Yeow, S. Velate and R. P. Steer, *Phys. Chem. Chem. Phys.* **2006**, *8*, 1298.

[38] W. I. White, in The Porphyrin, Vol. 5 (Ed: D. Dolphin), Academic Press, New York **1978**, Ch. 7.

[39] K. F. Wong, B. Bagchi and P. J. Rossky, *J. Phys. Chem. A* **2004**, *108,* 5752.

[40] Y. Liang, in *Ultrafast Dynamics of Metalloporphyrins, DNA and Iron-Lanthanide Clusters in the Liquid Phase*, KIT Scientific Publishing, Karlsruhe, Germany **2013**, Dissertation from Karlsruhe Institute of Technologie.

[41] W. D. Oosterbaan, V. Vrindts, S. Berson, S. Guillerez, O. Douhéret, B. Ruttens, J. D'Haen, P. Adriaensens, J. Manca, L. Lutsen and D. Vanderzande, *J. Mater. Chem.* **2009**, *19*, 5424.

[42] (a) P. Koh, S. Huettner, H. Komber, V. Senkovskyy, R. Tkachov, A. Kiriy, R. H. Friend, U. Steiner, W. T. S. Huck, J.-U. Sommer and M. Sommer, *J. Am. Chem. Soc.* **2012**, *134*, 4790; (b) D. E. Motaung, G. F. Malgas, C. J. Arendse, S. E. Mavundla, C. J. Oliphant and D. Knoesen, *Sol. Energy Mater. Sol. Cells* **2009**, *93*, 1674.

[43] (a) M. Surin, S. Cho, J. D. Yuen, G. Wang, K. Lee, P. Leclère, R. Lazzaroni, D. Moses and A. J. Heeger, *J. Appl. Phys.* **2006**, *100*, 33712/1; (b) David D. Moerman, R. Lazzaroni and O. Douhéret, *Appl. Phys. Lett.* **2011**, *99*, 093303.

[44] (a) A. Zen, J. Pflaum, S. Hirschmann, W. Zhuang, F. Jaiser, U. Asawapirom, J. P. Rabe, U. Scherf and D. Neher, *Adv. Funct. Mater.* **2004**, *14*, 757; (b) J. A. Merlo and C. D. Frisbie, *J. Phys. Chem. B* **2004**, *108*, 19169; (c) H. Yang, T. J. Shin, L. Yang, K. Cho, C. Y. Ryu and Z. Bao, *Adv. Funct. Mater.* **2005**, *15*, 671.

[45] (a) J. Weickert, R. B. Dunbar, H. C. Hesse, W. Wiedemann and L. Schmidt-Mende, *Adv. Mater.* **2011**, *23*, 1810; (b) M.-C. Chen, W.-C. Hung, A.-C. Su, S.-H. Chen and S.-A. Chen, *J. Phys. Chem. B* **2009**, *113*, 11124.

[46] J. Niklas, K. L. Mardis, B. P. Banks, G. M. Grooms, A. Sperlich, V. Dyakonov, S. Beaupré, M. Leclerc, T. Xu, L. Yu and O. G. Poluektov, *Phys. Chem. Chem. Phys.* **2013**, *15*, 9562.

[47] S. Richeter, C. Jeandon, J.-P. Gisselbrecht, R. Graff, R. Ruppert and H. J. Callot, *Inorg. Chem.* **2004**, *43*, 251.

[48] (a) E. Lee, B. Hammer, J.-K. Kim, Z. Page, T. Emrick, and R. C. Hayward, *J. Am. Chem. Soc.* **2011**, *133*, 10390; (b) L. G. Liu, G. H. Lu and X. N.Yang, *J. Mater. Chem.* **2008**, *18*, 1984.

[49] S. L. Fronk, C.-K. Mai, M. Ford, R. P. Noland and G. C. Bazan, *Macromolecules*, **2015**, DOI: 10.1021/acs.macromol.5b00986.

[50] S. Berson, R. De Bettignies, S. Bailly and S. Guillerez, *Adv. Funct. Mater*. **2007**, *17*, 1377.

[51] (a) T. J. Prosa, M. J. Winokur, J. Moulton, P. Smith and A. J. Heeger, *Macromolecules*, **1992**, *25*, 4364; (b) K. Tashiro, K. Ono, Y. Minagawa, M. Kobayashi, T. Kawai and K. Yoshino, *J. Polym. Sci., Part B: Polym. Phys.* **1991***, 29*, 1223.

[52] D. Moerman, N. Sebaihi, S. E. Kaviyil, P. Leclère, R. Lazzaroni and O. Douhéret, *Nanoscale*, **2014**, *6*, 10596.

CHAPTER 3

TOWARDS POLYTHIOPHENE-BASED CONJUGATED POLYELECTROLYTES

INTRODUCTION

Conjugated polyelectrolytes (**CPEs**) are defined as polymers with an extended π-conjugated backbone and ionic pendant groups, as they combine the properties of organic semiconductors and the charge-mediated characteristics of polyelectrolytes in a single functional material (Figure 3.1).[1] Three types of **CPEs** can be distinguished depending on the charge of ionic groups: cationic, anionic or zwitterionic **CPEs**. Cationic **CPEs** are mainly based on quaternary ammonium and pyridinium groups while anionic **CPEs** are based on carboxylate ($R\text{-}CO_2^-$), phosphonate ($R\text{-}PO_3^{2-}$) and sulfonate ($R\text{-}SO_3^-$) groups (Figure 3.1). **CPEs** have attracted tremendous interest in recent years, emerging as promising materials for a wide range of applications such as optoelectronic devices, biosensors or biomedical imaging.[2] In particular, **CPEs** have been widely studied as interfacial charge transport and extraction transporting layer materials in organic solar cells.[3] This additional layer induces the formation of an interfacial dipole leading to a reduced work function of the cathode.[4] Improvement of the photovoltaic performances has been observed and attributed to enhanced charge collection, reduced charge recombination and well-balanced charge carrier mobility.[5] Besides, orthogonal solubility with respect to the organic materials in the active layer ensures sequential surface deposition without damaging the underlying films. The variety of **CPE** structures exploited as interfacial layers to date is rather limited and is comprised mainly of thiophene- and fluorene-based (co)polymers with appended polar amine or ionic ammonium moieties.[2a,3a] It is rather surprising since **CPEs** exhibit significant versatility with respect to polymer structure, repeating units, side chains, molecular weight, etc., allowing to tune the optoelectronic properties, to control the nanoscale film morphology and to ensure compatibility with different active layers.[4]

The nature of these ionic groups impacts the solubility of **CPEs** in polar solvents. Scherf *et al.* have notably reported that the diblock copolyelectrolyte polyfluorene-*b*-polythiophene having pyridinium groups was less soluble than its ammonium analogue (**PF2/6-*b*-P3HTPyr** *vs.* **PF2/6-*b*-P3TMAHT**, Figure 3.1).[6] As the optical and electronical properties of theses polymers depend on the π-conjugated backbone, **CPEs** having the same backbone but different ionic side groups display generally the same absorption and photoluminescence profiles.[2c,7] Recently, Maes *et al.* reported the incorporation of imidazolium functionalized polythiophene as electron transporting layer in solar cells, which leads to higher PCEs than the previously reported ammonium functionalized polythiophene (**P3ImiHT** *vs.* **P3TMAHT**, Figure 3.1).[4c-d] This finding indicates that modifying the nature of ionic moieties in such **CPEs** could be a promising approach to further improve the device performances.

In addition to the type of ionic terminal groups, the effect of counterion can be also considered. Bazan *et al.* notably reported that modifying the counterion (bromide *vs.* tetrakis(imidazolyl)borate **BIm$_4$**) in a donor-acceptor based **CPE** copolymer leads to significant variations in charge transport, ionization potential and electron affinity properties (Figure 3.1).[8]

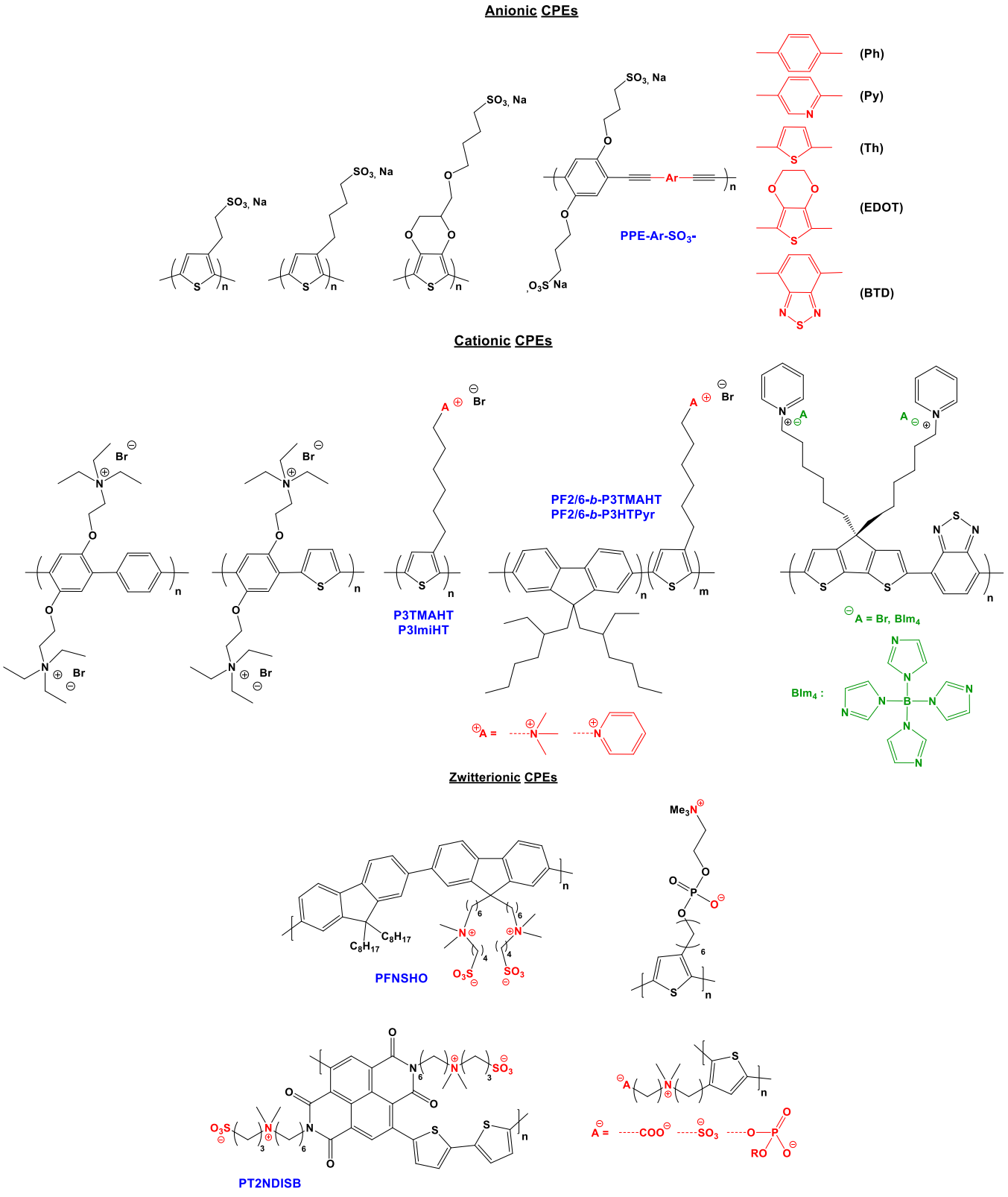

Figure 3.1 Representative examples of **CPEs** structures.[1]

Similarly, the thermal behavior of imidazolium-substituted polythiophenes was found to change completely when the bromide counterion was replaced by either **TFSI**$^-$ or **PF_6^-** (**P3ImiHT-Br/TFSI/PF_6**, Figure 3.1).[9] The counterion can also play a role in controlling the ordering and orientation of the polymer and hence, enabling the orientation of the dipole moment by exploiting the electrostatic self-assembly of the **CPE** with a liquid crystal or surfactant molecule.[10] The stability of the interfacial layer can be also greatly improved compared to the calcium layer often used.[10b]

Since device performance depends on both the optoelectronic properties and nanoscale morphology of the interlayer material, amphiphilic block copolyelectrolytes containing neutral and cationic polythiophene blocks can also help to control the orientation and ordering of the polymer *via* solvent-induced self-assembly.[11] Scherf *et al.* have in particular reported that all-conjugated cationic "rod-rod" block copolyelectrolytes **PF2/6-*b*-P3TMAHT** containing two electronically different conjugated blocks, *i.e.* neutral polyfluorene and ionic polythiophene blocks, exhibit solvent-mediated self-assembly in mixtures of selective and non-selective solvents, such as water-methanol and water-THF (Figure 3.1). The photoluminescence properties were modulated via the segregation of the two blocks.[6,13] Control of the nanomorphology of the self-assembled aggregates (vesicles, rods, etc.) can be obtained through judicious selection of the concentration, solvent or molecular weight of the polymer. Similar changes in nanophase morphology were also observed in all-conjugated cationic diblock copolymers composed of two polyfluorene blocks (neutral and ionic blocks) in protic or non-protic solvents (MeOH *vs.* THF).[13]

In this context, we have decided to seek further understanding concerning the influence of the ionic group, the counterion and the polymer structure (homopolymer *vs.* block copolymer) on the **CPEs** properties. In this chapter, the synthesis and characterization of polythiophene-based **CPEs** having various cationic side-chain groups (*i.e.* methylimidazolium, pyridinium, trimethylphosphonium and trimethylammonium) and counterions (*i.e.* bromide (**Br**$^-$), bis(trifluoromethane)sulfonimide (**TFSI**$^-$), and dodecylsulfate (**DS**$^-$)) will be described first (Figure 3.2). We have chosen to focus on polythiophene-based **CPEs** due to the availability of robust synthetic protocols (*e.g.* Kumada Catalyst Transfer Polycondensation), which allow the relatively straightforward design and preparation of multiple polymer topologies (homopolymers, random/block copolymers) with a high degree of control over the final structure and molecular weight.[12] Then, the optical, thermal and aggregation properties of these **CPEs** will be studied. Finally, their performances as cathode interfacial layer will be investigated with the goal to define clear guidelines on the chemical structure of **CPE** interlayers.

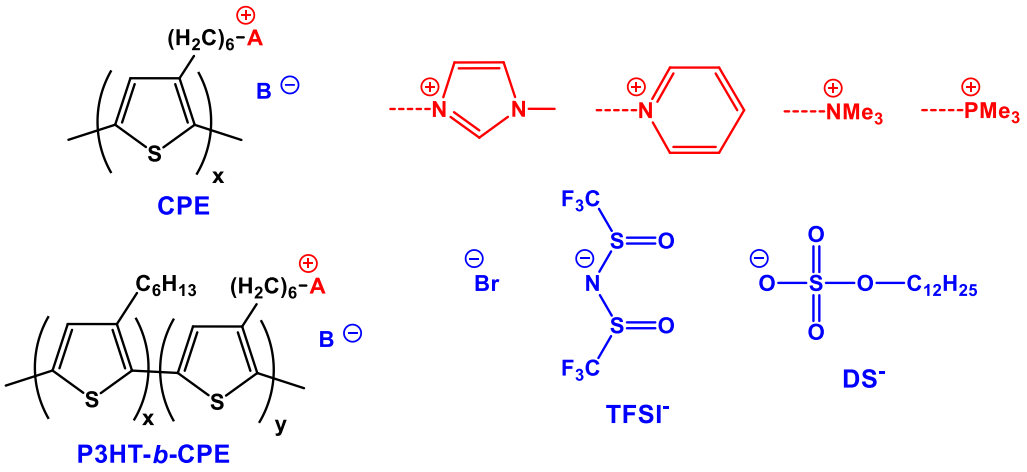

Figure 3.2 Structures of **CPEs** and **P3HT-*b*-CPEs** described in this chapter.

1. SYNTHESIS OF CONJUGATED POLYELECTROLYTES

Conjugated polyelectrolytes (**CPEs**) can be synthesized via two different methods. The first method relies on the polymerization of an ionic monomer whereas the second one is based on the post-polymerization modification of a neutral polymer. For example, polythiophene-based polyelectrolytes are generally obtained by modification of poly(3-bromoalkylthiophenes)[13] or by $FeCl_3$-catalyzed oxidative polymerization.[14] Most poly(arylenes) (phenylene, fluorene, 2,1,3-benzothiadiazole), poly(arylvinylenes) and poly(aryleneethylenes) are generally obtained by Suzuki,[15] Heck[16] and Sonogogashira[17] cross-coupling reactions (Figure 3.3).

In this work, the second strategy will be exclusively used for synthesizing polythiophene-based **CPEs** since in this case, the optoelectronic properties of the polythiophene backbone are predetermined by the polymerization method, i.e. the chain-growth Kumuda Catalyst Transfer Polycondensation (KCTP). Since the optoelectronic properties of polythiophene-based **CPEs** are also dependent on the topology (block copolymer *vs.* homopolymer), the ionic side-chain group and the counterion, a wide range of polymers have been synthesized to understand the structure-property relationship, in particular in view of their performances as cathode interfacial layer. The polythiophene-based **CPEs** were obtained by modification of poly(3-(6'-bromohexyl)thiophene (**P3HTBr**) precursor polymers, in order to benefit from the fact that the bromine atom at the end of the hexyl side chain can be easily substituted by trimethylamine, trimethylphosphine, N-methylimidazole or pyridine, leading to cationic **CPEs**. For our studies, four polymers have been synthetized, *i.e.* two **P3HTBr** homopolymers and two **P3HT-*b*-P3HTBr** diblock copolymers having a **3HT**:**3HTBr** composition around 50:50 and similar molecular weights between 11 000 and 15 100 $g.mol^{-1}$.

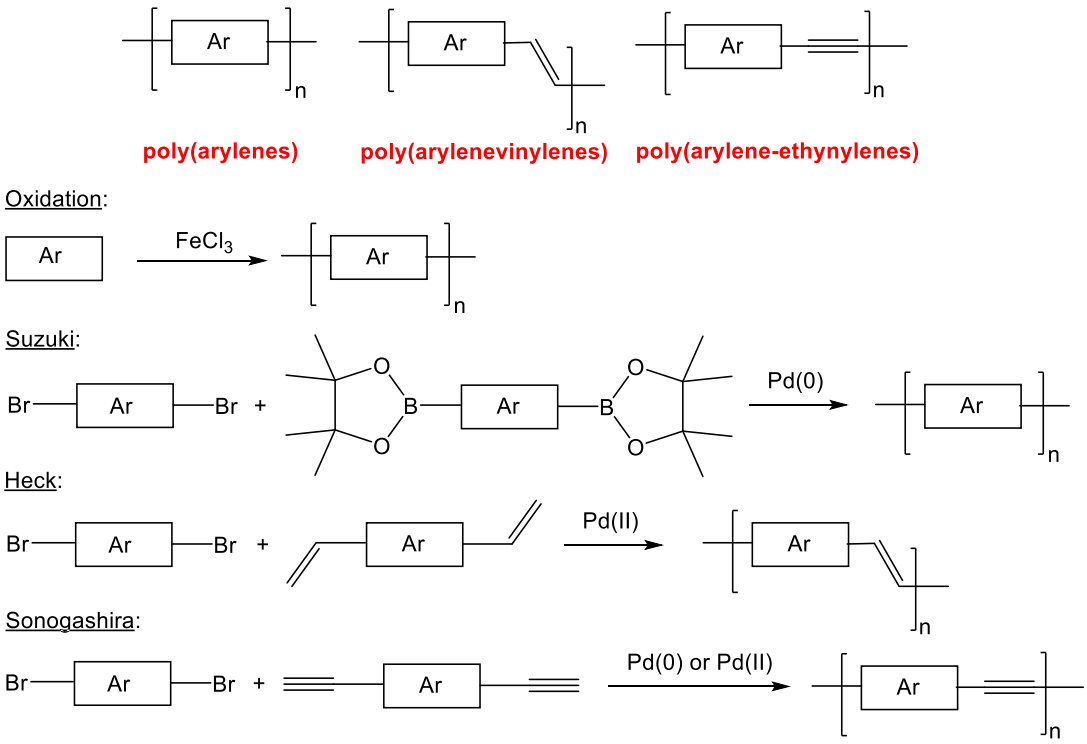

Figure 3.3 Examples of the most widely used polymerization methods; Ar represents aromatic structure.

1.1. SYNTHESIS OF THE MONOMERS

Before the polymerization, it is necessary to prepare the corresponding monomers: 2,5-dibromo-3-(6'-bromohexyl)thiophene (**3HTBr**) and 2-bromo-3-hexyl-5-iodothiophene (**3HT**)). The 2-bromo-3-hexyl-5-iodothiophene was synthesized following a procedure reported in the literature. **3HT** was obtained from the iodination of 2-bromo-3-hexylthiophene with N-iodosuccinimide (NIS) (Scheme 3.1).[18]

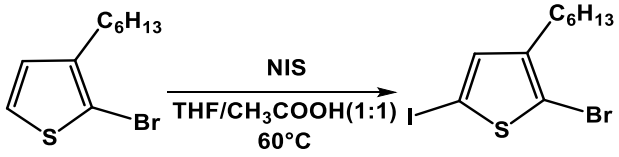

Scheme 3.1 Synthesis of 2-bromo-3-hexyl-5-iodothiophene.

The synthesis of the second monomer, 2,5-dibromo-3-(6'-bromohexyl)thiophene, was carried out following methods reported by Bauerle *et al.* and Clément *et al.* (Scheme 3.2).[19,20]

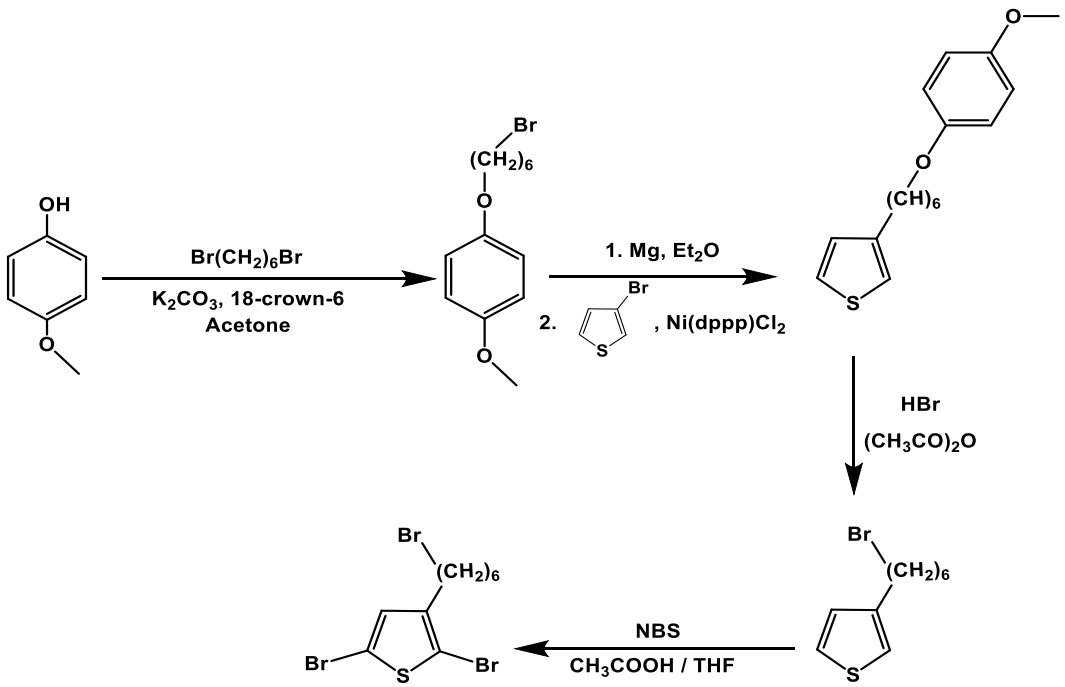

Scheme 3.2 Synthesis of 2,5-dibromo-3-(6'-bromohexyl)thiophene.

1.2. SYNTHESIS OF THE PRECURSOR POLYMERS : **P3HTBR** AND **P3HT-*B*-P3HTBR**

Poly(3-(6'-bromohexyl)thiophene) (**P3HTBr**) and poly[(3-hexylthiophene)-2,5-diyl]-*block*-poly[3-(6'-bromohexyl)thiophene-2,5-diyl] (**P3HT-*b*-P3HTBr**) were synthesized using the KCTP method (Scheme 3.3).

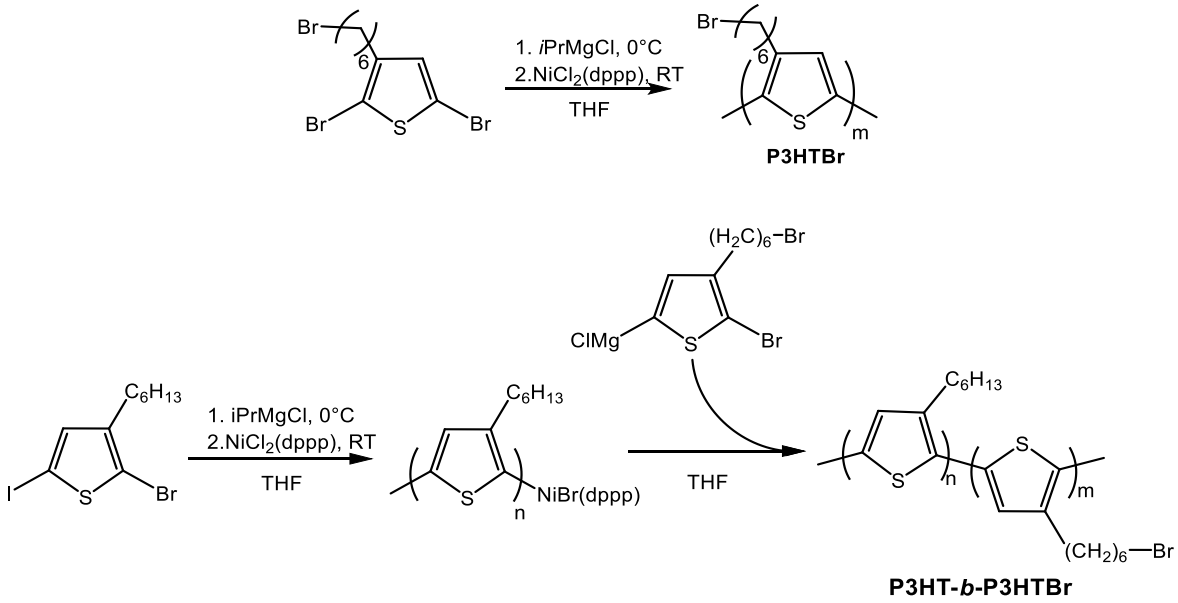

Scheme 3.3 Synthesis of **P3HTBr** (top) and **P3HT-*b*-P3HTBr** (bottom) via the KCTP method.

For the **P3HTBr** homopolymer, the **3HTBr** Grignard reagent was formed *in situ* by adding one equivalent of isopropylmagnesium chloride (iPrMgCl) in THF at 0°C. After 30 minutes under stirring, the Grignard reagent was cannulated on the nickel catalyst ($NiCl_2$(dppp)). The molar ratio between the monomer and the catalyst allows controlling the molecular weight of the polymer. Once the polymerization is finished, *i.e.,* the elution volume observed in SEC analysis has reached its maximum, the polymerization was quickly quenched by adding an aqueous solution of hydrochloric acid 5M, following the procedure reported by Yokozawa *et al.*[21] This quenching procedure prevents the polymer chains from undergoing dimerization, in order to maintain the narrow dispersity while efficiently removing inorganic impurities from the product.

This polymerization method was also used to prepare the **P3HT-*b*-P3HTBr** block copolymers. The **P3HT** block was first synthesized by polymerization of **3HT** with the Ni catalyst to obtain the **P3HT** macroinitiator with the nickel catalyst as end-group. When the first monomer was totally consumed (about 2-3 hours), the **3HTBr** Grignard reagent was added to the reacting solution to obtain the final diblock copolymer **P3HT-*b*-P3HTBr**. After the polymerization, the reaction mixture was also quenched with 5 M HCl, as discussed above. The formation of the final diblock copolymer **P3HT-*b*-P3HTBr** was followed by SEC analysis (Figure 3.4). The comparison of the elution profile of the **P3HT** "block obtained after the first step" to that of the final diblock copolythiophene, a clear shift to shorter elution volume was observed, which corresponds to a higher molecular weight of **P3HT-*b*-P3HTBr**, whilst maintaining a single peak, indicating the "living" character of the polymerization and the formation of the diblock copolymer.

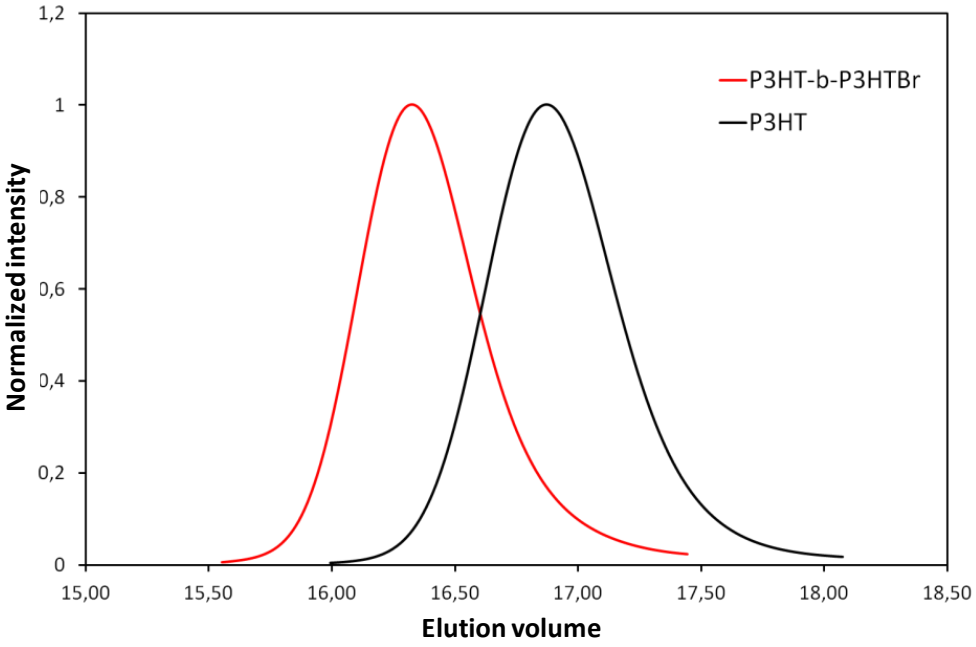

Figure 3.4 SEC profiles obtained during the synthesis of the **P3HT-*b*-P3HTBr** block copolymer.

As indicated above, four polymers having similar molecular weight have been synthesized. Their characteristic data are summarized in Table 3.1.

Table 3.1 Characteristic data for **P3HTBr** and **P3HT-*b*-P3HTBr** polymers.

Polymer	Yield (%)	M_n (g.mol^{-1})[a]	Đ	λ_{max} (nm)[b]	Molar ratio 3HT:3HTBr
P3HTBr - 1	81	14 900	1.39	448	-
P3HTBr - 2	73	13 600	1.36	448	-
P3HT-*b*-P3HTBr (1)	82	11 000	1.12	448	58:42
P3HT-*b*-P3HTBr (2)	82	15 100	1.12	448	59:41

[a] M_n was determined using Size Exclusion Chromatography (SEC) in THF (Standard: PS). [b] The maximal absorption was determined in the chloroform.

In addition to SEC analyses, these polymers were also characterized by MALDI-ToF mass spectrometry (Figure 3.5).[22] MALDI-ToF analysis of **P3HT-*b*-P3HTBr (1)** confirmed the covalent association of 3-(6'-bromohexyl)thiophene and 3-hexylthiophene. Indeed, the presence of *m/z* 166 and *m/z* 245 mass differences confirmed the presence of both monomer units inside the polymer chains. An absolute number-averaged molecular weight (M_n) of 7 980 g.mol^{-1} was determined by MALDI-ToF. Such a difference between the molecular weights obtained by SEC and MALDI-ToF is not unusual since SEC (using polystyrene as standard in THF) usually overestimates the molecular weight of poly(3-alkylthiophene)s by a factor of 1.2–1.3.[23]

The **P3HTBr** and **P3HT-*b*-P3HTBr** polymers were also characterized by ^{1}H NMR spectroscopy (Figure 3.6). A triplet at around 3.4 ppm, characteristic of the CH_2Br groups, is particularly observed in both ^{1}H NMR spectra. The composition of the diblock copolythiophene was determined by integrating the peaks observed at δ 0.9 and 3.4 ppm, assigned to the resonance of the terminal methyl groups of the hexyl side chains in the **P3HT** block and the methylene groups adjacent to the bromine atom in the **P3HTBr** block, respectively (signals e and b, Figure 3.6). From the integration of these two peaks, the **3HT:3HTBr** molar ratio for both copolymers was found to be very close to the feed molar ratio of 55:45.

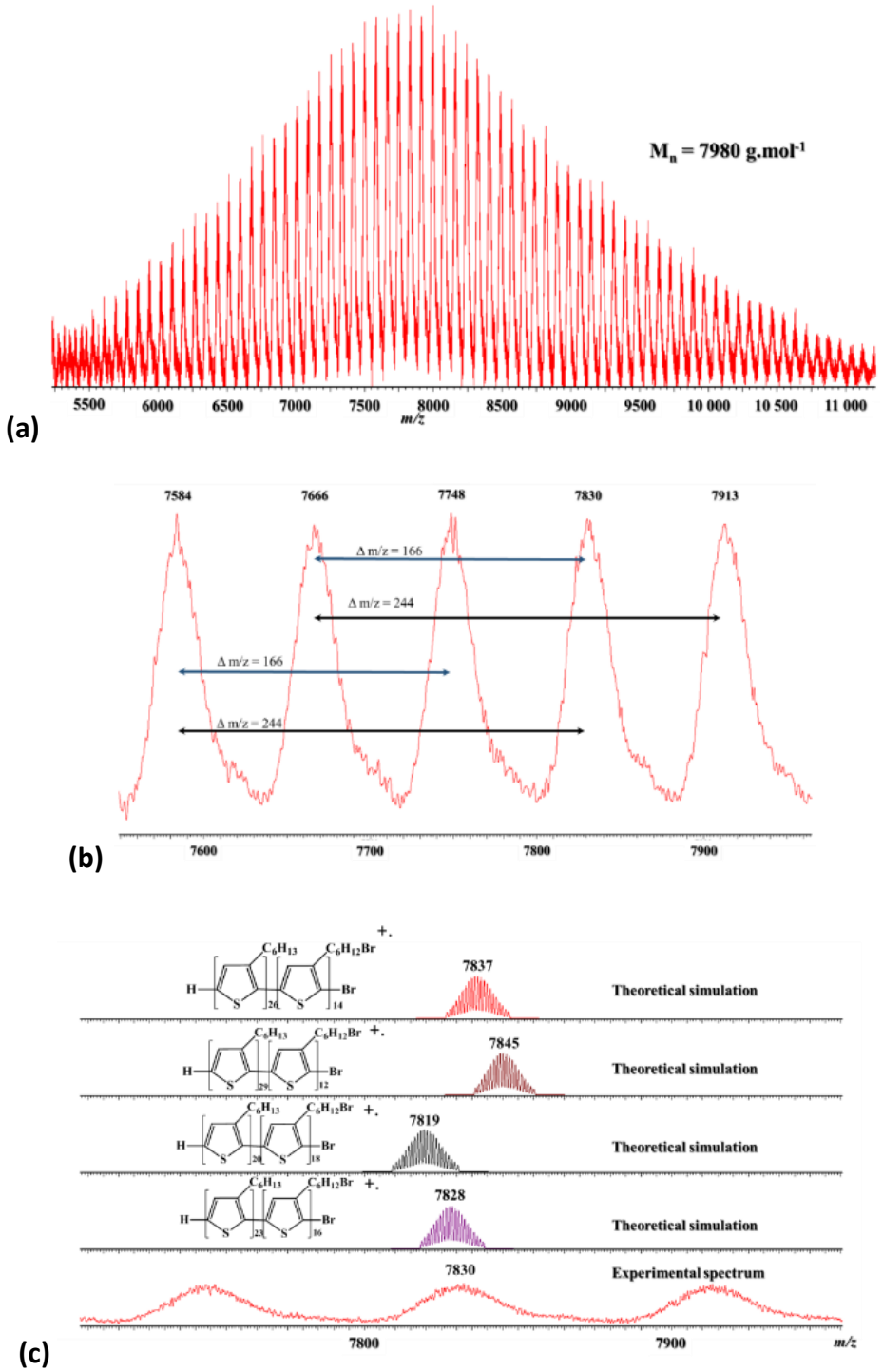

Figure 3.5 (a) Global MALDI-ToF mass spectrum recorded for **P3HT-*b*-P3HTBr (1)**; (b) Magnification between *m/z* 7 550 and *m/z* 7 960. Each signal of the distribution corresponds of an association of many different congeners having similar *m/z*; (c) Some of them are presented for the signal centered at *m/z* 7 830.

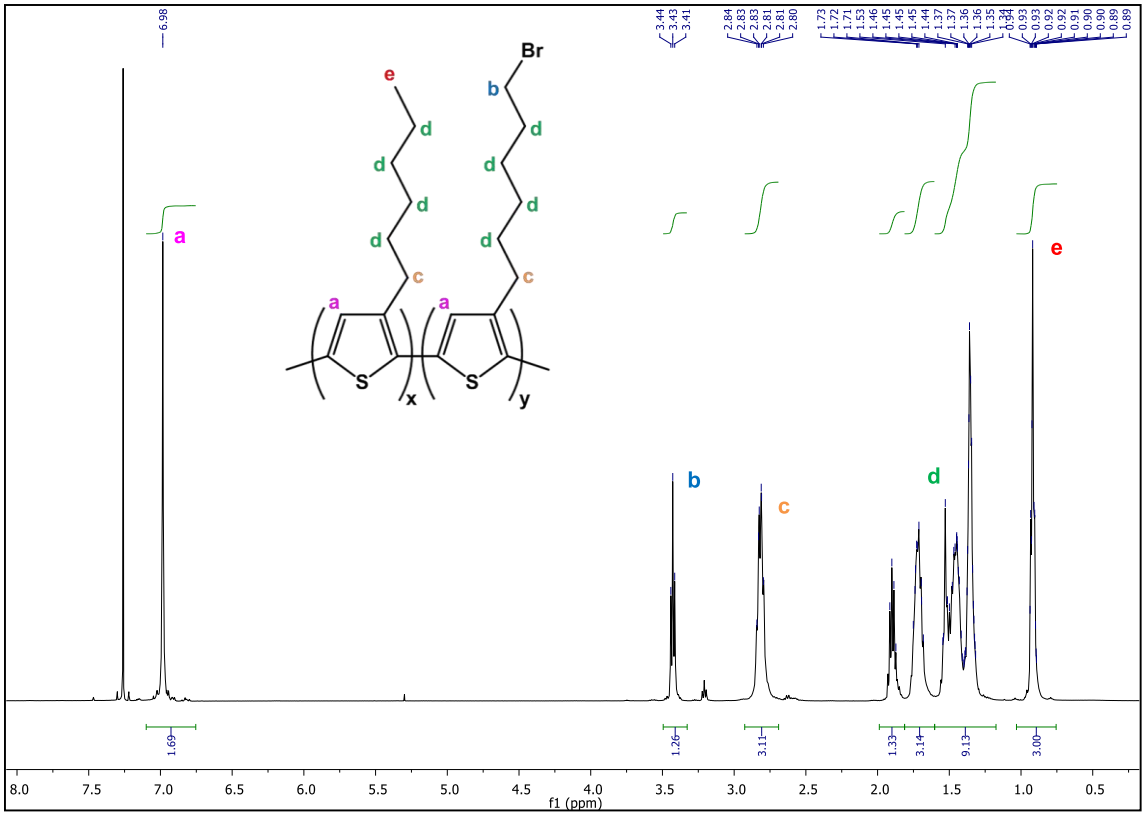

Figure 3.6 ^{1}H NMR spectrum of the **P3HT-*b*-P3HTBr** diblock copolymer in $CDCl_3$.

1.3. SYNTHESIS OF π-CONJUGATED POLYELECTROLYTES

The final step towards the **CPEs** and **P3HT-*b*-CPEs** polyelectrolytes involved the quaternization of the **P3HTBr** and **P3HT-*b*-P3HTBr** precursors with an excess of 1-methylimidazole, pyridine, trimethylamine or trimethylphosphine (Scheme 3.4).[11d,13b] After two days under reflux in chloroform, the **CPEs** are collected by filtration after precipitation into diethyl ether.

The conversion was monitored by ^{1}H NMR spectroscopy by following the shift of the terminal methylene group adjacent to the bromine atom at ~3.4 ppm (in $CDCl_3$) for the precursor polymer. Based on the ^{1}H NMR spectroscopy, the quaternization appeared to be quantitative. For example, the ^{1}H NMR spectrum of **P3HT-*b*-P3HTPMe$_3$,Br** is shown in Figure 3.7 (top). For the ionic diblock copolymers containing cationic nitrogen side groups, the quaternization was also confirmed by the N/S ratio values obtained from elemental analysis, which are very close to the expected values calculated on the basis of the composition of the precursor diblock copolymer.

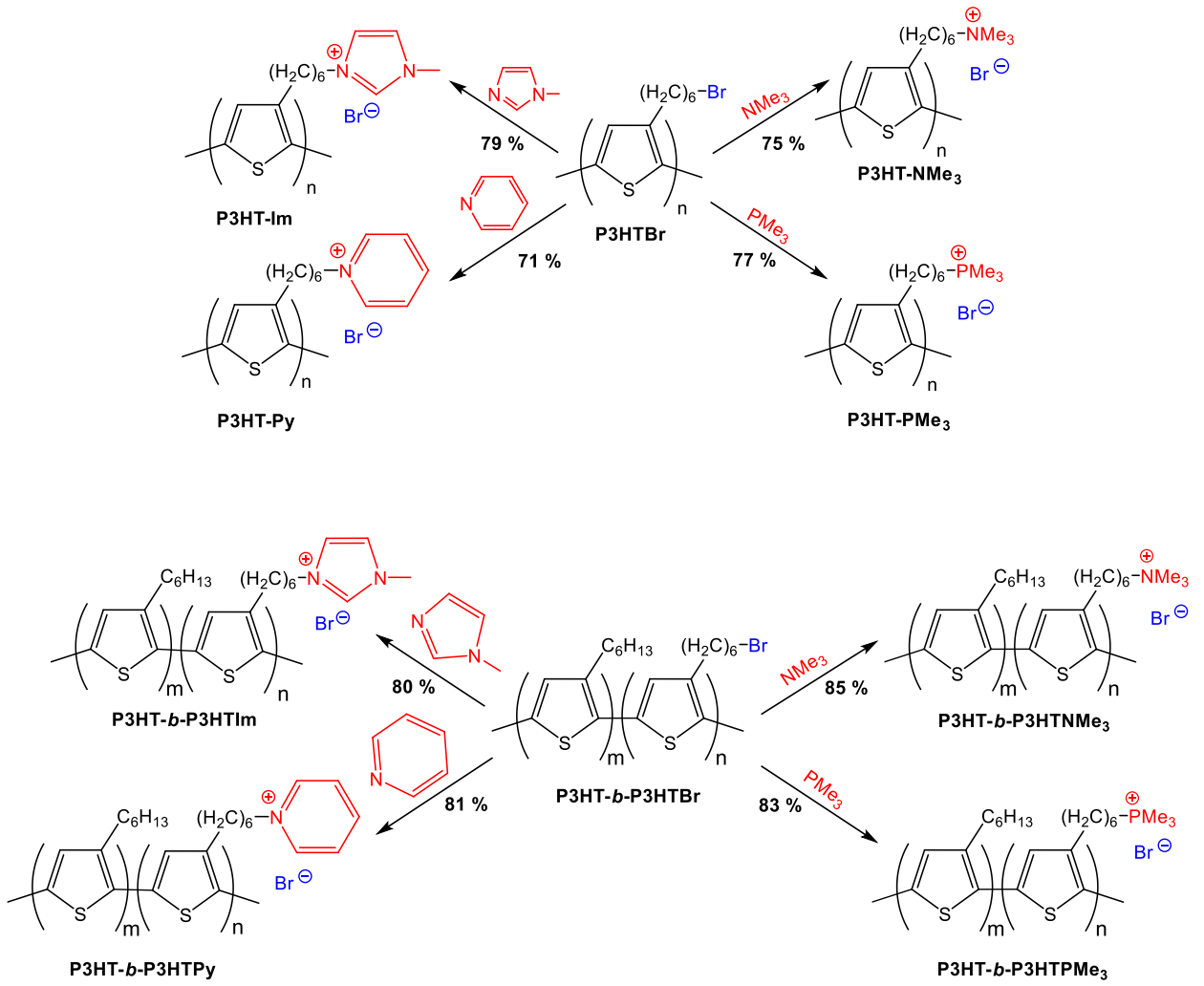

Scheme 3.4 Synthesis of homo- (top) and block co-polyelectrolytes (bottom).

In the case of **CPE-PMe$_3$**, a broad signal around 2-3 pm characteristic of the CH_2-P group is also observed on the ^{1}H NMR spectrum (Figure 3.7, top). The presence of the phosphorous atom is also confirmed by $^{31}P\{^1H\}$ NMR spectroscopy with a singlet around 27 ppm (Figure 3.7, bottom). The molecular weight of the cationic block copolymers was not measured by conventional SEC measurements because of the strong interaction of the copolymer with the columns used.

1.4. COUNTERION EXCHANGE

In 2012, Yang *et al.* have reported that a surfactant/polymer mixture (*i.e.* sodium dodecyl sulfate (SDS)/poly(3-(6'-trimethylammoniumhexyl)thiophene)) used as cathode interfacial layer in solar cells enhanced their stability and performances.[9b] The complexation of surfactants with cationic **CPEs** can induce modification in terms of solubility, optical and self-organization properties.[7,9a] As device performances are linked to these key properties, it is of crucial importance to understand the influence of the counterion on the **CPEs** performances as interfa-

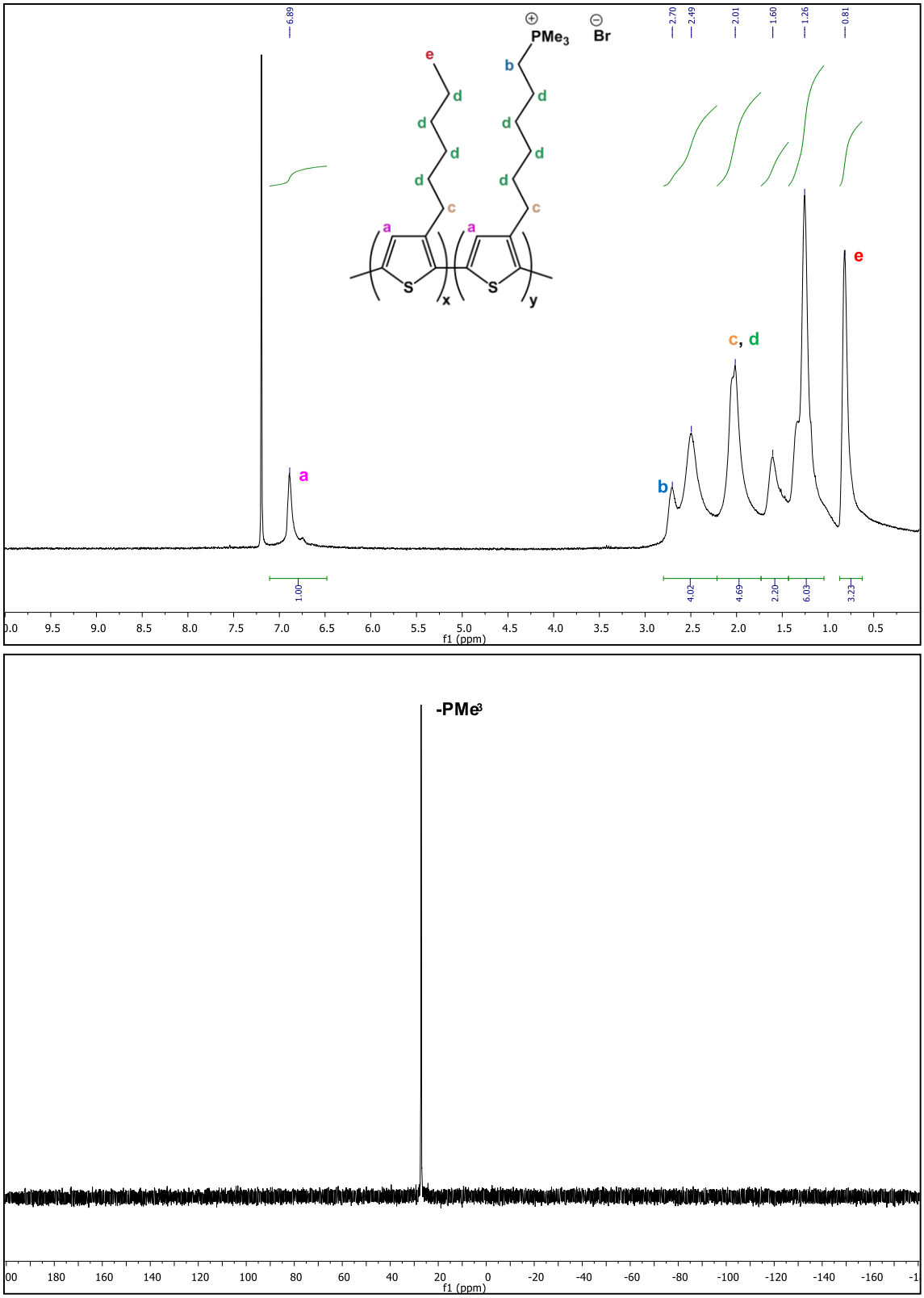

Figure 3.7 ^{1}H NMR spectrum of **P3HT-*b*-P3HTPMe$_3$,Br** (top) and $^{31}P\{^{1}H\}$ NMR spectrum of **P3HT-*b*-P3HTPMe$_3$,Br** (bottom) in $CDCl_3$.

-cial layer in OPVs. In this respect, the bromide anion was exchanged with various anions such as bis(trifluoromethane)sulfonimide (**TFSI**$^-$) and dodecylsulfate (**DS**$^-$) (Scheme 3.5)

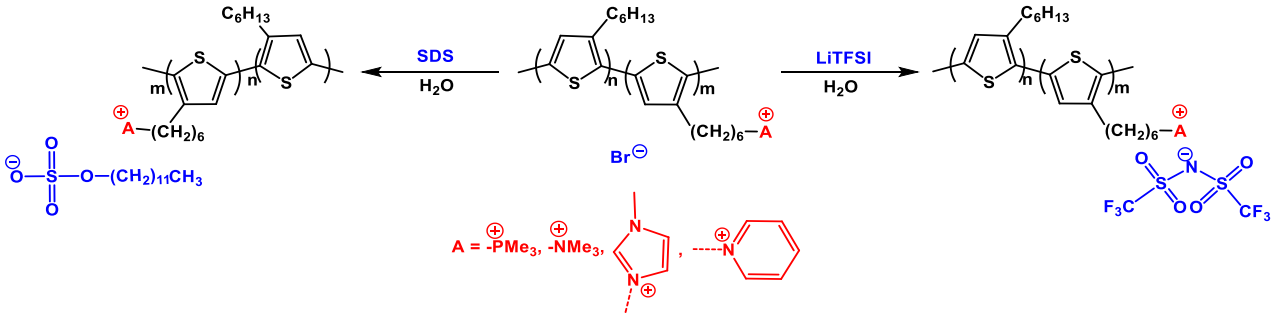

Scheme 3.5 Exchange reaction between the bromide and **DS** (left) / **TFSI** (right) anions.

The exchange reaction was carried out by adding ten equivalents of aqueous **LiTFSI** and **SDS** solutions to an aqueous polymer solution. The obtained polymers were collected by filtration after precipitation of **CPEs** into cold diethyl ether or acetone, depending on the nature of the counterion.

The presence of the **TFSI** anion in the **CPEs** was evidenced using $^{13}C\{^1H\}$ and ^{19}F NMR spectroscopies: for example, a quadruplet at around 120 ppm and a singlet at -79.8 ppm were observed on the ^{13}C and ^{19}F NMR spectra respectively, for **P3HT-*b*-P3HTIm,TFSI**, corresponding to the CF_3 groups (Figure 3.8). The substitution of the bromide ion by **DS** ions was confirmed by integrating in the ^1H NMR spectrum the signals around 3.9 and 2.9 ppm, which correspond to CH_2-OSO_3^- and CH_2-Th, respectively.

2. CPEs PROPERTIES

2.1. THERMAL PROPERTIES

In order to investigate the thermal properties of polyelectrolytes and block copolyelectrolytes, Rapid Heat–Cool (RHC) calorimetry measurements have been performed in collaboration with Dr. Niko Van den Brande and Pr. Bruno Van Mele (VUB, Belgium).

2.1.1. NATURE OF THE IONIC SIDE-CHAINS GROUPS

When comparing the second heating of the **CPE** diblock copolymers in RHC calorimetry measurements, a melting peak was observed at a similar temperature, around 205 °C, for all materials except for **P3HT-*b*-P3HTNMe$_3$,Br** (Figures 3.9 and 3.10). These melting transitions can be attributed to the **P3HT** block, which is known to be a fast-crystallizing conjugated polymer.

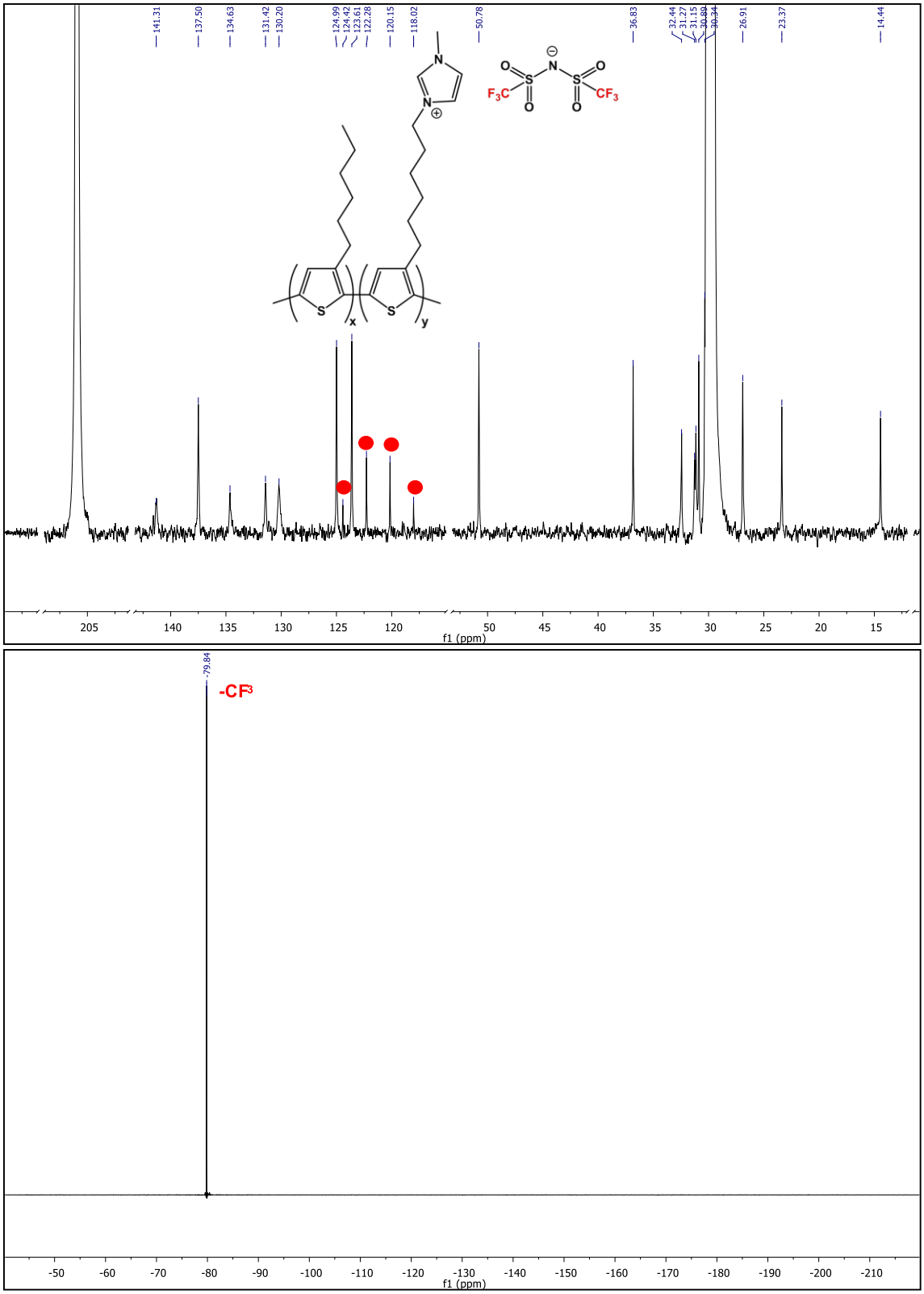

Figure 3.8 ^{13}C (top) and ^{19}F (bottom) NMR spectra of **P3HT-*b*-P3HTIm,TFSI** in acetone.

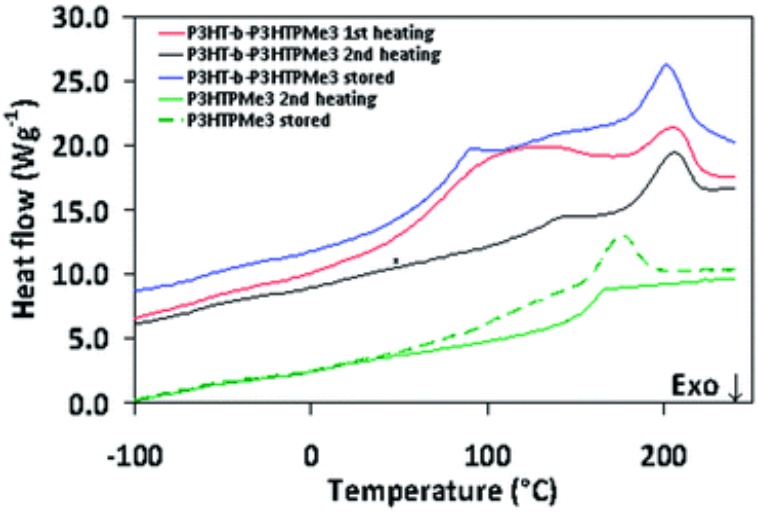

Figure 3.9 RHC thermograms of **P3HT-*b*-P3HTPMe$_3$,Br** showing the first heating (red), the second heating (black), and the curve after storage under ambient conditions (blue). For comparison, RHC thermograms of **P3HTPMe$_3$,Br** are also shown: second heating (dotted green) and after storage (solid green). The curves are shifted vertically for clarity.

A clear glass transition temperature (T_g) was also always present, due to the **CPE** block, as can be seen by comparing with the pure **CPE** materials. The T_g, the melting point (T_m) and enthalpy (ΔH_m) of the **P3HT** block are summarized for the four copolymers in Table 3.2. The thermal transitions observed by RHC during the second heating run evidenced the diblock copolymer architecture of the synthesized materials. The nature of the ionic side-group modifies the T_g by approximately 100°C, ranging from 57°C for imidazolium group, up to 159 °C for the ammonium group.

Table 3.2 Glass transition (T_g) of the **CPE** block and melting temperature (T_m) and enthalpy (ΔH_m) of the **P3HT** block for all **P3HT-*b*-CPE, Br** materials measured by RHC during the second heating run.

Polymer	T_g (°C)	T_m (°C)/ΔH_m (J.g^{-1})
P3HT-*b*-P3HTIm,Br	57	206/13.1
P3HT-*b*-P3HTPy,Br	75	204/10.2
P3HT-*b*-P3HTNMe$_3$,Br	159*	177/7.3
P3HT-*b*-P3HTPMe$_3$,Br	136	205/9.2

* Due to the overlap with the melting peak of the **P3HT** block, the T_g of the **P3HTNMe$_3$** block could not be determined in the block copolymer; instead, the value of the pure **P3HTNMe$_3$** polymer is given.

The thermogram of **P3HT-*b*-P3HTNMe$_3$,Br** clearly shows that the **P3HT** melting transition differs for this material (Figure 3.10). In this case, the T_g of the **P3HTNMe$_3$,Br** block overlaps with the **P3HT** melting peak and this high T_g value around 159°C is expected to strongly inhibit the crystallization process of the **P3HT** block. Indeed, in the temperature region of **P3HT**

crystallization during cooling, the **P3HTNMe$_3$,Br** block can impose mobility restrictions by concurrent vitrification, resulting in a lower melting temperature and enthalpy of the **P3HT** block (Figure 3.10, red and black curves). In contrast, the other **P3HT-*b*-CPE,Br** such as **P3HT-*b*-P3HTIm,Br** do not show this behavior (Figure 3.10, blue and green curves). It is interesting to note that the pure **P3HTIm,Br** polymer seems to be slightly crystalline with a small melting peak around 196°C, close to the **P3HT** melting, resulting in slightly higher melting enthalpy compared to the other materials.

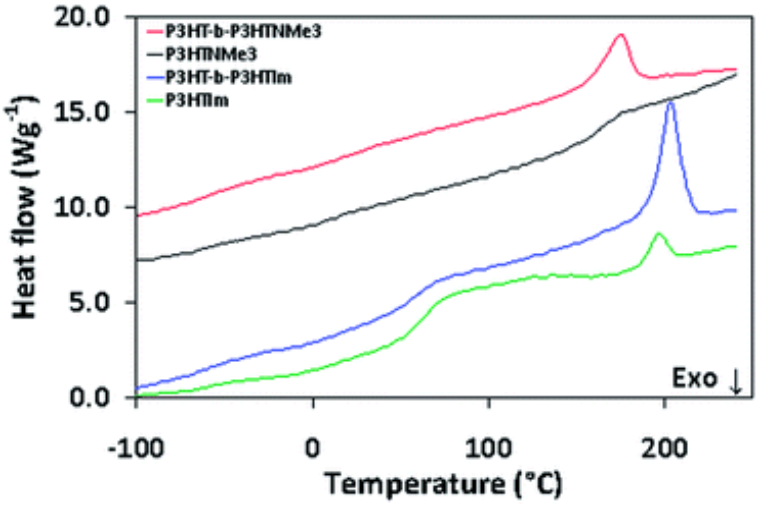

Figure 3.10 RHC thermograms of **P3HT-*b*-P3HTNMe$_3$,Br** (red) and **P3HT-*b*-P3HTIm,Br** (blue), during the second heating. For comparison, the second heating curves of the **P3HTNMe$_3$,Br** (black) and **P3HTIm,Br** (green) pure homopolymers are shown. The curves are shifted vertically for clarity.

The thermograms demonstrate the trends of the different **P3HT-*b*-CPE,Br** polymers during the second heating for the applied RHC conditions. Indeed, the values of T_g, T_m and ΔH_m strongly depend both on the chemical structure (block ratio, dispersity, nature of the end groups) and the experimental conditions (purification, drying, storage, etc). Moreover, the solvent-dependent assembly of the block copolyelectrolytes and the persistence of the solvent-induced nanomorphology after removal of the solvent are probably important for the thermal properties and their stability as well (see further in Part 2.3 “Aggregation behavior”). For example, the thermal properties of **P3HT-*b*-P3HTIm,Br** are still evolving in subsequent cool–heat cycles after the second heating; T_g increased from 57°C to above 70°C after ten cycles, while T_m decreases from 206°C towards 180°C in combination with a lowered ΔH_m from 13.1 J.g^{-1} to 8.5 J.g^{-1}. These findings suggest further changes in the nanomorphology as a result of thermal cycling, leading to a loss of perfection of the **P3HT** crystals, possibly with a concomitant loss of a minor amount of residual solvent from the ionic block. Similar effects were noticed for the other **P3HT-*b*-CPE,Br** polymers.

2.1.2. NATURE OF THE COUNTERIONS

During the first heating of all materials (imidazolium, ammonium, phosphonium and pyridinium derivatives) with the bromide counterion, a strong endothermal effect was observed, indicating the presence of a significant amount of water or solvent that evaporates upon heating. This effect disappeared during the second heating, where a glass transition temperature (T_g) is observed above room temperature for the four materials. The endothermal effect appears again when the copolymers are stored in the non-hermetic RHC crucibles under ambient conditions indicating the hydrophilicity of materials. As this effect is also present in the pure **P3HTPMe$_3$,Br** homopolymer (Figure 3.9, green curve), it can be linked to the bromide counterion. This finding has a great importance for potential applications, as water absorption will drastically decrease the T_g of the **CPE**, if the material is not kept under dry conditions.[24]

Exchanging the bromide for the **TFSI** ion resulted in considerably lower T_g values and a strong plasticizing effect was observed, as illustrated for the homopolyelectrolytes (Figure 3.11). For example, exchanging the conterion from **Br$^-$** to **TFSI$^-$** for the phosphonium **CPE** resulted in decreasing T_g from about 170°C to 50 °C, respectively. Since the **CPE** layer induces the formation of dipoles at the interface, the presence of water could obscure the underlying mechanisms, hindering the comparison between the different interfacial materials. Therefore, **CPEs** containing **TFSI** counterions, for which no hygroscopic character was observed, seem to be more suitable than those containing bromide counterions for interlayer applications.

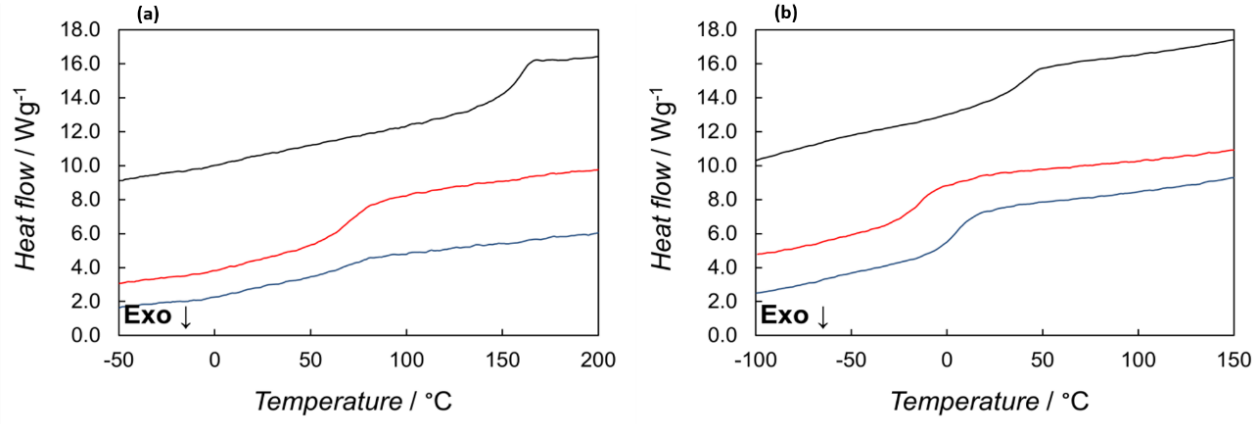

Figure 3.11 RHC heating profiles for imidazolium (red curve), pyridinium (blue curve) and phosphonium (black)–based **CPEs** having **Br$^-$** (a) or **TFSI$^-$** (b) as counterions. The curves are shifted vertically for clarity.

Compared to the **CPE,TFSI**, **CPE,DS** exhibit a different thermal behavior; for example, while **P3HTPMe$_3$,TFSI** shows a rather low T_g at 30°C, the **DS** analogue shows a clear T_g at about 67°C. The **P3HT-*b*-P3HTPMe$_3$,DS** block copolymer also exhibits a glass transition at about 70°C, followed by a clear melting peak at 206°C. The glass transition temperature of 70°C can be linked to the **P3HTPMe$_3$,DS** block, whereas the melting point is clearly higher (Figure 3.12).

Furthermore, the crystallization process is much faster, leading to a clear melting peak and a complete absence of cold crystallization after cooling at 500 K.min^{-1}. For comparison, a slower cooling rate of 20 K.min^{-1} was also considered for both materials, leading to similar thermograms. Based on these results, it seems that the crystallization and melting peaks of the copolymer can be attributed to the **P3HT** block. As **P3HT** crystallization is a fast process that takes place at higher temperatures, it will also hinder the crystallization of the **P3HTPMe$_3$,DS** block. A separate glass transition for the **P3HT** block is not observed, which can be explained by its high crystallinity. This behavior is similar to that reported for the **P3HT-*b*-P3HTPMe$_3$,Br** block copolymer.

Furthermore, as the M_n and the **3HT** molar ratio in the copolymer are 15 100 g.mol^{-1} and 0.59, respectively, the observed melting point of 206°C seems to fit with earlier results on **P3HT** with different molecular weights.[25] Even if T_g and T_m depend on the experimental conditions, *i.e.* molecular weight, dispersity, block ratio etc., the T_g observed for both **P3HTPMe$_3$,DS** and **P3HT-*b*-P3HTPMe$_3$,DS** are lower than for the **Br$^-$** analogues, indicating that the **DS$^-$** counterion plays a role in thermal properties, particularly concerning the free volume, due to its size. An increase in free volume for a similar temperature can be directly linked to a lower T_g. In addition, the flexible unit of the **DS$^-$** counterion may also enhance the plasticizing effect, as previously observed when SDS was used as an emulsifier.[26]

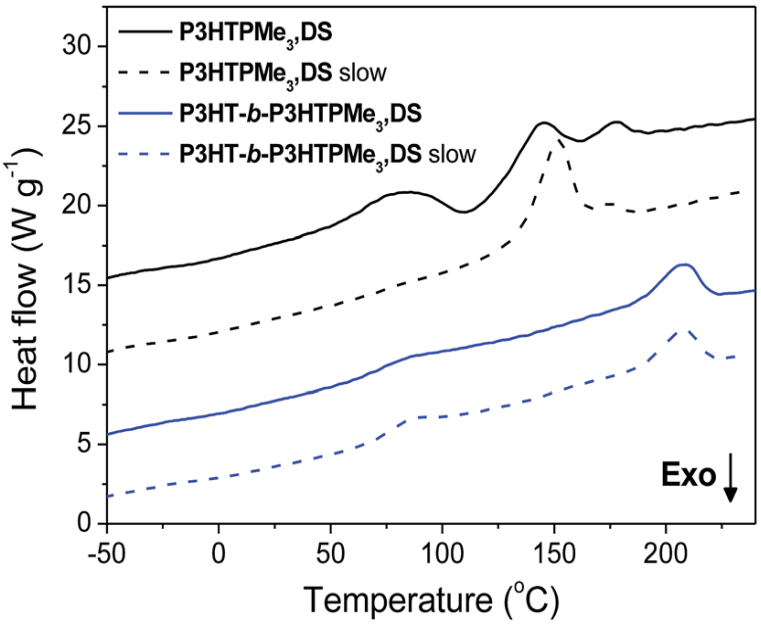

Figure 3.12 RHC thermograms of **P3HTPMe$_3$,DS** and **P3HT-*b*-P3HTPMe$_3$,DS** at 500 K.min^{-1} heating rate, for a preceding cooling rate of either 500 K.min^{-1} (solid lines) or 20 K.min^{-1} (dashed lines). The curves are shifted vertically for clarity.

2.2. OPTICAL PROPERTIES

The optical properties of the cationic **CPEs** in solution have been studied by UV-Vis absorption and photoluminescence (PL) spectroscopies in collaboration with Dr. Rachel C. Evans and Judith Houston (Trinity College of Dublin, Ireland).

The neutral polymers **P3HTBr** and **P3HT-*b*-P3HTBr** exhibit a broad absorption band with a maximum (λ_{max}) centered around 450 nm in chloroform, which is similar to the parent **P3HT,** as expected. After functionalization with the imidazolium, pyridinium, trimethylammonium or trimethylphosphonium moieties, the **CPE** and **P3HT-*b*-CPE** polymers become soluble in more polar solvents due to the presence of the pendant ionic groups, which overcome the hydrophobic π–π stacking interactions between the polythiophene backbones. We have also noted that **P3HT-*b*-P3HTPy** is less soluble in these solvents than its **P3HT-*b*-CPE** counterparts, indicating the reduced hydrophilic (or increased hydrophobic) character of the **P3HTPy** block, as previously reported by Scherf *et al.* for the polyfluorene-polythiophene diblock copolyelectrolyte analogue **PF2/6–P3HTPyr**.[6,13]

2.2.1. EFFECT OF THE TOPOLOGY

By changing the topology of these **CPEs** (block copolymers *vs.* homopolymers), the absorption maximum of the amphiphilic diblock copolythiophene was significantly red-shifted compared to the homopolymer, by about 70 nm for the **PMe$_3$,Br** based-**CPEs**, for example. This finding is consistent with an increased aggregation of the diblock copolymer.[10d]

P3HT-*b*-CPE,Br block copolymers exhibit solvatochromatic behavior, appearing dark red/brown in chloroform and dark violet in methanolic and aqueous solutions (Figure 3.12, a). This solvatochromatism is reflected in the corresponding UV-vis absorption and emission spectra, as shown in Figure 3.13, b for **P3HT-*b*-P3HTPMe$_3$,Br** where λ_{max} and λ_{em} are red-shifted from 450 and 588 nm in chloroform, to 520 and 711 nm in water and methanol, respectively. This shift is also accompanied by the emergence in the absorption spectrum of a vibronic structure in the latter solvents, which is assigned to the vibronic progression of the C=C stretching mode (ΔE = 0.15 eV).[27] This vibronic structure is moderate, which is consistent with **P3HT** adopting a "rigid-rod" conformation in block copolymers.[17,28]

P3HT has previously been reported to self-assemble into a lamellar-like structure built from interchain π–π stacking interactions between the planarized aromatic backbones of the polymer chains.[29] This supramolecular organization is accompanied by a bathochromic shift in the absorption spectrum and the presence of a vibronic structure, very similar to the behavior observed here for **P3HT-*b*-CPEs,Br** in MeOH and water. Water is expected to be a non-solvent for the hydrophobic, neutral **P3HT** block, with only low to moderate solubility anticipated in MeOH. The significant bathochromic shift indicates increased aggregation of the hydrophobic **P3HT** block in these poor solvents. The concomitant appearance of the vibronic structure

further suggests increased confinement and/or planarization of one or both of the blocks, thereby hindering free rotation of thiophene units along the polymer backbone.

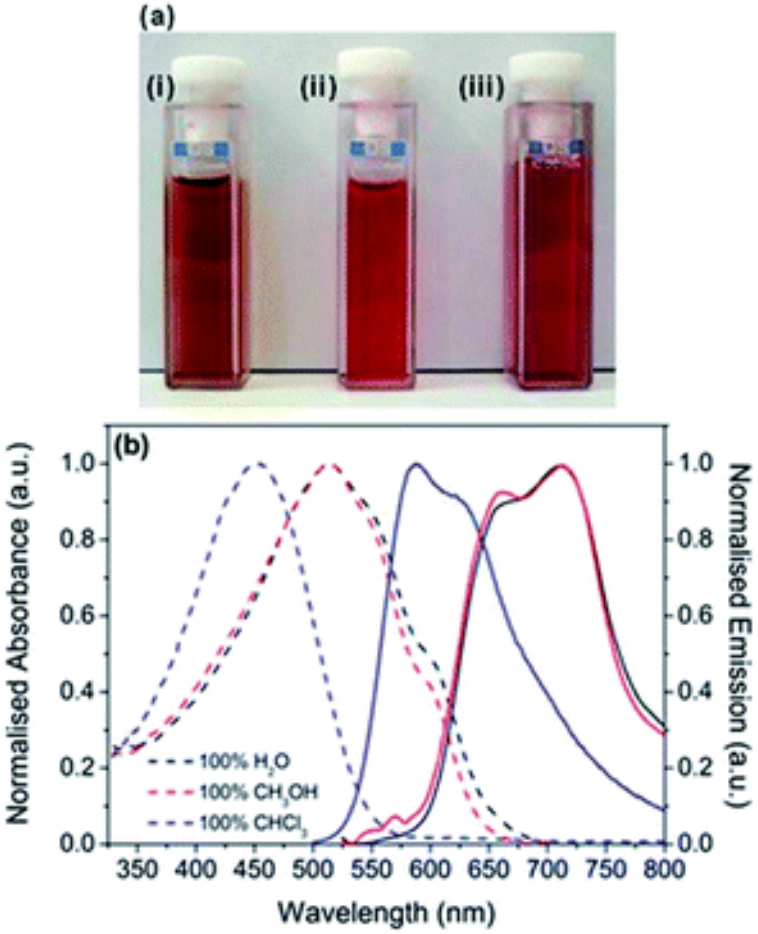

Figure 3.13 (a) Photograph of solutions of **P3HT-*b*-P3HTPMe$_3$,Br** in (i) $CHCl_3$, (ii) MeOH and (iii) H_2O. (b) Corresponding normalised UV-vis absorption and emission spectra of **P3HT-*b*-P3HTPMe$_3$,Br** in 100 % $CHCl_3$ (blue), 100 % H_2O (black) and 100 % MeOH (red).

The use of solvent mixtures was shown to be very effective for both breaking up the aggregates formed by **CPEs** homopolymers in aqueous solution and controlling segregation and self-organization of amphiphilic diblock copolymers. The UV-vis absorption and photoluminescence (PL) properties of **P3HT-*b*-CPE,Br** copolymers were thus further examined in MeOH/H_2O solvent mixtures from 0 to 100 % (v/v), as illustrated in Figure 3.14 for **P3HT-*b*-P3HTPy,Br**. The gradual increase in the volume of MeOH added to an aqueous solution of **P3HT-*b*-P3HTPy,Br** is accompanied by a concomitant increase in the absorbance, which reaches its maximum value at 50 % (v/v) MeOH-H_2O; above this, the absorbance drops off once again (Figure 3.14, a). A similar trend is observed in the corresponding PL spectrum, with the emission intensity again reaching its upper limit at 50 % (v/v) MeOH/H_2O (Figure 3.14, b). Notably, no shift in the absorption or emission maximum wavelength was observed, whatever the solvent mixtures used.

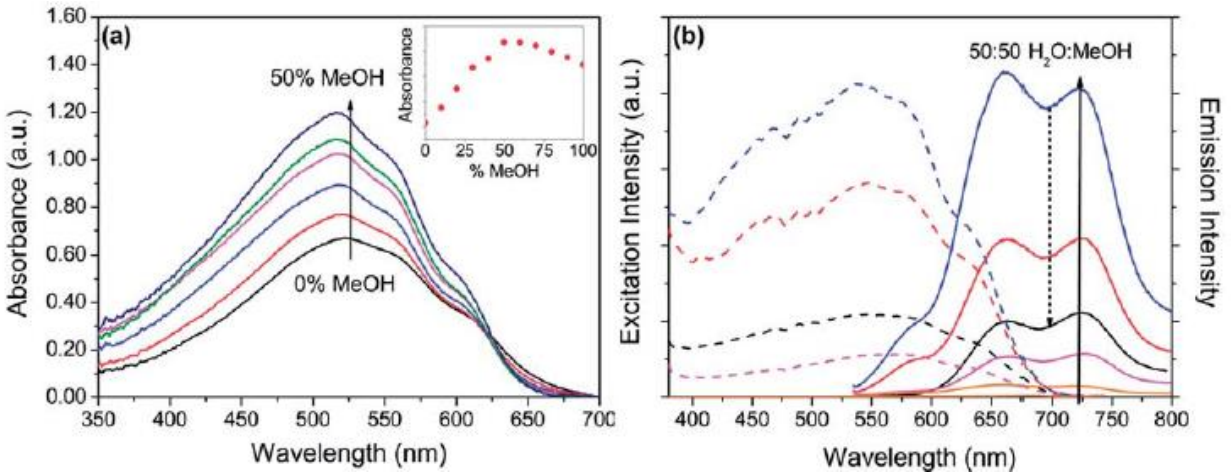

Figure 3.14 (a) UV-vis absorption spectra of **P3HT-*b*-P3HTPy,Br** in H_2O/MeOH solvent mixtures. (b) Selected excitation (λ_{em} = 730 nm) and PL (λ_{ex} = 515 nm) spectra of **P3HT-*b*-P3HTPy,Br** in 100 % MeOH (orange line), 70 % MeOH (violet line), 50 % MeOH (blue line), 30 % MeOH (red line) and 0 % MeOH (black line).

Fluorescence quantum yields (Φ_F) were determined to quantify the extent of the fluorescence enhancement in each solvent mixture (Figure 3.15). For **P3HT-*b*-P3HTPy,Br**, **P3HT-*b*-P3HTNMe$_3$,Br** and **P3HT-*b*-P3HTPMe$_3$,Br**, $\Phi_F \sim 0.5$ % in 100 % MeOH and $\Phi_F \sim 1.0$-1.5 % in 100 % H_2O were obtained. As the ratio of solvents in the mixture is varied, Φ_F gradually increases, reaching a maximum of $\Phi_F \sim 5.5$ % in 50 % (v/v) MeOH/H_2O. **P3HT-*b*-P3HTIm,Br** exhibits a slightly different trend; Φ_F remains constant at ~1.0-1.5 % across the range 100 % MeOH to 20/80 % (v/v) MeOH/H_2O, before doubling to $\Phi_F \sim 3$ % in 100 % H_2O. The increase in the fluorescence quantum yield in the mixed solvent systems suggests that the solubility is improved and polymer chains in one or both blocks are partially isolated.

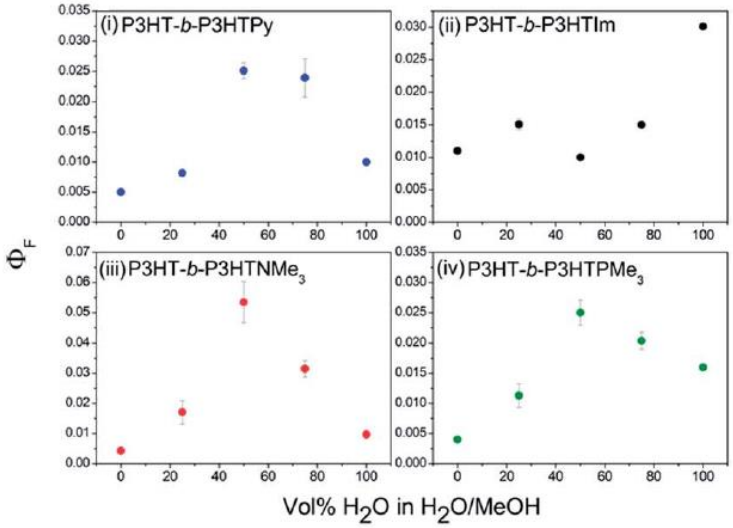

Figure 3.15 Fluorescence quantum yields (Φ_F) of **P3HT-*b*-CPEs,Br** in H_2O/MeOH solvent mixtures (0.35 µg.mL^{-1}).

2.2.2. NATURE OF THE IONIC SIDE-CHAIN GROUPS

The optical properties of π-conjugated polymers are determined by the chemical and electronic structure of the π-conjugated backbone. Consequently, the UV-vis absorption and photoluminescence spectra of conjugated polyelectrolytes having the same backbone are quite similar, even if the ionic side-chain groups are different (Table 3.3).

Reynolds *et al.* have indeed reported the same findings with poly(arylenethylene)s having the same π-conjugated backbone and different ionic groups : the UV-vis absorption and photoluminescence spectra were similar (Figure 3.16).[30] The maximal absorption and emission wavelengths were influenced by changing the nature of the aryl group inside the π-conjugated backbone.

Polymer	Absorption (λ_{max}/nm)			Emission (λ_{max}/nm)		
	$CHCl_3$	MeOH	H_2O	$CHCl_3$	MeOH	H_2O
P3HTIm,Br	-	440	445	-	-	-
P3HTPy,Br	-	440	464	-	-	-
P3HTNMe$_3$,Br	-	440	449	-	-	-
P3HTPMe$_3$,Br	-	440	450	-	-	-
P3HT-*b*-P3HTIm,Br	452	519 556 608	522	586 625	729	729
P3HT-*b*-P3HTPy,Br	455	517 556 607	520	580 619	721	723
P3HT-*b*-P3HTNMe$_3$,Br	452	518 556 607	518	592 631	721	722
P3HT-*b*-P3HTPMe$_3$,Br	455	516 556 607	516	588 627	707	710

Table 3.3 Absorption and photoluminescence maxima (λ_{max}) of the **CPE,Br** and **P3HT-*b*-CPE,Br** polymers in various solvents (PL excitation: 523 nm).

Figure 3.16 Picture of the **PPE-Ar-SO_3^-** fluorescence in methanol under UV illumination (from the left to the right: Ph, Py, Th, EDOT, BTD).[30]

2.2.3. NATURE OF THE COUNTERIONS

Association of **DS^-** with the related homopolymers **P3TMAHT**[31] and **P3ImiHT**[32] induced significant surfactochromic transitions in aqueous solution, which can be controlled by varying the surfactant fraction. However, these transitions are controlled to a large extent by the phase diagram of **SDS**, which differs in methanol[33] and water.[34] Exchanging **Br^-** counterion by **DS^-** results in the emergence of a vibronic structure for both 1:1 homo- and block copolymer:surfactant complexes. A moderate narrowing of the emission band was also observed (Figure 3.17).

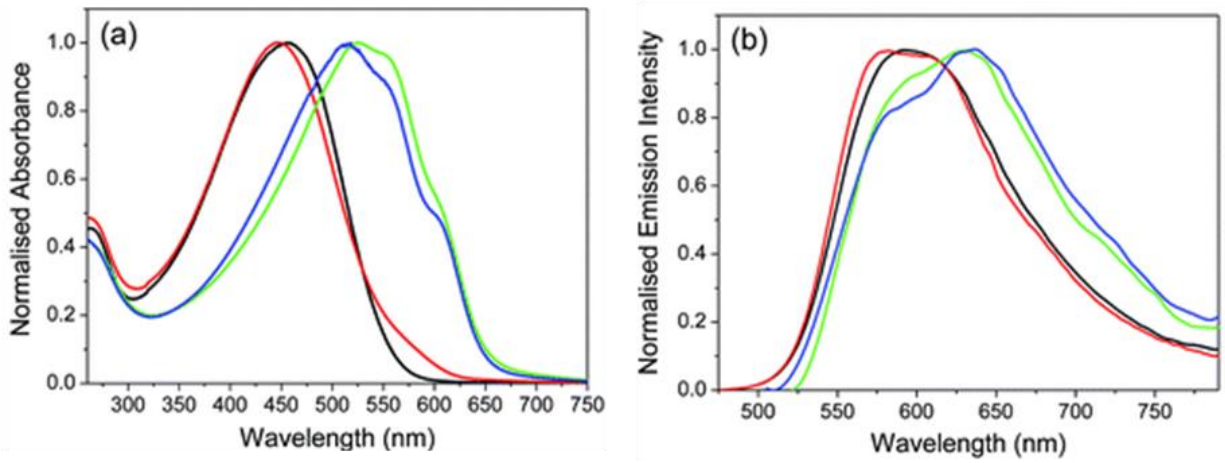

Figure 3.17 Normalized (a) UV-vis absorption and (b) emission spectra of **$P3HTPMe_3$,Br** (black line), **$P3HTPMe_3$,DS** (red line), **P3HT-*b*-$P3HTPMe_3$,Br** (green line) and **P3HT-*b*-$P3HTPMe_3$,DS** (blue line) in *d4*-MeOD (10 $mg.mL^{-1}$).

The addition of surfactants to **CPE** solutions is well-known to promote the dispersion of weakly soluble polymer aggregates by inhibiting interchain interactions, which are typically indicated by a blue-shift in the absorption/emission maximum, a narrowing of the emission band and the

emergence of a vibronic structure.[35] Indeed, for **P3HTPMe$_3$,DS** and **P3HT-*b*-P3HTPMe$_3$,DS** the **DS$^-$** counterion hinders polymer–polymer interchain interactions more effectively, thereby decreasing the nominal effective conjugation length for exciton migration.[36]

2.3. AGGREGATION BEHAVIOUR

The dependence of the optical properties of the **CPEs** on their chemical structure gives important informations on the behavior of the polymer chains at the molecular level. Since the optoelectronic properties and the nanoscale morphology of the polymers (which are intrinsically linked) determine their performance in devices, obtaining information about their structure in solution and in thin films is of crucial importance. To this aim, the aggregation behavior of **P3HT-*b*-CPEs** in solution and in thin films was investigated by dynamic light scattering (DLS), small-angle neutron scattering (SANS) and atomic force microscopy (AFM), in collaboration with Dr. Rachel C. Evans and Judith Houston (Trinity College of Dublin, Ireland).

2.3.1. NATURE OF THE IONIC SIDE-CHAIN GROUPS

DLS analysis was initially performed to determine the average hydrodynamic diameter (D_h) of **P3HT-*b*-CPE** aggregates in MeOH/H_2O mixtures (Figure 3.18). Samples typically exhibited a monomodal distribution of low polydispersity in all solvent mixtures investigated. The smallest aggregates were obtained in 100 % MeOH (from ~100 nm to 250 nm for **P3HT-*b*-P3HTPMe$_3$,Br**) and larger aggregates were found in 100 % H_2O (from ~100 nm to ~300 nm for **P3HT-*b*-P3HTNMe$_3$,Br**). The largest values (~400–600 nm) were obtained in ~40–60 % (v/v) MeOH–H_2O, which is consistent with the increased solubility of both **P3HT** and **CPE** blocks, resulting in swelling of the aggregate structure due to associated solvent molecules.

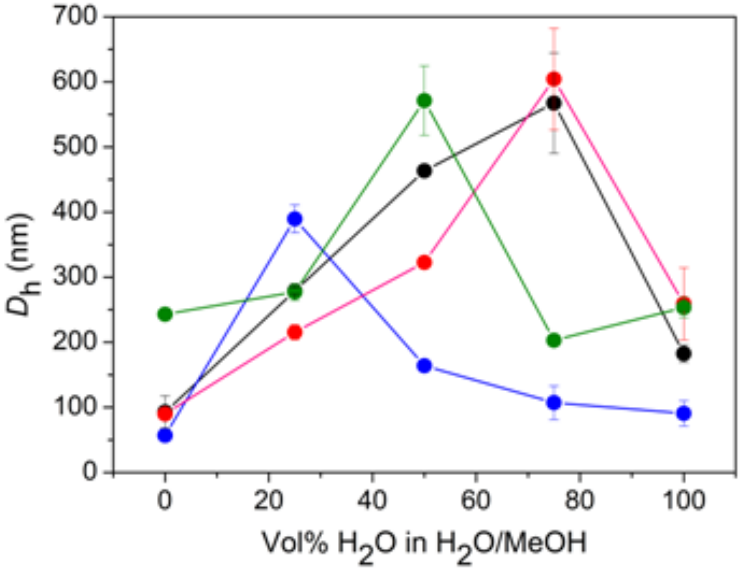

Figure 3.18 Hydrodynamic diameter (D_h, Z-average) measured for **P3HT-*b*-CPE,Br**; **CPEs** : pyridinium (blue), imidazolium (black), phosphonium (green) and ammonium (red).

To obtain deeper insight into the particle shape and nanoscale organization in solution, small-angle neutron scattering (SANS) studies were performed in deuterated solutions. As an example, the SANS data for **P3HT-*b*-P3HTPy,Br** in D_2O, *d4*-MeOD and their 50/50 (v/v) mixture are shown in Figure 3.19.

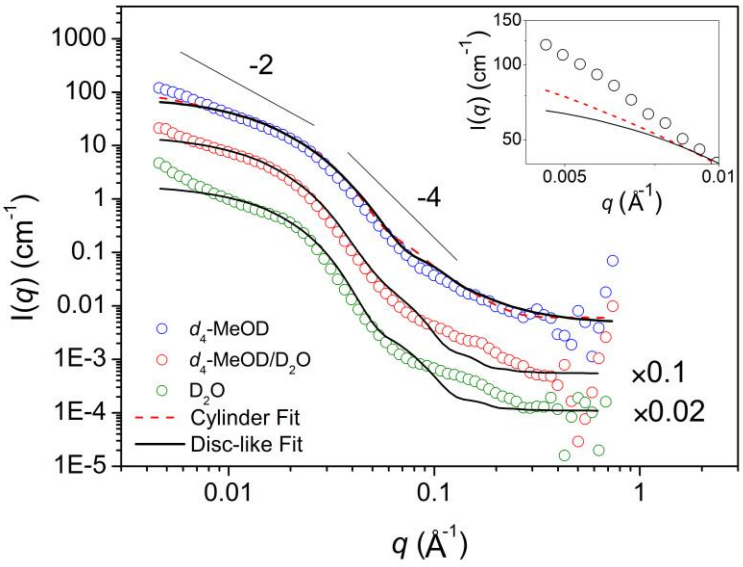

Figure 3.19 SANS data for **P3HT-*b*-P3HTPy, Br** in *d4*-MeOD, 50/50 (v/v) *d4*-MeOD–D_2O and D_2O (10 mg. mL^{-1}). The solid black lines show the disc-like fits obtained using the Core–Shell-Cylinder model for each solvent mixture. Only **P3HT-*b*-P3HTPy,Br** in *d4*-MeOD was found to be better fit by rods at low q, as shown by the red dashed line in the inset.

The sizes probed by the scattering techniques are in the order of 2π/q where q is the magnitude of the scattering vector, which depends on the wavelength (λ) and scattering angle (Θ), $q = \frac{4\pi\, Sin\,(\frac{\Theta}{2})}{\lambda}$.The SANS data in each solvent were fitted with a Core–Shell-Cylinder model using a non-linear least-squares method, including polydispersity and q-resolution smearing (fits shown as solid lines in Figure 3.19).[37] All the fits show that the aggregates must contain more than 30 % solvent, without any significant "dry core". Better fits were obtained with a 'core plus shell' model with a diffuse outer shell containing 85–95 % solvent. The exceptions were the samples in pure MeOD, where a thin shell (of ~2 nm) seems to have slightly less solvent (~ 65 %) than the core of the aggregate (~ 80 % solvent). The SANS data from the aggregates in MeOD are also more consistent with an elongated, rod-like structure, whilst the others are better fit as discs. The disc cases would also be equally well fitted as core–shell ellipsoids or as rather polydisperse core–shell spheres. There is no clear evidence in the SANS patterns of a sharp core–shell boundary, so a continuous radial variation in the solvent composition seems likely, though this would be more difficult to model. Aggregation numbers are in the range ~ 100 to ~ 300 copolymer chains.

For **P3HT-*b*-P3HTPy,Br** in *d4*-MeOD, depending on the starting imputed values of length and radius, the fits were thus found to converge to two slightly differing shapes:

- a rod with a core length (L_{core}) of ∼80 nm, a core radius (r_{core}) of ∼6 nm and a shell thickness (T_{shell}) of ∼ 2 nm;
- a disc with L_{core} ∼ 75 nm, r_{core} ∼ 30 nm and T_{shell} ∼ 1 nm.

As discussed above, the rod-like core–shell aggregate resulted in an improved fit at low q. The SANS data for **P3HT-*b*-P3HTPy,Br** in 50/50 (v/v) *d4*-MeOD–D_2O were also best modelled by a disc-like core–shell aggregate, revealing a wet core with L_{core} ∼ 11 nm and r_{core} ∼ 7.5 nm, and, a thick solvated shell (T_{shell} ∼ 9.5 nm). Fitting the SANS data of **P3HT-*b*-P3HTPy,Br** in D_2O similarly yielded a disc with a solvated core (L_{core} ∼ 9 nm and r_{core} ∼ 6 nm) and a very wet shell of T_{shell} ∼ 8 nm. The shell thickness corresponds to the fully extended length of the charged **P3HTPy** block. Therefore, it is likely that the drier core corresponds to the aggregated neutral **P3HT** blocks.

The scattering length densities (SLDs) of the neutral and charged **CPE** blocks are both ∼1.1×10^{-6} Å^{-2}. Therefore, they can only be distinguished by neutron scattering when one block is substantially more solvated than the other. The SANS data fits for **P3HT-*b*-P3HTPy,Br** in D_2O suggest the presence of aggregates with a highly swollen shell. Since D_2O is expected to be a selective solvent for the charged **CPE** block, the aggregate core may consist predominantly of the neutral **P3HT** blocks, surrounded by a highly solvated **CPE** shell. Indeed, **P3HT** chains might be packed within the aggregate core to minimize the interaction with the solvent. In 50/50 (v/v) *d4*-MeOD–D_2O, the core–shell aggregate structure is retained, but the solvent mixture results in improved solvation of both blocks, leading to an increase of both core radius and shell thickness. In MeOD, **P3HT-*b*-P3HTPy,Br** forms elongated core–shell cylindrical structures, with a solvated core and a drier shell. On the basis of the Hildebrand solubility parameters, MeOH is a relatively poor solvent for **P3HT** and should be a better solvent for the charged **CPE** block (δ ∼ 19.1 MPa$^{1/2}$ for **P3HT** and δ ∼ 29.7 MPa$^{1/2}$ for **CPE**, respectively[38]). We propose that in MeOD, **P3HT-*b*-P3HTPy,Br** forms core–shell aggregates in which the **P3HT** blocks predominantly occupy the core, but partial mixing of the two blocks across both domains can also occur.

Atomic force microscopy (AFM) was used to determine if the aggregates formed in solution could be transferred as thin films with the retention of their nanoscale organization, which is a key requirement for potential device applications. Solutions of **P3HT-*b*-CPE,Br** were drop cast onto mica substrates and revealed the occurrence of spheroids with a surface morphology and size critically depending on the deposition solvent. For example, AFM images recorded for **P3HT-*b*-P3HTIm,Br** are depicted in Figure 3.20.

Firstly, in MeOH, a honeycomb-like texture is observed on the aggregate surface with an average diameter of 128 ± 28 nm (Figure 3.20, a). The surface texture may be indicative of the fusion of several smaller structures into larger aggregates. Then, in water, slightly larger,

isolated aggregates are observed (average diameter ~ 147 ± 28 nm), with a much smoother surface morphology (Figure 3.20, b). Finally, in 50 % (v/v) MeOH/H_2O, amorphous films formed from large aggregates of much smaller, disc-like clusters, 50–80 nm in diameter, are observed (Figure 3.20, c). It should be noted that the SANS data indicate that the core–shell aggregates formed in solution are highly solvated. In contrast, the corresponding thin films were dried prior to AFM imaging. It is thus possible that removing the solvent during drying might lead to partial collapse or reorganization of the aggregates. This effect could be even more important for MeOH/water mixtures since methanol is more volatile than water, resulting in solvent gradient fluctuations.

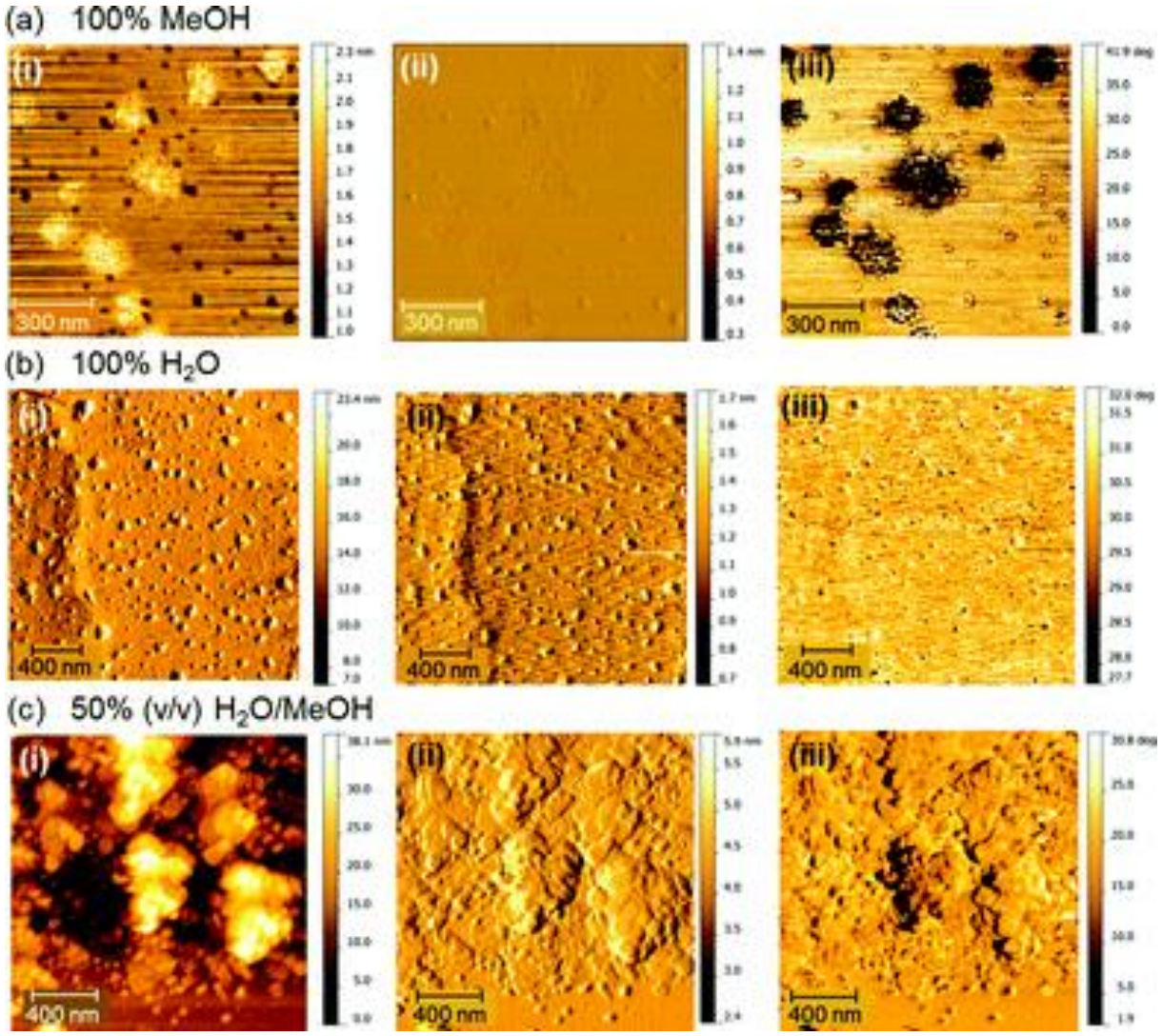

Figure 3.20 AFM tapping mode images of **P3HT-*b*-P3HTIm,Br** films drop-cast from (a) 100 % MeOH (7 µg.mL^{-1}), (b) 100 % H_2O (3.5 µg.mL^{-1}) and (c) 50 % (v/v) H_2O–MeOH (3.5 µg.mL^{-1}) onto mica: (i) height, (ii) amplitude and (iii) phase images, respectively.

A schematic representation of the proposed aggregate structures adopted by **P3HT-*b*-CPEs** in H_2O, MeOH and H_2O/MeOH mixtures is shown below (Figure 3.21). The smallest aggregates are formed in pure MeOH and exhibit a core–shell cylindrical structure comprised of a long "wet" core protected by a "dry" thin shell. Slightly larger aggregates are obtained in pure H_2O and consist of a drier core of aggregated, neutral **P3HT** blocks and a wet shell of well-dissolved **CPE** chains. The largest aggregates are formed in MeOH/H_2O mixtures, in which the core and shell are both well-solvated. This finding is in excellent agreement with the corresponding increase in the Φ_F values observed in MeOH/H_2O mixtures. Moreover, due to the higher solubility of the entire **CPE** chain, lower aggregation is expected for each structure, thereby reducing electrostatic repulsion between the highly solvated individual chains from which each aggregate is comprised. Reduced electrostatic repulsion may result in long-range assembly of multiple aggregates, which can explain the large D_h obtained by DLS and the textured extended sheets observed by AFM.

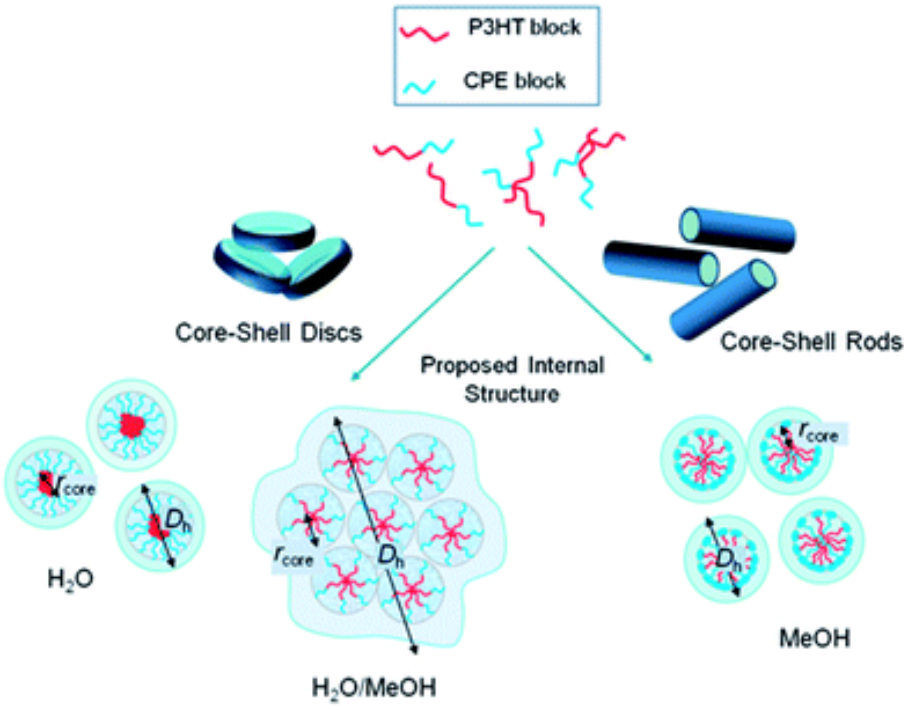

Figure 3.21 Schematic representation of the proposed internal aggregate structures of **P3HT-*b*-CPE,Br** in H_2O, MeOH and H_2O/MeOH mixtures.

2.3.2. NATURE OF THE COUNTERIONS

For **P3HTPMe$_3$,Br,** the SANS data suggest that the homopolymer adopts a rod-like conformation in solution.[39] The SANS data were independently fit to a rigid cylinder model[40] and a flexible cylinder model[41] (Figure 3.22, a) using a non-linear least-squares method and including q-resolution smearing. The rigid cylinder model describes the length and radius of an unbending, uniform rod- or disc-shaped aggregate, whereas the flexible cylinder model is used to describe a non-linear chain consisting of a number of locally stiff segments with persistence length, l_p. The

Kuhn length (L_{Kuhn}), or 2 × l_p, describes the stiffness of the chain. This model gave an improved fit to the data at low q with a reasonable L_{Kuhn} (225.6 Å) compared to the total cylinder length (900.5 Å), and a radius of 12.9 Å. From the estimated aggregation number (N_{agg}), each cylinder is comprised of 5–10 polymer chains, with L_{Kuhn} corresponding to the length of a single chain (220 Å) and the cylinder diameter (25.8 Å) approximating the thickness of two adjacent chains (~26 Å). The fitting data indicate that the cylinders are well-solvated, containing >85% solvent. Previously, the related homopolymers **P3TMAHT**[31] and **P3ImiHT**[32] in D_2O were found to form charged spherical aggregates (~80 and ~40 Å in diameter, respectively) with interparticle interactions. In contrast, **P3HTPMe$_3$,Br** in *d4*-MeOD better resembles the scattering profiles obtained from these related **CPEs** when combined with a small amount of **DS**$^-$ (**CPE**/surfactant charge ratio of 1 : 0.2). In both systems, the pure **CPE** aggregates are believed to disassemble and reorganize into **CPE**–surfactant cylinders.[31] This suggests that **P3HTPMe$_3$,Br** forms more ordered aggregates in *d4*-MeOD, with significant packing between **CPE** chains.

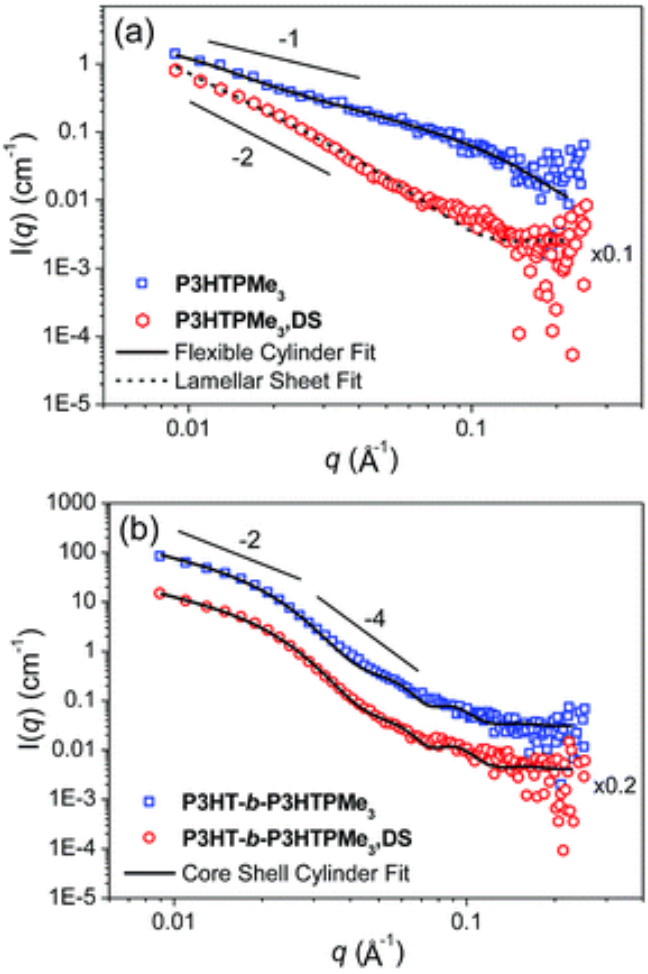

Figure 3.22 SANS data for (a) **P3HTPMe$_3$,Br** (blue) and **P3HTPMe$_3$,DS** (red) and (b) **P3HT-*b*-P3HTPMe$_3$,Br** (blue) and **P3HT-*b*-P3HTPMe$_3$,DS** (red). Total concentration of each sample was 10 mg mL^{-1} in *d4*-MeOD. Solid and dashed lines correspond to the fits to the models described in the text.

Counterion exchange results in a significant change in the scattering profile for **P3HTPMe$_3$,DS**, indicating scattering from sheet-like particles.[37] A lamellar sheet model provided a reasonable fit to the data (Figure 3.22, dashed line), yielding a sheet thickness of ~47 Å, with a slightly decreased solvent content (~ 50 %) than obtained for **P3HTPMe$_3$,Br**. The related **P3TMAHT** and **P3ImiHT** were also found to form sheet-like aggregates when combined with a 1 : 1 charge ratio of **SDS** in H_2O.[31a,32] However, the calculated sheet thicknesses were much thinner (~ 20 Å), corresponding to the solid-state d-spacing of poly(3-octylthiophene) and suggesting that the sheets are formed of interwoven **CPE**–surfactant structures rather than well-defined layers.[42] In contrast, the sheet thickness obtained here for **P3HTPMe$_3$, DS** (~ 47 Å) is in excellent agreement with the sum of the length of the individual SDS molecules (~ 25 Å)[43] and the solid-state d-spacing of poly(3-octylthiophene), suggesting that distinct **DS$^-$/CPE** layers are present. However, due to the similar scattering length densities (SLDs) for **P3HTPMe$_3$, Br** and **DS$^-$** (~1 × 10^{-6} Å^{-2}), the individual layers cannot be distinguished by this experiment. Nevertheless, the formation of sheet-like, rigid particles suggests more efficient packing of the **CPE** within lamellar sheets, potentially leading to the exclusion of *d4*-MeOD molecules and hence the lower solvent content.

The SANS data of **P3HT-*b*-P3HTPMe$_3$,Br** in *d4*-MeOD (Figure 3.22, b) yield a similar scattering profile to the pyridinium (Py) analogue previously studied. **P3HT-*b*-P3HTPMe$_3$,Br** aggregates fit to a dry core (~ 15 % solvent) with a radius (r_{core}) of 53.1 Å, length (L_{core}) of 572.8 Å, and a thick, wet shell (~ 86 % solvent) of 77.4 Å. Each aggregate contains ~300 chains. The SLDs of the neutral **P3HT** and the **P3HTPMe$_3$** blocks are both ~1 × 10^{-6} Å^{-2}. Therefore, they can only be distinguished by neutron scattering when one block is substantially more solvated than the other. A difference in solubility between amphiphilic copolymer blocks is known to lead to the formation of domains within **CPE** aggregates.[10a] Here, we observed core–shell cylinders with hydrophobic, neutral block cores and solvated, hydrophilic charged block shells. It should be noted that the phosphonium analogue appears to have a wetter and thicker shell than the pyridinium analogues previously studied. This result is in good agreement with the significantly larger hydrodynamic diameter obtained by dynamic light scattering for **P3HT-*b*-P3HTPMe$_3$,Br** in comparison to the pyridinium analogue.

Counterion exchange yields only subtle changes in the scattering profile for **P3HT-*b*-P3HTPMe$_3$,DS**, with the core–shell cylinder structure of the parent copolymer retained (Figure 3.22, b). Fitting with the core–shell cylinder model gave moderately elongated cylinder cores, L_{core} = 544.4 Å and r_{core} = 54.3 Å, with a slightly drier shell (~ 85 % solvent) with a shell thickness, T_{shell} = 74.0 Å. The core is slightly more solvated (~ 19 %) than the parent **P3HT-*b*-P3HTPMe$_3$,Br**. The shell thickness for the **CPE** with and without **DS$^-$** remains almost constant. The surfactant is expected to associate parallel to the **CPE** chains extending from the hydrophobic block core. This is consistent with the slightly lower N_{agg} ~ 230 obtained for **P3HT-*b*-P3HTPMe$_3$,DS**. As such, we do not expect an increase in the thickness of the **CPE** shell, only in the chain packing/density

within the shell, which is suggested by the subtle decrease in 'wetness'. Unfortunately, the similarity between the SLDs of the **CPE** block and surfactant means that we can only observe the 'global' shell structure. Future studies will involve contrast matching with d_{25}-**DS**$^-$ to try and pin-point the exact orientation of the **CPEs** within the **CPE,DS** complexes. Nevertheless, we can conclude that **DS**$^-$ counterion exchange has only a limited effect on the solution structure of **P3HT-*b*-P3HTPMe$_3$,DS**, with the hydrophobic **P3HT** core apparently retaining the cylindrical morphology of the pure diblock. In comparison, the less-aggregated homopolymer **P3HTPMe$_3$** is able to freely transform from semi-flexible cylinders to rigid sheets upon counterion exchange.

3. PHOTOVOLTAIC PROPERTIES

To investigate the behavior of **CPEs** as cathodic interlayers, bulk heterojunction (BHJ) polymer solar cells with a traditional architecture (glass/ITO/**PEDOT:PSS**/active layer/**CPE**/Al) were fabricated in collaboration with Pr. Wouter Maes and Dr. Jurgen Kesters (University of Hasselt, Belgium). The active layer **PCDTBT**:**PC$_{71}$BM** was used for **CPE,Br** and **CPE,TFSI** while **PBDTTPD**:**PC$_{71}$BM** was later used for **CPE,DS** for its high and reproducible performances (Figure 3.23).[44]

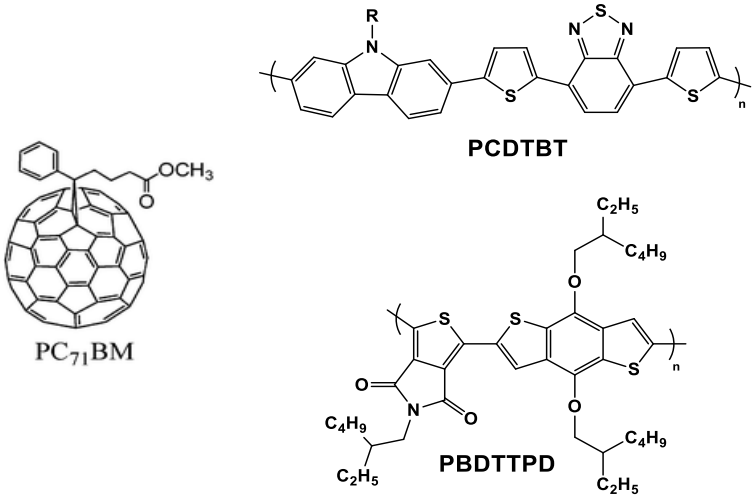

Figure 3.23 Structures of donor polymers and fullerene derivative used in the active layer of BHJ solar cells.

The **CPEs** bearing different cationic groups (*i.e.* trimethylammonium, trimethylphosphonium, methylimidazolium and pyridinium), counterions (*i.e.* **Br**$^-$, **TFSI**$^-$ and **DS**$^-$) and having different topology (homopolymer *vs.* copolymer) were used in BHJ solar cells as cathode interlayer, except pyridinium derivatives. This is because pyridinium-based **CPEs** are less soluble in methanol, the deposition solvent, than its counterparts. For this reason, in order to have the best possible comparison between the different interfacial materials, we decided to focus on the other **CPEs** materials. The **CPEs** interlayers were spin-coated directly on top of the active layer from methanol solutions (0.5 mg.mL^{-1}). The photovoltaic parameters obtained with these

CPEs are summarized in Table 3.4 and are compared to a device based on a traditional electrode Ca/Al.

3.1. HOMOPOLYMER *VS.* COPOLYMER CPES

Compared to the homopolymers, the copolymers lead to better PCEs with an average PCE of 4.98 % for the **CPEs,Br** vs. 5.80 % for the **P3HT-*b*-CPEs,Br**. This finding was already reported by Scherf *et al.* where the **P3HTNMe$_3$** homopolymer displayed lower PCEs than the **PF-*b*-P3HTNMe$_3$** block copolymer (Figure 3.1), 6.1% *vs.* 6.2% respectively in **PCDTBT:PCBM** devices.[45]

Table 3.4 Photovoltaic parameters of **PCDTBT**:**PC$_{71}$BM** polymer solar cells depending on the cathodic interlayer.

Active layer	Cathode interlayer	Voc (V)	Jsc (mA.cm^{-2})	FF	Average PCE (%)	Best PCE (%)
PCDTBT : PC$_{71}$BM	**Ca**	0.85	10.58	0.52	4.70	4.90
	P3HTIm,Br	0.87	10.83	0.50	4.68	4.92
	P3HTNMe$_3$,Br	0.89	11.14	0.56	5.50	5.84
	P3HTPMe$_3$,Br	0.90	11.36	0.56	5.72	6.09
	P3HT-*b*-P3HTIm,Br	0.89	11.31	0.58	5.85	6.44
	P3HT-*b*-P3HTNMe$_3$,Br	0.90	11.08	0.58	5.79	6.35
	P3HT-*b*-P3HTPMe$_3$,Br	0.87	11.10	0.59	5.81	6.06
PBDTTPD : PC$_{71}$BM	**Ca**	0.93	11.32	0.69	7.18	7.70
	P3HTIm,TFSI	0.92	11.57	0.70	7.44	8.08
	P3HTPMe$_3$,TFSI	0.92	11.73	0.71	7.72	8.30
	P3HTPMe$_3$,DS	0.93	13.20	0.70	8.65	8.83
	P3HT-*b*-P3HTPMe$_3$,DS	0.93	13.52	0.70	8.78	8.91

Bazan *et al.* also demonstrated, with contact angle measurements, that the ionic groups were accumulated at the surface.[45] This result is consistent with the aggregation behavior of the **CPEs** described above, where the aggregates present a hydrophobic core (neutral conjugated polymer backbone) and a hydrophilic shell (**CPE** moieties). To confirm this behavior, contact angle measurements could be performed in further studies of our block copolyelectrolytes.

It can be noted that the photovoltaic performances obtained for **P3HTNMe$_3$,Br** are significantly lower than those obtained in previous studies. This effect could be in part explained by the hygroscopic character of the bromide counteranion (*cf.* thermal properties). Considering

the formation of dipoles at the interface, the presence of water induces a lack of repeatability in the photovoltaic performances.

3.2. NATURE OF THE IONIC SIDE-CHAIN GROUPS

The incorporation of **CPEs,Br** as cathode interfacial layer leads to enhanced photovoltaic performances only for **CPE** derivatives bearing ammonium and phosphonium cationic groups. This finding is in contrast with those reported in the literature: Maes *et al.* have indeed reported that the imidazolium derivative afforded better performances than the ammonium one.[4c-d] These differences could be explained by the difference in the number average molecular weight, which is lower in this study than in Maes' work (10 000 *vs.* 30 000 g.mol^{-1}). Indeed, **CPEs,Br** having higher molecular weight yielded higher J_{SC} and PCEs. Besides, by changing the topology of the polyelectrolyte (homopolymer *vs.* block copolymer), the PCE trend is completely inverted: **P3HT-*b*-P3HTPMe$_3$,Br** displays the lowest efficiency, while its homopolymer analogue **P3HTPMe$_3$,Br** displays the highest one.

To further understand these photovoltaic performances, AFM analyses were recorded on the interfacial layers deposited onto the **PCDTBT**:**PC$_{71}$BM** photoactive layer. As examples, the AFM images obtained for **P3HT-*b*-CPEs,Br** are shown in Figure 3.24. The AFM images clearly demonstrate an incomplete coverage of the photoactive layer with the formation of islands with an average thickness of 4-6 nm. The deposit of the phosphonium-based copolyelectrolyte is even less complete; it exhibits a thin and random network of holes of around 100 nm diameter. Considering the percentage of surface coverage with the trend observed in obtained PCEs, it seems that these two parameters are potentially linked: **P3HT-*b*-P3HTPMe$_3$,Br** < **P3HT-*b*-P3HTNMe$_3$,Br** < **P3HT-*b*-P3HTIm,Br**.

By comparing the results obtained for each ionic group, it is difficult to identify a trend concerning their influence. This lack of reproducibility could be explained by the hydrophilic behavior of the bromide ion, as already discussed above. Thus, we decided to replace the bromide counterion by **TFSI** anion, for which no hygroscopic character was observed (*cf.* thermal properties).

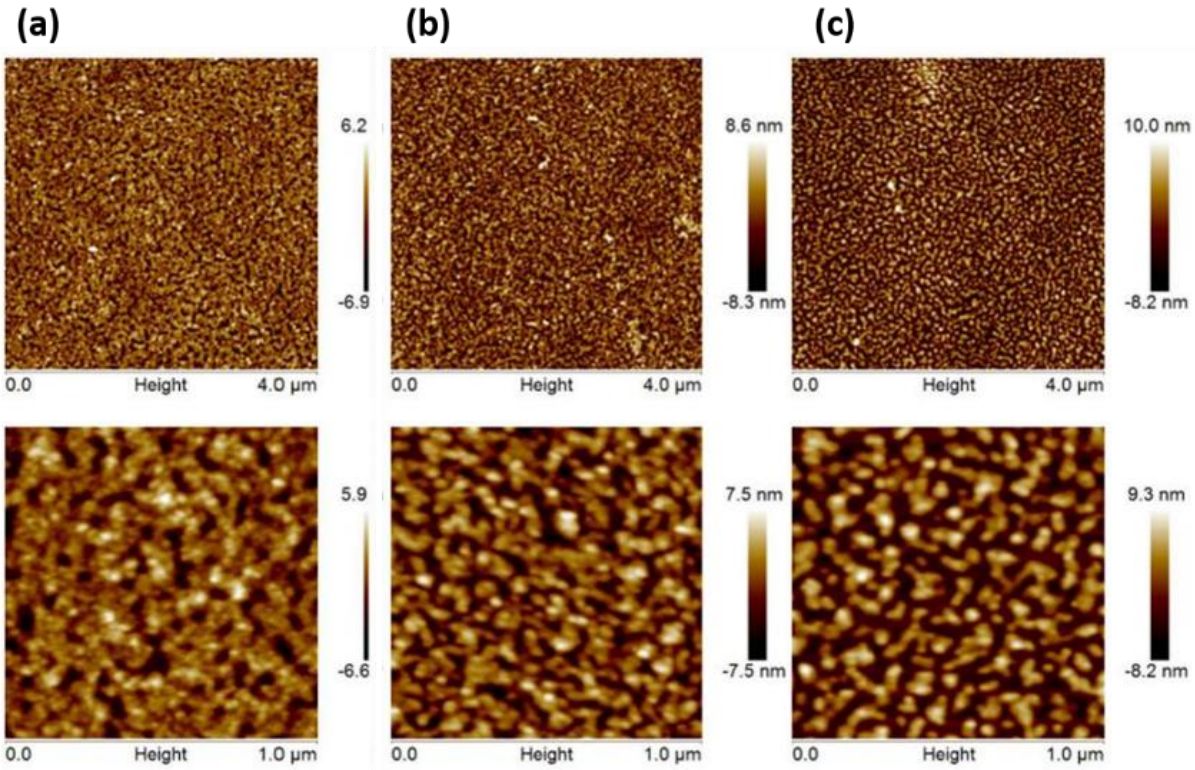

Figure 3.24 1 x 1 µm² AFM height images of (a) **P3HT-*b*-P3HTIm,Br**, (b) **P3HT-*b*-P3HTNMe$_3$,Br** and (c) **P3HT-*b*-P3HTPMe$_3$,Br** interlayers deposited on the **PCDTBT**:**PC$_{71}$BM** photoactive layer. The relative area covered by the **P3HT-*b*-CPE, Br** is 82, 68, and 50 %, respectively.

The PCEs obtained for solar cells based on **CPEs,TFSI** as interlayers are much higher than those based on **CPEs,Br**. Indeed, PCEs reached values until 5.72 % (**P3HTPMe$_3$,Br**) for **CPEs,Br** while values up to 6.27 % (**P3HTIm, TFSI**) were obtained for **CPEs, TFSI**. These values were further improved by using **PBDTTPD**:**PC$_{71}$BM** as the photoactive layer in OPVs: for example, PCEs of 7.72 % on average were obtained for **P3HTPMe$_3$,TFSI** *vs.* 6.16 % when using **PCDTBT**:**PC$_{71}$BM** as the photoactive layer.[46]

Concerning the relationship between the surface coverage and the PCEs, similar conclusions can be drawn for **CPEs,TFSI**. AFM images recorded on **P3HTPMe$_3$,TFSI** and **P3HTIm,TFSI** thin films clearly demonstrated an incomplete photoactive layer coverage with the formation of patches, as observed for **P3HT-*b*-CPEs,Br**. The differences observed in terms of PCEs (**P3HTIm,TFSI** < **P3HTPMe$_3$,TFSI**) seem to be linked with the surface coverage: 12 < 13 %, respectively (Figure 3.25, a). For **P3HTIm,TFSI** and **P3HTPMe$_3$,TFSI**, a strong "dewetting" is observed, with globule heights up to ~30–40 nm. Besides, the affinity between the layers is also a key point to enhance the efficiency: **P3HTIm,TFSI** displayed thickness values much higher than **P3HTPMe$_3$,TFSI** thus resulting in a better affinity and improved performances.

Furthermore, the coverage of a specific **CPE** material also differs when processed on top of a different active layer, as shown by Maes *et al.* The coverage of a diblock neutral/ionic

copolythiophene **P4** on top of **PCDTBT:PC$_{71}$BM** was clearly more homogeneous than on top of **PBDTTPD**:**PC$_{71}$BM**, possibly related to of the observed photovoltaic performance enhancement (Figure 3.25, b).[46]

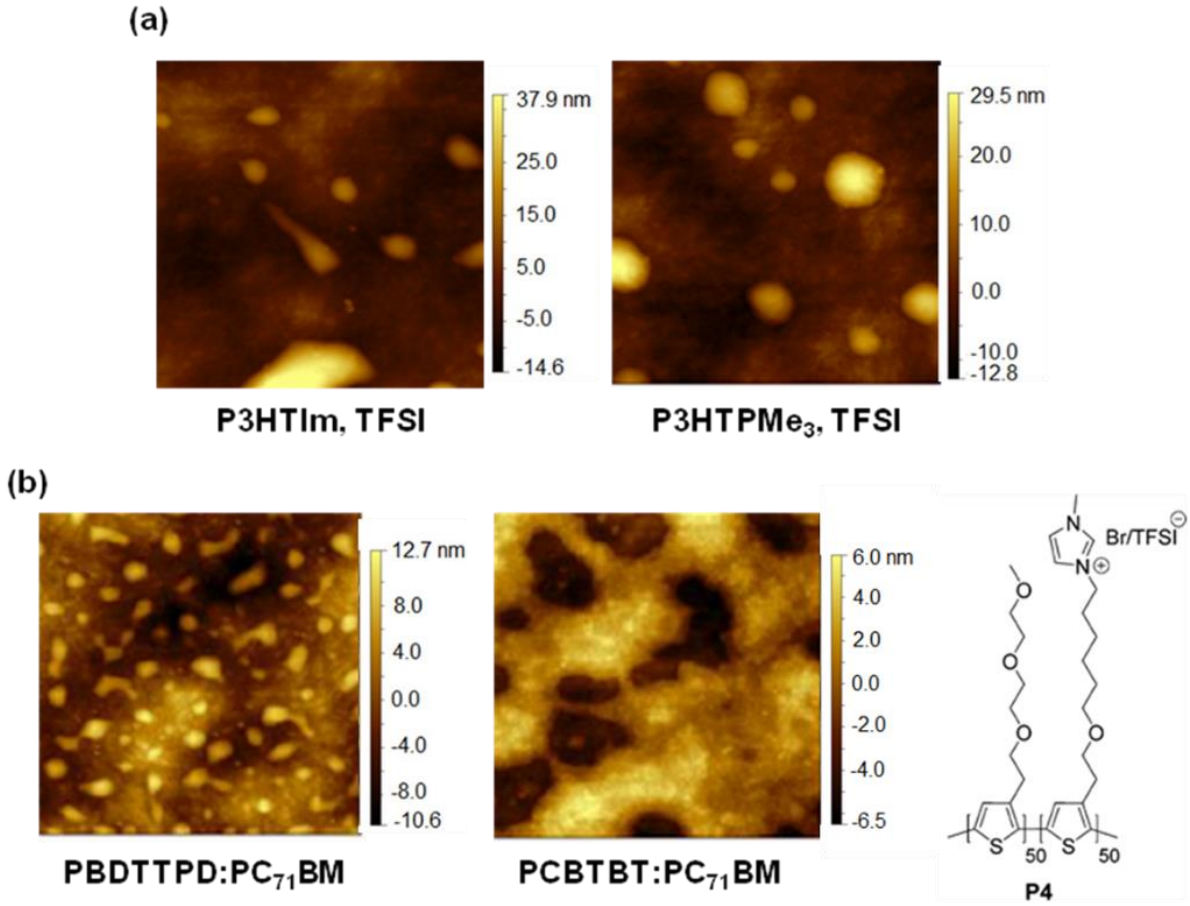

Figure 3.25 1 x 1 µm² **(a)** AFM height images of the polymer solar cells (**PBDTTPD**:**PC$_{71}$BM**) integrating **P3HTIm,TFSI (left)** and **P3HTPMe$_3$,TFSI (right)** as cathode interfacial layer. (b) AFM height images of devices with **P4,TFSI** cathode interlayer on the top of **PBDTTPD:PC$_{71}$BM** (left) and **PCDTBT:PC$_{71}$BM** (right) photoactive layers.

The hypothesis on the relationship between the surface coverage and the performances was supported by further electrical permittivity and impedance spectroscopy measurements.[46] Devices integrating **P3HT-*b*-CPEs,TFSI** interlayers are currently under investigation but the preliminary results are for now in good agreement with the results and the trends observed for their homopolyelectrolytes counterparts.

3.3. NATURE OF THE COUNTERION

As the counterion exchange from **Br$^-$** to **TFSI$^-$** was already discussed in the last section, we will focus in this part on the incorporation of the surfactants as counter-ions.

The introduction of **CPE** interlayers mostly affects the J_{SC}, resulting in significantly increased PCEs by about 20 %, from 7.18 to 8.65 and 8.78 % for the homopolymer and block copolymer surfactants, respectively (Figure 3.26, left). These values are significantly higher than those reported for polymer solar cells incorporating a **P3TMAHT,DS** complex as a cathode interlayer (PCE = 4.01 % for **P3HT:PC$_{61}$BM** and PCE = 6.47 % for **PTB7**:**PC$_{71}$BM**).[10b] A control device with pure methanol spin-coated on top of the photoactive layer also provided some efficiency increase up to 7.89 %, in accordance with previous findings.[4b,4547] These values were still significantly below the PCEs obtained upon incorporation of the **CPE** interlayers.

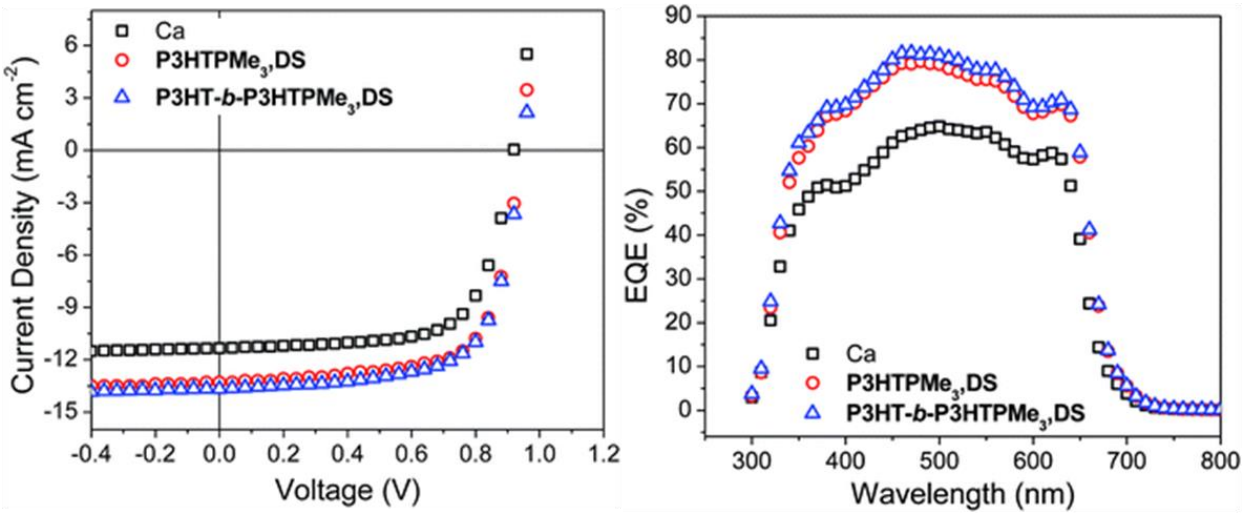

Figure 3.26 J–V (left) and EQE (right) curves for average performance **PBDTTPD**:**PC$_{71}$BM** solar cell devices produced with and without **CPE** interlayers (0.5 mg.mL^{-1} deposition solution).

From the EQE spectra, enhanced photocurrent generation over the entire absorption range can be observed upon incorporation of the surfactant interlayers (Figure 3.26, right). A maximum EQE of 65 % was obtained for the reference device, whereas the value increased to ~ 80 % for the devices with **CPE** cathodic interlayers. The current densities extracted from the EQE measurements (J_{EQE} = 13.06 and 13.39 mA.cm^{-2} for the **P3HTPMe$_3$,DS** and **P3HT-*b*-P3HTPMe$_3$,DS** interlayers, respectively) well correspond to the measured J_{SC} values.

AFM measurements were also performed to investigate the adhesion efficiency of **P3HTPMe$_3$,DS** and **P3HT-*b*-P3HTPMe$_3$,DS** on the **PBDTTPD:PC$_{71}$BM** photoactive layer (Figure 3.27). Different topographies were observed for the homo- and block polyelectrolytes, both showing non-complete active layer coverage after spin-coating. However, while **P3HT-*b*-P3HTPMe$_3$,DS** shows an improved affinity towards deposition on top of the photoactive layer, this phenomenon does not seem to have a major influence on the final device performance.

The solution-phase structure of the casting solution is expected to affect the morphology of the deposited layer. However, in this case, no direct correlation between the organization in solution deduced from the SANS data and the AFM morphology can be established. The SANS

experiments were performed at significantly higher solution concentrations than those employed for **CPEs** deposition (~10 × larger), which could explain this difference, most notably the absence of extended structures. Moreover, spin-coating is known to reduce the crystallinity of **P3HT** thin films as it prevents appropriate alignment of the polymer chains.[45a] Thermally-induced morphological instabilities due to the formation of non-equilibrium structures during device operation are also a consideration.[45b-d] A detailed study is now underway to determine the key relationships between the organization in solution, the film deposition process and the film morphology which underpin the significant enhancement in the PCEs observed here. **CPEs** having other counterions (octylsulfate and perfluorooctylsulfonate) are also currently under investigation.

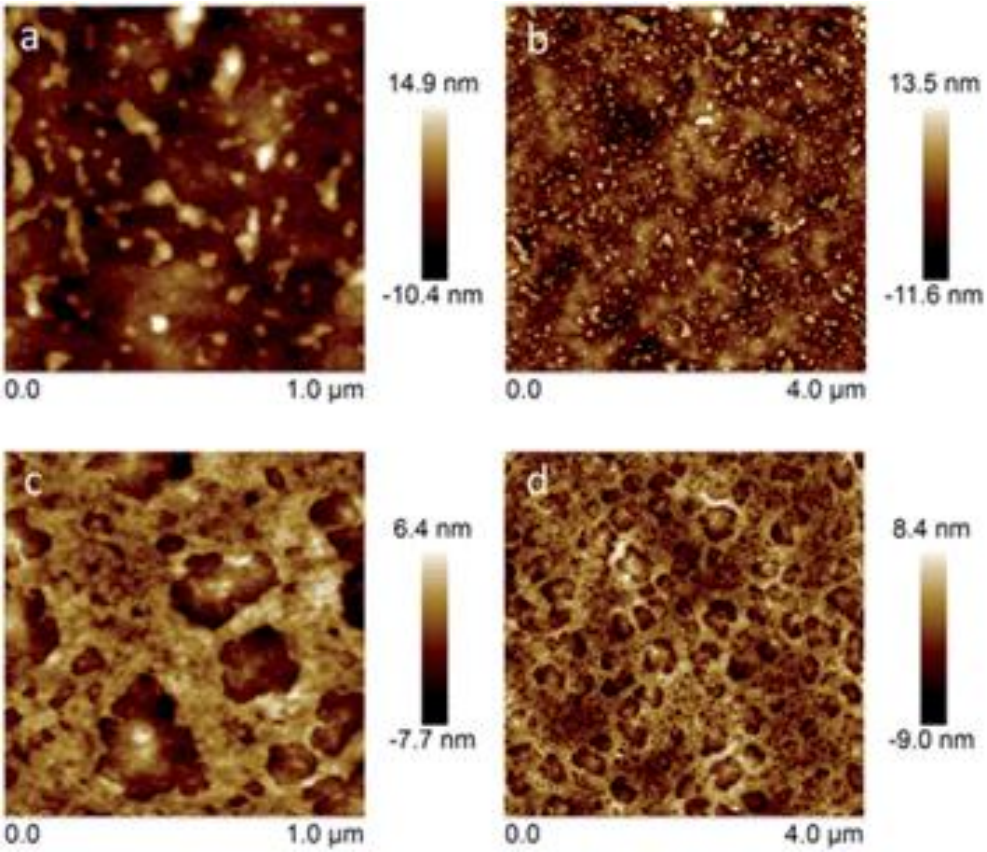

Figure 3.27 AFM height images (1 × 1 µm^2 and 4 × 4 µm^2) of **P3HTPMe$_3$,DS** (a and b) and **P3HT-*b*-P3HTPMe$_3$,DS** (c and d) interlayers deposited onto **PBDTTPD:PC$_{71}$BM** photoactive layers.

CONCLUSION

In this chapter, conjugated polyelectrolytes (**CPEs**) have been synthesized, characterized and used as cathode interfacial layers in bulk heterojunction (BHJ) solar cells. **CPEs** having different topologies, *i.e.* homopolymer *vs.* diblock copolymer, and bearing different cationic groups, *i.e.* imidazolium, pyridinium, phosphonium and ammonium, were obtained by nucleophilic substitution of the bromide atom from the bromide-based homo- and block copolymer

precursors. These precursor polymers, *i.e.* **P3HTBr** and **P3HT-*b*-P3HTBr**, were obtained using the Kumada Catalyst Transfer Polycondensation (KCTP) method, leading to polymers with controlled molecular weight and low dispersity. The influence of the nature of the counterion on the photovoltaic performance was also studied. Thus the bromide counterion (**Br^-**) was exchanged by the more hydrophobic bis(trifluoromethane)sulfonimide (**$TFSI^-$**) and the dodecylsulfate (**DS^-**) surfactant. It has been already reported that surfactants can favour the electrostatic self-assembly of the **CPE** chains, enabling the orientation of the dipole moment at the interface.

The introduction of the cationic groups on the side chains of the polymers resulted in an increasing solubility in polar solvents such as water and methanol. For **P3HT-*b*-CPEs** diblock copolymers, both blocks, *i.e.* neutral and cationic ones, enable solubilizing the copolymer in classical solvents of **P3HT** (chloroform, tetrahydrofuran) as well as in polar solvents, resulting in a solvatochromic behavior. As the optical properties of these polymers are linked to their π-conjugated backbone, the absorption and emission profiles were found to be independent of the nature of cationic group and counterion.

Regarding the thermal properties, the topology, the nature of the cationic group and the counterion were found to significantly affect the behavior of the **CPEs**. A clear signature of the diblock copolymer structure was observed: a glass transition temperature (T_g) characteristic of the **CPE** block and a melting temperature corresponding to the **P3HT** block. The T_g was found to be dependent on the nature of the **CPE** block as well as the counterion. For example, exchanging the **Br^-** for **$TFSI^-$** and **DS^-** ions resulted in considerably lower T_g values and a strong plasticizing effect was observed.

Regarding the aggregation behavior of these polymers in solution, dynamic light scattering (DLS) analyses demonstrated that the **CPE** particles were larger in methanol/water mixtures than in the pure corresponding solvents. In the methanol/water mixture, the aggregation of the polymer chains was reduced, resulting in swelling of the aggregate structure due to associated solvent molecules. The hydrodynamic diameter was thus increased. This finding was further confirmed by small-angle neutron scattering (SANS) analyses, which also showed that **P3HT-*b*-CPEs** formed core-shell (core: **P3HT**, shell: **CPE**) cylindrical aggregates in solution. The aggregate structures were found to be dependent on the solvent nature and could be transferred as thin films with the retention of their nanoscale organization, as observed by atomic force microscopy (AFM) analyses. This result is of crucial importance for potential device applications. Upon counterion exchange, a limited effect on the aggregation behavior was observed for the diblock copolymer: **P3HT-*b*-P3HTPMe$_3$,DS** retained the cylindrical core-shell morphology of the pure diblock. In comparison, the corresponding homopolymer was less-aggregated and thus, was able to freely transform from semi-flexible cylinders to rigid sheets upon counterion exchange from **Br^-** to **DS^-**.

Finally, the conjugated polyelectrolytes were used as cathode interfacial layers in BHJ solar cells. The introduction of these polymers resulted in a significant enhancement of the solar

cell performances. Compared to the homopolymers, the diblock copolymers afforded better PCEs and the photovoltaic performances were found to be dependent on the cationic group and the counterion. Regarding the cationic group, it seems that there is a correlation between the performances and the surface coverage determined by AFM analyses. Further analyses as the dielectric permittivity measurments were also done to correlate this hypothesis. Regarding the counterion, solar cells with bromide **CPEs** reached lower performances than those with **CPEs, TFSI**. This observation can be due to the hydrophilic character of the bromide counterion observed with thermal analyses, which complicates the repeatability and the interpretation of the results. The introduction of **CPEs,DS** as cathodic interfacial layers also provided better results than the bromide counterion with an enhancement of the performances by about 20 %. This preliminary study will be extended to other surfactants, such as octylsulfate (**OS^-**) and perfluorooctylsulfonate (**$PFOS^-$**), which could provide other self-assemblies of **CPEs** in this interlayer.

EXPERIMENTAL PROCEDURE

SYNTHESIS OF THE POLYTHIOPHENE POLYMER PRECURSORS

Synthesis of poly(3-(6'-bromohexyl)thiophene) (P3HTBr). 2,5-dibromo-3-(6'-bromohexyl)thiophene (1.16 g, 2.86 mmol) was dried by three successive azeotropic distillations with toluene and then, dry THF (13 mL) was added. A 2M solution of *i*PrMgCl in THF (1.40 mL) was added via a syringe, and the mixture was stirred at 0 °C for 30 min. Once the Grignard reagent was formed, the solution was cannulated in one portion to the Ni(dppp)Cl_2 catalyst (25 mg) in THF (13 mL) at 0°C. After stirring the reaction mixture for 3 h, the polymerization was quenched quickly by pouring HCl aq. (5 M) into the solution. The reaction mixture was stirred for 30 minutes. Then, the polymer was precipitated in cold MeOH and filtered. The product was washed with MeOH to yield **P3HTBr** as a red solid. **Yield:** 73 %. **^{1}H NMR ($CDCl_3$)**: δ 1.52 (m, 8H, CH_2), 2.85 (m, 2H, CH_2-Th), 3.45 (t, 2H, CH_2-Br, $^3J_{H-H}$ = 6.7 Hz), 7.0 (s, 1H, Th) ppm. **^{13}C{^{1}H} NMR ($CDCl_3$):** δ = 28.2, 28.8, 29.5, 30.5, 32.9, 34.2, 128.8, 130.8, 133.9, 139.8 ppm. **UV-vis ($CHCl_3$):** λ_{max} = 448 nm. **SEC (THF, PS standards):** M_n = 13 600 g.mol^{-1}, M_w = 18 500 g.mol^{-1}, $Đ$ = 1.36.

Poly[(3-hexylthiophene)-2,5-diyl]-*block*-poly[3-(6'-bromohexyl)thiophene-2,5-diyl] block copolymer (P3HT-*b*-P3HTBr). Two round-bottomed flasks (100 mL) were dried by heating under reduced pressure and cooled to room temperature. 2-Bromo-3-hexyl-5-iodothiophene (1.2 g, 3.3 mmol) was dried by three successive azeotropic distillations with toluene, and then, dry THF (15 mL) was added. A 2M solution of *i*PrMgCl in THF (1.65 mL) was added via a syringe, and the mixture was stirred at 0 °C for 30 min (solution A). Solution A was added in one portion to the Ni(dppp)Cl_2 catalyst (59 mg) in THF (10 mL). In the other flask, 2,5-dibromo-3-(6'-bromohexyl)thiophene (1.1 g, 2.7 mmol), previously dried by azeotropic distillation, was reacted

with *i*PrMgCl (1.35 mL) in a similar manner as 2-bromo-3-hexyl-5-iodothiophene (solution B). After stirring the reaction mixture for 3 h, solution B was added to the previous mixture via a syringe, and the resulting solution was stirred overnight. The reaction was then quenched quickly by pouring HCl aq. (5 M) into the solution and the solution was stirred for 30 minutes. Then, the polymer was precipitated in cold MeOH and filtered. The product was washed with MeOH to yield **P3HT-*b*-P3HTBr** as a red solid. **Yield:** 82 %. **^{1}H NMR ($CDCl_3$):** δ 0.90 (t, 3H, CH_3, $^3J_{H-H}$ = 6.8 Hz), 1.62 (m, 16H, CH_2), 2.80 (t, 4H, CH_2–Th, $^3J_{H-H}$ = 7.9 Hz), 3.42 (t, 2H, CH_2–Br, $^3J_{H-H}$ = 6.7 Hz), 6.98 (s, 2H, Th) ppm. **^{13}C{^{1}H} NMR ($CDCl_3$):** δ 14.3, 22.8, 28.1, 28.8, 29.4, 29.6, 30.5, 30.7, 31.8, 32.9, 34.0, 128.8, 130.7, 130.8, 139.8, 140.0 ppm. **UV-vis ($CHCl_3$):** λ_{max} = 450 nm. **SEC (THF, PS standards):** M_n = 11 000 g.mol^{-1}, M_w = 12 300 g.mol^{-1}, ~~Đ~~ = 1.12.

SYNTHESIS OF THE CONJUGATED POLYELECTROLYTES

General procedure for the synthesis of P3HTIm,Br and P3HTPy,Br polyelectrolytes. The **P3HTBr** (100 mg) was allowed to react with 1-methylimidazole (10 mL) or pyridine (10 mL) in refluxing chloroform (10 mL) for 2 days. After cooling to room temperature, the mixture was poured into Et_2O to precipitate the **P3HTIm,Br** and **P3HTPy,Br** polyelectrolytes. The crude polymers obtained were repeatedly washed with diethyl ether to remove excess of 1-methylimidazole or pyridine, and then, dried under vacuum at 40 °C. The **P3HTIm,Br** and **P3HTPy,Br** polymers were further purified in refluxing diethyl ether using a Soxhlet apparatus overnight and finally, dried under vacuum at 40 °C.

P3HTIm,Br. Yield: 79 %, **^{1}H NMR (CD_3OD):** δ 1.48 (m, 4H, CH_2), 1.75 (m, 2H, CH_2), 1.95 (m, 2H, CH_2), 2.87 (m, 2H, CH_2-Th), 3.97 (s, 3H, N–CH_3), 4.26 (t, 2H, CH_2-N, $^3J_{H-H}$ = 7.0 Hz), 7.15 (s, 1H, H_{Th}), 7.60 (s, 1H, H_{Im}), 7.70 (s, 1H, H_{Im}), 9.10 (s, 1H, H_{Im}) ppm. **^{13}C{^{1}H} NMR (CD_3OD):** δ 27.6, 30.5, 30.7, 31.9, 33.0 (CH_2), 62.9 (CH_2-N), 129.9, 130.6, 132.6, 135.1, 141.8, 146.4, 147.2 ppm. **UV-vis (MeOH):** λ_{max} = 441 nm. **Anal. calcd:** N/S 2.00, found 2.09.

P3HTPy,Br. Yield: 81 %, **^{1}H NMR (CD_3OD):** δ 1.52 (m, 4H, CH_2), 1.74 (m, 2H, CH_2), 2.08 (m, 2H, CH_2), 2.87 (m, 2H, CH_2-Th), 4.71 (t, 2H, CH_2-N, $^3J_{H-H}$ = 6 Hz), 7.11 (s, 1H, H_{Th}), 8.12 (m, 2H, H_{Pyr}), 8.59 (br., 1H, H_{Pyr}), 9.10 (m, 2H, H_{Pyr}) ppm. **^{13}C{^{1}H} NMR (CD_3OD):** δ 27.6, 30.5, 30.7, 31.9, 33.0 (CH_2), 62.9 (CH_2-N), 129.9, 130.6, 132.6, 135.1, 141.8, 146.4, 147.2 ppm. **UV-vis (MeOH):** λ_{max} = 444 nm. **Anal. calcd:** N/S 1.00, found 0.97.

General procedure for the synthesis of P3HTNMe$_3$,Br and P3HTPMe$_3$,Br homopolyelectrolytes. The **P3HTBr** homopolymer (100 mg) was introduced into a 100 mL two-necked flask equipped for stirring and dissolved in $CHCl_3$ (15 mL). 12 mL of a solution of trimethylamine or trimethylphosphine (1.0 M in THF) were added and the mixture was stirred at 40 °C for 48 h. After cooling to room temperature, the solvent mixture was evaporated and the residue was

dissolved in the minimum amount of $CHCl_3$ and poured into Et_2O to precipitate the **P3HTNMe$_3$,Br** or **P3HTPMe$_3$,Br** conjugated polyelectrolytes. The crude products obtained were repeatedly washed with diethyl ether and dried under vacuum at 40 °C. **P3HTNMe$_3$,Br** and **P3HTPMe$_3$,Br** were further purified with refluxing diethyl ether overnight using a Soxhlet apparatus and finally, dried under vacuum at 40 °C.

P3HTNMe$_3$,Br. Yield: 75 %, **^{1}H NMR (CD_3OD):** δ 1.50 (br., 4H, CH_2), 1.79 (br., 4H, CH_2), 2.46 (br., 2H, CH_2-Th), 3.15 (s, 9H, N-CH_3), 3.39 (br., 2H, CH_2-N), 7.13 (s, 1H, H_{Th}) ppm. **^{13}C{^{1}H} NMR (CD_3OD):** δ = 140.5, 133.9, 130.7, 129.3, 66.8, 52.7, 30.5, 30.4, 29.2, 26.3, 23.0 ppm. **UV-vis (MeOH):** λ_{max} = 442 nm. **Anal. calcd:** N/S 1.00, found 0.98.

P3HTPMe$_3$,Br. Yield: 77 %, **^{1}H NMR (CD_3OD):** δ 1.38-1.80 (m, 8H, CH_2), 1.91 (m, 9H, CH_3-P), 2.26 (m, 2H, CH_2), 2.86 (s, 2H, CH_2), 7.11 (s, 1H, H_{Th}) ppm. **^{13}C{^{1}H} NMR ($CDCl_3$):** δ = 140.2, 133.9, 130.7, 128.9, 30.9, 30.5, 29.2, 23.8, 23.7, 21.6, 7.35 (d, $^1J_{P\text{-}C}$ = 55 Hz) ppm. **^{31}P{^{1}H} NMR ($CDCl_3$):** δ = 27.1 (s) ppm. **UV-vis (MeOH):** λ_{max} = 442 nm.

General procedure for the synthesis of P3HT-*b*-P3HTIm,Br and P3HT-*b*-P3HTPy,Br block copolyelectrolytes. The **P3HT-*b*-P3HTBr** block copolymer (150 mg) was allowed to react with 1-methylimidazole (10 mL) or pyridine (10 mL) in refluxing chloroform (10 mL) for 2 days. After cooling to room temperature, the mixture was poured into Et_2O to precipitate the **P3HT-*b*-P3HTIm,Br** and **P3HT-*b*-P3HTPy,Br** polyelectrolytes. The crude polymers were repeatedly washed with diethyl ether to remove the excess of 1-methylimidazole or pyridine, and then, dried under vacuum at 40 °C. The **P3HT-*b*-P3HTIm,Br** and **P3HT-*b*-P3HTPy,Br** polymers were further purified in refluxing diethyl ether overnight using a Soxhlet apparatus and finally, dried under vacuum at 40 °C.

P3HT-*b*-P3HTIm,Br. Yield: 80 %, **^{1}H NMR ($CDCl_3$):** δ = 0.89 (br.), 1.19–1.47 (br.), 1.69 (br.), 1.90 (br.), 2.78 (br.), 3.19 (br.), 4.05 (br.), 4.34 (br.), 6.97 (br.), 7.74 (br.), 9.92 (br.) ppm. **^{13}C{^{1}H} NMR ($CDCl_3$):** δ = 14.2, 22.8, 26.3, 29.1, 29.4, 29.6, 30.5, 30.6, 31.8, 36.9, 50.1, 122.8, 124.1, 128.7, 130.6, 133.8, 136.7, 140.0 ppm. **UV-vis ($CHCl_3$):** λ_{max} = 452 nm. **Anal. calcd:** N/S 0.86, found 0.86.

P3HT-*b*-P3HTPy,Br. Yield: 81 %, **^{1}H NMR ($CDCl_3$):** δ = 0.91 (br.), 1.27–1.50 (br.), 1.70 (br.), 2.04 (br.), 2.80 (br.), 4.00 (br.), 6.96 (br.), 8.16 (br.), 8.60 (br.), 9.50 (br.) ppm. **^{13}C{^{1}H} NMR ($CDCl_3$):** δ = 15.4, 23.8, 27.1, 30.2, 30.5, 30.7, 31.7, 32.8, 33.2, 62.9, 129.8, 131.7, 134.9, 141.1, 146.3, 147.0 ppm. **UV-vis ($CHCl_3$):** λ_{max} = 455 nm. **Anal. calcd:** N/S 0.43, found 0.41.

General procedure for the synthesis of P3HT-*b*-P3HTNMe$_3$,Br and P3HT-*b*-P3HTPMe$_3$,Br block copolyelectrolytes. The **P3HT-*b*-P3HTBr** block copolymer (150 mg) was introduced into a 100 mL two-necked flask equipped for stirring and dissolved in $CHCl_3$ (15 mL). 12 mL of a solution of

trimethylamine or trimethylphosphine (1.0 M in THF) were added and the mixture was stirred at 40 °C for 48 h. After cooling to room temperature, the solvent mixture was evaporated and the residue was dissolved in the minimum amount of $CHCl_3$ and poured into Et_2O to precipitate the **P3HT-*b*-P3HTNMe$_3$,Br** or **P3HT-*b*-P3HTPMe$_3$,Br** polyelectrolytes. The crude products were repeatedly washed with diethyl ether and dried under vacuum at 40 °C. **P3HT-*b*-P3HTNMe$_3$,Br** and **P3HT-*b*-P3HTPMe$_3$,Br** were further purified with refluxing diethyl ether using a Soxhlet apparatus overnight and finally, dried under vacuum at 40 °C.

P3HT-*b*-P3HTNMe$_3$,Br. Yield: 79 %, **^{1}H NMR ($CDCl_3$):** δ = 0.90 (br.), 1.15–1.48 (m, br.), 1.71 (m, br.), 2.80 (br.), 3.35 (br.), 3.64 (br.), 6.95 (br.) ppm. **^{13}C{^{1}H} NMR ($CDCl_3$):** δ = 14.2, 22.8, 29.4, 29.6, 30.6, 31.8, 66.5, 128.7, 130.6, 133.8, 134.2, 140.0 ppm. **UV-vis ($CHCl_3$):** λ_{max} = 452 nm. **Anal. calcd:** N/S 0.43, found 0.40.

P3HT-*b*-P3HTPMe$_3$,Br. Yield: 80 %. **^{1}H NMR ($CDCl_3$):** δ = 0.90 (br.), 1.24–1.48 (br.), 1.70 (br.), 1.91 (br.), 2.12 (br.), 2.56 (br.), 2.80 (br.), 6.97 (br.) ppm. **^{13}C{^{1}H} NMR ($CDCl_3$):** δ = 10.0, 10.3, 15.2, 22.8, 23.6, 23.8, 30.4, 30.2, 30.7, 31.4, 31.7, 32.7, 32.9, 129.7, 131.7, 134.8, 141.0 ppm. **^{31}P{^{1}H}NMR ($CDCl_3$):** δ = 27.0 (s, 1P) ppm. **UV-vis ($CHCl_3$):** λ_{max} = 455 nm.

COUNTERION EXCHANGE

General procedure for the counterion exchange. The homo- or co-polyelectrolyte (100 mg) was dissolved in water (30 mL). The complete dissolution may require 24 hours at 35°C, depending on the polyelectrolyte. In parallel, an aqueous solution of LiTFSI or SDS (10 eq. against the **CPE** moiety in 1 mL) was prepared and subsequently added dropwise to the polyelectrolyte solution. The mixture was stirred for 16 hours at room temperature. The polymer was then collected by filtration, washed with water and diethyl ether and dried under vacuum.

P3HTIm,TFSI. Yield : 88 %, **^{1}H NMR (CD_3OD) :** δ = 1.60 (m, 8H, CH_2), 2.89 (m, 2H, CH_2-Th), 3.96 (s, 3H, CH_3-N), 4.31 (t, 2H, CH_2-N, $^3J_{H-H}$ = 6,9 Hz), 7.12 (s, 1H, Th), 7.60 (s, 1H, Im), 7.73 (s, 1H, Im), 9.11 (s, 1H, Im) ppm. **^{19}F NMR (CD_3OD) :** δ = -79.3 ppm.

P3HTNMe$_3$,TFSI. Yield: 83 %. **^{1}H NMR (CD_3OD) :** δ = 1.46 (br., 2H), 1.55 (br., 2H), 1.72 (br., 2H), 1,81 (br., 2H), 2.79 (br., 2H), 3.33 (br., 2H, CH_2-N), 6.93 (s, 1H), ppm. **^{13}C{^{1}H} NMR (CD_3OD) :** δ = 24.0, 27.2, 30.2, 30.6, 31.4, 53.6, 68.0, 121.3 (q, $^1J_{C-F}$ = 321.0 Hz), 129.5, 131.7, 135.0, 140.9 ppm. **^{19}F NMR (CD_3OD) :** δ = -80.1 ppm.

P3HTPMe$_3$,TFSI. Yield : 75 %. **^{1}H NMR (CD_3OD) :** δ = 1.49-1.68 (m, 6H), 1.71 (br., 2H), 1.80 (d, 9H, $(CH_3)_3P$, $^2J_{P-H}$ = 14.5 Hz), 2.18 (br., 2H), 2.78 (br., 2H), 6.90 (s, 1H) ppm; **^{13}C{^{1}H} NMR (CD_3OD) :** δ = 7.7, 8.1, 22,5, 23.9, 24.3, 29.5, 30.0, 30.7, 31.4, 32.1, 121.2 (q, $^1J_{C-F}$ = 321.0 Hz),

129.4, 131.6, 135.0, 141.2 ppm. **^{19}F NMR (CD_3OD) :** δ = -80.1 ppm. **^{31}P{^{1}H} NMR (CD_3OD) :** δ = 27.0 ppm.

P3HT-*b*-P3HTIm,TFSI. Yield : 90 %. **^{1}H NMR (CD_3OD) :** δ = 0.86 (m, 3H, CH_3), 1.60 (m, 8H, CH_2), 2.89 (m, 2H, CH_2-Th), 3.96 (s, 3H, CH_3-N), 4.31 (t, 2H, CH_2-N, $^{3}J_{H-H}$ = 6.9 Hz), 7.12 (s, 1H, Th), 7.60 (s, 1H, Im), 7.73 (s, 1H, Im), 9.11 (s, 1H, Im) ppm. **^{19}F NMR (CD_3OD) :** δ = -79.4 ppm. **UV-vis (MeOH):** λ_{max} = 442 nm. **UV-vis (Acetone)**: λ_{max} = 443 nm.

P3HT-*b*-P3HTNMe$_3$,TFSI. Yield : 90 %. **^{1}H NMR (CD_3OD) :** δ = 0.88 (m, 3H, CH_3), 1.53 (m, 8H, CH_2), 2.73 (m, 2H, CH_2-Th), 3.19 (s, 9H, CH_3-N), 3.44 (m, 2H, CH_2-N), 7.16 (s, 1H, Th) ppm. **^{19}F NMR (CD_3OD) :** δ = -79.2 ppm. **UV-vis (MeOH):** λ_{max} = 449 nm. **UV-vis (Acetone):** λ_{max} = 450 nm.

P3HT-*b*-P3HTPMe$_3$,TFSI. Yield : 91 %, **^{1}H NMR (CD_3OD) :** δ = 0.87 (m, 3H, CH_3), 1.31 (m, 8H, CH_2), 1.93 (d, 9H, CH_3-P, $^{2}J_{P-H}$ = 14.4Hz), 2.34 (m, 2H, CH_2-P), 2.89 (s, 2H, CH_2-Th), 7.14 (s, 1H, Th) ppm, **^{31}P{^{1}H} NMR (CD_3OD) :** δ= 27.1 (s, 1P) ppm. **^{19}F NMR (CD_3OD) :** δ = -79.2 ppm. **UV-vis (MeOH):** λ_{max} = 447 nm. **UV-vis (Acetone):** λ_{max} = 448 nm.

P3HTPMe$_3$,DS. Yield : 80 %. **^{1}H NMR (CD_3OD) :** δ = 0.87 (t, 3H, CH_2-CH_3, $^{3}J_{H-H}$ = 7.0 Hz), 1.24 (br., 16H), 1.48 (br., 2H), 1.53-1.67 (m, 4H), 1.75-1.90 (m, 4H), 2.89 (br., 2H), 3.14 (s, 9H, $N(CH_3)_3$), 3.39 (s, 2H), 3.97 (t, 2H, $^{3}J_{H-H}$ = 6.5 Hz, CH_2-O-SO_3^-), 7.11 (s, 1H) ppm. **^{13}C{^{1}H} NMR:** δ = 14.6, 23.8, 24.0, 27.0, 27.4, 29.8, 30.3, 30.4, 30.5, 30.6, 30.8, 30.9, 31.7, 33.1, 53.6, 67.8, 69.1, 130.1, 131.8, 135.0, 141.3 ppm. **UV-Vis (MeOH):** λ_{max} = 445 nm.

P3HT-b-P3HTPMe$_3$,DS. **Yield :**79 %, **^{1}H NMR (CD_3OD) :** δ = 7.10 (s, 1H), 3.96 (t, 2H, $^{3}J_{H-H}$ = 6.5 Hz, CH_2-O-SO_3^-), 2.89 (large, 2H), 2.27 (large, 2H), 1.88 (d, 9H, $(CH_3)_3$P, $^{2}J_{P-H}$ = 14.5 Hz), 1.78 (large, 2H), 1.68-1.52 (m, 8H), 1.35 (large, 2H), 1.32-1.22 (m, 16H), 0.87 (t, 3H, CH_2-CH_3, $^{3}J_{H-H}$ = 7.0 Hz) ppm. **^{13}C{^{1}H} NMR (CD_3OD)** : δ = 141.2, 134.8, 131.6, 130.0, 68.9, 32.9, 31.6, 31.5, 31.4, 30.7, 30.6, 30.5, 30.4, 30.3, 29.9, 23.7, 23.6, 22.3, 14.4, 7.8, 7.6 ppm. **^{31}P{^{1}H} NMR (CD_3OD) :** δ = 31.2 (s) ppm. **UV-Vis (MeOH):** λ_{max} = 448 nm. **UV-Vis (H_2O):** λ_{max} = 554, 592 nm.

OPV DEVICE FABRICATION AND CHARACTERIZATION

The low bandgap copolymer **PBDTTPD** with 2-ethylhexyloxy and octyl side chains on the BDT and TPD units respectively, was prepared according to a recently-developed continuous flow protocol.[42] **$PC_{71}BM$** ([6,6]-phenyl-C_{71}-butyric acid methyl ester) was obtained from Solenne. Bulk heterojunction (BHJ) polymer solar cells were fabricated using the traditional architecture glass/ITO/PEDOT:PSS/active layer/**CPE**/Al. Prior to processing, the indium tin oxide (ITO; Kintec, 100 nm, 20 Ohm.sq^{-1}) coated glass substrates were thoroughly cleaned using soap, demineralised water, acetone, isopropanol and a UV/O_3 treatment. **PEDOT:PSS** was then

deposited via spin-coating to obtain a layer thickness of ~30 nm. Further processing was carried out in a nitrogen-filled glovebox (O_2/H_2O < 0.1 ppm), initiated by a thermal treatment of 15 min at 130 °C to remove any residual water. The **PBDTTPD**:**$PC_{71}BM$** photoactive layer blend was then spin-coated in a 1:1.5 ratio with a total concentration of 20 mg.mL^{-1} from a mixture of chlorobenzene and 5 % (v/v) chloronaphthalene,[42] leading to an active layer thickness of ~110-120 nm. For the reference devices without a polyelectrolyte interlayer, Ca and Al electrodes were deposited with a thickness of ~30 and ~80 nm, respectively. For the devices employing the interlayer materials, the **CPEs** were spin-coated from methanol as a processing solvent in different concentrations (0.25, 0.5 and 1 mg.mL^{-1}) to optimize the solar cell parameters. The thickness of the **CPE** homopolymer layer was 12-20 nm, while the diblock copolymer layer was 6-10 nm thick. The devices were then finished off by the deposition of ~80 nm Al as the top electrode.

The J–V characteristics were measured using a Newport class A solar simulator (model 91195A), calibrated with a silicon solar cell to give an AM 1.5G spectrum.

External quantum efficiency (EQE) measurements were performed with a Newport Apex illuminator (100 W Xenon lamp, 6257) as light source, a Newport Cornerstone 130° monochromator and a Stanford SR830 lock-in amplifier for the current measurements. The light beam was mechanically chopped at 174/149 Hz. A silicon FDS100-CAL photodiode was employed as a reference cell.

For AFM imaging, a Bruker Multimode 8 AFM was used in PeakForce tapping mode, employing ScanAsyst. The images were produced with a silicon tip on a nitride lever with a spring constant of 4 N.m^{-1}.

REFERENCES

[1] *Conjugated polyelectrolytes. Fundamentals and Applications*, ed. B. Liu and G. C. Bazan, Wiley-VCH, Weinheim, **2013**.

[2] (a) W. Lee, J. H. Seo and H. Y. Woo, *Polymer*, **2013**, *54*, 5104; (b) A. Duarte, K.-Y. Pu, B. Liu and G. C. Bazan, *Chem. Mater.* **2011**, *23*, 501; (c) H. Jiang, P. Taranekar, J. R. Reynolds and K. S. Schanze, *Angew. Chem., Int. Ed. Engl.* **2009**, *48*, 4300; (d) C. Zhu, L. Liu, Q. Yang, F. Lu and S. Wang, *Chem. Rev.* **2012**, *112*, 4687; (e) G. Feng, J. Liang and B. Liu, *Macromol. Rapid Commun.,* **2013**, *34*, 705; (*f*) G. Feng, D. Ding and B. Liu, *Nanoscale*, **2012**, *4*, 6150.

[3] (a) Z. Hu, K. Zhang, F. Huang and Y. Cao, *Chem. Commun.* **2015**, *51*, 5572; (b) Z. He, H. Wu and Y. Cao, *Adv. Mater.* **2014**, *26*, 1006; (c) C. Duan, K. Zhang, C. Zhong, F. Huang and Y. Cao, *Chem. Soc. Rev.* **2013**, *42*, 9071.

[4] (a) C. He, C. Zhong, H. Wu, R. Yang, W. Yang, F. Huang, G. C. Bazan and Y. Cao, *J. Mater. Chem*. **2010**, *20*, 2617; (b) M. Y. Jo, Y. E. Ha, Y. S. Won, S. I. Yoo and J. H. Kim, *Org. Electron.* **2015**, *25*, 85; (c) J. Drijkoningen, J. Kesters, T. Vangerven, E. Bourgeois, L. Lutsen, D. Vanderzande, W.

Maes, J. D'Haen and J. Manca, *Org. Electron.* **2014**, *15*, 1282; (d) J. Kesters, T. Ghoos, H. Penxten, J. Drijkoningen, T. Vangerven, D. M. Lyons, B. Verreet, T. Aernouts, L. Lutsen, D. Vanderzande, J. Manca and W. Maes, *Adv. Energy Mater.* **2013**, *3*, 1180.

[5] (a) Z. He, C. Zhang, X. Xu, L. Zhang, L. Huang, J. Chen, H. Wu and Y. Cao, *Adv. Mater.* **2011**, *23*, 3086; (b) R. C. Evans, *J. Mater. Chem. C* **2013**, *1*, 4190.

[6] G. Tu, H. Li, M. Forster, R. Heiderhoff, L. J. Balk, R. Sigeland and U. Scherf, *Small* **2007**, *3*, 1001.

[7] C. V. Hoven, A. Garcia, G. C. Bazan and T.-Q. Nguyen, *Adv. Mater.* **2008**, *20*, 3793.

[8] (a) B. S. Gaylord, S. J. Wang, A. J. Heeger and G. C. Bazan, *J. Am. Chem. Soc.* **2001**, *123*, 6417; (b) R. Q. Yang, A. Garcia, D. Korystov, A. Mikkailovsky, G. C. Bazan and T.-Q. Nguyen, *J. Am. Chem. Soc.* **2006**, *128*, 16532.

[9] T. Ghoos, J. Brassinne, C.-A. Fustin, J.-F. Gohy, M. Defour, N. Van den Brande, B. Van Mele, L. Lutsen, D. J. Vanderzande and W. Maes, *Polymer*, **2013**, *54*, 6293.

[10] (a) L. Chen, C. Xie and Y. Chen, *Macromolecules*, **2014**, *47*, 1623; (b) Y.-M. Chang, R. Zhu, E. Richard, C.-C. Chen, G. Li and Y. Yang, *Adv. Funct. Mater.* **2012**, *22*, 3284.

[11] (a) A. Gutacker, S. Adamczyk, A. Helfer, L. E. Garner, R. C. Evans, S. M. Fonseca, M. Knaapila, G. C. Bazan, H. D. Burrows and U. Scherf, *J. Mater. Chem.* **2010**, *20*, 1423; (b) A. Gutacker, N. Koenen, U. Scherf, S. Adamczyk, J. Pina, S. M. Fonseca, A. J. M. Valente, R. C. Evans, J. Seixas de Melo, H. D. Burrows and M. Knaapila, *Polymer* **2010**, *51*, 1898; (c) M. Knaapila, R. C. Evans, A. Gutacker, V. M. Garamus, M. Torkkeli, S. Adamczyk, M. Forster, U. Scherf and H. D. Burrows, *Langmuir* **2010**, *26*, 5056; (d) A. Thomas, J. E. Houston, N. Van den Brande, J. De Winter, M. Chevrier, R. K. Heenan, A. E. Terry, S. Richeter, A. Mehdi, B. Van Mele, P. Dubois, R. Lazzaroni, P. Gerbaux, R. C. Evans and S. Clément, *Polym. Chem.* **2014**, *5*, 3352.

[12] (a) M. Chevrier, R. Di Ciuccio, O. Coulembier, P. Dubois, S. Richeter, A. Mehdi, S. Clément, **Functionalization of P3HT-based hydrid materials for photovoltaic applications** in *Novel Nanoscale Hybrids*, Wiley VCH (Eds. B. P. S. Chauhan), *accepted*; (b) A. Marrocchi, D. Lanari, A. Fachetti and L. Vaccaro, *Energy Environ. Sci.* **2012**, *5*, 8457.

[13] (a) J. C. Brendel, M. M. Schmidt, G. Hagen, R. Moos and M. Thelakkat, *Chem. Mater.* **2014**, *26*, 1992; (b) J. Rubio-Magnieto, A. Thomas, S. Richeter, A. Mehdi, P. Dubois, R. Lazzaroni, S. Clément and M. Surin, *Chem. Commun.* **2013**, *49*, 5483.

[14] M. Chayer, K. Faïd and M. Leclerc, *Chem. Mater.* **1997**, *9*, 2902.

[15] T. I. Wallow and B. M. Novak, *J. Am. Chem. Soc.* **1991**, *113*, 7411.

[16] Z. Peng, B. Xu, J. Zhang and Y. Pan, *Chem. Commun*. **1999**, 1855.

[17] C. Tan, M. R. Pinto and K. S. Schanze, *Chem. Commun.* **2002**, 446.

[18] Y. Zhang, T. Keisuke, H. Kouske and H. Kazuhito, *J. Am. Chem. Soc.* **2008**, *130*, 7812.

[19] P. Bäuerle, F. Würthner and S. Heid, *Angew. Chem. Int. Ed. Engl.* **1990**, *29*, 419.

[20] S. Clément, A. Tizit, S. Desbief, A. Mehdi, J. De Winter, P. Gebaux, R. Lazzaroni and B. Boury, *J. Mater. Chem.* **2011**, *21*, 2733.

[21] R. Miyakoshi, A. Yokoyama and T. Yokozawa, *Macromol*. *Rapid Commun*. **2004**, *25*, 1663.

[22] J. D. Winter, G. Deshayes, F. Boon, O. Coulembier, P. Dubois and P. Gerbaux, *J. Mass. Spectrom.* **2011**, *46*, 237.

[23] (a) A. E. Javier, S. R. Varshney and R. D. McCullough, *Macromolecules* **2010**, *43*, 3233; (b) A. Sui, X. Shi, S. Wu, H. Tian, Y. Geng and F. Wang, *Macromolecules* **2012**, *45*, 5436; (c) J. Liu, R. S. Loewe and R. D. McCullough, *Macromolecules* **1999**, *32*, 5777.

[24] R. Puffr and J. Šebenda, *J. Polym. Sci.*, **1967**, *16*, 79.

[25] D. Spoltore, T. Vangerven, P. Verstappen, F. Piersimoni, S. Bertho, K. Vandewal, N. Van den Brande, M. Defour, B. Van Mele, A. De Sio, J. Parisi, L. Lutsen, D. Vanderzande, W. Maes and J. V. Manca, *Org. Electron.* **2015**, *21*, 160.

[26] N. Grossiord, H. E. Miltner, J. Loos, J. Meuldijk, B. Van Mele and C. E. Koning, *Chem. Mater.* **2007**, *19*, 3787.

[27] M. Sundberg, O. Inganäs, S. Stafström, G. Gustafsson and B. Sjögren, *Solid State Commun.* **1989**, *71*, 435.

[28] (a) S. Wang and G. C. Bazan, *Chem. Commun.* **2004**, 2508; (b) H. D. Burrows, S. M. Fonseca, C. L. Silva, A. A. C. C. Pais, M. J. Tapia, S. Pradhan and U. Scherf, *Phys. Chem. Chem. Phys.* **2008**, *10*, 4420.

[29] (a) R. D. McCullough, S. Tristram-Nagle, S. P. Williams, R. D. Lowe and M. Jayaraman, *J. Am. Chem. Soc.* **1993**, *115*, 4910; (b) W. D. Oosterbaan, V. Vrindts, S. Berson, S. Guillerez, O. Douhéret, B. Ruttens, J. D'Haen, P. Adriaensens, J. Manca, L. Lutsen and D. Vanderzande, *J. Mater. Chem.* **2009**, *19*, 5424.

[30] X. Zhao, M. R. Pinto, L. M. Hardison, J. Mwaura, J. Muller, H. Jiang, D. Witker, V. D. Kleiman, J. R. Reynolds and K. S. Schanze, *Macromolecules* **2006**, *39*, 6355.

[31] (a) M. Knaapila, R. C. Evans, V. M. Garamus, L. Almásy, N. K. Székely, A. Gutacker, U. Scherf and H. D. Burrows, *Langmuir* **2010**, *26*, 15634; (b) R. C. Evans, M. Knaapila, N. Willis-Fox, M. Kraft, A. Terry, H. D. Burrows and U. Scherf, *Langmuir* **2012**, *28*, 12348.

[32] M. Knaapila, R. C. Evans, A. Gutacker, V. M. Garamus, N. K. Székely, U. Scherf and H. D. Burrows*, Soft Matter* **2011**, *7*, 6863.

[33] A. I. Mitsionis and T. C. Vaimakis, *Chem. Phys. Lett.* **2012**, *547*, 110.

[34] P. Kékicheff, C. Grabielle-Madelmont and M. Ollivon, *J. Colloid Interface Sci.* **1989**, *131*, 112.

[35] (*a*) H. D. Burrows, M. J. Tapia, S. M. Fonseca, S. Pradhan, U. Scherf, C. L. Silva, A. A. C. C. Pais, A. J. M. Valente, K. Schillén, V. Alfredsson, A. M. Carnerup, M. Tomšič and A. K. Jamnik, *Langmuir* **2009**, *25*, 5545; (*b*) M. J. Tapia, H. D. Burrows, A. J. M. Valente, S. Pradhan, U. Scherf, V. M. M. Lobo, J. Pina and J. Seixas de Melo, *J. Phys. Chem. B* **2005**, *109*, 19108.

[36] H. D. Burrows, V. M. M. Lobo, J. Pina, M. L. Ramos, J. Seixas de Melo, A. J. M. Valente, M. J. Tapia, S. Pradham and U. Scherf, *Macromolecules* **2004**, *37*, 7425.

[37] I. Livsey, *J. Chem. Soc.*, *Faraday Trans. 2* **1987**, *83*, 1445.

[38] *CRC Handbook of Chemistry and Physics*, ed. D. W. H. Rankin, Taylor & Francis, New York, **2009**.

[39] P. W. Schmidt, "Some Fundamental Concepts and Techniques Useful in Small-Angle Scattering Studies of Disordered Solids", in *Modern Aspects of Small-Angle Scattering*, ed. H. Brumberger, Kluwer Academic Publishers, Dordrecht, The Netherlands, **1995**, pp. 1–56.

[40] A. Guinier and G. Fournet, in *Small-Angle Scattering of X-Rays*, ed. John Wiley and Sons, New York, **1955**.

[41] (a) W.-R. Chen, P. D. Butler and L. J. Magid, *Langmuir* **2006**, *22*, 6539; (b) J. S. Pederson and P. Schurtenberger, *Macromolecules* **1996**, *29*, 7602.

[42] T. J. Prosa, M. J. Winokur, J. Moulton, P. Smith and A. J. Heeger, *Macromolecules* **1992**, *25*, 4364.

[43] N. A. Mazer, G. B. Benedek and M. C. Carey, *J. Phys. Chem.* **1976**, *80*, 1075.

[44] (a) G. Pirotte, J. Kesters, P. Verstappen, S. Govaerts, J. Manca, L. Lutsen, D. Vanderzande and W. Maes, *ChemSusChem* **2015**, *8*, 3228; (*a*) Y. Zou, A. Najari, P. Berrouard, S. Beaupré, B. R. Aïch, Y. Tao and M. Leclerc, *J. Am. Chem. Soc.* **2010**, *132*, 5330; (*b*) C. Cabanetos, A. El Labban, J. A. Bartelt, J. D. Douglas, W. R. Mateker, J. M. J. Fréchet, M. D. McGehee and P. M. Beaujuge, *J. Am. Chem. Soc.* **2013**, *135*, 4656; (*c*) J. A. Bartelt, J. D. Douglas, W. R. Mateker, A. El Labban, C. J. Tassone, M. F. Toney, J. M. J. Fréchet, P. M. Beaujuge and M. D. McGehee, *Adv. Energy Mater.* **2014**, *4*, 1301733.

[45] J. H Seo, A. Gutacker, Y. Sun, H. Wu, Y. Cao, U. Scherf, A. J. Heeger and G. C. Bazan, *J. Am. Chem. Soc.* **2011**, *133*, 8416.

[46] J. Kesters, S. Govaerts, G. Pirotte, J. Drijkoningen, M. Chevrier, N. Van den Brande, X. Liu, M. Fahlman, B. Van Mele, L. Lutsen, D. Vanderzande, J. Manca, S. Clément, E. Von Hauff and W. Maes, *ACS Appl. Mater. Interfaces* **2016**, *8*, 6309.

[47] H. Zhou, Y. Zhang, J. Seifter, S. D. Collins, C. Luo, G. C. Bazan, T.-Q. Nguyen and A. J. Heeger, *Adv. Mater.* **2012**, *25*, 1646.

CHAPTER 4

TOWARDS NEW DYES AND ELECTROLYTES FOR ALL-SOLID STATE DYE-SENSITIZED SOLAR CELLS

TOWARDS NEW DYES AND ELECTROLYTES FOR ALL-SOLID STATE DYE SENSITIZED SOLAR CELLS

INTRODUCTION

Over the past decades, dye-sensitized solar cells (DSSCs) pioneered by Grätzel group, have attracted considerable interest due to their low-cost production over silicon-based photovoltaic devices.[1] A DSSC consists of a mesoporous nanocrystalline n-type semiconductor, typically titanium oxide (TiO_2), sensitized with a dye, deposited onto an anode, immersed in a redox active electrolyte (generally triiodide/iodide ions) and completed by a counter electrode, *i.e.* a cathode (Figure 4.1). Upon illumination, dye molecules anchored onto TiO_2 absorb the incoming photons, allowing the transfer of the photoexcited electrons into the TiO_2 conduction band. The electrons are then transferred to the counter electrode, thus creating a current. The redox electrolyte reduces the oxidized dye molecules back to their ground state to enable continuous electron production.[2] Even if power conversion efficiencies (PCEs) of 13 % have been reached for liquid-electrolyte DSSCs,[3] increasing the efficiency and lifetime of the devices is a challenge that has to be met for potential successful commercialization, especially concerning the dye and the electrolyte, as discussed in Chapter 1.

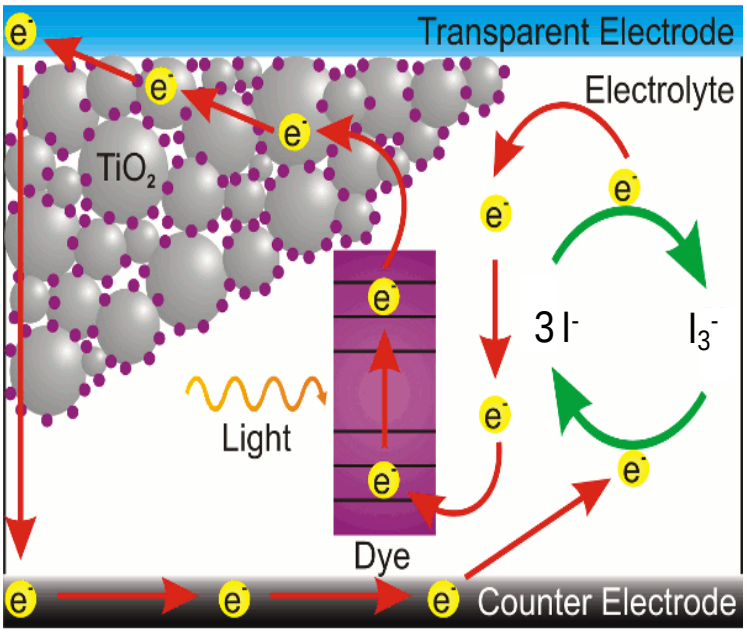

Figure 4.1 Schematic representation of a dye-sensitized solar cell.

The subject of this chapter falls into this context aiming at synthesizing new materials, *i.e.*, dyes and hole transport materials (HTMs) for efficient all solid-state dye-sensitized solar cells (ss-DSSCs). On one hand, chlorin dyes have been prepared from chlorophyll *a* extracted from microalgae (spirulina). On the other hand, **P3HT** and **P3HT**-based conjugated polyelectrolytes have been developed as HTMs for ss-DSSCs (Figure 4.2).

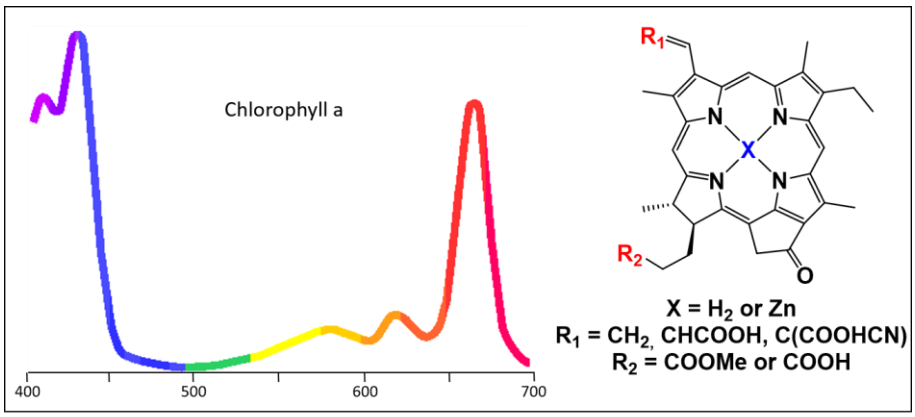

Chorophyll a derivatives for dye applications in DSSCs

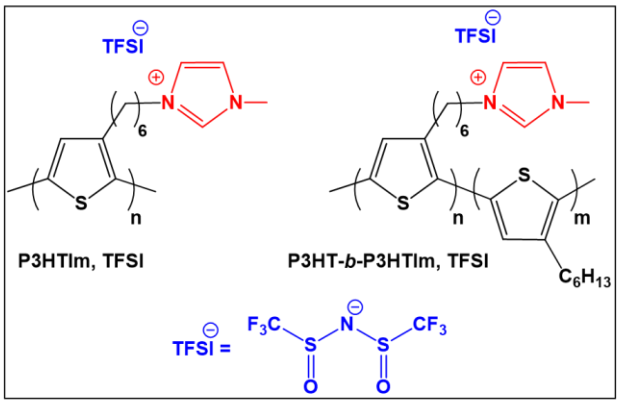

P3HT derivatives for electrolyte applications in DSSCs

Figure 4.2 Proposed structures for dyes and electrolytes.

1. CHLOROPHYLL DERIVATIVES AS DYES

As mentioned in Chapter 1, sensitizing dyes are traditionally made from ruthenium-based complexes, which have reached a record efficiency of 11.4 % in 2012 due to fairly broad absorption spectra.[4] However, their low molar extinction coefficients between 10 000 and 20 000 $M^{-1}.cm^{-1}$, their cost, their scarcity and environmental issues limit their applicability. In this context, organic and porphyrin dyes have emerged as promising cheaper and safer alternatives to the costly Ru sensitizers.[5] Organic dyes have in general, substantially higher molar extinction coefficients (50 000-200 000 $M^{-1}.cm^{-1}$) than ruthenium-based complexes but have typically narrower spectral bandwidths. Despite that, tailor-made organic dyes containing electron-rich (donor) and electron-poor (acceptor) groups connected through a π-conjugated bridge were reported leading to a maximum PCE of 10 %.[6] However, their performance over the years seems to stagnate (Figure 4.3).[7] At the same time, PCEs of porphyrin-sensitizers have considerably increased, leading to PCEs up to 13 % by using a molecularly engineered porphyrin sensitizer, coded **SM315** (Figure 4.4).[3]

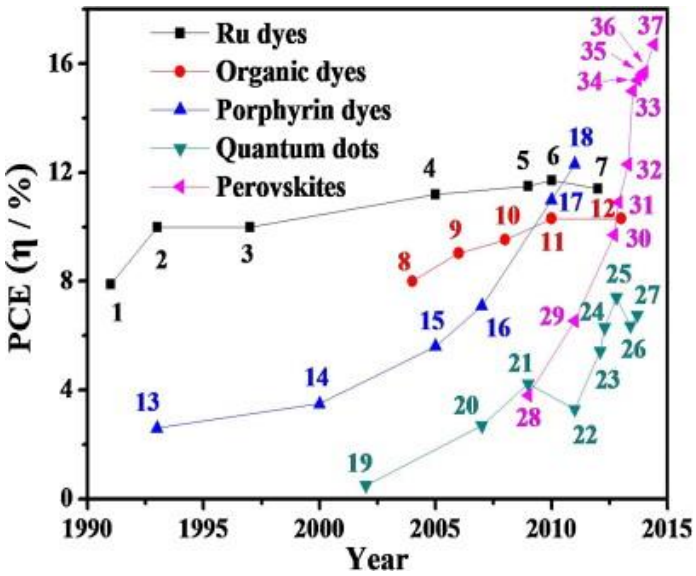

Figure 4.3 Progress in DSSCs PCEs from 1991 to 2015 on the basis of five representative sensitizers families labelled **1–7** for Ru-based complexes (■), **8–12** for organic dyes (●), **13–18** for porphyrin dyes (▲), **19-27** for quantum dots (▼), and **28-37** for perovskites (◀).[7]

Additionally, the production of materials from biomass resources has developed rapidly in recent years and has become one of the most important challenges of our future. As biomass is the only renewable source of atoms, its utilization to produce energy can have both economic and environmental benefits. Among the porphyrinoid sensitizer derivatives, compounds derived from naturally occurring chlorophylls are very promising for preparing affordable DSSCs owing to their low cost, their abundance in supply, their sustainability and the feasibility of molecular structure modification.[8] Chlorophyll *a* can be indeed easily and safely extracted from spirulina, an algae widely used as food supplement. This naturally occurring photosynthetic pigment plays an important role in light-harvesting pigment-protein complexes, absorbing light efficiently in the 400-450 nm and the 600-700 nm regions with molar extinction coefficient (ε) exceeding 10^5 $M^{-1}.cm^{-1}$, which is among the highest for small organic molecules. Moreover, by modifying their chemical structure, their LUMO orbital can be tuned to match the energy level of the conduction band of TiO_2 as well as their excited-state lifetime and their absorption profile. A few studies have been reported in the literature concerning the use of chlorophyll derivatives as sensitizers in liquid electrolyte-based DSSCs leading to PCEs up to around 8 %, similar to ruthenium-based DSSCs.[9] Concerning solid-state DSSCs, there are only a few reports in the literature describing the use of chlorophyll *a* derivatives as dye.[10] The introduction of solid-state electrolyte would allow to substantially improving the device durability. As mentioned above, the commonly used I_3^-/I^- liquid system is corrosive and dissolves many of the sealants and metal interconnects commonly used in the cells. Several approaches have been proposed to replace liquid electrolytes using either quasi-solid[11] or solid-state components.[12] In particular, the most efficient is based on push-pull organic sensitizer coded **Y123** and 2,2',7,7'-tetrakis(N,N-di-*p*-metoxyphenylamine)-9-9'-

spirobifluorene (**spiro-OMeTAD**) doped with a cobalt complex as HTM, leading to PCE of 7.2 %.[13] Other alternatives including organic[1b,2,14] and inorganic[15] compounds, as well as conjugated polymers[16] have been also reported and will be more detailed in the second part of this chapter (*cf.* **P3HT** derivatives as solid electrolyte).

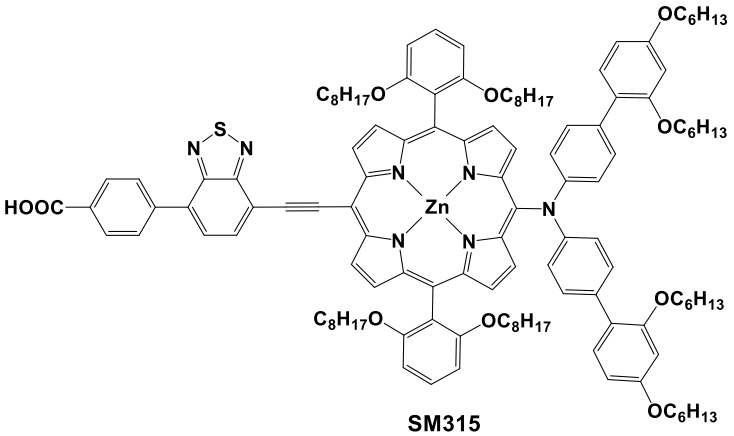

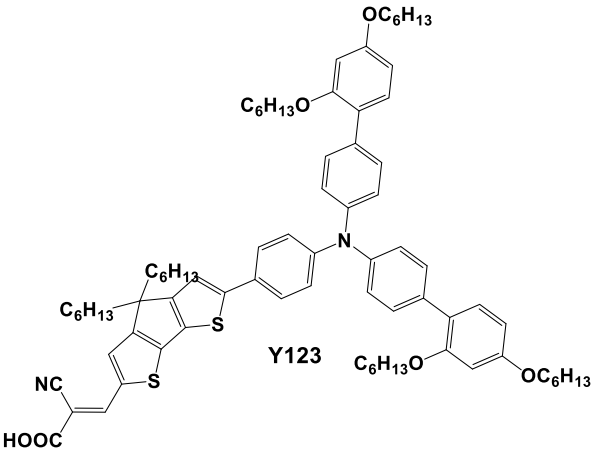

Figure 4.4 Chemical structures of the porphyrin sensitizer **SM315** and the co-sensitizer **Y123**, which yielded 13 % efficiency.

Herein, six derivatives bearing an anchoring group to graft onto TiO_2 have been synthesized to develop all-solid state solar cells with **spiro-OMeTAD** as HTM (Figure 4.5). Regarding the design of chlorophyll dyes, several requirements are needed: (i) the unstable magnesium central atom is removed to obtain the free-base derivative or replaced by a zinc central atom, (ii) the reactive phytyl chain is replaced by a more stable methyl ester group, (iii) the methyl ester in β-keto position (13) is replaced by hydrogen atoms to avoid parasitic reactions, (iv) an anchoring group is introduced on the dye structure to allow its grafting onto the semiconductor surface.[9b] The immobilization of the chlorophyll dye onto the surface of semiconducting TiO_2 nanoparticles is a key requirement in view of injecting electrons from the dye into the conduction band of the metal oxide and thus, obtaining good PCEs. The number and nature of anchoring groups and spacers, if any, should play a role in the photovoltaic process.[1b] The main features that must be fulfilled are (i) a strong bonding

in order to guarantee the stability of the adsorbed dye, (ii) the anchoring group must be close to the semiconductor surface, in order to facilitate orbital overlap, and (iii) the spacer should facilitate the perpendicular orientation of the dye to the semiconductor surface, and also, must be conjugated to avoid decoupling between orbitals.[1b] In this regard and following the state of art of dyes in DSSCs, three different anchoring groups, *i.e.* alkyl carboxylic acid, acrylic acid and cyanoacryclic acid, have been chosen in order to study their impact on the photovoltaic performances. To elucidate the relationship between the molecular structure of the dye and the photovoltaic efficiencies, UV-Vis absorption, adsorption behavior on TiO_2, density functional theory (DFT) calculations, incident photon-to-current efficiency (IPCE) and transient photovoltage decay measurements have been recorded. This allows to gain further insight into the design of chlorophyll sensitizer derivatives for more efficient green ss-DSSCs.

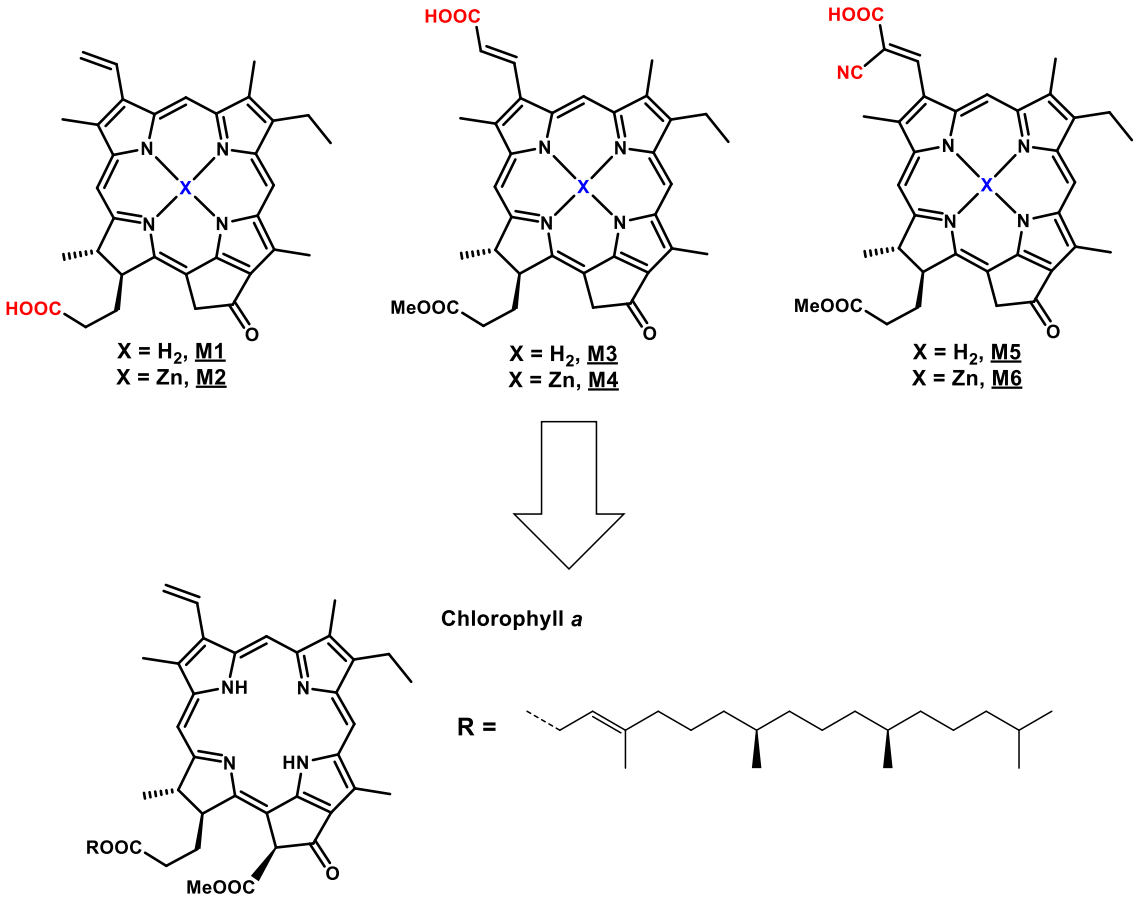

Figure 4.5 Proposed structures for dyes based on chlorophyll *a*.

1.1. SYNTHESIS OF CHLOROPHYLL *A* BASED DYES

The six derivatives presented above are all synthesized from the same intermediate: **methyl pyropheophorbide-*a*** (Scheme 4.1). The alkyl family (**M1**, **M2**) is obtained by hydrolysis of the methyl ester function whereas the vinyl (**M3**, **M4**) and cyanovinyl (**M5**, **M6**) families were prepared by the oxidation of the alkene into the corresponding aldehyde followed by Wittig and Knoevenagel reactions, respectively (Scheme 4.1).

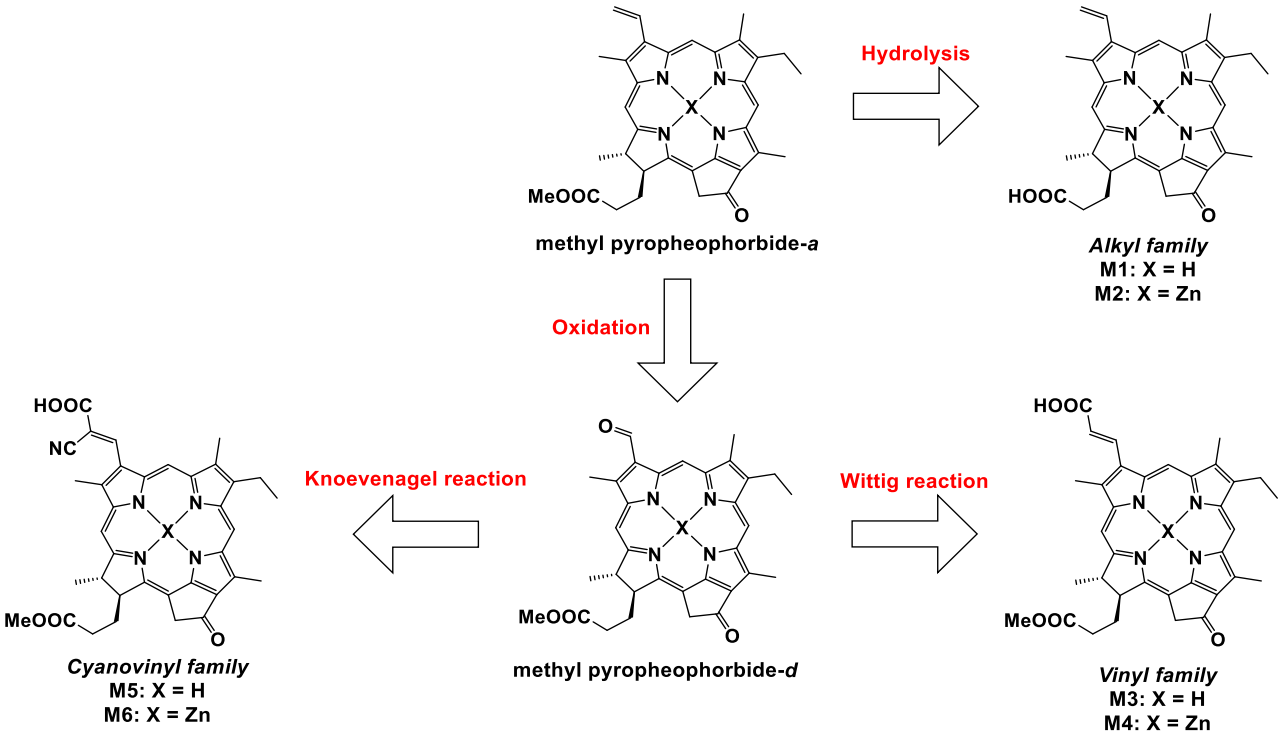

Scheme 4.1 Retrosynthetic strategy to obtain the chlorophyll *a* derivatives.

The synthesis of the intermediate **methyl pyropheophorbide-*a*** is reported in several publications and requires three steps from the chlorophyll *a* (Scheme 4.2).[17]

Chlorophyll *a* was firstly extracted from spirulina, a commercial alga. Around 200 grams of spirulina were placed into a thimble and chlorophyll *a* was extracted using a 2 liters Soxhlet apparatus with ethanol for 3 days (Figure 4.6). After the evaporation of the solvent, the green oil was treated with an aqueous 2M hydrochloric acid solution in acetone to remove the magnesium metal center of the chlorin. The demetalation of the chlorin is easily observed with the naked eye, due to the change in color of the reaction mixture going from green to dark brown. The reaction was also monitored by thin layer chromatography (TLC) and ^{1}H NMR spectroscopy. Indeed, a broad signal at around -2 ppm, corresponding to the inner protons of the chlorin is observed in the ^{1}H NMR spectrum.

Figure 4.6 Picture of the 2L Soxhlet apparatus used for the extraction of chlorophyll *a*.

Then, the phytyl chain of the free base chlorin was replaced by a methyl group through an acid-catalyzed transesterification. This step required few adjustments. When the first attempts were carried out at room temperature, two products were isolated. The ^{1}H NMR

spectrum of the first product displayed five singlets between 3 and 4 ppm, characteristic of the methyl groups in the transesterified compound. The ^{1}H NMR spectrum of the second product showed four singlets instead of the five expected. Moreover, this compound was found to be highly polar during the purification by chromatography. The most probable hypothesis was that this second product corresponds to the carboxylic acid analog. By treating this product in acidic conditions under reflux in methanol for one hour, the **methyl pheophorbide-*a*** was isolated quantitatively. Thus, from 2.6 g of extracted chlorophyll *a*, 920 mg of the **methyl pheophorbide-*a*** were isolated by recrystallization in a dichloromethane (DCM)/pentane mixture, after a transesterification reaction in methanol under reflux for 16 hours.

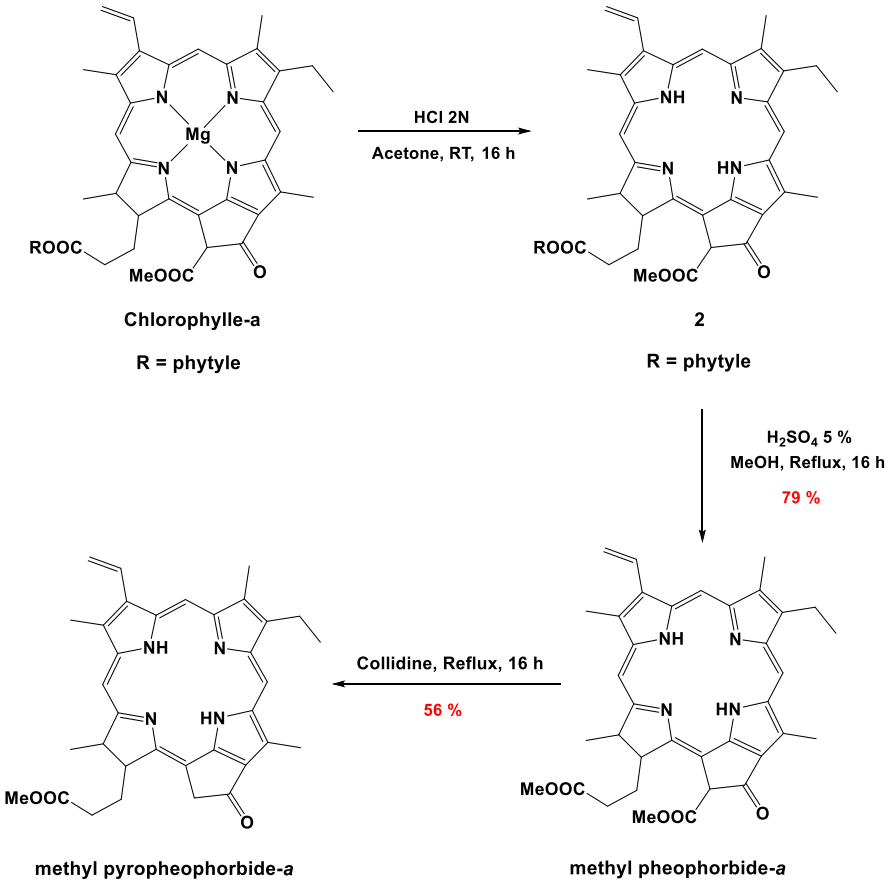

Scheme 4.2 Synthesis of the **methyl pyropheophorbide-*a***.

In a final step, the ester function located on the 13-position was cleaved under reflux in 2,4,6-collidine. As a few information was available concerning the reaction time, several attempts were needed to optimize the conditions. A reaction time too long, more than 48 hours for example, degraded the free-base chlorin. Indeed, nine singlets were observed, indicating that three derivatives from the chlorin were formed because of the three singlets characteristic from the protons at the positions 5, 10 and 20. Reflux in 2,4,6-collidine for 15 hours was finally sufficient to isolate the **methyl pyropheophorbide-*a*** with a 56 % yield after recrystallization in DCM/pentane mixture. In the ^{1}H NMR spectrum, one of the singlets

between 3 and 4 ppm characteristic from the methyl groups in the transesterified **methyl pheophorbide-*a*** disappears, indicating the completion of the decarboxylation (Figure 4.7). Furthermore, the signals characteristic from the 3^2 and 13^2 protons are now distinct.

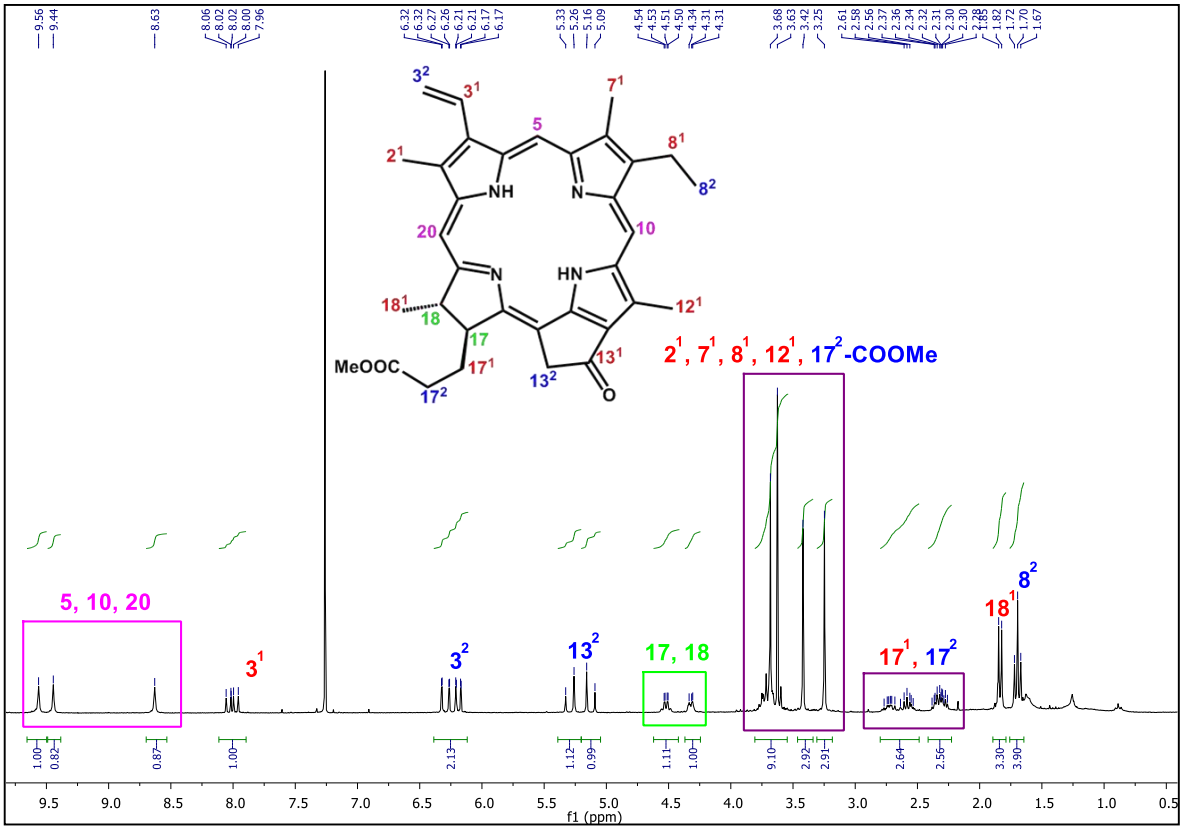

Figure 4.7 ^{1}H NMR spectrum of **methyl pyropheophorbide-*a*** in $CDCl_3$.

1.1.1. SYNTHESIS OF THE CARBOXYALKYL-BASED CHLORINS

With **methyl pyropheophorbide-*a*** in our hands, an acid hydrolysis of the ester group with concentrated hydrochloric acid (HCl) in acetone generated the free-base compound **M1** in 80 % yield (Scheme 4.3).

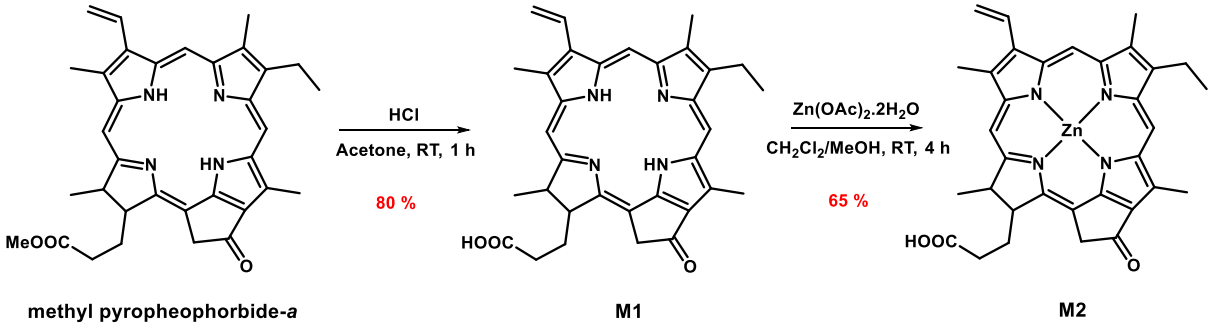

Scheme 4.3 Synthesis of the alkyl family composed of **M1** and **M2**.

The completion of the hydrolysis was indicated by the disappearance of one of the four singlets between 3 and 4 ppm in the ^{1}H NMR spectrum: the signal corresponding to the ester group in the **methyl pyropheophorbide-*a*** disappeared (Figure 4.8).

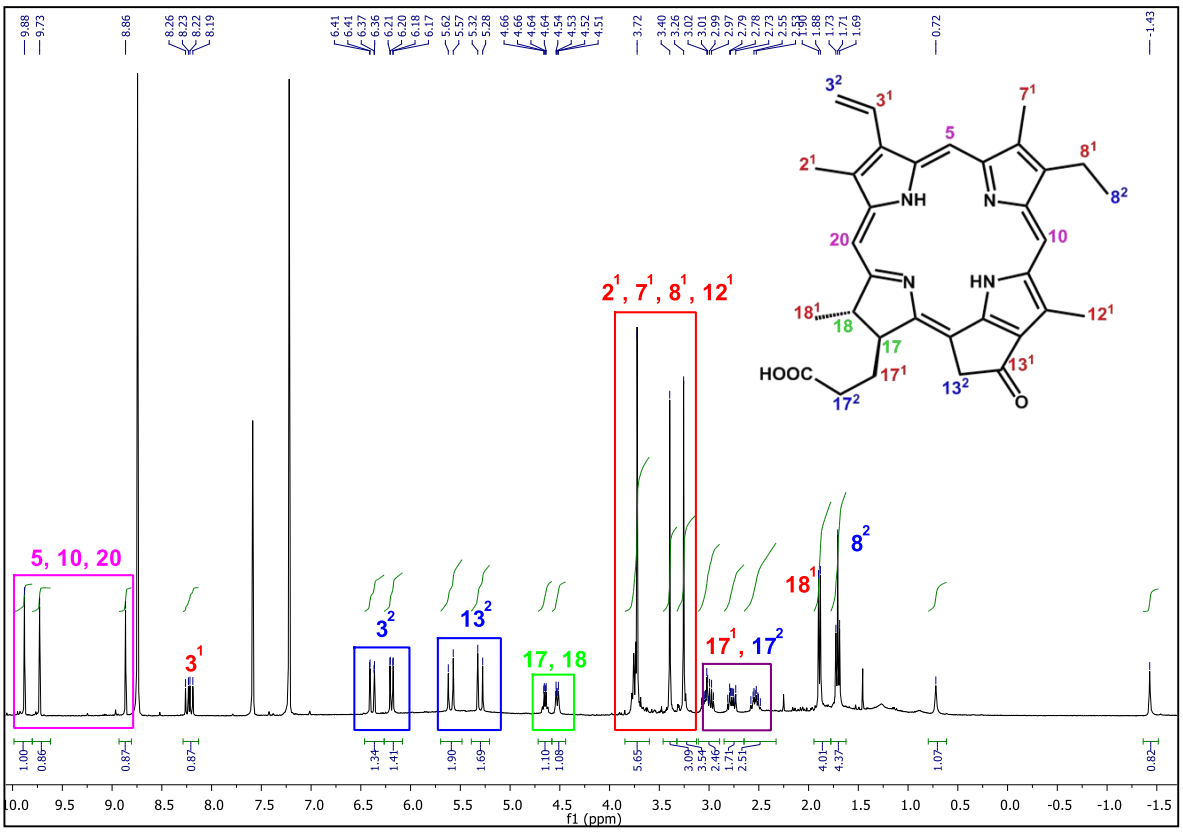

Figure 4.8 ^{1}H NMR spectra of the alkyl free-base **M1** in deuterated pyridine.

The free-base **M1** was then metalated using zinc(II) acetate ($Zn(OAc)_2$) in a DCM/methanol mixture (9/1, v/v). After 4 hours under stirring at room temperature, the complex **M2** was isolated in a 65 % yield. The metalation was easily observed using ^{1}H NMR and UV-vis spectroscopies, where the disappearance of the singlet at around -1.5 ppm, characteristic from the internal protons of the chlorin was observed as well as a blue shift of the Q_Y band from 668 to 657 nm, respectively.

Nevertheless, it is worth noting that the ^{1}H NMR spectrum was not so easy to record. Due to the possible coordination of the central zinc metal ion to the carbonyl functions of the chlorin, the solubility was found to be low in deuterated chloroform. In order to dissociate this complex and thus, to record a satisfactory ^{1}H NMR spectrum, the addition of several drops of deuterated methanol into the NMR tube improved the resolution as well as recording the NMR spectrum of **M2** in deuterated pyridine.

1.1.2. SYNTHESIS OF THE CARBOXYVINYL-BASED CHLORINS

The other carboxylic derivatives were obtained through Wittig and Knoevenagel condensation reactions from the corresponding aldehyde-functionalized chlorin, **methyl**

pyropheophorbide-*d* (Scheme 4.1).The oxidative cleavage of the alkene group from the **methyl pyropheophorbide-*a*** derivative was carried out following a synthetic procedure described in the literature using osmium tetroxide and sodium periodate in a dioxane/acetic acid/water mixture (200/15/1, v/v/v) (Scheme 4.4).[18]

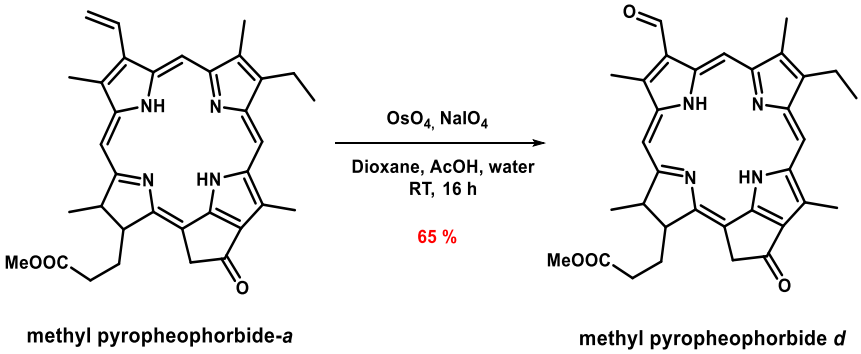

Scheme 4.4 Synthesis of **methyl pyropheophorbide-*d***.

In the ^{1}H NMR spectrum, the disappearance of the signals around 6 and 8 ppm, characteristic of the alkene function and the appearance of a new singlet at 11.55 ppm corresponding to the aldehyde group (3^1) were clearly observed. The other singlets of the protons at the *meso* positions (5, 10 and 20) are also shifted due to the presence of the aldehyde group (Figure 4.9). Finally, these results were supported by mass spectrometry (ESI) where a peak at *m/z* = 551.26 [M+H] was observed.

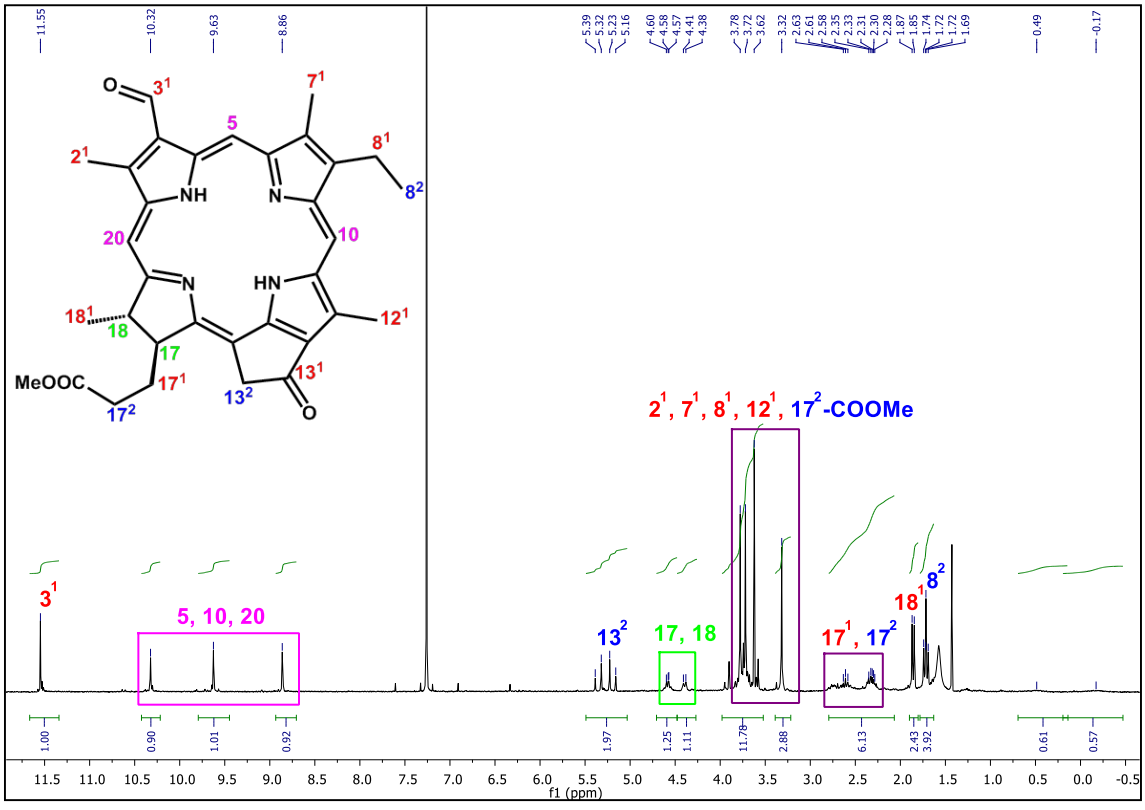

Figure 4.9 ^{1}H NMR spectrum of **methyl pyropheophorbide-*d*** in $CDCl_3$.

A Wittig reaction with (*tert*-butoxycarbonylmethylene)triphenylphosphorane (PPh_3=CH-COO*t*Bu) and **methyl pyropheophorbide-*d***, in toluene was then carried out following the reported procedure (Scheme 4.5).[9c] The *tert*-butoxy ester group of the free-base **chlorin-COOtBu** was then cleaved with trifluoroacetic acid (TFA) leading to **M3** in a 54 % global yield over two steps. Using the same conditions as described for chlorin **M2**, **M4** was obtained in a 87 % yield upon zinc metalation.

By analyzing **chlorin-COOtBu** by ^{1}H NMR spectroscopy, the disappearance of the signals at 11.55 ppm corresponding to the aldehyde group (3^1), the appearance of two new doublets at 9.07 and 7.00 ppm, characteristic of the vinyl protons and a new singlet at 1.74 ppm characteristic of the *tert*-butyl group were observed. As described previously, the singlets of the protons at the *meso* positions (5, 10 and 20) were also shifted due to the functionality modification (9.50, 9.47 and 8.67 *vs.* 10.32, 9.63 and 8.86 ppm). Upon reaction in TFA, the singlet characteristic of the *tert*-butyl group disappeared and a new doublet from the vinylic proton in α of the carboxylic acid appeared at around 9 ppm. As in complexes **M1**, **M2**, the metalation was easily observed using ^{1}H NMR and UV-Visible absorption spectroscopies.

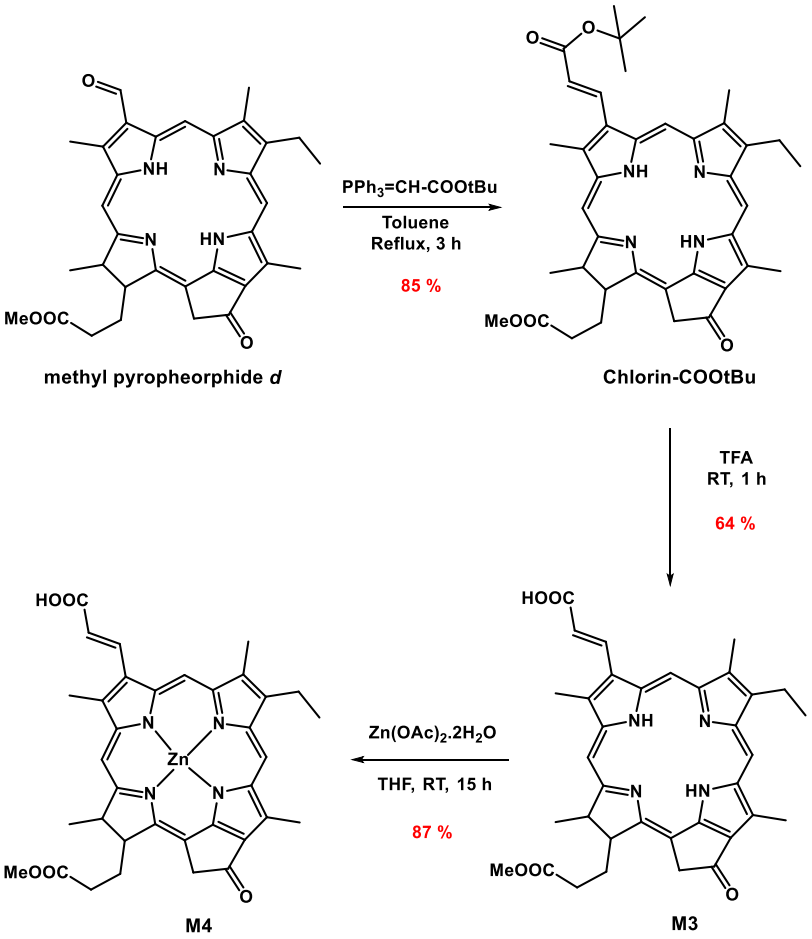

Scheme 4.5 Synthesis of the **chlorin-COOH** derivatives.

1.1.3. SYNTHESIS OF THE CYANOVINYL-BASED CHLORINS

The cyanoacrylic-based chlorins (**M5**, **M6**) were synthesized through a Knoevenagel condensation starting from the **methyl pyropheophorbide-*d*** aldehyde chlorin by reaction of cyanoacetic acid and ammonium acetate (NH_4OAc) under reflux in THF (Scheme 4.6, **M5** and **M6**). The free base **M5** bearing a cyano group was obtained in a 65 % yield after purification by column chromatography.

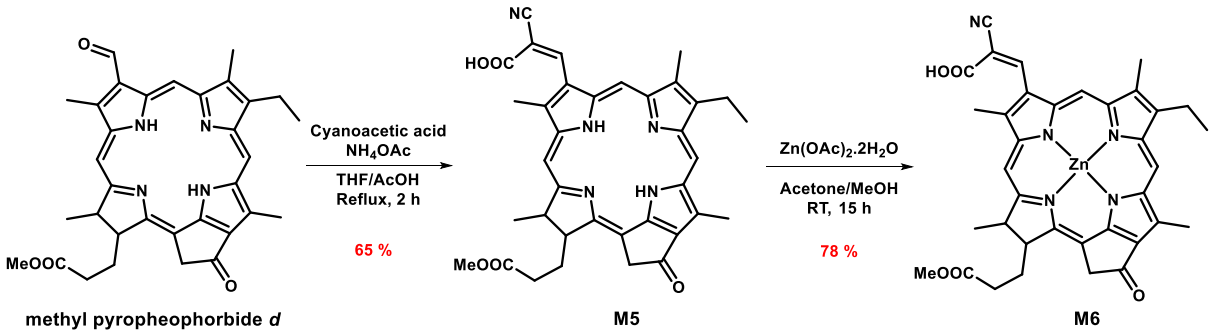

Scheme 4.6 Knoevenagel condensation of the **methyl pyropheophorbide-*d*** aldehyde chlorin, leading to compounds **M5** and **M6**.

In the ^{1}H NMR spectrum, the disappearance of the signals at 11.55 ppm corresponding to the aldehyde group (3^1) and the appearance of a new singlet at 9.56 ppm characteristic of the vinyl proton at were observed (Figure 4.10). The singlets of the protons at the *meso* positions (5, 10 and 20) were also shifted due to the functionality modification (9.62, 9.13 and 8.62 ppm *vs*. 10.32, 9.63 and 8.86 ppm).

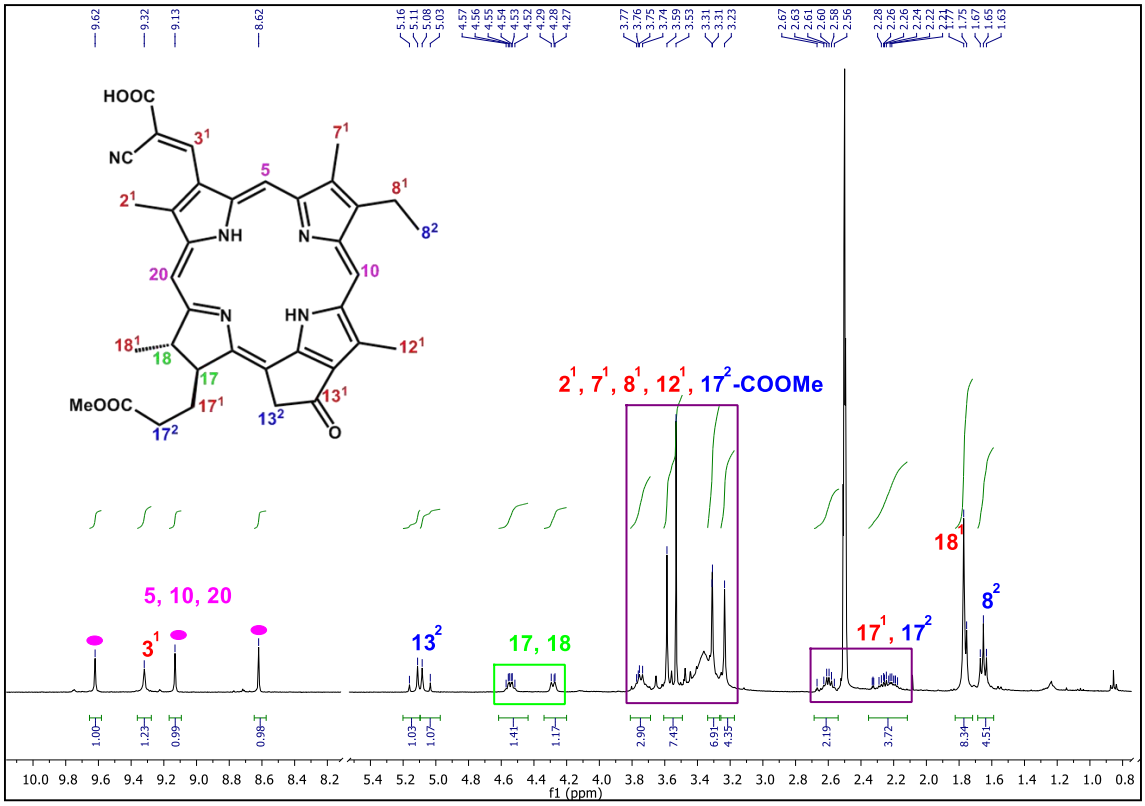

Figure 4.10 ^{1}H NMR spectrum of CNCOOH derivative **M5** in DMSO-*d6*.

Zinc metalation with $Zn(OAc)_2.2H_2O$ was then carried out in a THF/MeOH mixture (9/1, v/v). After stirring overnight at room temperature, the brown solution became green, which is the characteristic color of the zinc species. Zinc chlorin **M6** was obtained in a 78 % yield after purification by column chromatography.

1.2. CHLOROPHYLL *A* BASED ALL-SOLID-STATE DYE SENSITIZED SOLAR CELLS

These chlorophyll derivatives were then used to prepare all-solid-state dye-sensitized solar cells at the Institute XLIM in Limoges in collaboration with Dr. Johann Bouclé.

Before using the chlorin derivatives as dyes, solar cells with another organic dye commonly used in the lab, **D102**, were prepared in order to get familiar with the fabrication process. This dye showed a PCE value up to 4.1 % when associated with **spiro-OMeTAD**, commonly used as hole transport material (HTM) (Figure 4.11).[19] Once photovoltaic performances obtained with the **D102** were quite satisfactory and reproducible, solar cells with chlorins as dye were fabricated.

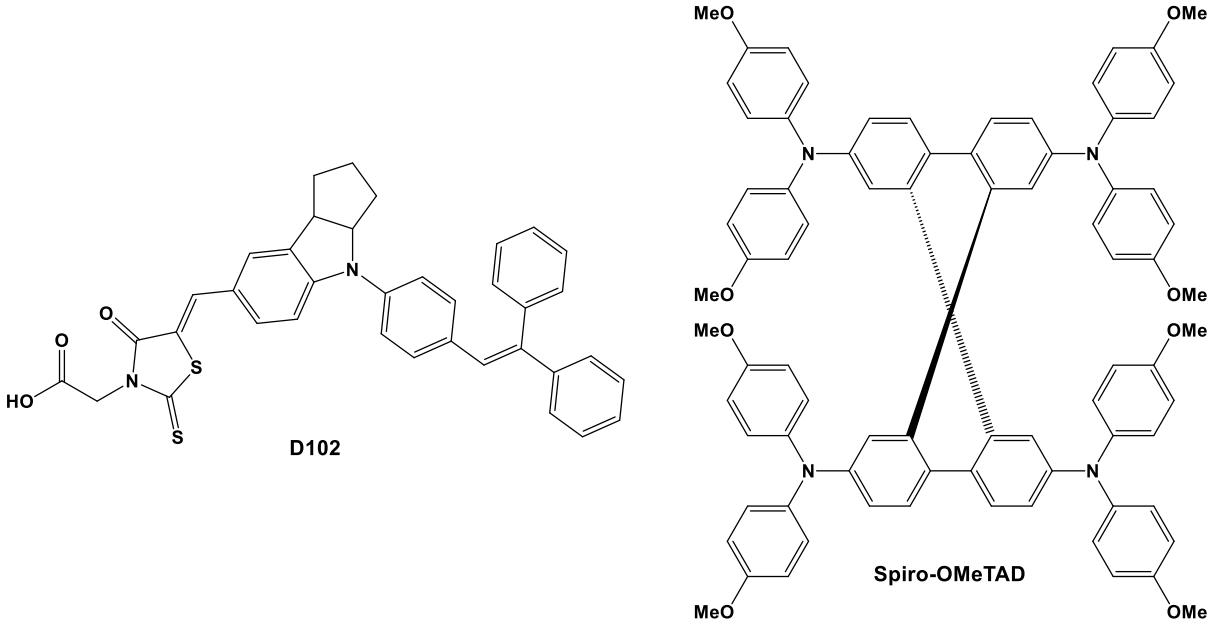

Figure 4.11 Structures of **D102** (dye) and **spiro-OMeTAD** (HTM).

Two device structures could be considered with either one or two pixels per FTO substrate. In order to have more results during the short stay in Limoges, the structure with two pixels, 0.149 cm^2 each, was used (Figure 4.12).

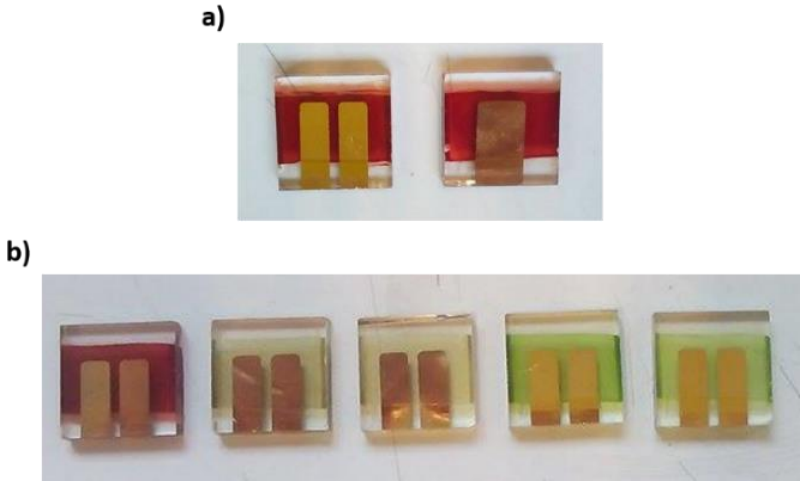

Figure 4.12 Pictures of solar cells based on **D102** with one or two pixels (a) and based on **D102** and chlorins (b).

1.2.1. INFLUENCE OF THE CO-ADSORBENT

Before preparing DSSCs based on chlorin dyes, the effect of adding a co-adsorbent for each chlorin family (free-base and zinc) was investigated. $\pi-\pi$ stacking of chlorin derivatives is advantageous to the light-harvesting due to the induced broadened absorption. However, these stacked aggregates also lead to lower PCEs. A typical way to reduce dye aggregation at the semiconductor interface is the use of co-adsorbents.[20] Their strong binding to the TiO_2 surface forces the displacement of dye molecules reducing their probability to self-aggregate. In addition, they allow passivating the TiO_2 surface repressing the recombination of the injected electrons with the electrolyte and modulating the position of the conduction band edge of TiO_2.[21] Nevertheless, the addition of co-adsorbents reduces the dye loading and thus the light-harvesting. Consequently, it is crucial to judiciously adjust the amount of co-adsorbent. Among co-adsorbents, chenodeoxycholic acid (**CDCA**), which is the most commonly studied studied in DSSC preparation was used in this work (Figure 4.13).[22]

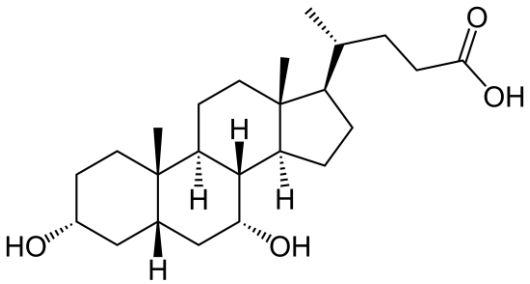

Figure 4.13 Chenodeoxycholic acid structure.

Dye impregnation was done in tetrahydrofuran (THF) at 0.3 mM for 15 hours and **CDCA** was added at different concentrations in dye solutions from 0 to 3 mM. UV-Vis measurements were first performed to analyze the adsorbed amount of dye **M2** on the TiO_2 electrodes (Figure 4.14). Dye **M2** at a concentration of 0.3 mM yielded absorbance values of 0.55 for the Soret band at around 420 nm and 0.25 for the last Q band at around 665 nm. Those

value dramatically decreased as the concentration of co-adsorbent was increased to 3 mM. This decrease is consistent with previous studies done in the literature.[23] The co-adsorbent tends indeed to decrease the rate of dye adsorption *via* a competitive anchoring process, thereby decreasing the dye concentration on the surface and thus, the dye aggregation.

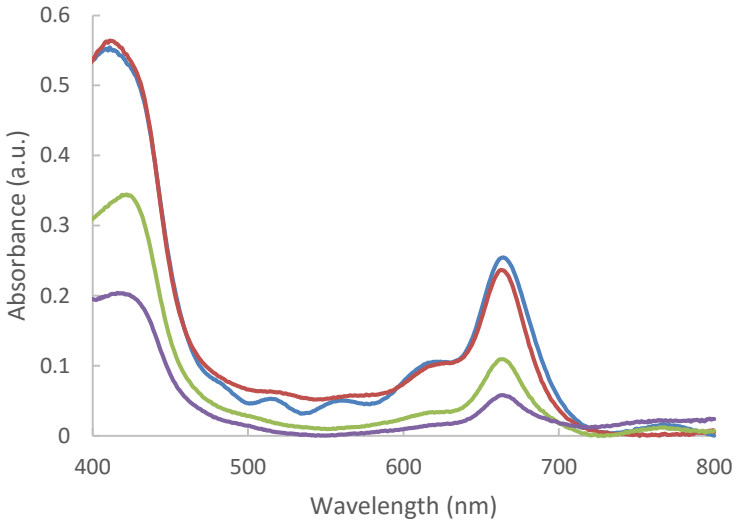

Figure 4.14 UV-Vis absorption spectra of ss-DSSCs prepared from solutions of dye **M2** (0.3 mM) with increasing co-adsorbent concentration (0 mM: blue line; 0.3 mM: red line; 1.5 mM: green line; 3 mM: purple line).

The photovoltaic performances of the devices employing dye **M2** were measured under AM 1.5 irradiation (100 mW/cm²) to study the impact of the **CDCA** molar ratio. The photocurrent density voltage curves (J-V) of the devices are presented in the Figure 4.15 and the detailed parameters are collected in the Table 4.1.

The devices where TiO_2 was sensitized only with dye **M2** lead to a PCE of 0.18 % (J_{SC} = 0.71 mA/cm², V_{OC} = 540 mV and FF = 47 %). When **M2** was combined with **CDCA**, the PCE increased reaching 0.53 % (J_{SC} = 1.73 mA/cm², V_{OC} = 650 mV and FF = 48 %) for a **M2**:**CDCA** molar ratio of 1:5. It is necessary to finely adjust the **M2**:**CDCA** molar ratio to find a satisfactory balance between preventing the dye aggregation and maintaining good optical densities. It is worth noting that device sensitized with **M2**-**CDCA** in a 1:5 molar ratio showed a strong improvement in PCE thanks to an increase in J_{SC} and V_{OC} while the dye coverage was decreased by about 50 %. This trend was evidenced for all chlorin dyes. By comparing the device performances obtained with different **CDCA** concentrations, an optimum concentration of co-adsorbent of 1.5 mM was chosen for the impregnation.

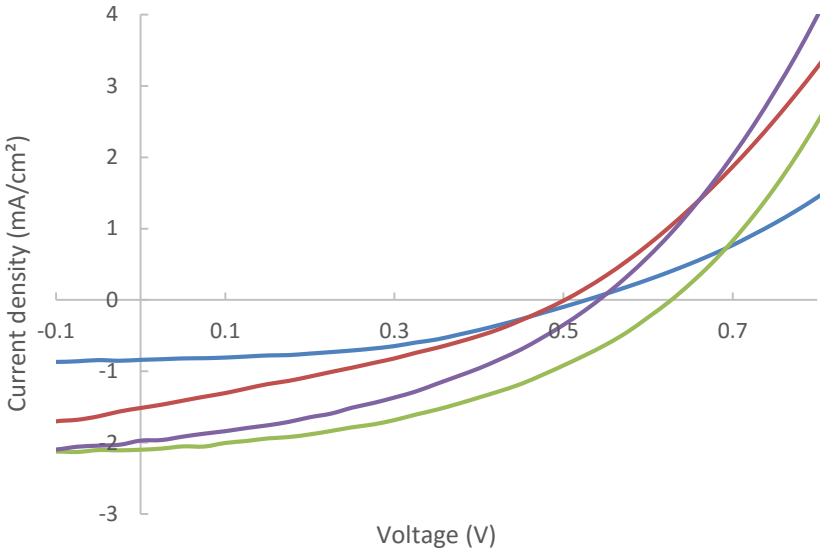

Figure 4.15 Current-voltage characteristics of ss-DSSCs prepared from solutions of dye **M2** (0.3 mM) with increasing co-adsorbent concentration (0 mM: blue line; 0.3 mM: red line; 1.5 mM: green line; 3 mM: purple line).

Table 4.1 Photovoltaic parameters of ss-DSSCs sensitized with **M2**: influence of the co-adsorbent concentration.

		V_{OC} (V)	J_{SC} (mA/cm²)	FF	PCE (%)
Without	**Average efficiency**	0.54	0.71	47	0.18
	Best efficiency	**0.54**	**0.83**	**44**	**0.19**
0.3 mM	**Average efficiency**	0.52	1.27	36	0.23
	Best efficiency	**0.50**	**1.51**	**33**	**0.25**
1.5 mM	**Average efficiency**	0.65	1.73	48	0.53
	Best efficiency	**0.68**	**1.54**	**53**	**0.56**
3 mM	**Average efficiency**	0.56	1.72	40	0.39
	Best efficiency	**0.54**	**1.96**	**40**	**0.42**

Figure 4.16 shows the incident photo-to-current efficiency (IPCE) spectra for ss-DSSCs incorporating **M2** without or with co-adsorbent. It can be seen that the photocurrent response of **M2**-basedDSSC with co-adsorbent (1.5 mM) exceeds 4 % for the last Q band at 675 nm, which is higher than the response obtained without co-adsorbent (2 % for the same wavelength). This result is clearly coherent with the current densities observed under illumination, where adding 1.5 mM of co-adsorbent for the impregnation enabled to double the current density value from 0.71 to 1.73 mA/cm². The increased quantum yield is ascribed to the inhibited dye aggregation in the presence of **CDCA** as co-adsorbent, which minimizes the intermolecular energy transfer and increases the electron injection efficiency.[21]

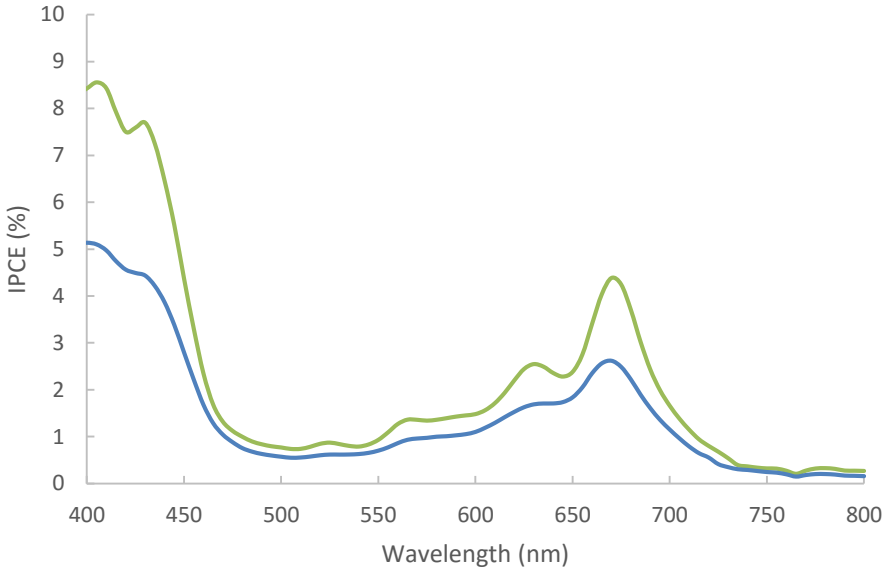

Figure 4.16 IPCE spectra of ss-DSSCs sensitized with **M2** depending on the co-adsorbent (0 mM: blue line; 1.5 mM: green line).

1.2.2. COMPARISON BETWEEN THE CHLORINS: IMPACT OF THE ANCHORING GROUP AND ZINC METAL CENTER

The dye impregnation of all chlorins was done in tetrahydrofuran (THF) at 0.3 mM for 15 hours and **CDCA** (1.5 mM) was added as co-adsorbent as discussed above. It is possible that this concentration is not the optimal one for each chlorin but it was preferable to have only one parameter to be modified to establish a clear comparison between the different chlorin dyes.

As in the previous study, UV-Vis absorption measurements were performed to analyze the amount of adsorbed dyes on the TiO_2 electrodes. All the dyes displayed almost the same absorbance values when grafted to the TiO_2 surface except for **M5** and **M6**, which seemed to present a higher amount of adsorbed molecules. This finding indicates that chlorins possess similar light-harvesting properties when used in ss-DSSCs.

To evaluate the results obtained for ss-DSSCs based on chlorin dyes, a solar cell fabricated using a well-known organic dye, **D102**, was used as the standard cell. Compared to the **D102** performances, those obtained with chlorin dyes are very low (Table 4.2). Nevertheless, only a few publications have described the fabrication of ss-DSSCs with chlorophyll derivatives and the values obtained here are in the same range than those reported.[24] They are even better than the performances obtained in some liquid-DSSCs with other chlorophyll derivatives.[25]

ss-DSSCs based on **M3** gave the highest PCE (0.77 %) thanks to the highest short-circuit current (J_{SC}), while the open-circuit photovoltage (V_{OC}) and fill factors (FF) were similar to those found with the other chlorin dyes, except for **M2** that gave a higher V_{OC} value.

Table 4.2 Photovoltaic parameters of ss-DSSCs sensitized with chlorin dyes.

		V_{OC} (V)	J_{SC} (mA/cm²)	FF	PCE (%)
M1	**Average efficiency**	0.54	1.99	42	0.45
	Best efficiency	**0.57**	**2.49**	**42**	**0.60**
M2	**Average efficiency**	0.65	1.73	48	0.53
	Best efficiency	**0.68**	**1.54**	**53**	**0.56**
M3	**Average efficiency**	0.56	2.14	46	0.54
	Best efficiency	**0.56**	**2.73**	**49**	**0.77**
M4	**Average efficiency**	0.54	1.62	49	0.43
	Best efficiency	**0.57**	**1.70**	**53**	**0.51**
M5	**Average efficiency**	0.54	1.16	54	0.34
	Best efficiency	**0.54**	**1.51**	**48**	**0.39**
M6	**Average efficiency**	0.53	0.97	52	0.26
	Best efficiency	**0.51**	**1.60**	**40**	**0.33**
D102	**Average efficiency**	0.76	10.01	49	3.73
	Best efficiency	**0.76**	**10.20**	**52**	**3.99**

The PCE values for ss-DSSCs based on chlorin dyes exceed 0.26 % in a ranking order: acrylic acid > alkyl acid > cyanoacrylic acid. These results are consistent with the TD-DFT calculations performed in collaboration with Dr. Laurent Lasser, Dr. David Beljonne and Pr. Roberto Lazzaroni (CMN, University of Mons, Belgium). The calculations show that all the LUMO+n orbitals have significant contribution on the vinyl group for **M4** while only the LUMO+3 orbital covers the alkyl carboxylic group for **M2** (Figure 4.17). This is critically important since the orbital overlap between the LUMO+n of the dye and the TiO_2 conduction band edge should be as large as possible in order to maximize the electron transfer probability.

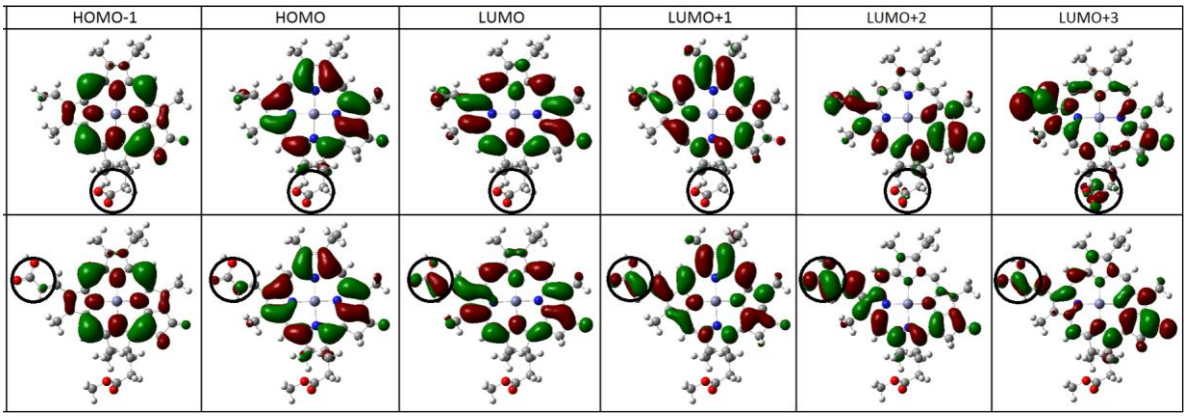

Figure 4.17 HOMO-1, HOMO, LUMO, LUMO+1, LUMO+2 and LUMO+3 molecular orbitals for **M2** (top) and **M4** (bottom) dyes. The COOH anchoring groups are circled in black.

Besides, it was found that the introduction of cyano groups strongly decreased the J_{SC} values, for example from 2.14 to 1.16 mA/cm² for **M3** and **M5** respectively, resulting in lower efficiencies from 0.54 to 0.34 %, respectively. This trend was already observed when chlorin

dyes were used in liquid DSSCs.[9a] Nevertheless, this difference in ss-DSSCs is not as dramatic as in liquid DSSCs. Indeed, adding cyano groups on the free-base chlorin **M3** drastically decreased the PCE in liquid DSSCs by about 75 % while in ss-DSSCs, the decrease represented only 37 %.[9c]

TD-DFT calculations showed a huge stabilization of the unoccupied orbitals due to the presence of the electron-withdrawing cyano group (Figure 4.18). The **M6** LUMO moves indeed down below the TiO_2 conduction band edge energy level, no longer allowing the electron injection to TiO_2 upon HOMO → LUMO transition (Figure 4.18). This result could explain the decrease in PCEs observed by adding cyano groups next to the carboxylic anchoring group.

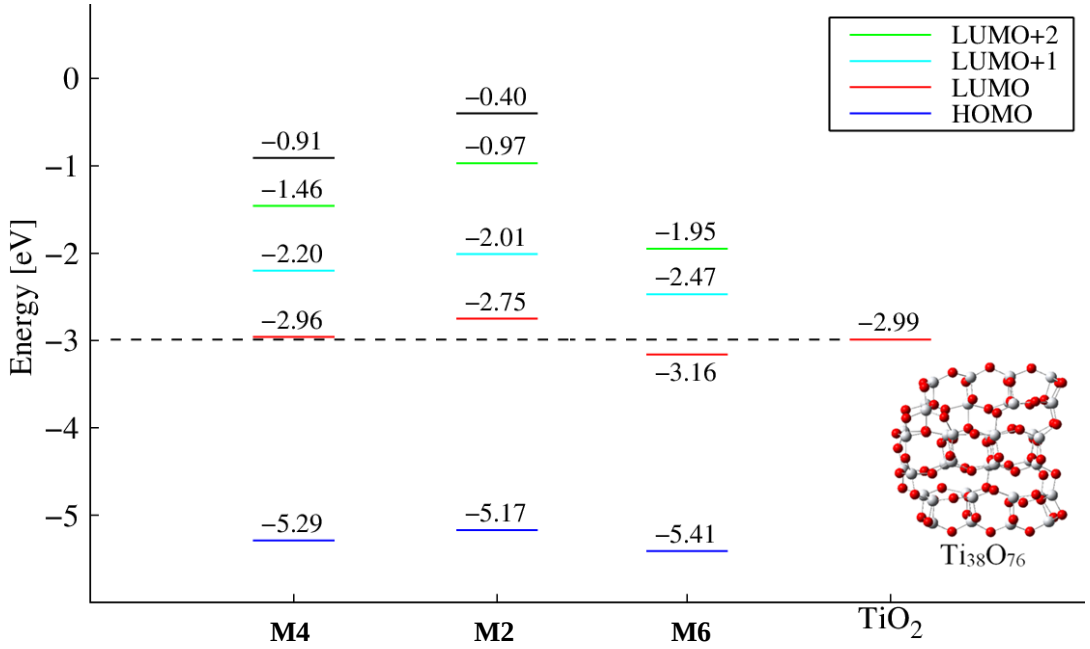

Figure 4.18 HOMO, LUMO, LUMO+1, LUMO+2, LUMO+3 energy levels of chlorin dyes **M2**, **M4** and **M6**. The values for the conduction band edge of the semiconductor calculated from a $Ti_{38}O_{76}$ cluster is added for comparison (dashed line).

When analyzing the performances of the zinc-metaled compounds, we observed that their performances were quite lower than their free-base analogs. All PCEs were lower due to the J_{SC} decrease except for chlorin **M2** which yielded higher PCEs than the free base **M1**. As the TD-DFT calculations concluded that adding the zinc atom has no significant effect on the unoccupied orbitals of the chlorins, one possible explanation of the PCE decrease could be the chelation phenomenon. Indeed, zinc metal can chelate the carbonyl group of the chlorin and thus, increase the aggregation compared to the free-base dyes.

To examine the recombination kinetics of chlorine-based ss-DSSCs, open-circuit voltage-decay (OCVD) measurements were carried out on the free-base chlorin dyes and compared to **D102**. As the number of anchoring group of the dyes is similar for each chlorin,

the observed differences in the kinetic recombination diagram might only be due to differences in the dye structure.

First, the observed change in slope between **D102** and the chlorin dyes indicates that different recombination mechanisms took place in ss-DSSCs sensitized with these compounds (Figure 4.19). The recombination for chlorin-sensitized solar cells appears to be faster than with **D102**, thus involving a V_{OC} loss. This result is coherent with the photovoltaic parameters obtained under illumination, where the chlorin dyes exhibit a V_{OC} around 600 mV compared to 760 mV for **D102**-based device.

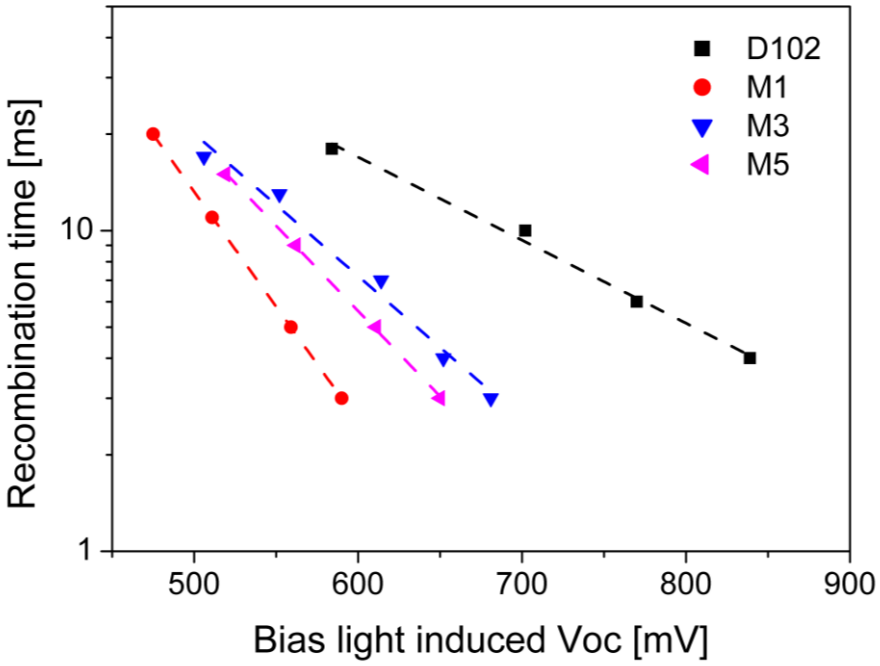

Figure 4.19 Electron recombination lifetime as a function of V_{OC} in chlorin- and **D102**-based ss-DSSCs.

Chlorin dyes **M3** and **M5** possess an enhanced electron lifetime in comparison with **M1** (*i.e.,* the slope is smaller), indicating that **M3** and **M5** form an organic layer in such a way to decrease the charge recombination at the titania/HTM interface. As the dye **M1** contains a non-conjugated anchoring group compared to dyes **M3** and **M5**, it can be supposed that the **M1** molecules lies flat on the TiO_2 surface, because of the larger flexibility of the spacer. Other calculations are underway to verify this hypothesis.

To add further understanding to the behavior of the chlorin-based DSSCs, a new collaboration with Dr. Malkiat Johal (Ponoma College, USA) is ongoing to get insight into the adsorption of these chlorin dyes onto the TiO_2 films using a quartz crystal microbalance measuements, with dissipation monitoring (QCM-D).[26] This work might allow correlating the adsorption of the chlorin dyes with the photovoltaic performances obtained when used in ss-DSSCs.

In order to improve the photovoltaic performances of these dyes, we decided to modify some parameters of the fabrication process such as the impregnation solvent or the TiO_2 layer thickness. All these studies were performed with **M2** since it was available in the largest quantity.

1.2.3. INFLUENCE OF THE SOLVENT

To determine if changing the nature of the solvent can improve the dye impregnation, three solvents have been studied: THF, ethanol and an acetonitrile/*tert*-butanol mixture (1/1, v/v) commonly used for **D102** impregnation. Taking into account the results obtained above, **M2** was combined with **CDCA** during the impregnation. The photovoltaic performances obtained for the devices are summarized in Table 4.3.

Table 4.3 Device performances obtained for **M2** for different solvent.

Solvent		V_{OC} (V)	J_{SC} (mA/cm²)	FF	PCE (%)
Ethanol	**Average efficiency**	0.59	2.10	49	0.60
	Best efficiency	**0.59**	**2.2**	**51**	**0.66**
THF	**Average efficiency**	0.65	1.73	48	0.53
	Best efficiency	**0.68**	**1.54**	**53**	**0.56**
ACN/tBuOH 1/1	**Average efficiency**	0.59	2.34	51	0.68
	Best efficiency	**0.59**	**2.47**	**49**	**0.71**

The devices for which the impregnation was done in ethanol and ACN/*t*BuOH gave slightly higher PCEs: 0.60 (J_{SC} = 2.1 mA/cm², V_{OC} = 590 mV and FF = 49 %) and 0.68 % (J_{SC} = 2.34 mA/cm², V_{OC} = 590 mV and FF = 51 %), respectively, compared to 0.53 % (J_{SC} = 1.73 mA/cm², V_{OC} = 650 mV and FF = 48 %) in THF. This improvement was especially due to the higher J_{SC} while the V_{OC} and the FF were almost similar. Impregnation in ethanol and ACN/tBuOH produced 21 and 35 % improvements in J_{SC}. In a first approximation, this enhancement could be due to a higher amount of dye molecules adsorbed onto the surface. However, the absorption bands are certainly more intense in ethanol than in THF but not in ACN/*t*BuOH (Figure 4.20).

The IPCE spectra recorded for **M2**-based ss-DSSCs indicated that the photocurrent response for the Qy band at 675 nm was higher for devices impregnated with ACN/tBuOH mixture than for those sensitized in THF and EtOH (Figure 4.21). This result could explain the current densities observed under illumination, where the impregnation in ACN/tBuOH led to higher J_{SC} values than in ethanol and THF.

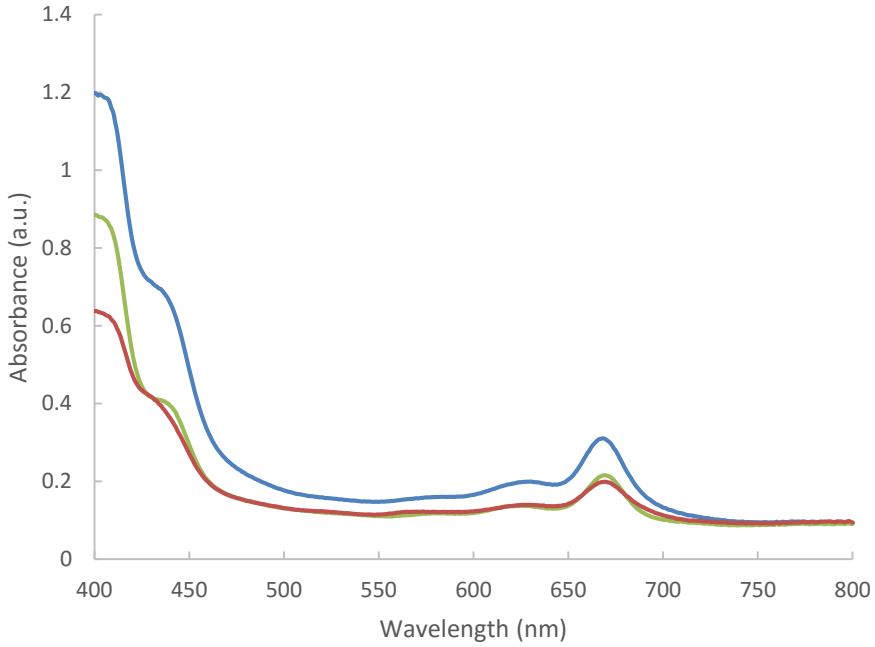

Figure 4.20 Absorption spectra of chlorin **M2** adsorbed onto TiO_2 films depending on the nature of the solvent (ethanol: blue line, THF: red line and ACN/tBuOH: green line).

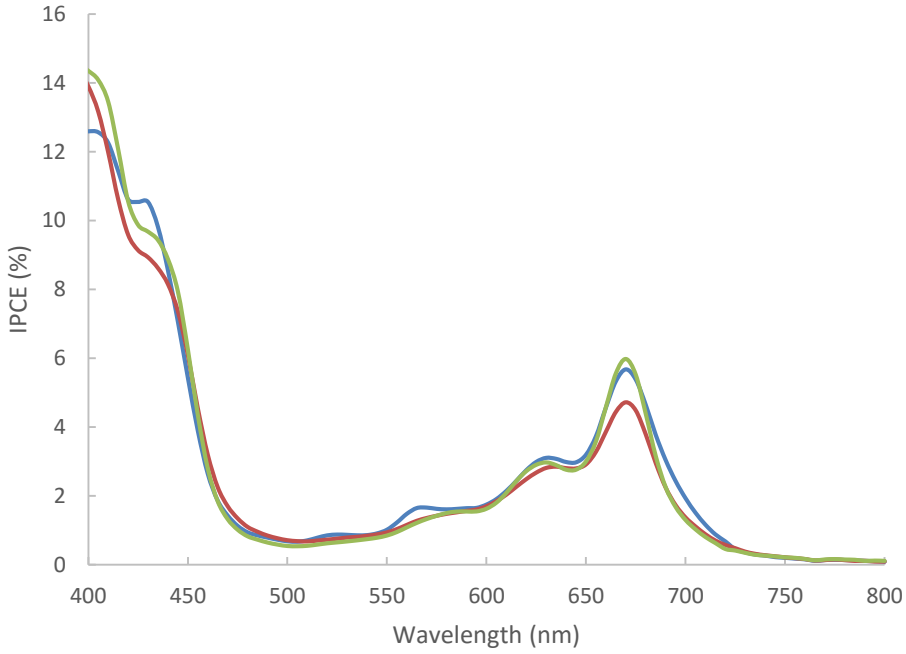

Figure 4.21 IPCE spectra of ss-DSSCs based on chlorin **M2** depending on the nature of the solvent (ethanol: blue line, THF: red line and ACN/*t*BuOH: green line).

1.2.4. INFLUENCE OF THE THICKNESS OF THE TiO_2 LAYER

As the solvent seems to weakly impact the absorption profile and device performances, the influence of TiO_2 layer thickness, an important key-parameter, was studied. Increasing the TiO_2 thickness could allow increasing the amount of adsorbed dye and thus, J_{SC}. For this

reason, ss-DSSCs having three different TiO_2 thicknesses were produced by changing the spin-coating conditions: 1.6 (reference), 3.2 and 3.6 µm. As expected, by increasing the TiO_2 thickness, the amount of dye **M2** adsorbed onto the surface was increased, as shown by the absorption spectra (Figure 4.22).

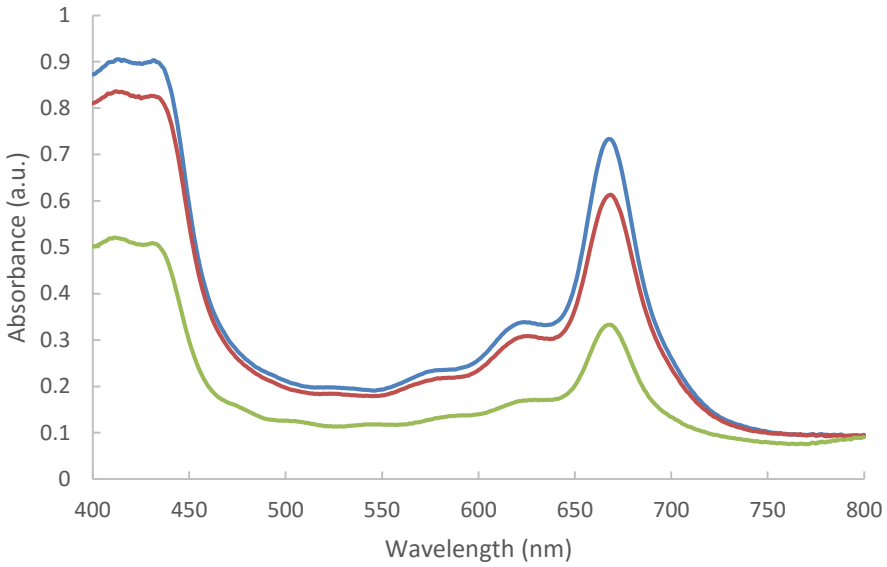

Figure 4.22 UV-Visible absorption spectra of **M2** adsorbed onto TiO_2 film with different thickness (1.6 µm: green line; 3.2 µm: red line; 3.6 µm: blue line).

However, by testing the solar cells under illumination, the performances were not improved compared to the reference at 1.6 µm (Table 4.4). This result can be due to the low pore filling by **spiro-OMeTAD**, leading to increased charge recombination and series resistance.[27] To overcome this problem, the impregnation time of **spiro-OMe-TAD** was increased during the process but unfortunately, a pore filling as high as in the reference was not achieved.

Table 4.4 Photovoltaic device performances obtained for **M2** depending on the TiO_2 thickness.

Thickness		Voc (V)	Jsc (mA/cm²)	FF	η (%)
1.6 µm	**Average efficiency**	0.55	1.51	0.53	0.44
	Best efficiency	**0.55**	**1.98**	**0.46**	**0.50**
3.2 µm	**Average efficiency**	0.51	0.70	0.28	0.10
	Best efficiency	**0.49**	**0.75**	**0.30**	**0.11**
3.6 µm	**Average efficiency**	0.46	1.18	0.29	0.16
	Best efficiency	**0.44**	**1.57**	**0.30**	**0.21**

Others conditions have been tested such as the concentration of the **spiro-OMeTAD** solution used for the spin-coating. Ding *et al.* have reported that the optimized solution concentration change from 180 mg/mL for 2.5 µm to 270 mg/mL for 5 µm-thick TiO_2 layers.[28] Following this finding, three different concentrations of the **spiro-OMeTAD** solution: 180, 225 and 270 mg/mL were attempted without changing the ratio with the additives.

Unfortunately, the process was not satisfactory for these series as shown by the reference where a PCE of only 0.15 % was reached. Thus, no conclusion can be drawn concerning the effect of the **spiro-OMeTAD** concentration (Table 4.5). It could be interesting to carry out new attempts in order to clearly evaluate the impact of the **spiro-OMeTAD** concentration on the chlorin-based devices performances.

Table 4.5 Photovoltaic device performances obtained for **M2** depending on the TiO_2 thickness and **spiro-OMeTAD** concentration.

Thickness	Concentration		Voc (V)	Jsc (mA/cm²)	FF	η (%)
Reference	**180 mg/mL**	**Average efficiency**	0.47	0.82	35	0.13
		Best efficiency	**0.47**	**1.01**	**35**	**0.17**
3.2 µm	**180 mg/mL**	**Average efficiency**	0.52	1.18	33	0.20
		Best efficiency	**0.52**	**1.45**	**35**	**0.26**
	225 mg/mL	**Average efficiency**	0.48	0.62	32	0.09
		Best efficiency	**0.49**	**0.70**	**42**	**0.15**
	270 mg/mL	**Average efficiency**	0.46	0.90	32	0.13
		Best efficiency	**0.45**	**1.04**	**32**	**0.15**

By changing several parameters such as the impregnation solvent, the TiO_2 thickness or the **spiro-OMeTAD** concentration, the PCEs were unfortunately not improved. Many other parameters could be modified to enhance the PCEs of the devices, but the time spent in Limoges was too short to test other possibilities. For example, H.C. Hassan *et al.* have reported satisfactory results by employing another HTM, a quasi-solid PVA-based electrolyte and have also shown that the PCEs could be improved by increasing the concentration of the additives in the electrolyte solution.[29]

2. **P3HT** DERIVATIVES AS SOLID ELECTROLYTE IN SS-DSSCS

As mentioned in Chapter 1, one important problem in DSSCs is their instability due to the liquid electrolyte. If the sealing of the device is not perfect, the liquid electrolyte gradually evaporates, and impurities such as water and oxygen molecules permeate into the cell.[2,30] Moreover, the I_3^-/I^- system is corrosive and dissolves many of the commonly used sealants and metal interconnects (such as silver, copper, aluminum and gold). The regeneration of the dye by this redox couple results also in a large loss (0.4-0.5 V) of voltage. To overcome these problems, the development of HTMs has been pursued to replace the liquid electrolyte. Among HTMs, **spiro-OMeTAD** is certainly the most studied, due to its capacity to transport holes and high solubility in organic media (Figure 4.10). Besides, its redox potential is more positive than that of the I_3^-/I^- couple, which is beneficial for increasing the V_{OC} of ss-DSSCs. Even if the use of **spiro-OMeTAD** as HTM in ss-DSSCs lead to PCE of around 7 %,[13] it suffers from some disadvantages such as its low hole mobility (10^{-4} $cm^2/(V.s)$) and its relatively complex multistep synthesis.[28] For these reasons, due to their better electrical

conductivity, organic conjugated polymers such as **PEDOT** and **P3HT** have also been the subject of great interest (Figure 4.23).[31] These conjugated polymers may also absorb light in addition to the dye molecules, which may be beneficial for extending the light-harvesting capacity of the cell. Also, the hole mobility may be higher for polymers such as **P3HT** which should be an advantage for faster hole transport. Recently, a conjugated polymer (poly(2,5-dihexyloxy-*p*-phenylene)-*b*-poly(3-hexylthiophene) (**PPP-*b*-P3HT**) was synthesized and applied as a solid state hole conductor in ss-DSSCs (Figure 4.22).[32] Thanks to its self-organization into highly ordered structure, the diblock copolymer leads to better hole mobility than the parent **P3HT** polymer and an improved PCE of 4.65 %.

Carrier hole mobility and recombination in ss-DSSCs can be also significantly improved by interfacial engineering[21] and chemical *p*-type doping of HTMs, *e.g.* with lithium bis(trifluoromethylsulfonyl)imide (LiTFSI), Co^{III} complexes, $SnCl_4$, etc.[13,33]

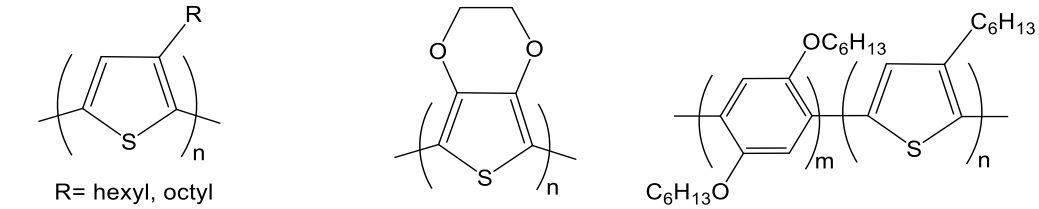

Figure 4.23 Chemical structures of conjugated polymer hole transporting materials.

In this context, **P3HT**-based conjugated polymers were synthesized to evaluate their potential as HTMs in ss-DSSCs. Following the interesting results reported for the **PPP-*b*-P3HT** diblock copolymer[32] and since ionic additives such as LiTFSI, 1-ethyl-3-methylimidazolium bis(trifuoromethylsulfonyl)imide (EMIM-TFSI) tend to reduce the charge recombination in DSSC,[34] **P3HT**-based conjugated polyelectrolytes (CPEs) were used as HTM in ss-DSSCs. In this regard, we decided to focus on **P3HT** bearing imidazolium ionic liquid-like side chains previously studied in Chapter 3 (Figure 4.24). Besides, in order to evaluate the influence of the molecular structure, *i.e.* homopolymer *vs.* diblock copolymer, corresponding imidazolium-based **P3HT** homopolyelectrolytes were studied. Finally, given that the infiltration of the polymer-based HTMs into TiO_2 pores is dependent on the molecular weight of the polymers, polymers with molecular weights of around 5 000 and 10 000 $g.mol^{-1}$ were studied (Figure 4.24).

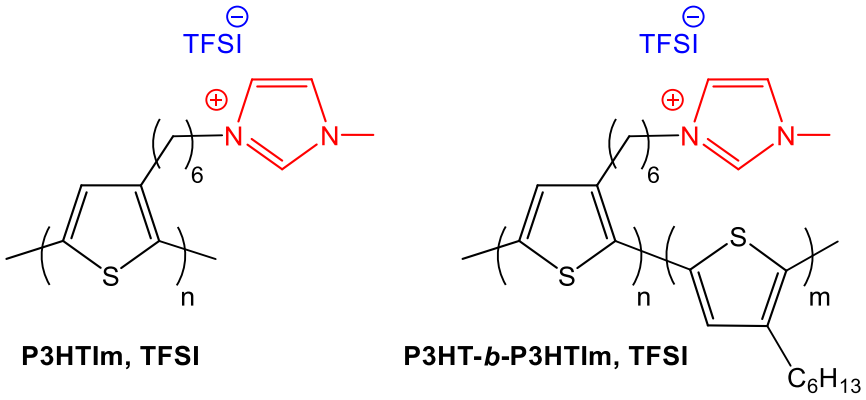

P3HTIm, TFSI **P3HT-*b*-P3HTIm, TFSI**

Figure 4.24 Molecular structures of the **P3HT**-based conjugated polyelectrolytes.

2.1. SYNTHESIS OF **P3HT** DERIVATIVES

The **P3HT** derivatives have been synthesized using the Kumada Catalyst Transfer Polycondensation (KCTP), combined with a quaternization procedure. More details on the synthesis have been already discussed in Chapters 2 and 3. The molecular parameters of the bromide polymer precursors are summarized in Table 4.6 below.

Table 4.6 Molecular weight and dispersity data for **P3HT**-based conjugated polyelectrolytes.

Polymer	M_n (kDa)[a,b]	M_w/M_n [a,b]	Yield (%)	Molar ratio 3HT/3HTBr
P3HTBr A	4.6	1.27	70	/
P3HTBr B	9.8	1.21	62	/
P3HT-b-P3HTBr A	6.2	1.20	60	58/42
P3HT-b-P3HTBr B	11.5	1.19	58	55/45

[a] M_n and M_w/M_n were determined by GPC analysis. [b] M_n and M_w/M_n are reported as their polystyrene equivalents. [c] The molar ratio between 3-hexylthiophene (**3HT**) and 3-(6'-bromohexyl)thiophene (**3HTBr**) repeating units was determined by ^{1}H NMR spectroscopy in $CDCl_3$.

2.2. **P3HT** DERIVATIVES AS HTM IN SS-DSSCS

ss-DSSCs including these polymer HTMs were prepared at the Institute XLIM in Limoges in collaboration with Dr. Johann Bouclé. As the fabrication process of the ss-DSSCs was already optimized with dye **D102** and **spiro-OMeTAD** as HTM, **P3HT**–based CPEs were tested in the same conditions to have a relevant comparison. The photovoltaic performances of these CPEs were also related to those obtained for a **P3HT** benchmark material (M_n = 23 000 g.mol^{-1}, $Đ$ = 1.24).

Dye impregnation was done in an acetonitrile/*tert*-butanol mixture at 0.3 mM for 15 hours without any co-adsorbent. HTM solutions were prepared in chlorobenzene with usual additives (*tert*-butylpyridine and bis(trifluoromethane)sulfonimide lithium salt) and stirred for 4 days at room temperature. Before spin-coating the polymer solutions onto the substrate, they were filtered on 0.2 µm Millipore. Commonly, the **spiro-OMeTAD** solution is

not filtered before spin-coating step but in this case, to make a clear comparison between the HTM, the **spiro-OMeTAD** solution was also filtered.

At this stage, the imidazolium-based homopolymers were not deposited on the cell because of a solubility issue. Indeed, these derivatives have to be solubilized in acetone which is inappropriate for the fabrication process since this solvent is used to clean the different layers of the cells. Besides, at the concentration of 20 mg/mL used for the HTM solution, their solubility were very low even upon heating. Thus, in the following sections, notations **A** and **B** will refer only to the diblock copolymers having molecular weights of around 5 000 and 10 000 $g.mol^{-1}$, respectively.

UV-Visible absorption measurements were firstly performed to analyze the amount of adsorbed dye **D102** on the TiO_2 electrodes and to determine the influence of the HTM layer on the absorption profile (Figure 4.25).

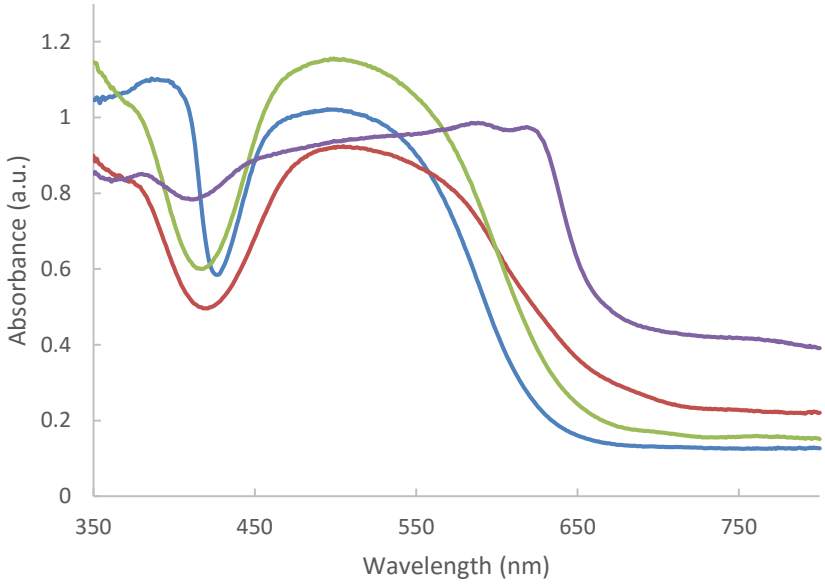

Figure 4.25 UV-visible absorption spectra of solar cells based on **D102** depending on the HTM (**spiro-OMeTAD** in blue, copolymer **A** in red, copolymer **B** in green and **P3HT** in purple).

The substrate **D102**/**spiro-OMeTAD** lead to a maximal absorbance of 1 around 500 nm. This value was the same for the substrate **D102**/**A** while it was significantly increased by 15 % at the same wavelength for the substrate **D102**/**B**. The substrate **D102**/**P3HT** displayed a different absorption profile. The intensity is almost the same but the profile is broadened compared to that of **D102**/**spiro-OMeTAD**, because of the intrinsic absorption of **P3HT** adding up onto that of **D102**. These UV-Vis data were in good agreement with the visual aspect of the substrates. After spin-coating of the different solutions, the color of the **spiro-OMeTAD** based substrate remained red while that with **P3HT** was almost black (Figure 4.26).

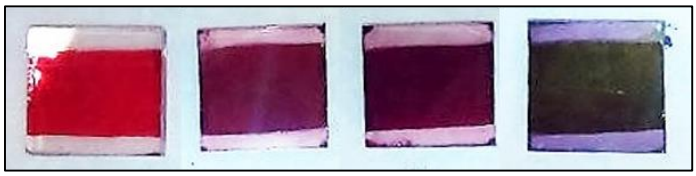

Figure 4.26 Photographs of ss-DSSCs substrates sensitized with **D102** after HTM spin-coating: from left to right, **spiro-OMeTAD**, copolymer **A**, copolymer **B**, **P3HT**.

Generally, when **P3HT** is applied as HTM in ss-DSSCs, the absorption profile remains approximately the same as that with **spiro-OMeTAD**.[35] Only a small increase in absorbance is generally observed when a **P3HT** solution is spin-coated on the samples. As the polymer absorbance at the maximum absorption is generally larger than 1 for a 200 nm-thick film, the thickness of the **P3HT** film deposited by spin-coating is less than 200 nm in the 2 µm-thick TiO_2 film.[36] The amount of the **P3HT** is generally very low, indicating that it cannot infiltrate the TiO_2 structure in ss-DSSCs completely, thus decreasing the performances compared **spiro-OMeTAD**.

Based on these findings and the UV-visible absorption spectra, the diblock copolymer **B** having higher molecular weight (10 000 $g.mol^{-1}$) seems to have a better pore infiltration than its analogue **A** with lower molecular weight (5 000 $g.mol^{-1}$).

The photovoltaic performances of the devices employing **D102** as the dye were measured under AM 1.5 irradiation (100 mW/cm^2) to study the performances of **P3HT** derivatives as HTM and to compare them to **spiro-OMeTAD**. The photocurrent density voltage curves (J-V) of the devices are presented in the Figure 4.27 and the detailed parameters are listed in Table 4.7.

Table 4.7 Photovoltaic parameters of ss-DSSCs sensitized with **D102** under simulated solar emission (100 $mW.cm^{-2}$, AM1.5G) as a function of the HTM: short-circuit current density (J_{SC}), open-circuit voltage (V_{OC}); fill factor (FF) and power conversion efficiency (η).

		Voc (V)	Jsc (mA/cm^2)	FF	PCE (%)
Spiro-OMeTAD	**Average efficiency**	0.73 (0.02)	9.23 (1.15)	49 (4)	3.32 (0.42)
	Best efficiency	**0.73**	**10.55**	**51**	**3.90**
A	**Average efficiency**	0.31 (0.01)	0.96 (0.07)	29 (1)	0.08 (0.01)
	Best efficiency	**0.32**	**1.06**	**30**	**0.10**
B	**Average efficiency**	0.68 (0.01)	3.39 (0.07)	34 (1)	0.80 (0.01)
	Best efficiency	**0.69**	**3.36**	**35**	**0.81**
P3HT	**Average efficiency**	0.63 (0.02)	11.12 (0.93)	53 (2)	3.71 (0.19)
	Best efficiency	**0.61**	**12.04**	**54**	**3.93**

The devices where copolymers **A** and **B** were used as HTM gave lower PCEs than **spiro-OMeTAD**: 0.08 % and 0.80 %, respectively. This result can be attributed to the poor infiltration of the copolymers compared to the **spiro-OMeTAD** as indicated by the value of the fill factor. This parameter is reduced by 41 and 31 % for the copolymers **A** and **B**,

respectively. Nevertheless, it was quite surprising that the polymer HTM with higher molecular weight leads to better performances. It was reported in the literature that the infiltration becomes less efficient when increasing the molecular weight of the polymer, especially for small TiO_2 nanoparticles (around 20 nm as in the Dyesol 18NR-T titania paste used for preparing our ss-DSSCs).[37] The increase in performances for the copolymer with higher molecular weight could be attributed to the mobility. A clear correlation between the charge carrier mobility in **P3HT** and the molecular weight has been already reported showing that the mobility can increase by one order of magnitude when increasing molecular weight.[38] Further mobility measurements on these copolymers could give more informations and will be carried out in the future.

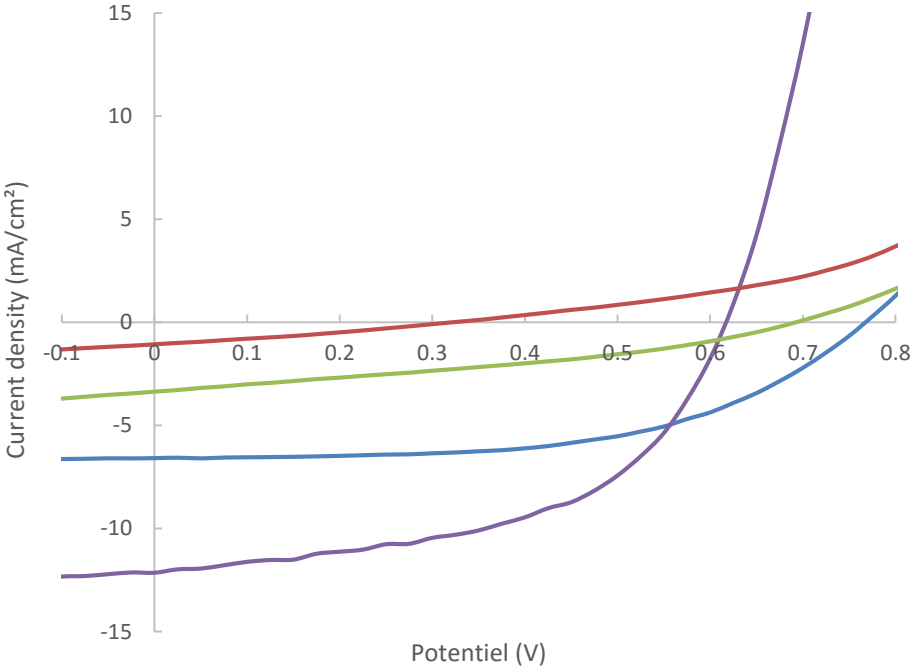

Figure 4.27 Current-voltage characteristics of ss-DSSCs sensitized with **D102** as a function of the hole transport material (**spiro-OMeTAD** in blue, copolymer **A** in red, copolymer **B** in green and **P3HT** in purple).

An interesting and unexpected result was the photovoltaic performances obtained with the **P3HT**. Interestingly, **P3HT** lead on average to similar results to those obtained for **spiro-OMeTAD** with dye **D102** (PCE = 3.71 %, J_{SC} = 11.12 mA/cm², V_{OC} = 630 mV, FF = 53 % for **P3HT** *vs.* PCE = 3.32 %, J_{SC} = 9.23 mA/cm², V_{OC} = 730 mV, FF = 49 %). To the best of our knowledge, it is the first example where **P3HT** shows the same performances than **spiro-OMeTAD** in organic ss-DSSCs. Generally, **P3HT** used in these researches is commercial and has higher molecular weight (until 50 kDa) and dispersity. Thanks to the KCTP method, the **P3HT** synthesized here exhibits low dispersities (below 1.3), which could explain a better organization and pore filling than those observed for commercial **P3HT**, and thus, better performances in solar cells.

To add further understanding on the infiltration of the polymers into TiO_2 pores, Scanning Electron Microscopy (SEM) analyses were performed on the cross-sections of the solar cells. In Figure 4.28, the cross-section of a TiO_2/**D102**/HTM solar cell is shown. On the glass substrate (bottom), the layer of conducting FTO (about 300-400 nm) and the dense TiO_2 layer (about 200-300 nm) are difficult to distinguish. On top, the mesoporous TiO_2 layer with a thickness between 1.6-2 µm depending on the sample can be seen, similar to the step-profilometer measurements. The cross-section images of **spiro-OMeTAD** and **P3HT** devices revealed also a clear contribution of HTMs. A thin layer of **P3HT** and **spiro-OMeTAD** materials was also observed on the top of the mesoporous TiO_2. By comparison, the polymer contributions in cross-sections of copolymers **A** and **B**-based DSSCs are not clearly observed at the surface (Figure 4.28, c and d). The SEM images obtained for these copolymers are coherent with the previous UV-vis absorption spectra indicating a very low amount of infiltrated polymer. Even if the copolymer **B** leads to better PCEs than the copolymer **A**, the effect is not visible on the SEM images. The infiltration of the copolymer **B** into TiO_2 pores did not seem to be better than that of the copolymer **A**. By examining the SEM images, it can be also inferred that **P3HT** has well infiltrated into the mesoporous TiO_2 electrodes.

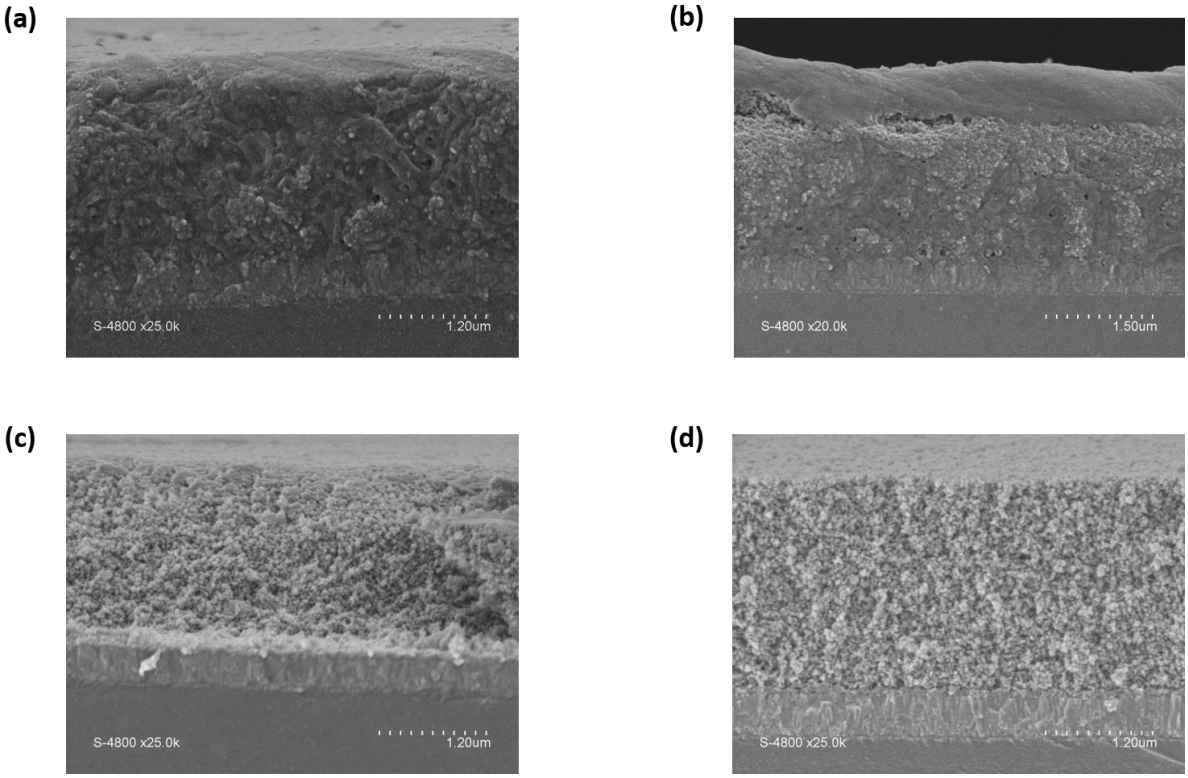

Figure 4.28 Cross section SEM images of **D102**-based solar cell devices spin-coated with (a) **spiro-OMeTAD**, (b) **P3HT**, (c) copolymer **A** and (d) copolymer **B**, with the additives *tert*-butylpyridine and LiTFSI.

Table 4.8 Photovoltaic parameters of ss-DSSCs sensitized with **D102** under simulated solar emission (100 mW.cm^{-2}, AM1.5G) as a function of the HTM: short-circuit current density (J_{SC}), open-circuit voltage (V_{OC}); fill factor (FF) and power conversion efficiency (η).

		Voc (V)	Jsc (mA/cm²)	FF	η (%)
Spiro-OMeTAD	**Average**	0.76	10.01	49	3.73
	Maximum	**0.76**	**10.20**	**52**	**3.99**
A	**Average**	0.70	3.67	40	1.03
	Maximum	**0.72**	**3.72**	**46**	**1.22**
B	**Average**	0.71	4.26	40	1.22
	Maximum	**0.71**	**4.54**	**47**	**1.52**
P3HT	**Average**	0.64	11.91	58	4.35
	Maximum	**0.71**	**11.39**	**60**	**4.78**

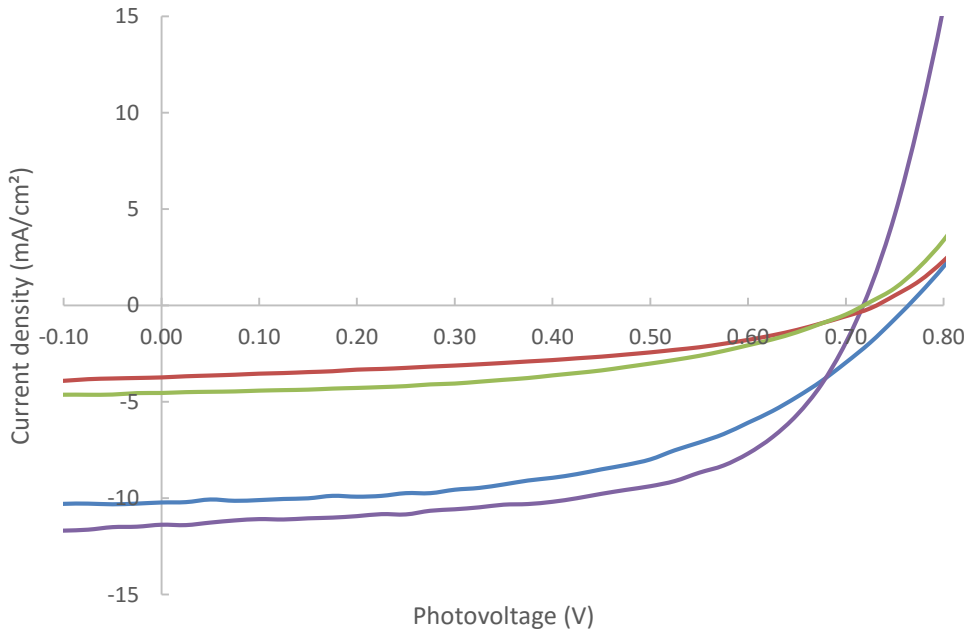

Figure 4.29 Current-voltage characteristics of ss-DSSCs sensitized with **D102** as a function of the hole transport material (**spiro-OMeTAD** in blue, copolymer **A** in red, copolymer **B** in green and **P3HT** in purple).

Regioregular **P3HT** is known to have a planar backbone, leading to a higher crystallinity in thin film, and this effect is even more amplified upon annealing.[39] Thus, thermal annealing at 150°C for 5 minutes was carried out before the evaporation of Au electrodes in order to improve the device performances. As shown in the Figure 4.29 and the Table 4.8, PCEs were improved for all HTMs.

The devices where copolymers **A** and **B** were used as HTM still gave lower photovoltaic efficiencies than **spiro-OMeTAD** but they were significantly increased upon annealing: 1.03 % (J_{SC} = 3.67 mA/cm², V_{OC} = 700 mV, FF = 40 % and 1.22 % (J_{SC} = 4.26 mA/cm², V_{OC} = 710 mV,

FF = 40 %) for copolymers **A** and **B,** respectively. The performances of the devices based on **P3HT** were enhanced up to 4.8 %, leading to an increase by about 20 % compared to the un-annealed device. The performances of the cells filled with **spiro-OMeTAD** were only increased by about 2 %. It was already shown that **LiTFSI** additive can favor the **spiro-OMeTAD** oxidation upon high thermal annealing temperatures that is detrimental for the performances.[40] For solar cells with **P3HT** as the HTM, the V_{OC} and fill factor increased significantly from 0.64 to 0.70 V and 54 to 60 % on average, respectively while J_{SC} remained constant.

Therefore, we assume that the enhancement of device performances can be due to the different local polymer morphology for the annealed device, thus inducing a decrease of charge-recombination.

To further investigate the morphology of the HTM layer, atomic force microscopy (AFM) images were recorded on un-annealed and annealed **P3HT**-based devices and compared to the **spiro-OMeTAD**-based devices (Figure 4.30). The device with **spiro-OMeTAD** HTM exhibit a granular morphology characteristic of the TiO_2 mesoporous structure and an average roughness of 7.8 nm, suggesting a flat and compact HTM layer (Figure 4.30, a). However, the formation of larger grains is observed for the device with **P3HT** HTM, increasing the film thickness and surface roughness (~ 18.4 nm). Upon annealing, the AFM images show the formation of crystalline fibrils, typical of the **P3HT** in an ordered packing (Figure 4.30, c and d).

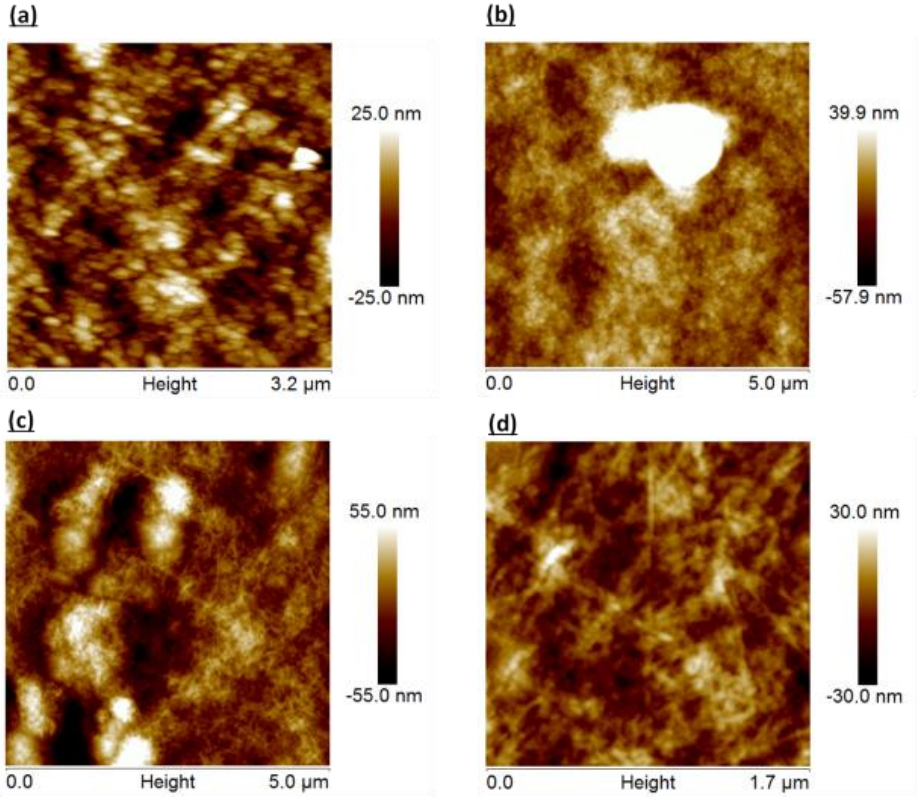

Figure 4.30 TM-AFM images of (a) **spiro-OMeTAD**-based device, (b) **P3HT**-based device without annealing, (c, d) **P3HT**-based device after thermal annealing; (d) is a zoom of (c).

To add further understanding to the annealing-induced enhancement of PCE, hole mobility measurements were performed in a field-effect transistor configuration (Figure 4.31). Whatever the treatment, the hole mobility in **P3HT** was found to be much higher than that of **spiro-OMeTAD**, *e.g.* 10^{-3} *vs.* 10^{-5} $cm^2.s^{-1}.V^{-1}$ (Table 4.9).This value further increased upon thermal annealing up to 80°C and then, decreased. The apparently lower mobility at higher annealing temperature is likely due to the rapid degradation of the polymer in air. Indeed, it is well-known that **P3HT** annealed up to 150°C in an inert atmosphere exhibits increased field effect mobility compared to as-prepared devices.

Table 4.9 Mobility values obtained for **P3HT** and **spiro-OMeTAD** materials deposited on FETs as a function of the annealing temperature.

Annealing temperature	Hole mobility of P3HT ($cm^2.V^{-1}.s^1$)	V_{th} (V)	I_{ON}/I_{OFF}	Hole mobility of spiro-OMeTAD ($cm^2.V^{-1}.s^1$)
Without	4.3 x 10^{-3}	25.7	128	1.2 x 10^{-5}
80°C	6.2 x 10^{-3}	22.6	233	2.0 x 10^{-5}
100°C	5.7 x 10^{-3}	25.2	105	1.3 x 10^{-5}
120°C	4.0 x 10^{-3}	26.7	*Not measured*	*Not measured*

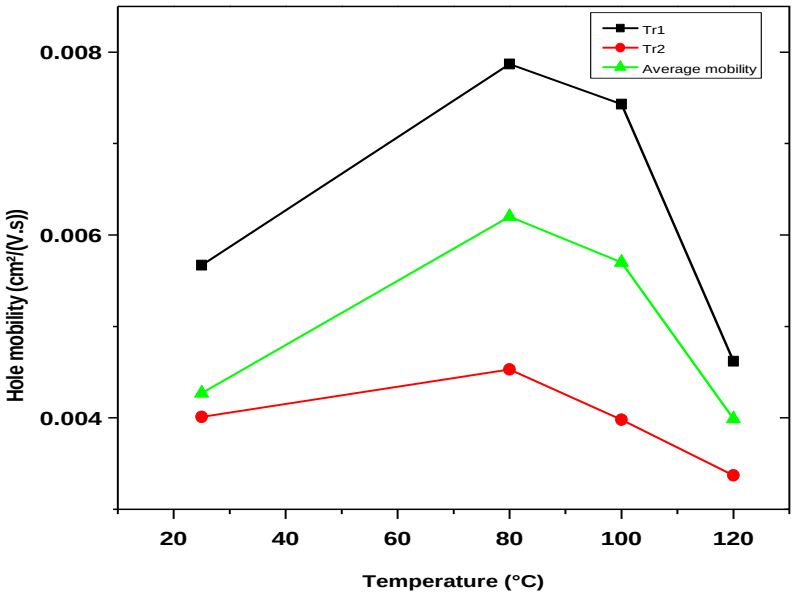

Figure 4.31 Hole mobility *vs.* annealing temperature (each point corresponds to the average value obtained for 4 transistors).

This finding was further confirmed by examining the series resistances determined from the J-V curves of **P3HT-** and **spiro-OMeTAD-**based devices. A decrease of about 10 % of the series resistance after thermal treatment implies that the charge carrier mobility increased

upon annealing (Table 4.10). This allows decreasing charge recombination, which induces better V_{OC} and FF, as discussed above.

Table 4.10 Series resistance calculated from J-V plots in the dark for the best J-V characteristics of **P3HT** and **spiro-OMeTAD**-based devices as a function of thermal annealing. The annealing time for all devices is 5 minutes.

HTM	Series resistance (Ω)
Spiro-OMeTAD	122.0
Spiro-OMeTAD upon annealing	119.0
P3HT	53.8
P3HT upon annealing	48.1

CONCLUSION

In summary, different dyes synthesized from chlorophyll *a* and **P3HT**-based hole transport materials have been evaluated in all-solid state dye-sensitized solar cells.

Concerning chlorophyll *a*-based dyes, six derivatives bearing different anchoring groups, *i.e.* alkyl carboxylic acid, acrylic acid and cyanoacrylic acid, have been synthesized. As porphyrin derivatives are known to self-aggregate, a first study was carried out to evaluate the need of co-adsorbent, since the dye aggregation has a detrimental effect on the photovoltaic performances. In the case of chlorophyll *a*-based dyes, it was demonstrated that the addition of co-adsorbent improves the device performance. By analyzing the photovoltaic performances of these dyes, it appeared that free-base chlorins provide better results than their zinc analogues and also, that the vinylic carboxylic acid anchoring group provide the best PCE (0.77 %). The observed trends regarding these biomass-based dyes have been analyzed in more details by combining UV-visible absorption spectroscopy, TD-DFT calculations and recombination kinetics studies in order to give further understanding to these systems.

In the second part of this chapter, we focused on the HTMs used in ss-DSSCs. **Spiro-OMeTAD** is the most commonly HTM used in ss-DSSCs but it presents some disadvantages such as its expensive multistep synthesis and its low mobility. Thus, conjugated polymers such as **P3HT**, well-known for its high hole mobility have been envisaged for replacing it. As ionic liquid additives have been found to be efficient in combination with **P3HT**, we proposed to combine these two features in one single material. As such, **P3HT**-based conjugated polyelectrolytes bearing ionic liquid-like side chains have therefore been synthesized to be used as HTMs in ss-DSSCs. Following the same process than that used with **spiro-OMeTAD**, different CPEs with different molecular weights (5 000 and 10 000 $g.mol^{-1}$) and topology (homopolymer *vs.* block copolymer) have been studied as HTM in order to evaluate them as HTM and also, to try determining a structure-properties relationship. Among the block copolyelectrolytes, the one with the highest molecular weight (10 000 $g.mol^{-1}$) lead to the best PCE (1.22 % after annealing). No difference concerning the pore infiltration was clearly

observed between these polymers using SEM. Thus, it is suspected that hole mobility, which is known to increase with the molecular weight, could explain this result. Further mobility measurements have to be carried out in the future to confirm this hypothesis. A very interesting result was the performances reached by **P3HT**. Indeed, this polymer showed better PCE values than **spiro-OMeTAD** (4.78 *vs*. 3.99 % after annealing), which is the first example where **P3HT** is a more suitable HTM for ss-DSSCs than **spiro-OMeTAD**. This finding was also supported by UV-visible absorption, SEM and AFM analyses that show an excellent infiltration and organization of the polymer. Additional studies should be done to provide further understanding of this system. It could be interesting to see if this result is confirmed with other organic dyes, to identify the influence of the molecular weight on the performances, as well as the influence of additives.

EXPERIMENTAL PROCEDURE

1. SYNTHESIS OF THE CHLOROPHYLL *A* BASED DYES

Synthesis of methyl pheophorbide-*a*.[41] Chlorophyll *a* was extracted from spirulina powder (200 g), purchased from AlgoSud using a Soxhlet apparatus with ethanol for 3 days. The solvent was then evaporated under reduced pressure. The green residue (3.9 g) was dissolved in acetone (500 mL) and a 2M hydrochloric acid solution (250 mL) was added. The resulting brown mixture was stirred at room temperature for 16 hours. When judged complete, the solvent was evaporated under reduced pressure. The residue was poured into water and the organic layer was extracted with diethyl ether. The combined extracts were dried over $MgSO_4$, filtered and evaporated under reduced pressure. The crude brown oil was then stirred with sulfuric acid (25 mL) in methanol (500 mL) under reflux for 18 hours. The resulting solution was evaporated under reduced pressure, diluted with water (200 mL), neutralized with aqueous saturated $NaHCO_3$ and extracted with dichloromethane. The combined extracts were dried over $MgSO_4$, filtered, evaporated under reduced pressure and recrystallized from a DCM/pentane mixture to give the *title compound* as a dark solid (2.09 g, 79 %). **^{1}H NMR ($CDCl_3$, 300 MHz):** δ 9.51, 9.37, 8.57 (s, each 1H, 5-, 10-, 20-H), 7.98 (dd, 1H, $^3J_{H\text{-}H}$ = 17.7, 11.5 Hz, 3^1-H), 6.23 (m, 3H, 3^2-CH and 13^2-CH), 4.46, 4.20 (d, each 1H, $^3J_{H\text{-}H}$ = 7.9 Hz, 17- and 18-H), 3.89, 3.69, 3.58, 3.40, 3.21 (s, each 3H, 2^1-, 7^1-, 12^1-CH_3, 13^2-COOMe, 17^2-COOMe), 3.66 (m, 2H, 8^1-CH_2)2.64-2.24 (m, 4H, 17^1-,17^2-CH_2), 1.82 (d, 3H, $^3J_{H\text{-}H}$ = 7.2 Hz, 18^1-CH_3), 1.67 (t, 3H, $^3J_{H\text{-}H}$ = 7.5 Hz, 8^2-CH_3) ppm. **Maldi-ToF** calcd for $C_{39}H_{39}N_4O_5$ $[M+H]^+$ *m/z* 606.284, found 606.282. **UV-Vis: λ_{max} (CH_2Cl_2):** 412, 506, 538, 610, 668 nm.

Synthesis of methyl pyropheophorbide-*a*. Methyl pheophorbide-*a* (1 g, 1.65 mmol) was dissolved in 2,4,6-collidine (100 mL) and stirred under reflux for 15 hours. When finished, the solvent was evaporated at 10^{-3} mbar pressure and the residue was recrystallized from a DCM/pentane mixture to give the *title compound* as a dark solid (740 mg, 56 %). **^{1}H**

NMR ($CDCl_3$, 300 MHz): δ 9.56, 9.44, 8.63 (s, each 1H, 5-, 10-, 20-H), 8.01 (dd, 1H, $^3J_{H-H}$ = 17.9, 11.5 Hz, 3^1-H), 6.24 (m, 2H, 3^2-CH), 5.29, 5.13 (d, each 1H, $^3J_{H-H}$ = 20.0 Hz, 13^2-CH_2), 4.52, 4.32 (m, each 1H, 17- and 18-H), 3.73 (m, 2H, 8^1-CH_2), 3.68, 3.63, 3.42, 3.25 (s, each 3H, 2^1-, 7^1-, 12^1-CH_3, 17^2-COOMe), 2.47 (m, 4H, 17^1-,17^2-CH_2), 1.84 (d, 3H, $^3J_{H-H}$ = 7.2 Hz, 18^1-CH_3), 1.70 (t, 3H, $^3J_{H-H}$ = 7.6 Hz, 8^2-CH_3) ppm. **Maldi-ToF** calcd for $C_{34}H_{36}N_4O_5$ $[M]^+$ *m/z* 548.279, found 548.275. **UV-Vis; λ_{max} (CH_2Cl_2):** 410, 510, 540, 610, 668 nm.

Pyropheophorbide-a (M1). To a solution of methyl pyropheophorbide-*a* (150 mg, 2.74 mmol) in acetone (15 mL) was added concentrated hydrochloric acid (5 mL). After 30 minutes under stirring, the mixture was poured into water and extracted with dichloromethane. The organic layer was then washed with a saturated solution of $NaHCO_3$ and water until neutrality. The organic layer was dried over $MgSO_4$, filtered and concentrated under reduced pressure. The solid was then recrystallized from a DCM/pentane mixture to give the title compound as a dark solid (129 mg, 88 %). **^{1}H NMR (300 MHz, $CDCl_3$):** δ 9.50, 9.39, 8.58 (s, each 1H, 5, 10, 20-H), 7.98 (dd, $^3J_{H-H}$ = 17.8, 11.5 Hz, 1H, 3^1-H), 6.22 (m, 2H, 3^2-CH), 5.18 (m, 2H, 13^2-CH_2), 4.49, 4.41 (m, each 1H, 17-,18-H), 3.64 (m, 3H, 8^1-CH_2 and 12^1-CH_3), 3.40 (2-CH_3), 3.23 (s, 3H, 7-CH_3), 2.70-2.30 (m, 4H, 17^1,17^2-CH_2), 1.82 (d, $^3J_{H-H}$ = 7.1 Hz, 3H, 18^1-CH_3), 1.68 (t, $^3J_{H-H}$ = 7.5 Hz, 4H, 8^2-CH_3) ppm. **^{13}C{^{1}H} NMR (101 MHz, Pyr):** δ 196.0, 176.1, 172.8, 162.4, 155.7, 151.7, 149.5, 145.8, 142.0, 138.7, 137.0, 136.7, 136.3, 132.5, 131.7, 130.0, 128.9, 123.0, 107.4, 104.9, 97.9, 94.5, 52.7, 50.7, 48.8, 32.3, 31.1, 23.7, 20.0, 18.1, 12.5, 12.3, 11.6 ppm. **Maldi-ToF** calcd for $C_{33}H_{34}N_4O_3$ *m/z* 534.263, found 534.290. **UV-Visible (THF):** λ_{max} (ε) 414 (77 500), 507 (8 200), 536 (6 600), 310 (5 300), 668 (33 600) nm**.**

Methyl pyropheophorbide-*d*.[18] A solution of $NaIO_4$ (4.75 g, 22.2 mmol) in a water/acetic acid mixture (30 mL/2 mL) was added with a syringe pump at a rate of 1 mL/min to a solution of methyl pyropheophorbide-*a* (2 g, 3.65 mmol) and OsO_4 (40 mg, 0.16 mmol) in dioxane (400 mL). The reaction mixture was stirred overnight at room temperature and poured into water. The organic layer was extracted with chloroform, dried over $MgSO_4$, filtered and concentrated under reduced pressure. The crude product was recrystallized from a DCM/pentane mixture to yield the title compound (1.31 g, 65 %). **^{1}H NMR (300 MHz, $CDCl_3$):** δ 11.55 (s, 1H, CHO), 10.32, 9.63, 8.86 (s, each 1H, 5, 10, 20-H), 5.35, 5.19 (d, each 1H, $^3J_{H-H}$ = 20.1 Hz, 13^2-CH_2), 4.58, 4.39 (d, each 1H, $^3J_{H-H}$ = 8.1 Hz, 17-,18-H), 3.78, 3.72, 3.62, 3.32 (s, 3H, 2^1-, 7^1-, 12^1-CH_3, 17^2-COOMe), 3.75 (m, 2H, 8^1-CH_2), 2.61-2.32 (m, 4H, 17^1-,17^2-CH_2), 1.86 (d, 3H, $^3J_{H-H}$ = 7.2 Hz, 18^1-CH_3), 1.73 (t, 3H, $^3J_{H-H}$ = 7.6 Hz, 8^2-CH_3) ppm**. MS(ESI)** calcd for $C_{33}H_{35}N_4O_4$ $[M+H]^+$ *m/z* 551.26, found 551.27. **UV-Visible ($CHCl_3$)**: λ_{max} 400, 414, 510, 541, 610, 669 nm.

Methyl *trans*-3^2-*tert*-butylcarboxypyropheophorbide-*a* (Chlorin-COO*t*Bu). To a solution of methyl pyropheophorbide-*d* (86 mg, 0.157 mmol) in toluene (16 mL) was added (*tert*-

butoxycarbonylmethylene)triphenylphosphorane (178 mg, 0.473 mmol). The resulting mixture was stirred under reflux for 3 hours, then cooled to room temperature and purified by column chromatography on silica gel (DCM/Et_2O, 19/1) to give the title compound as a black solid (87 mg, 85 %). **^{1}H NMR (300 MHz, $CDCl_3$):** δ 9.44, (s, 1H, 10-H), 9.38 (s, 1H, 5-H), 8.97 (d, 1H, $^3J_{H-H}$ = 16.1 Hz, 3^2-CH), 8.62 (s, 1H, 20-H), 6.91 (d, 1H, $^3J_{H-H}$ = 16.2 Hz, 3^1-CH), 5.22, 5.06 (d, each 1H, $^3J_{H-H}$ = 20.1 Hz, 13^1-CH_2), 4.45 (m, 1H, 18-H), 4.25 (d, 1H, $^3J_{H-H}$ = 8.2 Hz, 17-H), 3.58 (m, 5H, 12^1-CH_3 and 8^1-CH_2), 3.54, 3.44, 3.17 (s, each 3H, 2^1-CH_3, 7^1-CH_3, 17^2-COOMe), 2.52, 2.23 (m, each 2H, 17^1-CH_2 and 17^2-CH_2), 1.77(d, 3 H, $^3J_{H-H}$ = 7.2 Hz, 18^1-CH_3), 1.75 (s, 9H, CH_3), 1.66 (t, 3H, $^3J_{H-H}$ = 8 Hz, 8^2-CH_3) ppm. **HRMS(ESI)** calcd for $C_{39}H_{45}N_4O_5$ $[M+H]^+$ *m/z* 649.3390, found 649.3387.

Methyl *trans*-3^2-carboxypyropheophorbide-*a* (M3). Chlorin-COOtBu (117 mg, 0.180 mmol) was dissolved in trifluoroacetic acid (6.5 mL). The green solution was stirred for 3 hours at room temperature and then, poured into water. The organic layer was extracted with DCM, dried over $MgSO_4$, filtered and concentrated *under vacuum*. The brown residue was purified by column chromatography on silica gel (DCM/MeOH, 19/1) to give the title compound as a black solid (68 mg, 64 %). **^{1}H NMR (600 MHz, $CDCl_3$/Pyr):** δ 9.41 (s, 1H, 10-H), 9.37 (s, 1H, 5-H), 9.03 (d, 1H, $^3J_{H-H}$ = 16.1 Hz, 3^2-CH), 8.56 (s, 1H, 20-H), 7.04 (d, 1H, $^3J_{H-H}$ = 16.1 Hz, 3^1-CH), 5.17, 5.01 (d, each 1H, $^3J_{H-H}$ = 19.2 Hz, 13^2-CH_2), 4.40, 4.20 (m, each 1H, 17-, 18-H), 3.54, 3.48, 3.36, 3.10 (s, each 3H, 2^1-, 7^1-, 12^1-CH_3, 17^2-COOMe), 3.53 (m, 2H, 8^1-CH_2), 2.60, 2.50 (m, each 1H, 17^2-CH_2), 2.20 (m, 2H, 17^1-CH_2), 1.72 (d, 3H, *J* = 7.5 Hz, 18^1-CH_3), 1.57 (t, 3H, $^3J_{H-H}$ = 7.7 Hz, 8^2-CH_3), 0.08, -1.97 (s, each 1H, NH) ppm. **^{13}C{^{1}H} NMR (151 MHz, $CDCl_3$/Pyr):** δ 195.6, 173.1, 170.7, 169.1, 160.7, 154.7, 151.0, 149.4, 148.5, 144.7, 140.3, 138.1, 136.3, 135.5, 135.4, 133.5, 131.9, 130.7, 128.5, 126.3, 123.2, 106.2, 103.6, 96.7, 93.5, 51.6, 51.3, 49.6, 47.8, 30.7, 29.6, 22.9, 19.2, 17.2, 12.4, 11.8, 11.0 ppm. **HRMS(ESI)** calcd for $C_{35}H_{36}N_4O_5$ $[M+H]^+$ *m/z* 593.2841, found 593.2845. **UV-Visible (THF):** λ_{max} (ε) 417 (33 000), 513 (4 600), 545 (3 600), 621 (2 700), 681 (17 000) nm.

Methyl 3^2-carboxy-3^2-cyano-pyropheophorbide-*a* (M5). To a solution of **methyl pyropheophorbide-*d*** (200 mg, 0.363 mmol) and cyanoacetic acid (6.18 g, 72.6 mmol) in THF (20 mL) was added ammonium acetate (2.80 g, 36.3 mmol). The mixture was refluxed for 1 hour, poured into water and extracted with DCM. The extract was dried over $MgSO_4$, filtered and concentrated under vacuum. The residue was then recrystallized from a DCM/pentane mixture to give the title compound as a dark solid (145 mg, 65 %). **^{1}H NMR (400 MHz, DMSO)**: δ 9.62, 9.32, 9.13, 8.62 (s, each 1H, 5-, 10-, 20-, 3^1-CH), 5.14, 5.06 (d, each 1H, $^3J_{H-H}$ = 19.9 Hz, 13^1-CH_2), 5.06, 4.54 (m, each 1H, 17-, 18-H), 3.75 (m, 2H, 8^1-CH_2), 3.59, 3.53, 3.31, 3.23 (s, each 3H, 2^1-, 7^1-, 12^1-CH_3, 17^2-COOMe), 2.60, 2.24 (m, each 2H, 17^1-, 17^2-CH_2), 1.77 (d, 3H, $^3J_{H-H}$ = 7.5 Hz, 18^1-CH_3), 1.67 (t, 3H, $3J_{H-H}$ = 7.7 Hz, 8^2-CH_3) ppm. **^{13}C{^{1}H} NMR (101 MHz, DMSO):** δ 195.2, 176.5, 172.9, 167.7, 163.2, 160.1, 156.6, 152.0, 149.8, 147.1, 145.3, 145.0, 143.0, 142.7, 137.2, 135.1, 133.1, 132.9, 131.6, 120.5, 119.1, 105.3, 105.1, 98.4, 92.7,

66.4, 66.2, 66.0, 65.7, 65.5, 51.0, 50.1, 47.7, 47.6, 29.9, 29.2, 24.0, 23.8, 23.6, 23.5, 23.4, 23.0, 18.5, 17.2, 13.2, 12.0, 10.4 ppm. **HRMS ESI$^+$** calcd for $C_{36}H_{36}N_5O_5$ $[M+H]^+$ *m/z* 618.2716, found 618.2717.

General procedure for the zinc metalation. A saturated methanol solution of zinc acetate dihydrate ($Zn(OAc)_2.2H_2O$) (10 mL) was added to a THF solution (50 mL) of metal-free chlorin (50 mg). After stirring overnight, the solution turned from brown to green. The mixture was filtered off and the filtrate was concentrated under vacuum. The crude material was then recrystallized from a DCM/pentane mixture to afford the desired zinc complex.

M2: (80 %). **^{1}H NMR (400 MHz, Pyr):** δ 9.84, 9.69, 8.83 (each s, each 1H, 5, 10, 20-H), 8.19 (dd, $^3J_{H-H}$ = 17.8, 11.6 Hz, 1H, 3^1-H), 6.35, 6.15 (m, each 1H, 3^2-CH_2), 5.56, 4.61 (m, each 1H, 13^2-CH_2), 4.61, 4.48 (m, each 1H, 17-,18-H), 3.70 (m, 5H, 8^1-CH_2 and 12^1-CH_3), 3.36 (2^1-CH_3), 3.22 (s, 3H, 7^1-CH_3), 2.93, 2.73 (m, each 2H, 17^1,17^2-CH_2), 1.85 (d, $^3J_{H-H}$ = 7.2 Hz, 3H, 18^1-CH_3), 1.67 (t, $^3J_{H-H}$ = 7.6 Hz, 4H, 8^2-CH_3) ppm. **Maldi-ToF** calcd for $C_{33}H_{32}N_4O_3Zn$ *m/z* 596.177, found 596.180. **UV-Visible (THF):** λ_{max} (ε) 405 (23 800), 427 (39 500), 570 (2 500), 609 (4 400), 657 (22 000) nm**.**

M4: (87 %). **^{1}H NMR (400 MHz,$CDCl_3$-Pyr) :** 9.41 (s, 1H, 10-H), 9.37 (s, 1H, 5-H), 9.03 (d, 1H, $^3J_{H-H}$ = 16.1 Hz, 3^2-CH), 8.56 (s, 1H, 20-H), 7.04 (d, 1H, $^3J_{H-H}$ = 16.1 Hz, 3^1-CH), 5.17, 5.01 (d, each 1H, $^3J_{H-H}$ = 19.2 Hz, 13^2-CH_2), 4.40, 4.20 (m, each 1H, 17-, 18-H), 3.54, 3.48, 3.36, 3.10 (s, each 3H, 2^1-, 7^1-, 12^1-CH_3, 17^2-COOMe), 3.53 (m, 2H, 8^1-CH_2), 2.60, 2.50 (m, each 1H, 17^2-CH_2), 2.20 (m, 2H, 17^1-CH_2), 1.72 (d, 3H, $^3J_{H-H}$ = 7.5 Hz, 18^1-CH_3), 1.57 (t, 3H, $^3J_{H-H}$ = 7.7 Hz, 8^2-CH_3) ppm. **HRMS ESI$^+$** calcd for $C_{35}H_{34}N_4O_5Zn$ $[M+H]^+$ *m/z* 655.1899, found 655.1901. **UV-Visible (THF):** λ_{max} (ε) 414 (37 600), 436 (54 500), 531 (3 500), 576 (4 900), 621 (7 900), 671 (40 100) nm**.**

M6: (78 %). **^{1}H NMR (400 MHz, DMSO-*d*6):** 9.62, 9.13, 8.62 (s, 1H each, 5-, 10-, 15-, 20-H), 9.32 (s, 1H, 3'-H), 5.14, 5.05 (d, 1H each, $^3J_{H-H}$ = 19.9 Hz, 15'-H), 4.55 (dd, 1H, $^3J_{H-H}$ = 7.4, 2.5 Hz, 18-H), 4.28 (d, 1H, $^3J_{H-H}$ = 8.2 Hz, 17-H), 3.59, 3.53, 3.31, 3.23 (s, 3H each), 2.60, 2.24 (m, 4H), 1.76 (d, 3H, $^3J_{H-H}$ = 7.7 Hz, 18^1-CH_3), 1.65 (t, 3H, $^3J_{H-H}$ = 7.6 Hz, 8^2-CH_3) ppm. **HRMS ESI$^+$** calcd for $C_{36}H_{35}N_5O_5Zn$ $[M+H]^+$ *m/z* 680.1852, found 680.1851. **UV-Visible (THF):** λ_{max} (ε) 434 (48 300), 532 (3 800), 579 (4 700), 625 (7 900), 670 (36 800) nm**.**

2. SYNTHESIS OF THE **P3HT** BASED ELECTROLYTES

Quaternisation method. Block copolymer **P3HT-*b*-P3HTBr** (150 mg) was dissolved in chloroform (10 mL). Methylimidazole (10 mL) was then added to the orange solution and the mixture was stirred under reflux for 2 days. Once the reaction was finished, the resulting

mixture was poured into cold diethyl ether. The purple precipitate was then filtered and washed with diethyl ether using a Soxhlet apparatus.

3. PHOTOVOLTAIC CHARACTERIZATION

Device fabrication. FTO-coated conducting glass substrates were cleaned by an ultrasonic treatment with water, acetone and isopropanol for 10 minutes each before being treated for 5 minutes by UV-ozone. A compact TiO_2 layer was deposited by spray-pyrolysis at 450°C from a solution of titanium isopropoxide and acetylacetone in ethanol followed by annealing at 450°C for 20 minutes. A nanoporous TiO_2 layer was then deposited by spin-coating from a solution of a commercial TiO_2 paste (DSL 18NRT, Dyesol) in ethanol containing anatase nanoparticles (average size: 20 nm). The layers were then gradually annealed from 250°C up to 500°C over 45 minutes. The substrates were then treated in a 0.02 M $TiCl_4$ aqueous solution for 2 hours, rinsed with water and annealed at 450°C for 45 minutes. The electrodes were finally immersed in dye solutions that may also contain chenodeoxycolic acid as co-adsorbent for 15 hours in the dark. After rinsing the electrodes, the hole conductor layer was deposited by spin-coating from a **spiro-OMeTAD** or **CPE** solution in chlorobenzene containing *tert*-butylpyridine and LiTFSI as additives. Gold top electrodes were finally evaporated under vacuum (10^{-6} mbar) using shadow masks that define two active areas per substrate (around 0.149 cm² each).

Cell characterization. The photovoltaic performances of the cells were measured using a mask with an aperture area of 0.149 cm². The cell was illuminated by AM 1.5G solar simulator calibrated with a radiometer to provide an incident irradiance of 100 mW.cm^{-2} at the surface of the cell. The J-V measurements were performed using a Keithley model 2400 digital source meter by applying independent external voltage to the cell and by measuring the photogenerated current out from the cell.

REFERENCES

[1] (a) B. O'Regan, M. Grätzel, *Nature* **1991**, *353*, 737; (b) A. Hagfeldt, G. Boschloo, L. Sun, L. Kloo and H. Pettersson, *Chem. Rev.* **2010**, *110*, 6595.

[2] B. E. Hardin, H. J. Snaith, M. D. McGehee, *Nat. Photonics* **2012**, *6*, 162.

[3] S. Mathew, A. Yella, P. Gao, R. Humphry-Baker, B. F. E. Curchod, N. Ashari-Astani, I. Tavernelli, U. Rothlisberger, Md. K. Nazeeruddin and M. Grätzel, *Nature Chem.* **2014**, *6*, 242.

[4] L. Han, A. Islam, H. Chen, C. Malapaka, B. Chiranjeevi, S. Zhang, X. Yang and M. Yanagidaa, *Energy Environ. Sci.* **2012**, *5*, 6057.

[5] (a) W. Zeng, Y. Cao, Y. Bai, Y. Wang, Y. Shi, M. Zhang, F. Wang, C. Pan and P. Wang, *Chem. Mater.* **2010**, *22*, 1915; (b) L.-L. Li and E. W.-G. Diau, *Chem. Soc. Rev.* **2013**, *42*, 291.

[6] A. Yella, R. Humphry-Baker, B. F. E. Curchod, N. A. Astani, J. Teuscher, L. E. Polander, S. Mathew, J.-E. Moser, I. Tavernelli, U. Rothlisberger, M. Grätzel, Md. K. Nazeeruddin and J. Frey, *Chem. Mater.* **2013**, *25*, 2733.

[7] M. Ye, X. Wen, M. Wang, J. Iocozzia, N. Zhang, C. Lin and Z. Lin, *Mater. Today*, **2015**, *18*, 155.

[8] G. Calogero, A. Bartolotta, G. Di Marco, A. Di Carlo and F. Bonaccorso, *Chem. Soc. Rev.* **2015**, *44*, 3244.

[9] (a) S.-I. Sasaki, X.-F. Wang, T. Ikeuchi and H. Tamiaki, *J. Porphyrins Phthalocyanines* **2015**, *19*, 517; (b) X.-F. Wang, H. Tamiaki, L. Wang, N. Tamai, O. Kitao, H. Zhou and S.-I. Sasaki, *Langmuir* **2010**, 26, 6320; (c) X.-F. Wang, O. Kitao, H. Zhou, H. Tamiaki and S.-I. Sasaki, *Chem. Commun.* **2009**, 1523.

[10] H. C. Hassan, Z. H. Z. Abidin, F. I. Chowdhury and A. K. Arof, *Int.l J. Photoenergy* **2016**, http://dx.doi.org/10.1155/2016/3685210; (b) D. J. Godibo, S. T. Anshebo and T. Y. Anshebo, *J. Braz. Chem. Soc.* **2015**, *1*, 92.

[11] S. M. Zakeeruddin and M. Grätzel, *Adv. Funct. Mater.* **2009**, *19*, 2187.

[12] J. Bouclé and J. Ackermann, *Polym. Int.* **2012**, *61*, 355.

[13] J. Burschka, A. Dualeh, F. Kessler, E. Baranoff, N. Cevey, C. Yi, M. Nazeeruddin and M. Gratzel, *J. Am. Chem. Soc.* **2011**, *133*, 18042.

[14] J. Wu, Z. Lan, J. Lin, M. Huang, Y. Huang, L. Fan and G. Luo, *Chem. Rev.* **2015**, *115*, 2136.

[15] (a) G. Hodes and D.Cahen, *Acc. Chem. Res.* **2012**, *45*, 705 ; (b) I. Chung, B. Lee, J. He, R. P. H. Chang and M. G. Kanatzidis, *Nature* **2012**, *485*, 486.

[16] (a) K. Murakoshi, R. Kogure, Y. Wada and S. Yanagida, *Chem. Lett.* **1997**, 471; (b) S. Tan, J. Zhai, M. Wan, Q. Meng, Y. Li, L. Jiang and D. Zhu, *J. Phys. Chem. B* **2004**, *108*, 18693; (c) E. Lancelle-Beltran, P. Prene, C. Boscher, P. Belleville, P. Buvat and C. Sanchez, *Adv. Mater.* **2006**, *18*, 2579; (d) R. Zhu, C. Y. Jiang, B. Liu and S. Ramakrishna, *Adv. Mater.* **2009**, *21*, 994; (e) G. Mor, S. Kim, M. Paulose, O. Varghese, K. Shankar, J. Basham and C. Grimes, *Nano Lett.* **2009**, *9*, 4250; (f) F. Giacomo, S. Razza, F. Matteocci, A. Epifanio, S. Licoccia, T. Brown and A. Carlo, *J. Power Sources* **2014**, *251*, 152.

[17] H. Tamiaki, M. Amakawa, Y. Shimono, R. Tanikaga, A. R. Holzwarth, K. and Schaffner, *Photochem. Photobiol.* **1996**, *63*, 92.

[18] D. G. Johnson, W. A. Svec and M. R. Wasielewski, *Isr. J. Chem.* **1988**, *28*, 193.

[19] L. Schmidt-Mende, U. Bach, R. Humphry-Backer, T. Horiuchi, H. Miura, S. Ito, S. Uchida and M. Grätzel, *Adv. Mater.* **2005**, *17*, 813.

[20] Z. S. Wang, Y. Cui, Y. Dan-oh, C. Kasada and K. Hara, *J. Phys. Chem. C* **2007**, *111*, 7224.

[21] S. Zhang, X. Yang, C. Qin, Y. Numata and L. Han, *J. Mater. Chem. A* **2014**, *2*, 5167.

[22] (a) M. K. Nazeeruddin, R. Humphry-Baker, M. Grätzel, N. Wöhrle, D. Schnurpfeil, G. Schneider, G. Hirth and A. Trombach, *J. Porphyrins Phthalocyanines*, **1999**, *3*, 230; (b) S. Qu, W. Wu, J. Hua, C. Kong, Y. Long and H. Tian, *J. Phys. Chem. C* **2010**, *114*, 1343.

[23] N. R. Neale, N. Kopidakis, J. van de Lagemaat, M. Grätzel and A. J. Frank, *J. Phys. Chem. B* **2005**, *109*, 23183.

[24] H. C. Hassan, Z. H. Z. Abidin, M. A. Careem and A. K. Arof, *High Perform. Polym.* **2014**, *26*, 647.

[25] (a) S. Erten-Ela, K. Ocakoglu, A. Tarnowska, O. Vakuliuk and D. T. Gryko, *Dyes Pigm.* **2015**, *114*, 129; (b) K. Ocakoglu, S. Erten-Ela, K. S. Joya and E. Harputlu, *Inorg. Chim. Acta*, **2016**, *439*, 30.

[26]H. K. Wayment-Steele, L. E. Johnson, F. Tian, M. C. Dixon, L. Benz and M. S. Johal, *ACS Appl. Mater. Interfaces*, **2014**, *6*, 9093.

[27] (a) I.-K. Ding, N. Tétreault, J. Brillet, B. E. Hardin, E. H. Smith, S. J. Rosenthal, F. Sauvage, M. Grätzel and M. D. McGehee, *Adv. Funct. Mater.* **2009**, *19*, 2431; (b) H. J. Snaith, R. Humphry-Baker, P. Chen, I. Cesar, S. M. Zakeeruddin and M. Grätzel, *Nanotechnology*, **2008**, *19*, 424003.

[28] I.-K. Ding, J. Melas-Kyriazi, N.-L. Cevey-Ha, K. G. Chittibabu, S. M. Zakeeruddi, M. Grätzel and M. D. McGehee, *Org. Electron.* **2010**, *11*, 1217.

[29] H.C. Hassan, Z. H. Z. Abidin, F. I. Chowdhury and A. K. Arof, *Int. J. Photoenergy*, **2016**, http://www.hindawi.com/journals/ijp/aip/746963/

[30](a) H. S. Jung and J.-K. Lee, *J. Phys. Chem. Lett.* **2013**, *4*, 1682; (b) L. M. Peter, *J. Phys. Chem. Lett.* **2011**, *2*, 1861.

[31] W. D. Oosterbaan, V. Vrindts, S. Berson, S. Guillerez, O. Douheret, B. Ruttens, J. D'Haen, P. Adriaensens, J. Manca, L. Lutsen and D. Vanderzande, *J. Mater. Chem.* **2009**, *19*, 5424.

[32] W. C. Chen, Y.-H. Lee, C.-Y. Chen, K.-C. Kau, L.-Y. Lin, C.-A. Dai, C.-G. Wu, K.-C. Ho, J. K. Wang and L. Wang, *ACS Nano* **2014**, *8*, 1254.

[33] (a) M. Xu, Y. Rong, Z. Ku, A. Mei, X. Li and H. Han, *J. Phys. Chem. C* **2013**, *117*, 22492; (b) A. Abate, D. J. Hollman, J. Teuscher, S. Pathak, R. Avolio, G. D'Errico, G. Vitiello, S. Fantacci and H. J. Snaith, *J. Am. Chem. Soc.* **2013**, *135*, 13538.

[34] (a) A. Abrusci, R. S. Santosh Kumar, M. Al-Hashimi, M. Heeney, A. Petrozza and H. J. Snaith, *Adv. Funct. Mater.* **2011**, *21*, 2571; (b) H. J. Snaith and L. Shmidt-Mende, *Adv. Mater.* **2007**, *19*, 3187.

[35] L. Yang, U. B. Cappel, E. L. Unger, M. Karlsson, K. M. Karlsson, E. Gabrielsson, L. Sun, G. Boschloo, A. Hagfeldt and E. M. J. Johansson, *Phys. Chem. Chem. Phys.* **2012**, *14*, 779.

[36] K. M. Coakley and M. D. McGehee, *Chem. Mater.* **2004**, *16*, 4533.

[37] E.M.J. Johansson, S. Pradhan, E. Wang, E. L. Unger, A. Hagfeldt and M. R. Andersson, *Chem. Phys. Lett.* **2011**, *502*, 225.

[38] R. J.Kline, M. D. McGehee, E. N. Kadnikova, J. Liu and J. M. J. Fréchet, *Adv. Mater.* **2003**, *15*, 1519.

[39] S. Cho, K. Lee, J. Yuen, G. Wang, D. Moses, A. J. Heeger, M. Surin and R. Lazzaroni, *J. Appl. Phys.* **2006**, *100*, 114503.

[40] Y. Fang, Xi. Wang, Q. Wang, J. Huang, and T. Wu, *Phys. Status Solidi A*, **2014**, *211*, 2809.

[41] K. Smith, D. A. Goff and D. J. Simpson, *J. Am. Chem. Soc.* **1985**, *107*, 4946.

CHAPTER 5

CHARACTERIZATION METHODS

MATERIALS

All reagents were purchased from Fisher, Sigma-Aldrich, Alfa Aesar and Fluorochem, and used without further purification. Dry THF, diethyl ether, toluene and CH_2Cl_2 were obtained by a solvent purification system PureSolve MD5 from Innovative Technology.

NUCLEAR MAGNETIC RESONANCE

^{1}H, $^{13}C\{^{1}H\}$, ^{19}F, and $^{31}P\{^{1}H\}$ NMR spectra were recorded on a Bruker Avance 400 or 600 MHz spectrometers at room temperature in deuterated solvents ($CDCl_3$, CD_2Cl_2, DMSO-d_6, CD_3OD-d_4, acetone-d_6) and referenced to tetramethylsilane (TMS) at 0 ppm. All chemical shifts (δ) and coupling constants (J) are expressed in parts per million (ppm) and Hertz (Hz), respectively.

SIZE EXCLUSION CHROMATOGRAPHY

Size Exclusion Chromatography (SEC) analyses were performed on a Polymer Laboratories liquid chromatograph equipped with a PL-DG802 degasser, an isocratic HPLC pump LC 1120 (flow rate = 1 mL min^{-1}), a Marathon autosampler (loop volume = 200 mL, solution conc. = 1 mg mL^{-1}), a PL-DRI refractive index detector and three columns: a PL gel 10 mm guard column and two PL gel Mixed-B 10 mm columns (linear columns for separation of MW_{PS} ranging from 500 to 10^6 Daltons). The eluent used was THF at a flow rate of 1 mL.min^{-1} at 35 °C. Polystyrene standards were used to calibrate the SEC.

MASS SPECTROMETRY

Matrix-assisted laser desorption/ionization time-of-flight (MALDI-ToF) mass spectra were recorded using a Water QToF Premier mass spectrometer equipped with a nitrogen laser, operating at 337 nm with a maximum output of 500 J m^{-2} delivered to the sample in 4 ns pulses at 20 Hz repeating rate. Mass analyses were performed in reflection mode at a resolution of about 10 000. All samples were analyzed using (DCTB) trans-2-[3-(4-tert-butylphenyl)-2-methylprop-2-enylidene]malononitrile. This matrix was prepared as a 40 mg.mL^{-1} solution in $CHCl_3$.[1] The matrix solution (1 µL) was applied to a stainless steel target and air dried. Polymer samples were dissolved in $CHCl_3$ to obtain 1 mg.mL^{-1} solutions. 1 µL aliquots of these solutions were applied onto the target area already bearing the matrix crystals and air dried. For the recording of the single-stage MS spectra, the quadrupole (rf-only mode) was set to pass ions from *m/z* 500 to *m/z* 15 000, and all ions were transmitted into the pusher region of the time-of-flight analyzer where they were mass analyzed with 1 s integration time.

OPTICAL ANALYSES

UV-Visible absorption spectra were recorded at room temperature on Cary UV50 or Shimadzu UV2401 PC UV/Vis scanning spectrometers.

Fluorescence spectra were recorded at room temperature on a Fluorolog-3 (Horiba Jobin Yvon) spectrophotometer. Emission and excitation spectra were corrected for the wavelength response of the system using correction factors supplied by the manufacturer. Fluorescence quantum yields (Φ_F) were measured using *meso*-5,10,15,20-tetraphenylporphyrin (TPP) in toluene as a standard (Φ_F = 0.11).[2]

INFRARED SPECTROSCOPY

Fourier transform infrared (FTIR) spectra were recorded using a Bruker Tensor 27 spectrometer.

ATOMIC FORCE MICROSCOPY

At the University of Mons, the AFM measurements were performed on an Icon Bruker microscope in tapping mode at room temperature. The silicon cantilevers used were NCHV tips with nominal resonance frequency of 320 kHz. Samples for AFM measurements were generally prepared by drop casting xylene solutions of the polymer (0.1 $mg.mL^{-1}$) onto mica substrates, and then placed under saturation with xylene vapor for 16 h.

On the other hand, at the University of Hasselt, the AFM measurements were performed using an Asylum Research MFP-3D™ instrument mounted on an anti-vibration plinth, in tapping mode at room temperature under ambient conditions. The silicon cantilevers used were 125 µm in length and had a resonance frequency of 150 kHz.

The C-AFM measurements were performed in air on a Bruker Multimode microscope equipped with a Nanoscope V controller and an Extended TUNA external module for current detection. A PtIr5 conductive coating on etched Si probes ensured good electrical contact at the tip–sample contact, while low spring constant and deflection set-point guaranteed low contact forces, preventing mechanical or electrical damage upon scanning. Samples for measurements were also prepared by drop casting xylene solutions of the polymer (0.1 $mg.mL^{-1}$) onto patterned glass/ITO substrates, followed by slow solvent evaporation for 16 h to favor the self-organization of the polymer chains into fibers.

All raw AFM images were visualized and analyzed using the Nanoscope analysis or the Gwyddion 2.31 software.

THERMAL ANALYSES

THERMOGRAVIMETRIC ANALYSES

Thermogravimetric analysis (TGA) was conducted on a TA Instrument Q500. Samples were first held at a constant temperature, and then, heated to 800 °C at a rate of 20 $°C.min^{-1}$ under an inert atmosphere (nitrogen).

DIFFERENTIAL SCANNING CALORIMETRY ANALYSES

Differential Scanning Calorimetry (DSC) characterization was performed using a DSC Instrument Q200 under an atmosphere of nitrogen at a heating/cooling rate of 10 $°C.min^{-1}$. All DSC analyses were performed using an aluminum pan with a sample of approximately 5-10 mg.

RAPID HEAT-COOL CALORIMETRY ANALYSES

Rapid Heat–Cool (RHC) calorimetry experiments were performed on a prototype RHC from TA Instruments, equipped with liquid nitrogen cooling and specifically designed for operation at high

scanning rates.[3] RHC measurements were performed at 500 K.min^{-1} in aluminum non-hermetic crucibles, using neon (6 mL.min^{-1}) as a purge gas.

X-RAY DIFFRACTION ANALYSES

Powder XRD analyses were carried out on a Philips X'pert Pro MPD diffractometer using Cu Kα1 radiation (λ = 1.5406 Å) in Bragg-Brentano scanning mode with a 2θ angle range from 4 to 40˚ (or 4 to 53°), and a time per step of 50 or 300 s, depending on the sample.

CRYSTALLOGRAPHIC ANALYSES

Crystal evaluation and data collection were performed on a Rigaku-Oxford Diffraction Gemini-S diffractometer with sealed-tube Mo Kα radiation using the CrysAlis Pro program (Agilent, 2012). This program was also used for the integration of the frames using default parameters, correction for Lorentz and polarization effects, and for empirical absorption correction using spherical harmonics with symmetry-equivalent and redundant data. All structures were solved using the ab initio iterative charge flipping method using the Superflip program and they were refined using full-matrix least-squares procedures as implemented in CRYSTALS on all independent reflections with I > 2σ(I).

DYNAMIC LIGHT SCATTERING ANALYSES

Dynamic light scattering measurements were performed using a Zetasizer Nano series nano-ZS (Malvern Instruments, U.K.) in the back-scattering configuration (175°). Cumulant analysis of the correlation function was used to determine the mean hydrodynamic diameter (Z-average) and the polydispersity of each sample.[4]

SMALL ANGLE NEUTRON SCATTERING ANALYSES

SANS was carried out on a Sans2d and a LOQ small-angle diffractometers at the ISIS Pulsed Neutron Source (STFC Rutherford Appleton Laboratory, Didcot, U.K.).[5]

For **CPE, Br**, a simultaneous q-range of 0.004–0.6 Å^{-1} was achieved utilizing an incident wavelength range of 1.75–16.5 Å separated by time-of-flight and employing an instrument setup of $L_1 = L_2 = 4$ m, with the 1 m^2 detector offset vertically 150 mm and sideways 150 mm.

For **CPE, DS**, a simultaneous q-range of 0.009–0.24 Å^{-1} was achieved utilizing an incident wavelength range of 2.2–10.0 Å separated by time-of-flight and employing a fixed sample-detector distance of 4.1 m. $q = (4\pi/\lambda)\sin(\theta/2)$, where λ is the wavelength and θ is the scattering angle.

Samples were prepared in deuterated solvents, to provide good neutron scattering contrast. Each raw scattering dataset was corrected for the detector efficiencies, sample transmission and background scattering and converted to scattering cross-section data ($\partial\Sigma/\partial\Omega$ *vs.* q) using the instrument-specific software.[6] These data were placed on an absolute scale (cm^{-1}) using the scattering from a standard sample (a solid blend of hydrogenated and perdeuterated polystyrene) in accordance with established procedures.[7]

REFERENCES

[1] J. De Winter, G. Deshayes, F. Boon, O. Coulembier, P. Dubois and P. Gerbaux, *J. Mass Spectrom.* **2011**, *46*, 237

[2] P. G. Seybold and M. Gouterman, *J. Mol. Spectrosc*. **1969**, *31*, 1

[3] (a) R. L. Danley, P. A. Caulfield and S. R. Aubuchon, *Am. Lab.* **2008**, *40*, 9; (b) S. Wouters, F. Demir, L. Beenaerts and G. Van Assche, *Thermochim. Acta* **2012**, *530*, 64.

[4] International Organisation for Standardisation (ISO), *International Standard ISO22412 Particle Size Analysis – Dynamic Light Scattering*, **2008**.

[5] R. K. Heenan, S. E. Rogers, D. Turner, A. E. Terry, J. Treadgold and S. M. King, *Neutron News* **2011**, *22*, 19.

[6] From http://www.mantidproject.org

[7] G. D. Wignall and F. S. Bates, *J. Appl. Crystallogr.* **1987**, *20*, 28.

GENERAL CONCLUSION AND OUTLOOKS

The aim of this thesis was the development of new π-conjugated systems for photovoltaic applications. For this purpose, two types of solar cells, *i.e.*, bulk heterojunction (BHJ) and dye-sensitized (DS) solar cells, have been considered and different approaches have been envisaged in an attempt to enhance the device efficiency. These approaches have been detailed through three chapters after having reported the state of art on that topic.

Chapter 2 deals with the improvement of the light-harvesting in bulk-heterojunction solar cells based on **P3HT**:**PCBM**. Poly(3-hexylthiophene) (**P3HT**) suffers from a narrow absorption spectrum in regard to the solar emission spectrum, which limits the power conversion efficiency (PCE) of the corresponding devices. One approach proposed in the literature to increase the light harvesting of the **P3HT**:**PCBM** photoactive layer, is the incorporation of a third component, a chromophore having an absorption profile at higher wavelength. The combination of the absorption properties of **P3HT** and the chromophore is expected to extend the light-harvesting and enhance the photocurrent. Among the chromophores, porphyrins were chosen in this work due to their unique optical properties that can be modulated through chemical modification. One major disadvantage of the use of such chromophores is their tendency to self-aggregate, which may disturb, especially in ternary blends, the organization of the **P3HT**, which is a crucial point in view of an efficient charge transport. To overcome this limitation, two strategies of functionalization, *i.e.* pending along and located at the extremity of the P3HT chains, were developed to incorporate porphyrins to the **P3HT** backbone. In the first approach, **P3HT** copolymers decorated with 10 % of fluorinated or non-fluorinated porphyrin sensitizers have been successfully prepared through the coordination of the central zinc ion of the porphyrin moieties with an imidazole-functionalized polythiophene copolymer. The relevance of this approach was first demonstrated using a model compound, *i.e.* 3-(6'-imidazolhexyl)thiophene (**TIm**), which corresponds to the thiophene monomer units bearing an imidazole ligand in the **P3HT-*r*-P3HTIm** copolymer. By using a combination of ^{1}H NMR, UV-vis absorption spectroscopies, mass spectrometry and X-ray diffraction, the 1:1 complex stoichiometry was evidenced. Binding constants around 10^{3}-10^{4} M^{-1} were found by exploiting the optical data. These copolymers displayed excellent thermal stability as well as a significant contribution of both complexed moieties, *i.e.* polythiophene and porphyrin. However, a blue-shift of the **P3HT** absorption was observed upon complexation, which seems to indicate that porphyrins tend to disturb the organization of **P3HT** in the solid-state. This finding was confirmed by studying the morphological properties of the materials, where a lack of crystallinity was demonstrated, thus resulting in very low photovoltaic performances when combined with **PCBM** in the active layer of BHJ solar cells. In the second approach, chain ends containing π-extended porphyrins were introduced on **P3HT** using a one-pot procedure based on the chain growth polymerization of **3HT** and arylisocyanide. Three **P3HTs** end-functionalized with this π-extended porphyrin having different composition and

molecular weight have been prepared by tuning the molar ratio between **3HT** and porphyrin (between 10 and 30 %) and the amount of nickel catalyst. Regarding their properties, in contrast with the supramolecular strategy, this second approach was found to not disturb the well-known self-assembling properties of **P3HT**, a key requirement for efficient charge transport properties. By introducing these π-extended porphyrin chain ends, the absorption profile of the polymer was extended to higher wavelengths thanks to the combination of the absorption profile of both **P3HT** and porphyrin. Nevertheless, the molar ratio in porphyrin has to be judiciously adjusted. By increasing the molar ratio up to 30 %, the porphyrin end-functionalized polymer was found to be amorphous and no structured morphology was observed. The end-functionalized polymer with the best morphological properties, *i.e.* having a porphyrin molar ratio of 10 %, was introduced as the donor in the active layer of BHJ solar cells with **$PC_{61}BM$** as the acceptor material leading to very poor PCE (<0.1 %). Additional studies are necessary to determine if these low performances are intrinsically due to the nature of the donor material or to the fabrication process, as only a series of three cells has been tested. AFM analyses should be performed on end-functionalized **P3HT**:**$PC_{61}BM$** mixtures to determine whether the morphology remains well-structured by adding the acceptor compound. Other cells could be further fabricated by changing the deposition conditions to ensure the fibrillar structuration. If the future results are encouraging, other porphyrin derivatives with extended spectral feature could be incorporated following this strategy.

Another way to improve the efficiency in BHJ solar cells is the incorporation of interfacial layers between the photoactive layer and the electrode, in order to enhance the charge transfer and collection. In Chapter 3, conjugated polyelectrolytes (CPEs) have been synthesized, characterized and used as cathode interfacial layers in bulk heterojunction (BHJ) solar cells. CPEs having different topology, *i.e.* homopolymer *vs.* diblock copolymer, and bearing different cationic groups, *i.e.* imidazolium, pyridinium, phosphonium and ammonium, were obtained by nucleophilic substitution from the bromide-based homo- and block copolymers precursors. These precursors, *i.e.* **P3HTBr** and **P3HT-*b*-P3HTBr**, were obtained using the Kumada Catalyst Transfer Polycondensation (KCTP) method, leading to polymers with controlled molecular weight and low dispersity. The influence of the nature of the counterion on the photovoltaic performance was also studied. Thus, the bromide counterion (**Br^-**) was exchanged by the more hydrophobic bis(trifluoromethane)sulfonimide (**$TFSI^-$**) and dodecylsulfate (**DS^-**) surfactant. The introduction of the cationic groups on the side chains of the polymers resulted in an increasing solubility in polar solvents such as water and methanol. For **P3HT-*b*-CPEs** diblock copolymers, both blocks, *i.e.* neutral and cationic, enable solubilizing the diblock copolymer in classical solvents of **P3HT** (chloroform, tetrahydrofuran) as well as in polar solvents (methanol, water), resulting in a solvatochromic behavior. As the optical properties of these polymers are governed by their π-conjugated backbone, the absorption and emission profiles are independent of the

nature of cationic group and counterion. Regarding the thermal properties, the topology, the nature of the cationic group and the counterion were found to significantly affect the behavior of the CPEs. A clear signature of the diblock copolymer structure was observed: a glass transition temperature (T_g) characteristic from the **CPE** block and a melting temperature corresponding to the **P3HT** block. The T_g was found to be dependent on the nature of the **CPE** block as well as the counterion. For example, exchanging **Br**$^-$ for **TFSI**$^-$ and **DS**$^-$ ions resulted in considerably lower T_g values and a strong plasticizing effect was observed. Regarding the aggregation behavior of these polymers in solution, dynamic light scattering (DLS) analyses demonstrated that the **CPE** particles are larger in methanol/water mixtures than in the pure corresponding solvents. In the methanol/water mixture, the aggregation of the polymeric chains is reduced, resulting in swelling of the aggregate structure due to associated solvent molecules. The hydrodynamic diameter was thus increased. This finding was further confirmed by small-angle neutron scattering (SANS) analyses where it was also shown that **P3HT-*b*-CPEs** form core-shell (core: **P3HT**, shell: **CPE**) cylindrical aggregates in solution. The aggregate structures were found to be dependent on the solvent nature and could be transferred as thin films with the retention of their nanoscale organization, as observed by atomic force microscopy (AFM) analyses. This result is of crucial importance for potential device applications. Upon counterion exchange, a limited effect on the aggregation behavior was observed for the diblock copolymer. Indeed, **P3HT-*b*-P3HTPMe$_3$,DS** retains the cylindrical core-shell morphology of the pure diblock copolymer. In comparison, the corresponding homopolymer is less-aggregated and thus, is able to freely transform from semi-flexible cylinders to rigid sheets upon counterion exchange from **Br**$^-$ to **DS**$^-$. Finally, the conjugated polyelectrolytes were used as cathode interfacial layer in BHJ solar cells. The introduction of these polymers resulted in a significant enhancement of the solar cells performances. Compared to the homopolymers, the diblock copolymers afford better PCEs and the photovoltaic performances were found to be dependent on the cationic group and the counterion. Regarding the cationic group, it seems that there is a correlation between the performances and the surface coverage determined by AFM analyses. Regarding the counterion, solar cells with brominated **CPEs** reached lower performances than those with **CPEs,TFSI**. This observation can be due to the hydrophilic character of the bromide counterion observed with thermal analyses, which complicates the repeatability and the interpretation of the results. The introduction of **CPEs,DS** as cathodic interfacial layers provided also better results than the bromide counterion with an enhancement of the performances by about 20 %. This preliminary study will be extended to other surfactants, such as octylsulfate (**OS**$^-$) and perfluorooctylsulfonate (**PFOS**$^-$), which could also favor the CPEs self-assembly in the interlayer and thus, enable the orientation of the interfacial dipole moment.

After the bulk-heterojunction solar cells, Chapter 4 was devoted to dye-sensitized solar cells (DSSCs). Despite the high reported efficiencies for liquid-electrolyte DSSCs (up to 13 %),

these cells present several disadvantages that have to be overcome for the potential commercialization of this technology. In particular, the I_3^-/I^- system, commonly used as the liquid electrolyte, is corrosive and dissolves the sealants and the metal interconnects of the cell. Besides, the most currently used dyes are based on ruthenium and are thus rare, expensive and toxic. Therefore, alternatives are necessary to replace the liquid electrolyte and the expensive Ru dyes. In this work, new dyes based on chlorophyll *a* have been proposed as well as **P3HT** derivatives, to be used as hole transport materials. Regarding the dyes, six derivatives bearing different anchoring groups, *i.e.* alkyl carboxylic acid, acrylic acid and cyanoacrylic acid, have been synthesized. As porphyrin derivatives are known to self-aggregate, a study was carried out to determine if a co-adsorbent is necessary. It is well-known that dye aggregation is detrimental to the photovoltaic performances. As expected, it was demonstrated that the co-adsorbent is beneficial for improving the device performance of chlorophyll *a* dyes as it prevents the aggregation of the dye and thus, the decrease of electron transfer. From the solar cell performances, it appeared that the free base chlorins provide better results than their zinc analogues and also, that the vinylic one provides the best photovoltaic performances (η = 0.77 %). These biomass-based dyes have been analyzed in more details by UV-visible absorption spectroscopy, TD-DFT calculations and recombination kinetic studies in order to understand the observed trends and to give further understanding to these systems. Several parameters have been modified in an attempt to improve the device performances such as the titanium oxide thickness, the impregnation solvent or the **spiro-OMeTAD** concentration. Other changes could be done regarding for example the replacement of **spiro-OMeTAD** by another hole transport material. Other chlorin dyes could also be designed: for this preliminary study, the chlorins used as dyes are relatively easy to prepare. It could be interesting to design from this model push-pull systems, which have already demonstrated their efficiency in devices, by adding for example donor groups (amine, carbazole, etc.) in the 20-position.

Spiro-OMeTAD is known as the best hole transporter material (HTM) used in ss-DSSCs but it presents some disadvantages, such as its expensive multistep synthesis and its low mobility. Thus, it has been envisaged to replace it by conjugated polymers such as **P3HT**, well-known for its high hole mobility. As the polyelectrolytes used as cathodic interfacial layer in Chapter 3 yielded satisfying results, their use as HTM in ss-DSSCs has been envisaged. Following the same procedure as used with **spiro-OMeTAD**, different homo- and co-polyelectrolytes have been studied in order to evaluate their potential as HTM and also, to determine a structure-properties relationship. In summary, copolyelectrolytes have shown the best results, in particular that having the highest molecular weight around 10 000 $g.mol^{-1}$. No clear difference concerning the pore infiltration was observed between these polymers using SEM. Thus, it is suspected that the hole mobility, which is known to increase with the molecular weight, could explain this result. Further mobility measurements have to be carried out in the future to further understand these systems. An interesting result was nevertheless the performances

reached with **P3HT**. Indeed, this polymer showed better results than **spiro-OMeTAD** (4.78 *vs.* 3.99 %), which is the first example where **P3HT** is a more suitable HTM for ss-DSSCs. This finding was also supported by UV-visible absorption, SEM and AFM analysis that show an excellent infiltration and organization of the polymer. Additional studies should be performed to provide further understanding of this system. In particular, it could be interesting to determine whether the improvement is also observed with other organic dyes, to identify the influence of the molecular weight on the performances, the influence of additives or the influence of annealing temperatures/times.

TOWARDS NEW π-CONJUGATED MATERIALS FOR PHOTOVOLTAIC APPLICATIONS

Among renewable energies, the sunlight has by far the highest theoretical potential to meet the worldwide need in energy. Photovoltaic devices are thus currently the subject of intense research for low-cost conversion of sunlight into electrical power. In particular, organic photovoltaics have emerged as an interesting alternative to produce electricity due to their low manufacturing cost compared to silicon solar cells, their mechanical flexibility and the versatility of the possible chemical structures. In this dissertation, we focused our research on the development of new organic π-conjugated materials for organic solar cells applications. Two types of solar cells have been studied during this work: bulk heterojunction and dye-sensitized solar cells. The charge transfer leading to the photocurrent is usually based on (i) a polymer donor and a fullerene acceptor in BHJ solar cells, such as the widely studied poly(3-hexylthiophene) (**P3HT**) and [6,6]-phenyl-C_{61}-butyric acid methyl ester (**PCBM**) materials and (ii) a metal oxide (titanium oxide) sensitized with a dye and an electrolyte in DSSCs. Despite power conversion efficiencies have reached 5 and 13 % respectively for these two types of devices, they still display several drawbacks that limit their commercialization. **P3HT** displays a narrow absorption of the solar spectrum thus limiting the conversion efficiency. To overcome this limitation, we combined P3HT with chromophores, *i.e.* porphyrins, having an extending absorption. Then, to ensure better charge transfer and extraction within the device, a cathode interfacial layer based on cationic π-conjugated polyelectrolytes was added, Finally, dyes extracted from the biomass (chlorophyll derivatives) were synthesized to replace the expensive ruthenium dyes in DSSCs. Since liquid electrolytes are volatile and corrosive, which considerably limit the DSSCs stability, solid polymer electrolytes were also developed as an alternative.

VERS DE NOUVEAUX SYSTEMES π-CONJUGUES POUR DES APPLICATIONS PHOTOVOLTAIQUES

Le développement des énergies renouvelables est aujourd'hui devenu un enjeu mondial majeur comme alternative aux énergies fossiles dans la production d'énergie. Parmi elles, l'énergie solaire est considérée comme la source la plus prometteuse, permettant de couvrir l'ensemble des besoins énergétiques liés à l'activité humaine. Les cellules photovoltaïques les plus performantes aujourd'hui, entre 16 et 18 % en modules, sont composées de silicium, un semi-conducteur inorganique. Cependant, leur coût de production élevé a nécessité le développement de matériaux alternatifs moins couteux. Parmi les voies explorées, les cellules solaires organiques ont émergé comme une alternative prometteuse pour produire l'électricité à faible coût. Le sujet de cette thèse s'intègre dans ce contexte de recherche. Deux types de cellules solaires ont été étudiés : les cellules à hétérojonction en volume (BHJ) et sensibilisées au colorant (DSSCs). Le courant photogénéré repose généralement (i) dans les cellules BHJ, sur le transfert entre de charge entre un polymère donneurs et un accepteur d'électrons(fullerène), tels que le couple poly(3-hexyl)thiophène (**P3HT**) et [6,6]-phényl-C_{61}-butanoate de méthyle (**PCBM**), et (ii) dans les DSSCs, la sensibilisation de la surface d'un semi-conducteur inorganique tel que l'oxyde de titane par un colorant et la présence d'un électrolyte, jouant le rôle de médiateur redox. Bien qu'ayant atteint des rendements de photoconversion respectifs de 5 et 13 %, ces cellules nécessitent des améliorations pour une commercialisation à grande échelle. Tout d'abord, les performances des cellules BHJ à base de P3HT sont considérablement limitées par sa faible absorption, ne couvrant pas la globalité du spectre solaire. Afin de pallier ce problème, nous avons combiné le **P3HT** avec des chromophores, *i.e.* des porphyrines, ayant une absorption plus étendue. Ensuite, pour assurer une meilleure extraction des charges au sein du dispositif, une couche interfaciale cathodique à base de polyélectrolytes π-conjugués a été ajoutée. Enfin, des colorants extraits de la biomasse ont été préparés afin de remplacer les colorants coûteux à base de ruthénium. En outre, les électrolytes liquides étant volatils et corrosifs, ce qui limite considérablement la stabilité des DSSCs, des électrolytes solides à base de polymères ont été étudiés comme alternative.